Emission Tunability, Triplet State Harvesting, and Photon Up-conversion Properties in Selected Organic-Inorganic Hybrid Cu(I)-Based Frameworks

विद्या वाचस्पति की

उपाधि की अपेक्षाओं की आंशिक पूर्ति में प्रस्तुत शोध प्रबंध

A thesis submitted in partial fulfillment of the requirements for the degree of Doctor of Philosophy

द्वारा / By

जॉय चटर्जी / Joy Chatterjee

पंजीकरण सं. 20162016 / Registration No. 20162016

शोध प्रबंध पर्यवेक्षक: प्रो. पार्थ हाजरा / Thesis Supervisor: Prof. Partha Hazra

भारतीय विज्ञान शिक्षा एवं अनुसंधान संस्थान पुणे

INDIAN INSTITUTE OF SCIENCE EDUCATION AND RESEARCH PUNE

2024

Dedicated to my parents,

Mr. Premanshu Chatterjee

Mrs. Atreyi Chatterjee

Declaration

I declare that this written submission represents my idea in my own words and where others' ideas have been included; I have adequately cited and referenced the original sources. I declare that I have acknowledged collaborative work and discussions wherever such work has been included. I also declare that I have adhered to all principles of academic honesty and integrity and have not misrepresented or fabricated or falsified any idea/data/fact/source in my submission. I understand that violation of the above will be cause for disciplinary action by the Institute and can also evoke penal action from the sources which have thus not been properly cited or from whom proper permission has not been taken when needed. The work reported in this thesis is the original work done by me under the guidance of Prof. Partha Hazra.

Joy Chatterjee

Signature of the student

Certificate

Certified that the work incorporated in the thesis entitled "*Emission Tunability, Triplet State Harvesting, and Photon Up-conversion Properties in Selected Organic-Inorganic Hybrid Cu(I)-Based Frameworks*" Submitted by Joy Chatterjee was carried out by the candidate, under my supervision. The work presented here or any part of it has not been included in any other thesis submitted previously for the award of any degree or diploma from any other University or institution.

Date 05/07/2024

Supervisor

Acknowledgment

I am overwhelmed to be one step closer to completing my incredible PhD journey. Success and failure, ups and downs, sorrow and joy were integral to this scientific upbringing process of PhD curriculum. Hopefully, I have made sufficient progress towards meeting the requirements. At the end of this journey, I want to sincerely thank specific individuals who were associated with me along this journey and contributed to my scientific upbringing.

First of all, I would like to sincerely acknowledge my thesis supervisor, **Prof. Partha Hazra**, for providing me with the opportunity of working in his lab at IISER Pune. His inspiring guidance and ceaseless motivation have always been instrumental to me. I am thankful for his support and invaluable insights he has shared throughout my research journey. I would like to sincerely thank my Research Advisory Committee (RAC) members, **Prof. Pankaj Mandal (IISER Pune)**, **Prof. Pramod P. Pillai (IISER Pune)**, and **Prof. Divya P. Ottoor (Savitribai Phule Pune University)**, for presiding over my RAC meetings, and providing valuable insights through scientific discussions.

I would like to thank my senior lab members (**Dr. Rajkumar**, **Dr. Sagar**, **Dr. Bibhisan**, **Dr. Konoya**, **Dr. Aslam, and Dr. Imtiyaz**) who trained me in several scientific and technical aspects as well as maintained a friendly atmosphere in the lab. I am especially grateful to **Dr. Rajkumar**, **Dr. Sagar**, and **Dr. Konoya**, who generously trained me in handling lab equipment and developing approaches toward experimental design. I am indebted to my present lab members (**Mr. Abhijit**, **Mr. Madhusudan**, **Ms. Sundaravalli**, **Ms. Anwesha**, **Dr. Sandhya**, and **Ms. Priyanka**) for joining my scientific endeavor, maintaining the spontaneous relationship and group activities. I am especially thankful to my colleague and friend, **Mr. Abhijit**, for his companionship, generous assistance, and immense scientific discussions.

I sincerely acknowledge all our collaborators who have significantly contributed to my research projects, **Prof. Pankaj Mandal (IISER Pune)**, **Prof. Mukul Kabir (IISER Pune)**, and **Prof. Atikur Rahman (IISER Pune)**. I am thankful to **Dr. Prakash Panwaria** for his insights and for performing theoretical calculations in my projects. I would like to thank **Ms. Riteeka Tanwar**, **Ms. Anupama S.**, **Mr. Avinash Mahapatra**, **Mr. Sajid Saikia**, **Mr. Vijay Vittal**, and **Dr. Madan D. Ambhore** for their generous effort and contributions to my research projects.

I am thankful to **Prof. Shabana Khan (IISER Pune)** and **Dr. Sakya S. Sen (NCL Pune)** for giving me the opportunity to work with them and for providing several insights. I would like to sincerely acknowledge **Prof. Angshuman Nag (IISER Pune)** for providing accessibility to the low-temperature measurements.

I would like to thank the current Chair (**Prof. Nirmalya Ballav**) and former Chairs (**Prof. H. N. Gopi** and **Prof. M. Jayakannan**) of the Department of Chemistry, IISER Pune for their excellent leadership and for encouraging scientific exchange within the department. I would like to acknowledge the contribution of the current director, **Prof. Sunil S. Bhagwat**, and former directors, **Prof. Jayant B. Udgaonkar** and **Prof. K. N. Ganesh**, for their contribution to building up the institution and providing a vibrant research environment.

I would like to thank all my friends here at IISER Pune. Especially, I am forever indebted to my friend **Indra** for his unconditional support during my ups and downs. He has always been my friend, philosopher, and guide, nurturing my intellectual growth with boundless love and care. I consider myself truly blessed to have him as my friend. My gratitude extends to his wonderful family members (**Nanu**, **Jethu**, **Chhotopisi**, and **Papai**) for their warm affection and constant care. I am profoundly indebted to my senior and friend, **Korak da**, for his unwavering support, care, and guardianship. He has always been a source of inspiration, wisdom, and motivation for me. Together, Indra and Korak da built a second family for me, a *home-away-from-home*. I am indebted to my friends, **Suman**, **Sumit da**, and **Susmita di** for their presence, good wishes, and support. I am thankful to my friends **Moushakhi** and **Prakash** for their immense help and good wishes in several aspects from research to daily life. I am thankful to all my batchmates for maintaining a lively relationship and exchange.

I am grateful to **Prof. Nishad Matange (IISER Pune)** for giving me the opportunity to learn music from him. His distinguished personality and wisdom have always been a source of inspiration, motivation, and guidance for me during my time at IISER Pune.

I would like to thank all the non-teaching staff and technical experts of our department and IISER Pune, especially **Mr. Mayuresh Kulkarni**, **Dr. Sandeep Kumar Mishra**, **Mr. Nitin Dalvi**, **Mr. Mahesh Jadhav**, **Dr. Abhijit Biswas**, **Dr. Sandeep Kanade**, and **Mr. Sanjay Kumar Meena** for their generous help in need.

I would like to sincerely thank **IISER Pune** and **DST-SERB, Govt. of India** for the fellowship and research funding. I deeply acknowledge the **National Supercomputing Mission, Govt. of India** for facilitating easy access to theoretical calculations with high computational cost. I am thankful to **DST-SERB, Govt. of India** and **Infosys Foundation** for covering the expenses of my participation in the international conference.

I am indebted to my teachers from my College and School years, especially **Mr. Samir Kumar**, **Mr. Kashinath Das**, **Dr. Sudipta Chatterjee (Serampore College, Hooghly, West Bengal)**, **Dr. Subhasree Ghosh (Serampore College, Hooghly, West Bengal)**, **Dr. Rudraksha Nath Bhattacharya (Serampore College, Hooghly, West Bengal)**, **Prof. Uday Chand Ghosh**

(Presidency University, Kolkata, West Bengal), and **Dr. Kunal Roy (Scottish Church College, Kolkata, West Bengal)**, who played a crucial role in laying the foundation of my knowledge in Physics, Chemistry, and Mathematics during my academic journey.

I am thankful to my friends, **Hijal Chatterjee**, **Dibya Sankar Chattopadhyay**, and **Dwaipayan Roychowdhury** for their companionship and generous contribution to my intellectual development. I am also thankful to Kakima (**Mrs. Bani Chatterjee**) and Kaku (**Mr. Dilip Kumar Chatterjee**) for their affection, support, and contribution to my academic journey.

Ma (**Mrs. Atreyi Chatterjee**) and Baba (**Mr. Premanshu Chatterjee**) are the happiest to see me at this stage. I cannot thank them enough for whatever I have achieved today, and the achievement is owing to their wisdom, unconditional love, support, faith, and sacrifice. I dedicate my PhD thesis to them. I am forever indebted to my Dada (**Mr. Subhro Chatterjee**) and Boudi (**Mrs. Riya Chatterjee**) for being constant support and well-wishers. They have always been a source of unwavering care and love for me. I am forever indebted to my **Dadin (maternal grandmother)**, **Katan (paternal grandmother)**, my nearest family members, my aunts (**Mrs. Pratima Chakrabarti**, **Mrs. Sarbani Chatterjee**, **Mrs. Indrani Chakraborty**), uncles (**Late Mr. Makhan Ranjan Chakrabarti**, **Mr. Sanjay Chatterjee**, **Mr. Pradip Chakraborty**), brothers and sisters (**Mr. Siddhartha Shankar Chakrabarti**, **Mr. Saptarshi Chatterjee, Mrs. Saswati Chatterjee Bansal**), Kakima (**Mrs. Shila Chatterjee**), and Boudi (**Mrs. Papiya Chakrabarti**) for their unconditional love and support.

I am deeply indebted to the rich cultural heritage and essence of my motherland, India and Bengal. Their timeless traditions, vibrant culture, and profound wisdom have nurtured my soul and played a pivotal role in shaping who I am today.

Synopsis

The thesis aims to explore the emission tunability, triplet harvesting pathways, and non-linear photon up-conversion properties in some selected Cu(I) and Cu(I)-iodide-based clusters, complexes, and coordination polymers by using ligand engineering-based methodologies. The triplet harvesting pathways particularly include phosphorescence, thermally activated delayed fluorescence, and self-trapped excitonic emission. The central motivation of the thesis evolves from a perspective of establishing the structure-property relationship in the aforementioned systems. The thesis is divided into five chapters,

Chapter 1: Introduction to the Photoluminescence of Cu(I)-Based Emitters: Fundamentals and Photophysical Properties.

In this chapter, I introduce the phenomenon of luminescence and its background, particularly from the perspective of coinage metal-based luminescent materials. Furthermore, the previous luminescence studies of copper nanoclusters and their applications have been discussed. The role of triplet state harvesting in enhancing the luminescence yield and the phenomenon of thermally activated delayed fluorescence (TADF) were introduced. TADF in coinage metal-based emitters, as well as several Cu(I)-iodide-based clusters, complexes, and polymers have been discussed. Moreover, the photon up-conversion properties were also introduced and elaborated. In the concluding part, I describe the motivation and objective of the thesis.

Chapter 2: Intrinsic-to-Extrinsic Emission Tuning in Luminescent Cu Nanoclusters by *in-situ* Ligand Engineering.

This chapter focuses on the development of a unique methodology for tuning emission from blue to green-yellow in luminescent Cu nanoclusters (CuNCs) through an *in-situ* ligand replacement process. At first, the successful synthesis of dithiol-templated blue and red-emitting CuNCs in a single-pot process was achieved. This was followed by an *in-situ* ligand replacement using the oxidized form of the L-ascorbic acid, which was used as a reducing agent in the nanocluster formation process. The ligand-replaced nanocluster exhibits a green-yellow emission. The blue emissive nanoclusters exhibit excitation-independent emission from metal-centered core states, while the green-yellow emissive nanoclusters show excitation-dependent emission from ligand-centered surface states. The study utilizes excited state dynamics and ultrafast spectroscopy to distinguish between these emissions as well. The emission tuning process is driven by the oxidized form of the reducing agent, eliminating the need for an external agent, covering almost the entire visible spectrum, and showcasing excellent emission tunability. L-ascorbic acid plays a significant role in modulating the emission properties of

nanomaterials, with potential applications in ligand engineering. The red emissive nanoclusters were found to be covalently linked dithiol-templated CuNC superstructures, suitable for LED applications. The nanocluster system and the developed protocol carry the potential for the fabrication of highly efficient LED devices with broadband color tunability and applications in multicolor printing technology**.**

Chapter 3: Activation of TADF in Photon Up-converting Crystals of Dinuclear Cu(I)-iodide Complexes by Ligand Engineering.

This study investigates the development of highly emissive Cu(I)-iodide complexes through ligand engineering by eradicating a particular decay pathway and thereby activating TADF. The study presents a novel strategy for achieving TADF in Cu(I)-iodide complexes, which traditionally suffer from inefficient TADF due to competitive cluster-centered (^{3}CC) states. By utilizing ligand engineering the Cu···Cu bonding interaction was suppressed in Cu_2I_2 complexes, which successfully enhances the exciton recovery via TADF from (metal+halide)-to-ligand charge transfer ($^{1/3}$(M+X)LCT) states, achieving high quantum yields and substantial structural rigidity. The complex-1 coordinated with 3-cyanopyridine has a higher Cu···Cu bonding interaction and exhibited radiative decay through ^{3}(M+X)LCT and ^{3}CC states. On the other hand, when two 3-cyanopyridine on each Cu atom were replaced by a PPh_3 ligand, the Cu···Cu bonding interaction diminished due to an increase in the Cu-Cu distance and the radiative decay was found to occur via TADF from $^{1/3}$(M+X)LCT states. This was utilized in the fabrication of a warm-white light-emitting pc-LED. Due to the presence of high charge-transfer nature and bulk phase polarizability, the non-linear photon upconversion properties of these complexes were studied. The complex-1 showed excellent third-harmonic generation properties, and both the complexes exhibit multi-photon excited luminescence. Overall, the findings of this research provide valuable insights into designing efficient OLED devices and photon upconversion systems, highlighting the potential of Cu(I) iodide complexes as a versatile platform for advanced light-emitting materials.

Chapter 4: Ligand-mediated Staircase-to-Cubane Structural Switch in Photon Up-converting Crystals of Cu(I)-Iodide-based Polymers: From TADF to Self-trapped Excitonic Emission.

In this work, we report a staircase-to-cubane structural switch in Cu(I)-iodide-based polymers resulting from the different coordination behavior of two π*-acceptor ligands. The staircase polymeric structure coordinated with 3-cyanopyridine shows efficient exciton recovery through TADF from (metal+halide)-to-ligand charge transfer ($^{1/3}$(M+X)LCT) states having a singlet-triplet splitting value of ~0.009 eV. On the other hand, the cubane polymeric structure

coordinated with 3-aminopyridine exhibits strong cluster-centered (^{3}CC) orange emission at room temperature. The temperature-dependent photoluminescence studies prove that the ^{3}CC state, in this case, appears as a self-trapped excitonic state with a high degree of exciton-phonon coupling. The (M+X)LCT emission also emerges at the low-temperature region, which is much higher in energy compared to that of the staircase polymer. It shows a much higher electron-donating effect of the amino group compared to the cyano group in modulating the emission energy of the charge transfer state. The high degree of exciton-phonon coupling in the centrosymmetric crystal of the cubane polymer also leads to the emergence of third-order non-linearity. These polymer crystals exhibit efficient two-photon excited luminescence properties as well. Additionally, we have synthesized a non-centrosymmetric Cu(I)-iodide coordination polymer. Non-centrosymmetry in these Cu(I)-iodide-based polymeric crystals can lead to the emergence of several prodigious properties like second-harmonic generation, bulk photovoltaic effect, and so on. We report a non-centrosymmetric Cu(I)-iodide staircase polymer coordinated with 2-amino-3-methylpyridine. The crystal structure and non-covalent interactions in the bulk phase have been reported. These properties can be utilized in several applications, such as laser technologies, photocatalysis, self-powered photodetectors, and so on.

Chapter 5: Thesis Summary and Future Outlook.

In this chapter, we summarize the key results of all the chapters in a collective manner and provide a perspective of future research directions based on the outputs of this thesis.

Table of Contents

Chapter 1:

Introduction to the Photoluminescence of Cu(I)-Based Emitters: Fundamentals and Photophysical Properties

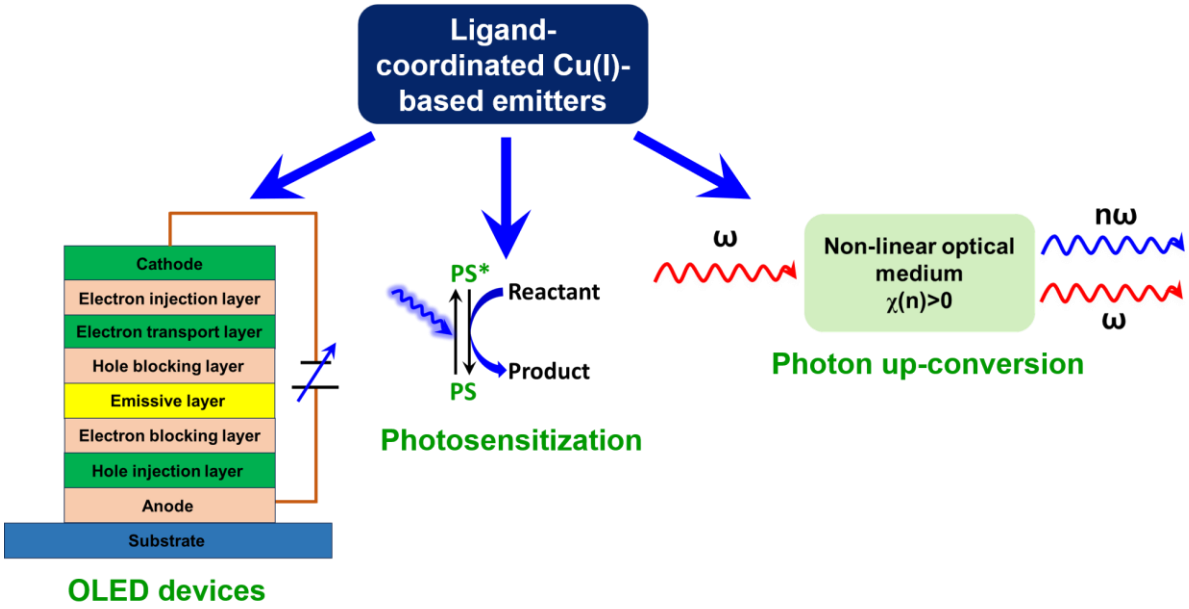

1.1. Photoluminescence of coinage metal-based materials: The background

Photoluminescence is one of the most useful and relevant outcomes of light-matter interaction that is prevalent in numerous natural processes. The term "luminescence" is derived from the Latin word “lumen”, meaning light.[1] It was first coined as “luminescenz” by German physicist Eilhard Wiedemann in 1888.[1] Different types of luminescence are classified based on their excitation methods. Specifically, photoluminescence refers to the emission of light resulting from the direct photoexcitation of the emitting species. The atoms or molecules are excited to a higher energy quantum state by absorbing light, which is known as an optically excited state. This is followed by the consequent release of the excited state energy resulting in the radiative relaxation of the atom/molecule to the ground state through ejecting lower energy photons. Atoms are devoid of any vibrational or rotational degrees of freedom, as a result, they only have electronically excited states. On the other hand, molecules have multiple rotational and vibrational degrees of freedom. As a result, the electronic excited states are entangled with the vibrational and rotational motions of the molecules. Therefore, the ground state and excited state electronic energies of a molecule are expressed as a function of nuclear coordinates and represented by a diagram called the Jablonski diagram[2] (**Figure 1.1**). The molecule excited to a higher electronic state can release its energy through several processes such as vibrational relaxation, internal conversion, geometry reorganization, radiative relaxation, and so on (**Figure 1.1**). It can also undergo radiationless transition to other states having different spin multiplicities, which is known as intersystem crossing (**Figure 1.1**). The first unified presentation of photoluminescence was given by Sir George Gabriel Stokes in 1852, where he described this phenomenon as the dispersive reflection of light.[3] Since the publication of this historic paper on photoluminescence by Stokes, the journey of photoluminescent organic and inorganic compounds started. The study of photoluminescence in coinage metal complexes with d^{10} configuration was first reported by Dori and co-workers in 1970.[4] Coinage metals are the nontoxic and nonradioactive elements under group 11 of the periodic table. These are also called noble metals because of their strong resistance towards corrosion and abundance in pure form. Photoluminescence properties of coinage metal-based materials have been studied extensively, which expands from inorganic/organometallic complexes to higher order frameworks like metal clusters, coordination polymers, etc.[5–7] These materials find broad applications in the fields of optoelectronics, photosensitization, photocatalysis, bioimaging, sensing, and so on.[5–7]

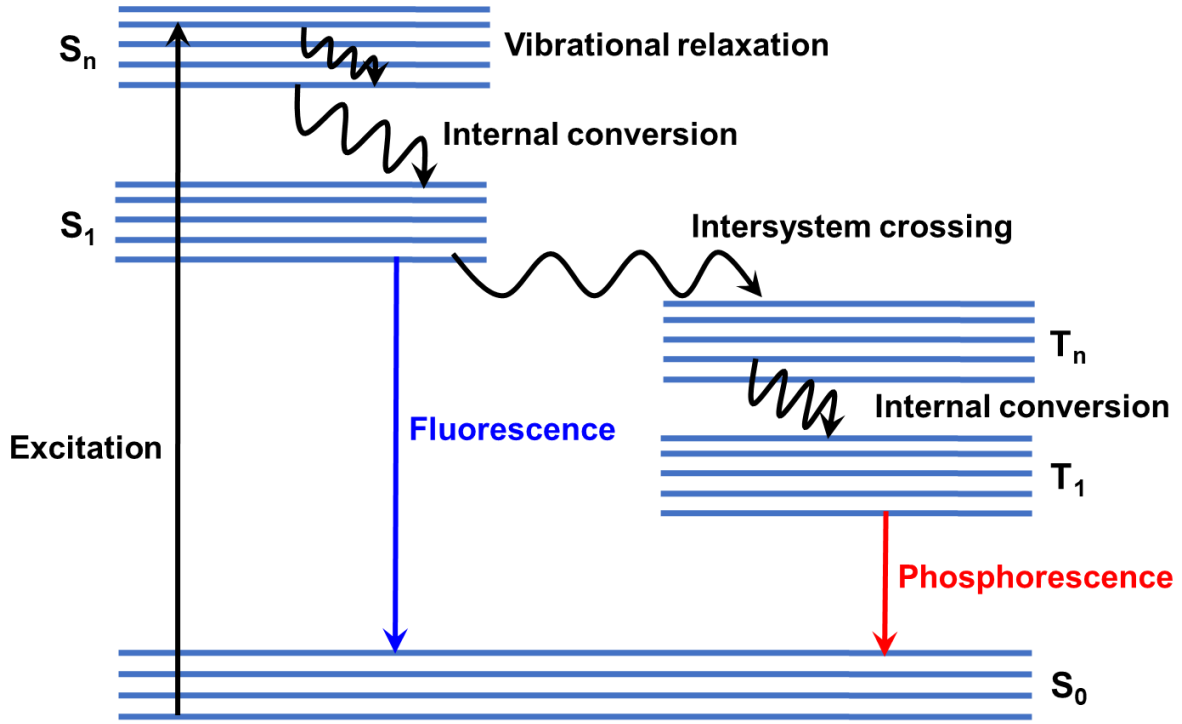

Figure 1.1. Jablonski diagram for a typical molecular emitter. S_0, S_1, T_1, S_n, and T_n represent singlet ground state, lowest singlet excited state, lowest triplet excited state, higher excited singlet states, and higher excited triplet states respectively.

1.2. Coinage metal nanoclusters

1.2.1. Gold and silver nanoclusters: luminescence, protecting ligands, and applications

The journey of the luminescent metal nanoclusters started in early 2000 when Dickson and co-workers synthesized gold nanoclusters, stabilized by poly(amidoamine) (PAMAM).[8] They synthesized a series of gold clusters containing 5, 8, 13, 23, and 31 gold atoms, satisfying the magic number criteria outlined by the well-known Jellium model for metal clusters. These size-adjustable gold clusters exhibit tunable emission ranging from UV to near IR wavelengths (**Figure 1.2a**). The absorption and emission features of these clusters are directly correlated to $N^{-1/3}$, where N is the number of gold atoms.[8,9] These characteristics are in accordance with the spherical Jellium model for metal clusters, unlike the semiconductor nanocrystals or quantum dots, which have a dependence upon $N^{-2/3}$.[8,9] Subsequently, it was realized that these particles are structurally and behaviourally distinct from quantum dots because allowing these particles to grow further would result in the formation of bulk metal instead of forming bulk semiconductors. Hence, these new types of nano-sized materials were named metal nanoclusters. In terms of electronic structure, metal nanoclusters exhibit discrete molecule-like energy states, whereas their larger counterparts, metal nanoparticles, possess continuous energy levels and display the remarkable phenomenon of surface plasmon resonance (**Figure 1.3**).[10]

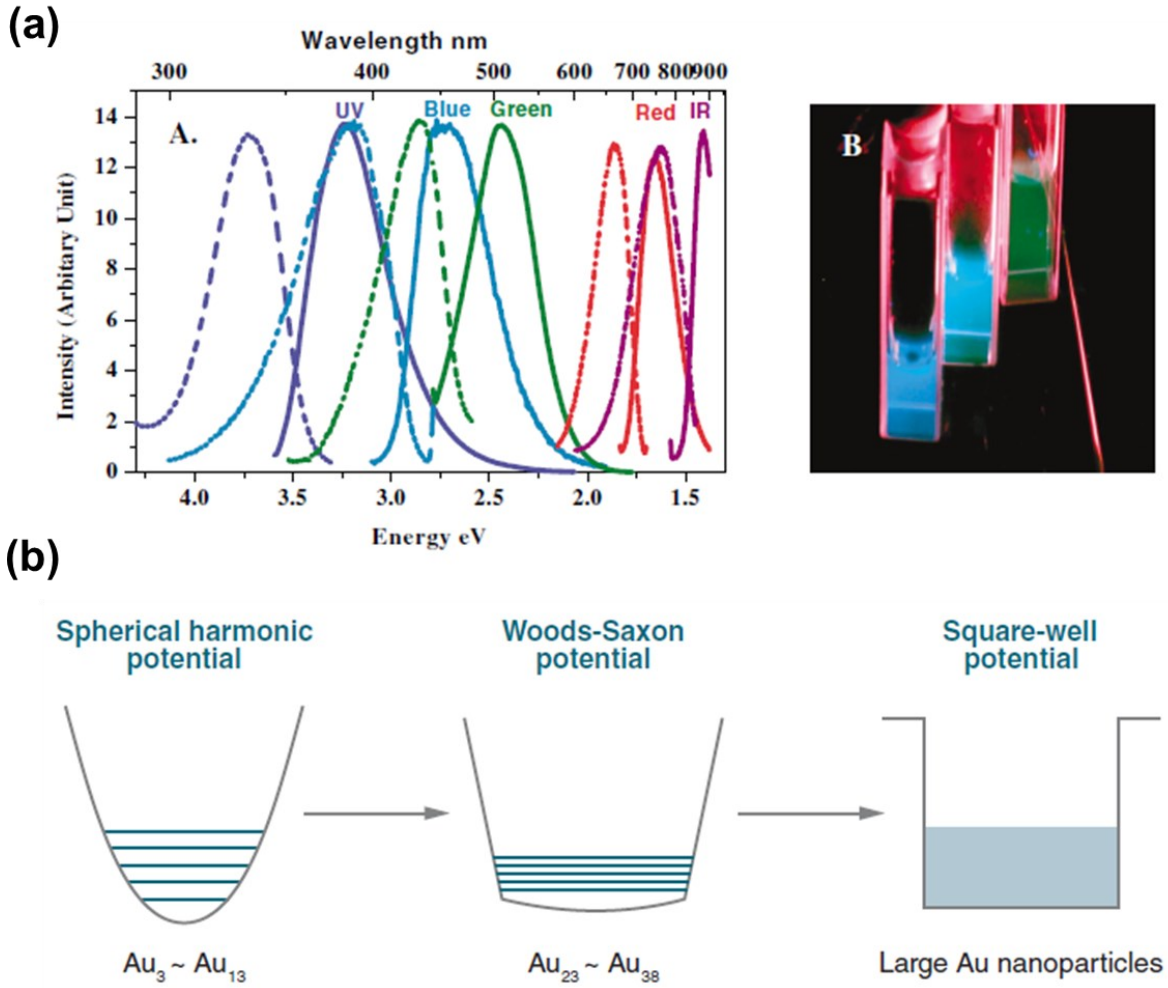

Figure 1.2. (a) Excitation spectra (dashed) and emission spectra (Solid) of Au nanoclusters of different sizes indicating size-dependent emission (left), cuvette images of emission coming from Au nanoclusters with different sizes (excited at 366 nm) (right). *Reprinted with permission from ref.*[8]; *Copyright (2004) by the American Physical Society.* (b) The schematic shows size-dependent surface potentials of Au nanoclusters across different size scales. For the smallest Au clusters (ranging from Au_3 to Au_{13}), the cluster-emission energies can be accurately described by the energy-scaling law $E_{Fermi}/N^{1/3}$, where N represents the number of atoms in each cluster. This indicates that the electronic structure transitions in these small Au clusters are well-represented by a spherical harmonic potential. As the cluster size increases, minor anharmonicities start to distort the potential well. At larger sizes, this potential gradually transforms into a Woods-Saxon potential surface, and eventually, it becomes a square-well potential, which is characteristic of electrons in large metal nanoparticles. *Used with permission of Annual Reviews, Inc., from ref.*[9]*; permission conveyed through Copyright Clearance Center, Inc.*

The discretization of the energy levels within this size domain is attributed to the quantum confinement effect, which is responsible for its size-dependent emission characteristics.[10–12] Therefore, the metal nanoclusters are considered as a "missing link" between single metal atoms and plasmonic metal nanoparticles (**Figure 1.3**). Over the past decade, there has been

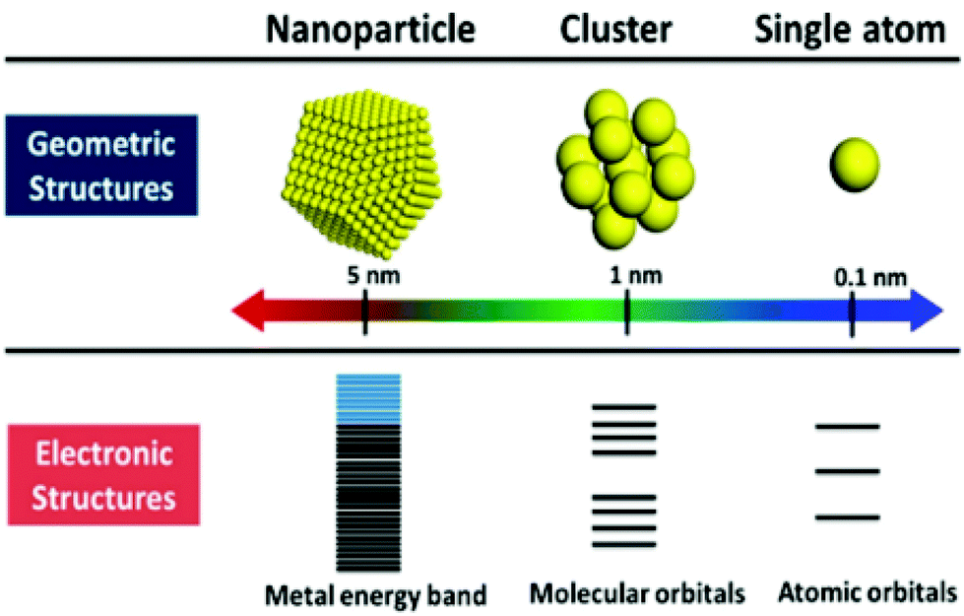

Figure 1.3. Size-dependent evolution of electronic structure in metal nanoclusters. *Reused with permission from the American Chemical Society.*[10]

significant exploration and investigation into noble metal nanoclusters, particularly those composed of gold and silver. These nanoclusters have been synthesized and extensively examined utilizing alkane-thiols as well as other amido or phosphine ligands to serve as protective agents.[13–15] The utilization of these ligands is driven by their robust affinity to the metal surfaces, ensuring stability, and facilitating bright photoluminescence across various environments. Coinage metal nanoclusters stabilized by several kinds of thiol, amido, and phosphine groups have opened up promising avenues in various fields such as optoelectronics, catalysis, ion sensing, bio-sensing, and bio-imaging.[16] Their stability and distinct photoluminescence characteristics make them potential candidates for a wide array of applications. Notably, they have emerged as compelling alternatives to both inorganic quantum dots and organic fluorescent dyes owing to their photostability, high photoluminescence yield, water-solubility, lesser cytotoxicity, and size-tunability.[12,17,18]

Initially, much of the research focused on the synthesis, self-assembly, and optical properties of gold and silver nanoclusters.[12,18] Gold and silver nanoclusters were synthesized using proteins as templates; for instance, bovine serum albumin (BSA), human serum albumin (HSA), pepsin, and so on.[19–21] The reduction of gold and silver ions is achieved using $NaBH_4$ as a reducing agent. and several thiol and amino acid residues of these proteins are responsible for the effective stabilization of these nanoclusters. Alongside this, several PAMAM-based dendrimers have also been effectively utilized in synthesizing these nanoclusters.[22,23] Subsequently, several small molecular ligands having thiol and amine functional groups were also employed as protecting agents in the nanocluster synthesis. These ligands include

glutathione, cysteine, cysteamine, 6-mercaptohexanoic acid, 3-mercaptopropionic acid, 2-phenylethanethiol, aromatic thiols, several amino acids, and so on.[24–30] Along with the wide range of applications, the photoluminescence mechanisms have also been explored by using ultrafast spectroscopic methods.[31–33] However, gold and silver are heavy and expensive metals; on the contrary, the use of lighter coin-age metal, copper, associated with the same group, is more cost-effective than gold and silver. Additionally, Higher thermal and electrical conductivity makes copper nanomaterials appropriate for fabricating energy harvesting and storage devices.[34] Furthermore, copper has significant roles in various biological processes as well.[35,36] Hence, the focus of the research shifted towards developing and exploring the potential of copper nanoclusters with a view to identifying their unique properties and potential applications.

1.2.2. Copper nanoclusters: an overview

Initial research works on copper nanoclusters were focussed mainly on deciphering multiple synthetic strategies and characterization methods. The typical synthetic protocols are template-assisted, ligand-assisted, electrochemical synthesis, and etching method. In 1998 Crooks and co-workers published a paper where they used poly(amidoamine) (PAMAM) starburst dendrimers as capping agent to synthesize CuNCs.[37] Hydroxyl surface groups of PAMAM interacts with the cluster surface. Dendrimer was mixed with $CuSO_4$ in aqueous solution, followed by reduction of Cu(II) ions to CuNCs by $NaBH_4$. In the same year, Balogh and co-workers introduced the synthesis of CuNCs stabilized with PAMAM in organic solvent.[38] In 2001, McCarley's group synthesized Cu(II)–poly(propylene imine) dendrimer complexes with a di-aminobutane (DAB) core in methanol. Sequentially the complex was converted into reduced CuNCs with the addition of $NaBH_4$ in it.[39] Another photo-reductive synthesis of CuNCs was reported by Zhang et al. They demonstrated the synthesis of CuNCs by using poly(methacrylic acid) template modified with penta-erythritoltetrakis 3-mercaptopropionate, followed by photoreduction of the Cu(II) aqueous solution under UV light irradiation.[40] Apart from these polyethyleneimine (PEI) and polyvinylpyrrolidone (PVP) has also been used as templates.[41,42] DNA is known to be another important template for copper nanoclusters. In 2010, Mokhir's group showed that random double-stranded DNA (dsDNA) can be utilized as capping agent to stabilize CuNCs by using L-ascorbic acid as mild reducing agent. The resulting nanoclusters showed photoluminescence intensity in the range of 580–600 nm.[43] By changing the length of DNA strand, photophysical properties of the nanoclusters can be modulated. However, effect of the sequence and arrangement of the nucleobases on the

formation and properties of CuNCs were still unknown. In 2015, Ouyang and co-workers studied the formation of CuNCs with various dsDNA sequence combinations. They concluded that random sequences or a handful of specific sequences were not able to form luminescent nanoclusters, rather adenine and thymine rich sequences were able to encapsulate the Cu ions resulting in to the formation of red luminescent species.[44]. Moreover, Wang's group utilized different ssDNA templates for synthesizing CuNCs, including random ssDNA, poly(adenine) (poly A), poly(thymine) (poly T), poly(cytosine) (poly C), and poly(guanine) (poly G).[45] Besides these works, Prof. Mukherjee and co-workers has also used glutathione capped CuNCs as a discriminating sensor for identifying single base mismatched DNA and fully matched DNA sequence.[46] Proteins and peptides were also used as templates. Prof. T. Pradeep known for his extensive studies in exploring structural aspects of metal nanoclusters by using mass spectroscopic techniques, showed BSA stabilized Cu nanoclusters to be an efficient sensor for Pb^{2+} ions.[47] Liao and co-workers introduced a synthesis in 2015, where they added H_2O_2 solution into the BSA-$CuSO_4$ mixture.[48] In this work, H_2O_2 acted as an oxidizing agent which cleaved the disulfide linkages of BSA protein and increased the degree of exposure of free amino groups, which can accelerate the formation rate of CuNCs. On the other hand, Wang and co-workers prepared BSA-protected CuNCs by applying another reducing agent hydrazine hydrate.[49] Yeast extract containing various kinds of proteins, carbohydrates and amino acids, was also applied as a template and at the same time as a reducing agent to synthesize CuNCs.[50] Huang's group introduced trypsin as a reducing and protecting agent to synthesize CuNCs.[51] Chicken egg white was used as a template to synthesize CuNCs.[52] In 2020, Prof. Chattopadhyay and co-workers synthesized bovine serum albumin (BSA) capped CuNCs which had an effective anti-cancer activity against human cervical and lung cancer cells.[53] He also showed another CuNC assembly capped with lysozyme and used for labelling cervical cancer cells.[54] Degrees of freedom of bigger macromolecular templates are quite lesser in number, hence sometimes the control over the size of the nanocluster, no longer remains specific. This results into the formation of bigger nanoparticles which are non-luminescent in nature. So, in addition to these efforts, researchers introduced small molecules and ligands which can protect the nanoclusters, and keeping its fluorescent nature unperturbed. Chen and co-workers prepared CuNCs by using 2-mercapto-5-n-propylpyrimidine (MPP) as capping ligand and $NaBH_4$ as a reducing agent.[55] Following this pathway, researchers have used different kind of small molecular capping agents such as GSH, penicillamine, phenylethanethiol, dihydrolipoic acid, mercaptobenzoic acids, cysteamine, L-Cysteine, and 3-mercaptotrimethoxysilane.[56–65] All these are thiolate and amine-based ligands. The binding

sites of the ligands, along with their conformational diversities and reaction conditions, played a very crucial role in modulating the photophysical properties of the CuNCs. All these photophysical modulations contributed in biolabeling, bioimaging, metal ion sensing, and various other applications. Chang and co-workers used three isomers of mercaptobenzoic acid as capping agents to synthesize CuNCs.[61] By using different positional isomers one can change the optical properties of nanoclusters. Other than thiolate and amine-based molecules, carboxylate residue molecules are also reported to be good precursor for synthesizing CuNCs. Tannic acid, cholic acid, and ascorbic acid have been used to synthesize highly luminescent CuNCs.[36,66,67] Along with these works, Mukherjee and co-workers showed glutathione-capped CuNCs to be used as a cell imaging probe for marking cancerous cells and detecting Fe^{3+} ions selectively.[68] The same group in 2015, illustrated a blue emitting human serum albumin (HSA) capped CuNC which showed efficient FRET with coumarin-153 dye and also was fabricated to be an efficient nanothermometer.[69] Purkayastha and his group applied L-cysteine capped CuNCs to find the nature of various hydrophilic and hydrophobic pockets of BSA protein.[70] The same group also showed an efficient photoinduced electron transfer (PET) from transition metal complexes to cyan-emitting CuNCs.[71]

1.2.3. Role of ligands in the nanocluster emission

In the initial phases of nanocluster research, the mechanistic framework of the nanocluster emission was primarily based on the quantum confinement effect and the metal-centered excited states. Metal-centered excited states are mainly comprised of the inter-band transitions from d-band to sp-band; and the quantum confinement effect results in the discretization of the d-band and sp-band.[72,73] The size-dependent emission tunability of nanoclusters also comes from the quantum confinement effect in the metal-centered excited states. Consequently, the emission tunability of CuNCs was directly correlated to the spherical Jellium model like the AuNCs, and the relation between the emission energy and the size of the respective nanoclusters was given by $E_g=E_{Fermi}/N^{1/3}$. Prof. Rogach and co-workers have discussed in their review article that emission properties of copper nanoclusters protected by several nitrogen and sulfur donor ligands like the poly(methacrylic acid), PVP/dihydrolipoic acid, mercaptobenzoic acids, penicillamine, are not in accordance with the spherical Jellium model.[74] In these cases, emission energy does not follow the size of the nanoclusters obtained from the mass spectroscopic techniques. Consequently, the Jellium model is broadly applicable in the nanoclusters, which are protected with weakly bound ligands and show singlet emission in the

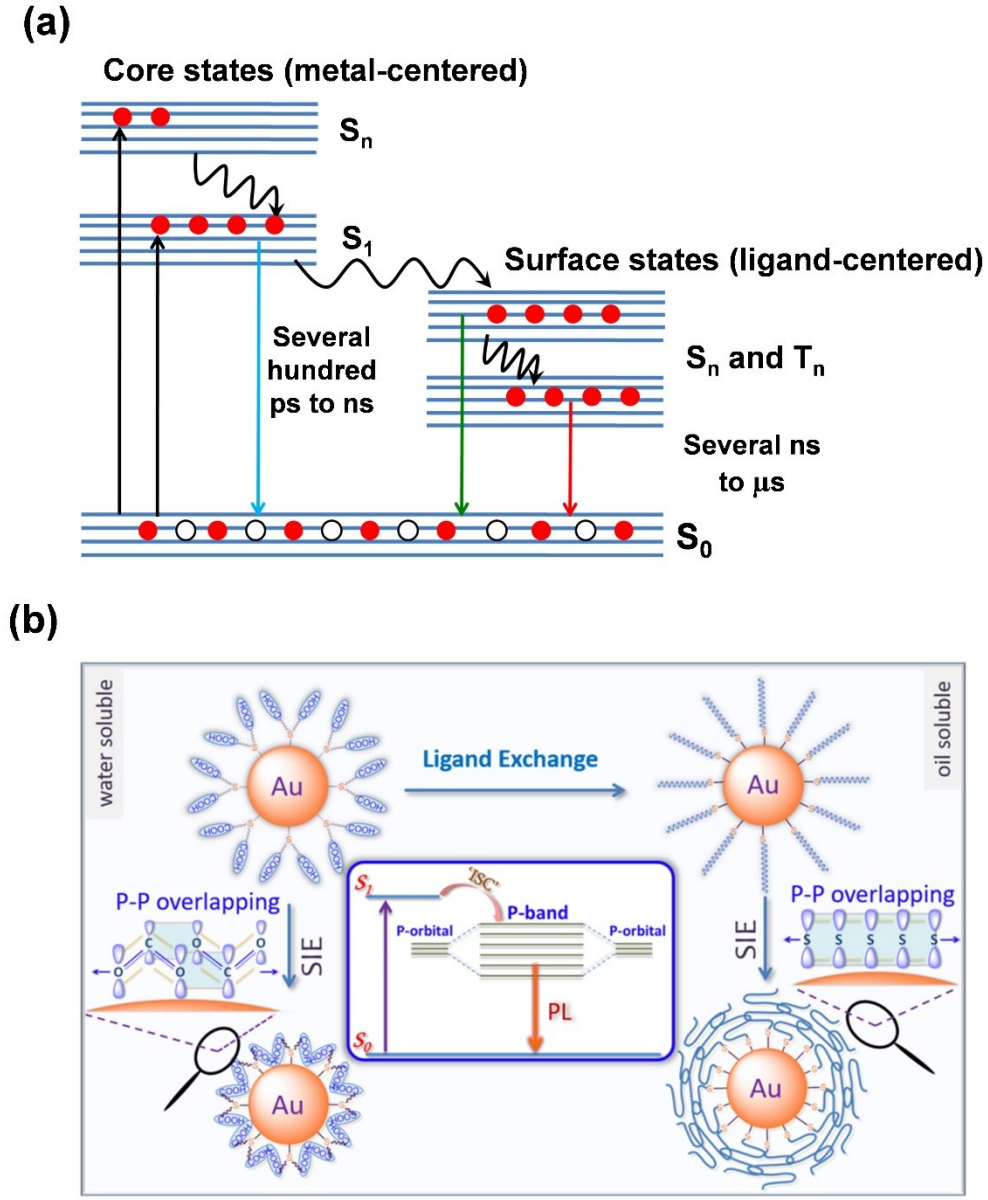

Figure 1.4. (a) Metal-centered and ligand-centered excited states and their respective mechanisms, (b) Ligand-assembly-mediated P band intermediate state dominates photoluminescence emission. The schematic illustrates the ligand exchange process and the solvent-induced emission (SIE) properties of Au nanoclusters. The inset shows the energy-level structure of Au nanoclusters in a water and ethanol mixed solution. The p-band, formed by the overlapping p-orbitals of electron-rich sulfur and oxygen heteroatoms from well-organized surface ligands, serves as an intermediate or dark state to modulate the optoelectronic properties. *Reused with permission from Springer Nature*.[72]

UV to blue region. In case of strongly protected nanoclusters, Cu-ligand interfacial surface states have crucial role to play. Further research explores that nitrogen and sulfur-donor-protected copper nanoclusters have metal-centered excited states and ligand-centered excited states (**Figure 1.4a**).[75–78] Metal-centered excited states are characterized by a predominant contribution from metal orbitals, whereas ligand-centered excited states exhibit a higher

involvement of ligand orbitals. When emission arises from metal-centered excited states following excitation, it's termed as metal-centered emission (MCE) or intrinsic emission. This type of emission typically conforms to Kasha's rule, displaying excitation-independent emission and falls under the category of fluorescence. Conversely, emission originating from ligand-centered excited states is referred to as ligand-centered emission (LCE) or extrinsic emission (**Figure 1.4b**). LCE is notably red-shifted compared to MCE and encompasses a mixed emission behavior, combining fluorescence and phosphorescence characteristics. With appropriate structural adjustments, tuned excited singlet and triplet states may lead to the observation of delayed fluorescence.

1.2.4. Journey towards emission tunability and emission enhancement

Several methodologies have been explored in order to tune the emission wavelength of the copper nanoclusters. For instance, metal atom tailoring, ligand engineering, modulation of electronic effects of the ligands, regulation of intra- and inter-cluster metallophilic interactions, structural modulations in the self-assembly, and so on. Panda and co-workers reported the cellulose-directed synthesis of copper nanoclusters, where they obtained size-tailored copper nanoclusters with metal compositions Cu_{12}, Cu_{20}, and Cu_{34}.[79] These nanoclusters exhibited sequential color tunability with blue, cyan, and green emissions. Patra and co-workers synthesized $Cu_{34\text{-}32}$ and Cu_{25} from the etching of larger plasmonic Cu nanoparticles.[80] Red emissive $Cu_{34\text{-}32}$ clusters were synthesized at room temperature by using excess glutathione and blue emissive Cu_{25} cluster was synthesized at higher temperature by digestive ripening process. Red emissive $Cu_{34\text{-}32}$ clusters also exhibited aggregation-induced emission. Mak and co-workers recently reported a strategy for the formation of cocrystals of two carboranylthiolate-protected copper nanoclusters with different metal compositions.[81] The cocrystal exhibits a dual emission comprised of green and orange bands emerging from Cu_{16} and Cu_{14} clusters, respectively. The incorporation of Cu atoms as dopants also has been reported to enhance the stability and photoluminescence of gold nanoclusters.[82] The emission tunability has also been achieved by tailoring the electronic effects of the ligands. Zhang and co-workers synthesized a series of aromatic thiol-templated self-assembled CuNC architectures, where the electron-donating and electron-withdrawing effects were employed to tune the yellow-to-red emission of these self-assembled architectures.[83] These architectures were nanoribbons, and they used -F, -Cl, -Br, $-CH_3$, and -OMe groups as para-substituents of protecting aromatic thiol ligands. It was found that the degree of orbital hybridization increases with increasing electron-donating effect of the ligand and sequential red-shift of the emission

band was observed. Patra and co-workers have shown morphological evolution in the self-assembly of CuNCs by utilizing the positional isomerism of dimethylbenzenethiol ligand.[84] These morphologies include rods, platelets, and ribbon-like structures. Zhang and co-workers demonstrated that the self-assembly-induced emission of CuNCs can be modulated by tuning the inter-nanocluster distance. These modulations can be controlled by carefully arranging the experimental conditions. In this way, green-to-red emission tunability was achieved.[85] Hao and co-workers prepared glutathione-capped copper nanoclusters (GSH-CuNCs) as fluorescent materials, exploring their assembly in various organic solvents to enhance fluorescence properties.[86] The resulting assemblies exhibit multicolor fluorescence emission, which can be tuned from yellow to purple by changing the solvent. Additionally, these assemblies serve as stimuli-responsive nano-switches with reversible control. In their seminal paper, Zhang and co-workers presented a method to enhance the luminescence intensity of 1-dodecanethiol (DT)-capped copper nanoclusters (Cu NCs) through self-assembly, leading to strong emission.[87] The compact and ordered assemblies of Cu NCs, formed via self-assembly, enable control over emission properties, with resulting structures exhibiting mechanochromic and thermochromic luminescent properties suitable for applications in white light-emitting diodes. The competitive modulation of inter-cluster and intra-cluster cuprophilic interaction is the key factor in the emission tuning in this case. Liu and co-workers in another seminal paper, introduced a pH-guided method to create stable luminescent protein/copper nanocluster hybrids.[88] Using l-cysteine, CuNCs exhibit reversible pH-responsive behavior, forming stable red-emitting aggregates at pH 3.0 and becoming soluble with weak luminescence at extreme pH values. In the study reported by Wu et al., it was demonstrated that the self-assembly of ligand-capped Au_{15} nanoclusters into 2D sheets revealed the role of dipolar and van der Waals attractions.[89] By controlling these interactions, the thickness and morphologies of the assembled structures can be manipulated. Konishi and co-workers showed that [core+exo]-type $[Au_8]^{4+}$ clusters shift from fluorescence to phosphorescence-type emission when they aggregate.[90] The aggregated clusters emit strongly at ~700 nm in the solid state, demonstrating the potential for unique materials design. Xie and co-workers showed a method to impart amphiphilicity to sub-2-nm metal nanoclusters by patching hydrophilic clusters with hydrophobic cations.[91] By preparing amphiphilic $Au_{25}(MHA)_{18}$ nanoclusters through phase-transfer reactions, the clusters demonstrate good solubility in solvents with different polarities and self-assemble similarly to molecular amphiphiles, expanding their potential applications in research. Our group introduced a new method for producing stable fluorescent copper nanoclusters (CuNCs) using l-cysteine within reverse micelles.[75] The CuNC fluorescence, exhibiting excitation-dependent

emission, was analyzed through time-correlated single photon counting (TCSPC) and femtosecond fluorescence up-conversion, revealing intricate dynamics from core and surface states.

1.3. Importance of triplet-state harvesting for emission enhancement and thermally activated delayed fluorescence (TADF)

1.3.1. Triplet-state harvesting.

Enhancing the emission yield of luminescent coinage metal-based materials remains a critical objective across various disciplines such as optoelectronics, photosensitization, and bioimaging. This pursuit involves concerted efforts to suppress non-radiative decay pathways in luminescent materials, like self-assembly, and increasing rigidity of the surroundings, etc., as mentioned in the previous section. However, a persistent challenge arises from the fundamental principles of spin statistics governing radiative recombination in luminescent materials. According to the spin-statistics theorem, electrically excited carrier recombination inside photoluminescent materials produces 25% of the singlet excitons and 75% of the triplet excitons.[92] In conventional organic emitters, 75% of the triplet excitons are lost through non-radiative decay and only show feeble luminescence at very low temperatures within a solid matrix.[93] As a result, the internal quantum efficiency of the emitter becomes limited to 25%. Therefore, it's very important to utilize the triplet excitons through radiative pathways so that higher internal quantum efficiency can be achieved and this field of utilizing triplet excitons is called triplet state harvesting. In the case of photo-excitation, the molecule is optically excited to a higher energy electronic excited state with conserved spin-multiplicity. However, it can undergo a non-radiative isoenergetic spin-inversion leading to the formation of another excited state with different spin-multiplicity.[94,95] The spin-inversion process is not allowed in the doctrine of non-relativistic quantum mechanics; however, within the framework of relativistic quantum mechanics, this spin-inversion phenomenon is governed by spin-orbit coupling and is called intersystem crossing (ISC).[94,95] In heavy metal complexes, spin-orbit coupling is reasonably strong primarily due to a larger effective nuclear charge, and as a result, the rate of intersystem crossing is also much higher compared to organic emitters.[96] Therefore, transition metal complex emitters emerged as a potential candidate for efficient triplet-state harvesting. In 1998, Forrest and co-workers first reported a red-emitting phosphorescent complex, 2,3,7,8,12,13,17,18-octaethyl-21*H*,23*H*-porphyrine platinum (II) (PtOEP) which exhibited 23% of internal quantum efficiency (IQE) and 4% of external quantum efficiency (EQE) upon embedded with a fluorescent host emitter and was used in the organic light-emitting diode

(OLED).[92] Afterward, several platinum (II) and iridium (III) complexes were utilized in the development of phosphorescent OLEDs and included in commercially processed displays like mobile phones, television, and so on.[97–102] However, the development of these emitters encountered several significant limitations. These heavy metals are the least earth-abundant and most expensive; alongside these metals can cause severe contamination of agricultural lands and water bodies.[103–105] Due to the presence of low-energy triplet states, the emission colors of the phosphorescent OLEDs are limited to green and red in most cases; hence, the blue-emitting OLEDs are extremely important to producing high-resolution displays.[106] Another intrinsic limitation related to the strong vibrational coupling of triplet excited states, which results in triplet-polaron annihilation (TPA).[106] Polarons are quasiparticles formed due to the strong interaction of excitons with the phonon modes in the solid state. Polarons with high energy levels are responsible for the degradation of devices[106], while unstable radical cations within the complex lead to either complex isomerization or ligand dissociation[107,108]. Therefore, novel methodologies for triplet-state harvesting are needed to develop future-generation OLED devices.

1.3.2. Thermally activated delayed fluorescence (TADF)

In response to the need for potential candidates for future-generation OLEDs, Adachi and co-workers introduced TADF as a potential mechanism for fabricating highly efficient OLED devices.[93] The phenomenon of TADF or E-type delayed fluorescence has been known for a long time. It was first noticed in eosin molecules and was marked by the letter "E" which stands for eosin.[109] The emitter in its singlet excited state can undergo radiationless spin-inversion induced by spin-orbit coupling and form a triplet state through the ISC process. The energy difference between singlet and triplet states is given by ΔE_{ST}. When the energy gap (ΔE_{ST}) between the singlet and triplet states is minimal and comparable to the thermal energy at room temperature, the population of triplet states can revert back to the singlet state (**Figure 1.5**). Consequently, emission occurs from the singlet state, causing a delay compared to the fluorescence process, which typically occurs at the nanosecond timescale. This separate emission mechanism is termed delayed fluorescence (**Figure 1.5**). The process of transitioning from the triplet to the singlet state is called reverse intersystem crossing (RISC). Given that the rate of delayed fluorescence involves a thermally assisted energy uphill process, the energy gap between the singlet and triplet states is evidently crucial for achieving efficient TADF. The RISC rate constant k_{RISC} can be expressed by the Boltzmann distribution relation given as[110],

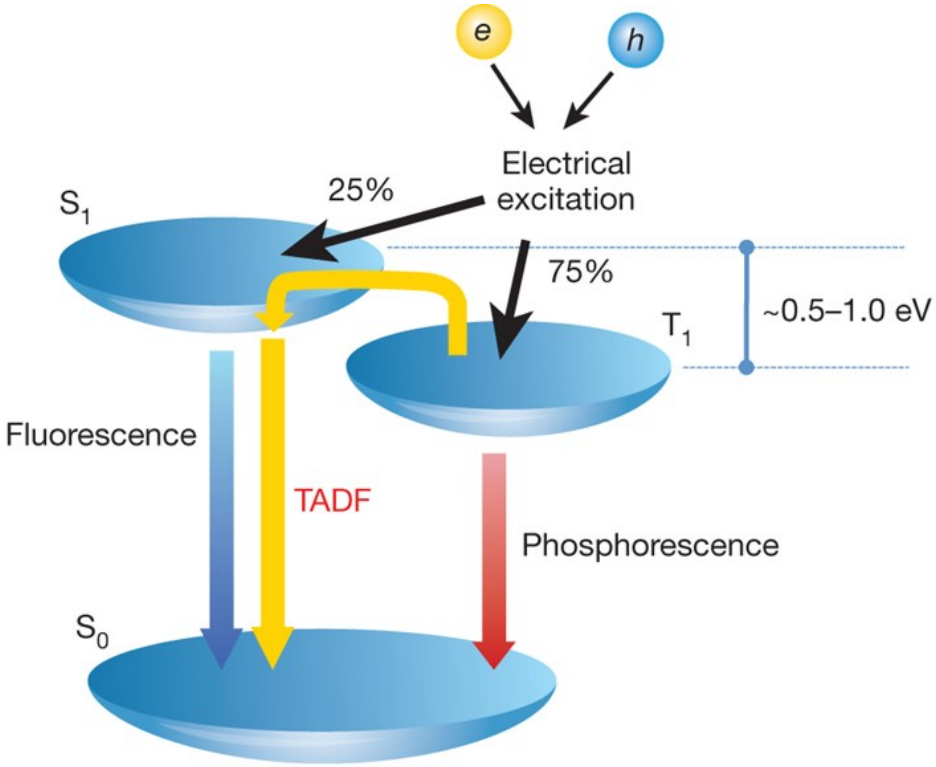

Figure 1.5. Schematic representation of the TADF process. *Reused with permission from Springer Nature.*[93]

$$k_{RISC} \propto \exp\left(-\frac{\Delta E_{ST}}{k_B T}\right) \qquad \text{Eq 1.1}$$

ΔE_{ST} can be defined as the activation energy gap between the single and lowest triplet state, and it can be correlated with exchange stabilization energy (K_{HL}) according to the following equations[111]

$$E_{S_1} = h_H + h_L + J_{HL} + K_{HL} \qquad \text{Eq. 1.2}$$

$$E_{T_1} = h_H + h_L + J_{HL} - K_{HL} \qquad \text{Eq. 1.3}$$

$$\Delta E_{ST} = 2K_{HL} \qquad \text{Eq. 1.4}$$

$$J_{HL} = \iint d\vec{r_1}\, d\vec{r_2}\, H(\vec{r_1})\, H(\vec{r_1})\, \frac{1}{r_{12}}\, L(\vec{r_2})\, L(\vec{r_2}) \qquad \text{Eq. 1.5}$$

$$K_{HL} = \iint d\vec{r_1}\, d\vec{r_2}\, H(\vec{r_1})\, H(\vec{r_1})\, \frac{1}{r_{12}}\, L(\vec{r_2})\, L(\vec{r_2}) \qquad \text{Eq. 1.6}$$

Here, h_H and h_L denote the one-electron energy of the HOMO and LUMO orbitals, respectively, while J_{HL} is the Coulomb repulsion energy between electron 1 on the HOMO and electron 2 on the LUMO, and K_{HL} denotes the corresponding electron exchange energy. It is evident from Eq. 1.4 that the ΔE_{ST} is directly correlated to the exchange stabilization energy. In order to obtain a small ΔE_{ST}, the integral K_{HL} between frontier molecular orbitals (FMOs) is required to be as small as possible, indicating that a very small orbital overlap between the highest occupied molecular orbital (HOMO) and lowest unoccupied molecular orbital (LUMO) is necessary to induce a strong RISC process.[112] In order to obtain a small ΔE_{ST}, one of the efficient ways is to design molecules having strong electron-donating and electron-accepting groups so that the HOMO and LUMO are spatially separated, thereby giving rise to a very small exchange stabilization energy K_{HL}.[113,114] Several pioneering works have been reported since then by using donor-acceptor-based charge-transfer organic emitters where HOMO and LUMO are spatially well-separated resulting in a very small ΔE_{ST} and high RISC rate.[115–118]

1.3.3. Coinage metal complexes as TADF emitters

The major shortcoming of organic TADF luminophores is their weak spin-orbit coupling (SOC), which limits the rate of intersystem crossing (ISC). In purely organic molecules, the radiative decay rate of the lowest singlet state (S_1) is typically one to three orders of magnitude faster than the reverse intersystem crossing (RISC) rate.[119] Consequently, these molecules exhibit both prompt fluorescence (PF) on a nanosecond timescale and delayed fluorescence (DF) on a microsecond to millisecond timescale.[120–122] The extended lifetime of DF introduces a significant risk of efficiency roll-off at high current densities in OLEDs.[123–126] This issue arises because the population of triplet excitons becomes saturated in the lowest triplet state (T_1), preventing the consumption of additional excitons and leading to exciton-quenching processes such as triplet-triplet annihilation, triplet-polaron annihilation, polaron quenching, or field-induced quenching.[127,128] On the other hand, organometallic and other coordination complexes containing transition metals show remarkably stronger SOC compared to purely organic moieties. As a result, the DF lifetime is significantly reduced, and the efficiency roll-off effects at higher current densities would be curtailed. In this context, organometallic and coordination complexes containing coinage metals have emerged as potential candidates due to their d^{10} electronic configuration.[129,130] The d^{10} configuration has a particular advantage as it prevents the excited complex from undergoing non-radiative decay via d-d transitions resulting in an intrinsically high quantum yield. In order to induce sufficient charge transfer character, the metal is coordinated to a ligand having low-energy vacant π^* orbitals. Here, the

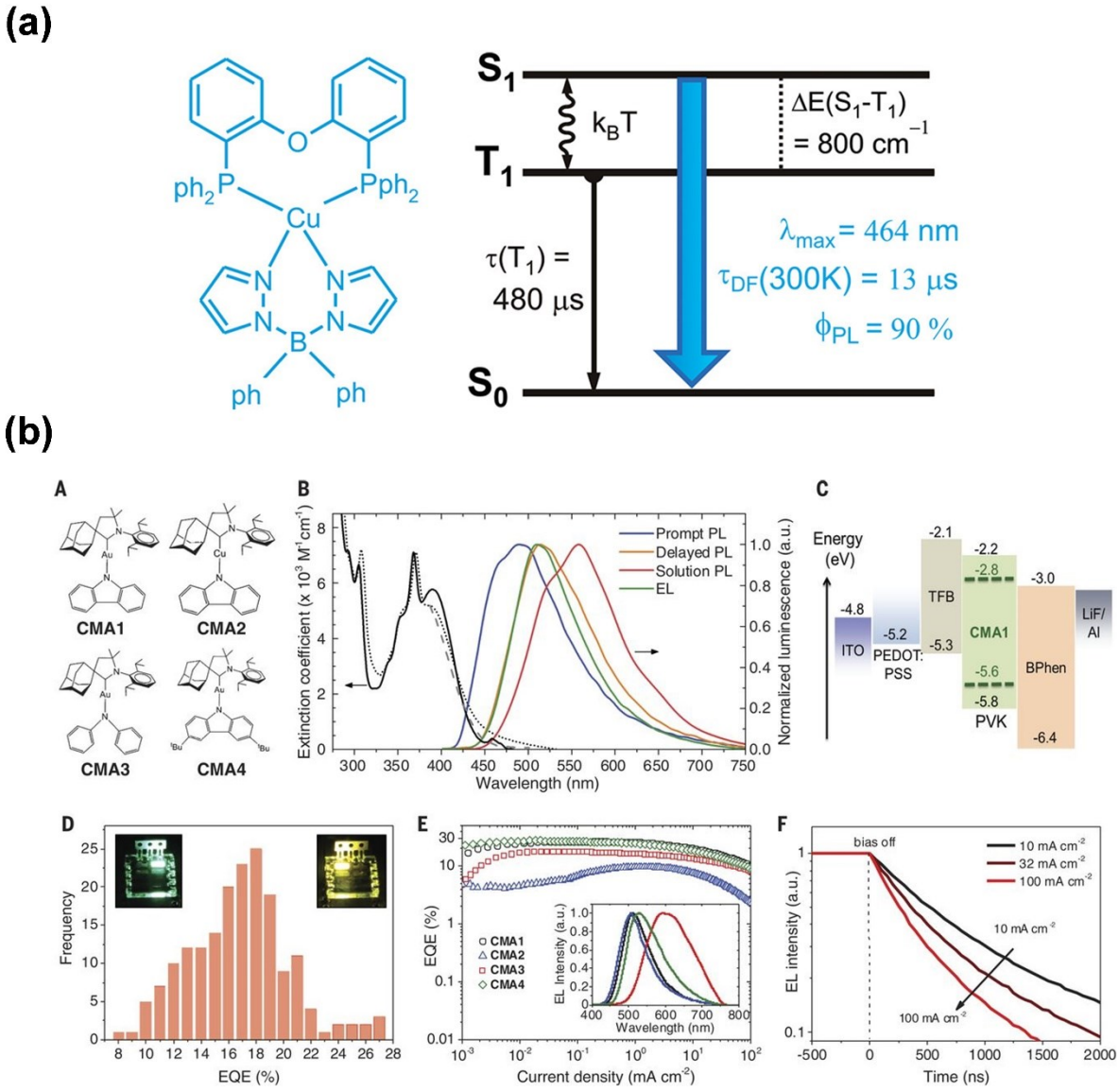

Figure 1.6. (a) Cu(pop)(NN), with pop = bis(2-(diphenylphosphanyl)phenyl)ether and NN = bis(pyrazol-1-yl)borohydrate (pz_2BH_2), a blue-cyan TADF emitter and its pictorial depiction of the TADF mechanism. *Reprinted with permission from ref.*[134]*; Copyright (2011) American Chemical Society.* (b) Structures, absorption, and emission spectra of CMA emitters along with their energy diagram of the device, electroluminescence performances, EQE (%) vs. current density plot, and transient electroluminescence profiles. *From ref.*[140]; *Reprinted with permission from AAAS.*

filled d orbitals constitute the highest occupied molecular orbitals and the lowest unoccupied orbitals are located over the π* orbitals of the ligand. Therefore, the low-energy optical transitions are metal-to-ligand charge transfer (MLCT) in nature and have sufficient spatial separation between HOMO and LUMO.[131,132] As a result, the ΔE_{ST} becomes reasonably lower, and the complexes can exhibit a higher RISC rate (**Figure 1.6a**). Consequently, numerous seminal works have emerged, focusing on coinage metal-based TADF emitters. Peters and co-workers reported a TADF-active bis(phosphine)diarylamido dinuclear copper(I) complex with

a 57% quantum yield.[132] OLEDs with the complex as an emissive dopant achieved a maximum external quantum efficiency of 16.1%, effectively harvesting triplet excitons through delayed fluorescence. McMillin and co-workers investigated how structural distortions affect the photophysical properties of copper phenanthroline complexes.[133] Different ligands were examined, revealing that flattening distortions strongly impact spectroscopic properties, especially when bulky substituents are absent in the 2,9 positions of the ligand. Steric interactions and packing forces play crucial roles in determining photoluminescence behavior. Yersin and co-workers introduced luminescent copper(I) complexes showing high emission quantum yields of up to 90%.[134] Their emission arises from metal-to-ligand charge-transfer states, with thermally activated delayed fluorescence (TADF) behavior enabling efficient singlet and triplet exciton harvesting, promising for applications like OLEDs and light-emitting electrochemical cells (LEEC). Yersin and co-workers in their another paper, discussed TADF in Cu(I) complexes, emphasizing small energy separations ($\Delta E_{ST} < 1000$ cm^{-1}) for high quantum yields and short decay times.[135] Efficient TADF results from minimal HOMO–LUMO overlap, with case studies showing radiative decay times under 5 µs. In 2015, Yersin and co-workers presented a new class of low-cost, brightly luminescent Cu(I) compounds for OLEDs and other photonic applications.[136] These materials exhibit over 90% quantum yield with short emission decay times. Emission arises from both the singlet (80%) and triplet (20%) states due to TADF, and effective SOC significantly reduces overall decay time and enhances performance. In 2017, Yersin and co-workers reported an Ag(I) complex exhibiting TADF with 1.4 µs decay time and 100% quantum yield.[137] Its performance is due to a small singlet-triplet energy gap, highly allowed transitions, and a rigid structure, making it ideal for OLED applications. In 2017, Yersin and co-workers designed and presented four Ag(I) complexes as efficient TADF emitters.[138] Among them, the structure with high molecular rigidity showed the best performance with a 1.4 µs decay time and 100% quantum yield, due to the suppression of non-radiative decay pathways. Despite the impressive achievements of these emitters, an intrinsic obstacle is associated with the MLCT excited states that restricts the use of these complexes in OLED devices and photosensitization applications. In MLCT transitions, an electron is excited from the metal-centered HOMO to the ligand-centered LUMO. This causes the metal center, initially in a +1 oxidation state to be transiently oxidized to a +2 oxidation state (M(II)) with a d^9 configuration. Consequently, the complex undergoes a Jahn-Teller distortion, shifting from a tetrahedral to a square-planar geometry.[139] This significant excited state distortion leads to substantial energy loss through non-radiative decay, resulting in a weak emission yield. To mitigate this energy loss, Bochmann and co-workers developed a new class

of linear coinage metal complexes.[140] These complexes feature a metal coordinated with a π electron-donating amide group on one side and a π*-accepting cyclic aryl amino carbene (CAAC) on the other (**Figure 1.6b**). This class of complexes exhibits low-lying ligand-to-ligand charge transfer (LL'CT) excited states and have spatially well-separated HOMO and LUMO, resulting in a small ΔE_{ST} and a high rate of RISC. The absence of metal-centered d orbitals in the optical transitions of these complexes also eliminates the possibility of Jahn-Teller-like distortions in the excited state. They fabricated OLED and achieved nearly 100% internal quantum efficiency and high brightness (**Figure 1.6b**). These complexes utilize triplet states efficiently, with luminescence within 350 nanoseconds and a near-zero singlet-triplet energy gap, maintaining strong oscillator strength. In 2019, Thompson and co-workers in their seminal paper, reported two-coordinate CAAC-Cu(I)-amides achieving >99% photoluminescence efficiency and microsecond lifetimes, resulting in efficient blue-emitting OLEDs.[141] These complexes suppress nonradiative decay and reduce reorganization energies, with temperature-dependent interactions between singlet and triplet states. Eventually, several pioneering investigations have been reported in this field, including other coinage metals, modulating the donor substituent effect, modulating conformational flexibility of the donor moieties, introducing other carbene moieties (monoamido-amino carbenes, diamido carbenes, N-heterocyclic carbenes), substituting the functional groups in the carbene moieties, regulating the energy of LL'CT and locally excited (LE) states, and so on.[142,143,152–157,144–151] In order to minimize the excited state distortion another class of coinage metal complexes was introduced. In these complexes, two metal atoms are connected with two halide atoms, which act as a bridge between two metal atoms, forming a rhombic M_2X_2 structure coordinated with organic ligands.[135,158] The halide-bridged structure provides additional rigidity to coinage metal complexes, which reduces the extent of the distortions in the excited states. Amongst all the halides, iodide was found to be the most suitable bridging halide due to its larger size and higher polarizability compared to other halides.[159] These properties make iodide ideal for forming stable covalent bonds with two metal atoms simultaneously, thereby stabilizing the bridged rhombic complex. The fully filled p orbitals of iodide also participate in forming HOMO of this rhombic structure along with the d orbitals of the metal atom. As a result, the charge transfer process of this class of complexes is called (metal+halide)-to-ligand charge transfer ((M+X)LCT).[158] Additionally, the spatial separation between HOMO and LUMO remains unaltered like MLCT complexes, thereby retaining the ΔE_{ST} much lower and the RISC rate higher. Several higher-order structures of this particular class of complexes were also synthesized, including cubic clusters, stair-case-shaped trimeric structures, coordination

polymers, and so on. These structures exhibit excellent thermochromic and mechanochromic properties, along with finding suitable applications in the field of optoelectronics.

1.4. Triplet state harvesting in Cu(I)-iodide-based clusters, complexes, and coordination polymers

1.4.1. Cu(I)-iodide clusters: (Metal+halide)-to-ligand charge transfer ((M+X)LCT) and cluster-centered (CC) emission

The term Cu(I)-iodide cluster typically refers to the $Cu_4I_4L_4$ (L = ligand) cluster. Here, four Cu atoms and four I atoms are corner-shared in a distorted cubic framework, with each copper atom coordinated to four organic ligands that have low-lying π* orbitals.[160–162] In these clusters, HOMO is located over the Cu (3d) and I (5p) orbitals, on the other hand, the LUMO is situated over the low-lying π* orbitals of the ligand (**Figure 1.7a, 1.7c**).[160–162] As a result, the lowest energy electronic transition is (M+X)LCT in nature (**Figure 1.7a, 1.7c**). This state is comprised of spatially well-separated electron and hole, thereby reducing the singlet-triplet energy gap (ΔE_{ST}), and can exhibit TADF. Interestingly, in these clusters, an electron can also be excited from the HOMO to a higher energy vacant orbital with significant Cu···Cu bonding character, leading to the formation of another excited state (**Figure 1.7b, 1.7d**). In this transition, no ligand-centered orbitals are involved, and the charge density remains confined within the copper iodide cluster. Therefore, this excited state is called the cluster-centered (CC) excited state (**Figure 1.7b, 1.7d**).[160–162] This energy of this state is highly sensitive towards Cu···Cu bonding interaction, hence a decrease in the Cu-Cu distance can significantly stabilize the energy of this state. Additionally, this state undergoes a higher distortion upon the vertical excitation resulting in a large Stokes' shift compared to (M+X)LCT emission. The ^{3}CC state is populated at the expense of ^{3}(M+X)LCT state by overcoming a thermal energy barrier and at room temperature, and ^{3}CC state becomes the most emissive, thereby making (M+X)LCT emission negligible.[160–162] At lower temperatures, the population of the ^{3}(M+X)LCT state cannot overcome the energy barrier due to a lack of sufficient thermal energy, and the proportion of the ^{3}(M+X)LCT emission increases. As a consequence, these Cu_4I_4 cubane-type clusters exhibit excellent thermochromic properties by virtue of a correlated regulation of ^{3}(M+X)LCT and ^{3}CC emission bands.[160–162] The geometric and energetic characteristics of these two states were also explored by means of electronic structure calculations.[163,164] The photophysical properties of these clusters have been explored by several means, such as

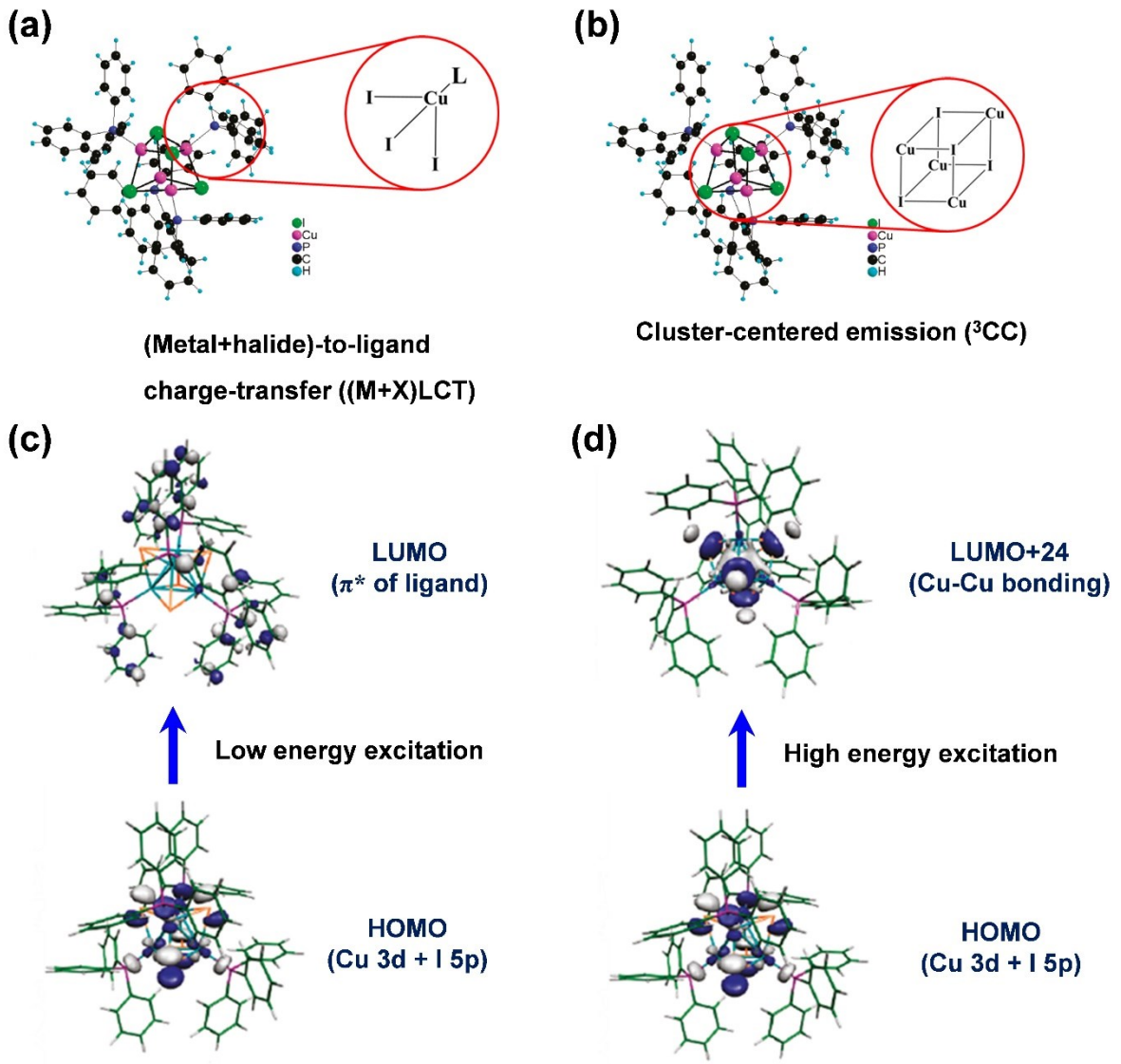

Figure 1.7. Molecular origin of (a) (M+X)LCT emission and (b) CC emission by using $Cu_4I_4(PPh_3)_4$ cluster as an example. (c) HOMO-to-LUMO transition for (M+X)LCT excited state, and (d) HOMO-to-LUMO+24 transition for CC excited state in $Cu_4I_4(PPh_3)_4$ cluster. *Adapted with permission from ref.*[160]*; Copyright (2011) American Chemical Society.*

modulations in the electronic effects of the ligands, modulation of the accessibility of the low-lying π* orbitals, and so on. In 2011, Perruchas and co-workers synthesized three Cu_4I_4 cubane-type clusters by coordinating with triphenylphosphine (PPh_3), tricyclopentylphosphine ($Pcpent_3$), and diphenylpropylphosphine (PPh_2Pr) as ligands.[160] These three ligands are electronically different due to differences in the accessibility of low-lying π* orbitals. Amongst these three clusters, $Pcpent_3$ coordinated Cu_4I_4 did not show any (M+X)LCT emission band due to a lack of low-lying π* orbitals, but PPh_3 and PPh_2Pr coordinated Cu_4I_4 clusters exhibited both (M+X)LCT and CC emission bands. These two clusters manifest excellent reversible luminescence thermochromism, and this study represents a thorough demonstration of the origin of these two different emissions. Another seminal work from the same groups showed

structural variation between the cubane- and stair-case-type Cu_4I_4 framework and their different photophysical characteristics.[161] In 2018, Perruchas and co-workers showed the energy of (M+X)LCT states can be regulated by modulating electronic effects in PPh_3 ligand.[162] This led to reversible luminescence thermochromism along with emission tunability in these clusters. Several other ligands like diphenylphosphine substituted dibenzofuran, and pyridine derivatives have been used as ligands in Cu_4I_4 cluster formation, which shows excellent properties like electroluminescence and aggregation-induced emission, and so on.[165–167]

1.4.2. Cu(I)-iodide complexes

Despite exhibiting excellent thermochromic properties and strong CC emission, Cu_4I_4 cubane-type clusters suffer from suppressed (M+X)LCT emission. The lowest exchange stabilization energy is obtained from these charge transfer states, which consequently results in small ΔE_{ST} and shows TADF properties. However, in Cu_4I_4 clusters harvesting the excitons through TADF from $^{1/3}$(M+X)LCT states is not feasible. In this context, Cu_2I_2 rhombic complexes play a crucial role in order to effectively harvest the triplet excitons. These complexes have strong (M+X)LCT emissions, which have been found to manifest efficient TADF. In 2007, Tsuboyama and co-workers explored luminescent copper(I)halide complexes with 1,2-bis[diphenylphosphino]benzene (dppb) as a ligand.[168] These complexes exhibited intense blue-green photoluminescence in the solid state with microsecond lifetimes. In solution, emission was weaker with shorter lifetimes and red-shifted spectra. Proposed models explained the photophysics, and electroluminescence devices using one complex as a green emissive dopant showed moderate efficiency. In 2010, Peters and co-workers synthesized a bis(phosphine)diarylamido dinuclear copper(I) complex with a 57% quantum yield showing E-type delayed fluorescence, confirmed by spectroscopy and photoluminescence decay. In OLEDs, it achieved a 16.1% external quantum efficiency by efficiently harvesting triplet excitons. Its function in OLEDs was further examined using EPR, cyclic voltammetry, and photoluminescence.[132] A modular family of highly emissive PyrPHOS-copper iodide complexes has been synthesized by Bräse and co-workers for potential use in OLEDs.[158] These complexes exhibit excellent photoluminescence properties, with high quantum efficiencies in both powders and thin films. Preliminary testing in devices confirms their suitability for OLED applications. Bräse, Yersin, and co-workers reported a series of highly luminescent dinuclear copper(I) complexes featuring a butterfly-shaped metal-halide core and covering the visible spectrum with quantum yields up to 96%. DFT calculations indicate tunable luminescence via

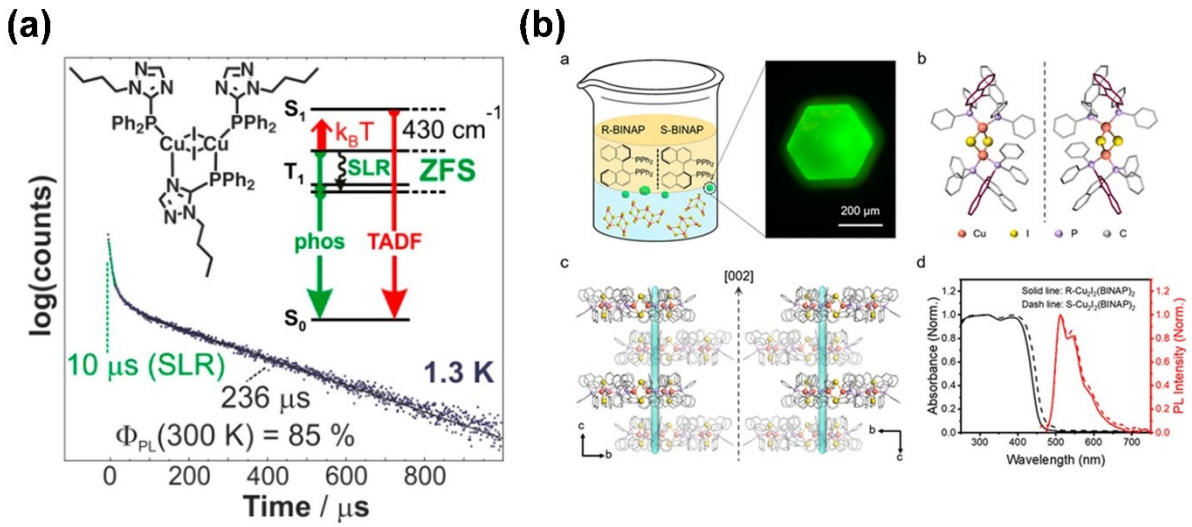

Figure 1.8. (a) Bright TADF emission from $Cu_2(\mu\text{-}I)_2$(1*N*-*n*-butyl-5-diphenyl-phosphino-1,2,4-triazole)$_3$ and its mechanism, *Reprinted with permission from ref.*[173]*; Copyright (2018) American Chemical Society.* (b) Cu_2I_2((R/S)-2,2′-bis(diphenylphosphino)-1,1′-binaphthalene)$_2$ shows circularly polarized TADF emission. *Reprinted with permission from ref.*[171]*; Copyright (2021) American Chemical Society.*

ligand modifications, with emission maxima from 481 nm to 713 nm. One compound shows thermally activated delayed fluorescence with a short decay time of 6.5 µs, making these complexes suitable for singlet harvesting in OLEDs.[169] In 2014, Yersin and co-workers synthesized di-nuclear Cu(I) compounds with TADF showing over 90% quantum yields at 300 K. Emission comes 80% from the singlet state and 20% from the triplet state, enhanced by SOC. This dual emission reduces decay time and is promising for OLED applications.[136] Aravena and co-workers reported efficient TADF (≈80%) in an iodine-bridged CuI dimeric complex and its related monomer.[170] Both show similar singlet-triplet splittings (≈580 cm^{-1}), with the dimer having a longer triplet lifetime (90.0 µs) compared to the monomer (46.0 µs). Calculations reveal iodine's role in SOC and the importance of orbital degeneracies, suggesting design strategies to enhance TADF by modifying nuclearity. Yao and co-workers presented chiral phosphine-copper iodide hybrid clusters and their crystalline assemblies capable of amplified CPL (**Figure 1.8b**).[171] These clusters assemble into chiral crystalline CPL materials, including hexagonal platelet-shaped microcrystals and highly oriented crystalline films. Utilizing the high crystalline feature of the thin film, they demonstrate an electroluminescent device with bright electroluminescence reaching 1200 cdm^{-2}. Two luminescent CuI coordination polymers, Cu-3-tpyb and Cu-4-tpyb, were synthesized by Kato and co-workers.[172] They exhibited blue-to-yellow thermally activated delayed fluorescence (TADF) and mechanochromic luminescence. Emission switched from TADF to phosphorescence upon grinding-induced amorphization. Yersin and co-workers in their seminal paper, showed the

Cu(I) complex $Cu_2I_2(P^N)_3$ exhibits both bright TADF and phosphorescence at room temperature, boasting a total quantum yield of 85% and an emission decay time of 7 μs (**Figure 1.8a**).[173] Its small singlet-triplet energy gap of 430 cm^{-1} facilitates short-lived phosphorescence with a decay time of 52 μs (T = 77 K) and distinct zero-field splitting, making it potentially useful in solution-processed OLEDs for efficient singlet and triplet harvesting. In 2013, Yersin and co-workers again showed that di-nuclear Cu(I) complexes with aminophosphane ligands exhibit strong blue and green luminescence with short decay times.[174] At low temperatures, emission originates from a triplet state, while at higher temperatures, TADF occurs, enabling efficient harvesting of singlet and triplet excitons for potential OLED applications. The study by Bräse and co-workers reported the effects of substituents and modifications on the phosphine moiety of NP-bridging ligands in dinuclear Cu(I) complexes, enabling color tuning across the visible spectrum.[175] Various complexes were synthesized and analyzed, with the best OLED performance observed for Cu-1b-H, achieving high brightness (5900 cd/m^{-2}) and good current efficiency (3.79 cd/A). Kato and co-workers presented two new luminescent dinuclear Cu(I) complexes, Cu-py and Cu-pyz, synthesized with N-heteroaromatic diphosphine ligands.[176] These complexes exhibit solid-state luminescence with emission color tuning from green to reddish-orange and show thermally activated delayed fluorescence at 298 K. Their stability in chloroform allows for the creation of emissive films via solution-doping. Glueck and co-workers synthesized and characterized copper phosphine halide complexes, showing yellow-green luminescence under UV light.[177] The luminescence, attributed to (M + X)LCT excited states, was studied using emission spectroscopy and DFT calculations. Dispersion-corrected DFT provided insights into structural metrics, particularly Cu−Cu distances. Bräse, Baumann and co-workers synthesized a highly stable dinuclear NHetPHOS-complex (complex 1) with a decomposition temperature of 290°C. When incorporated into thin films, complex 1 exhibited very high photoluminescence quantum yield, comparable to other efficient complexes.[178] Yersin and co-workers used femtosecond time-resolved spectroscopy to study the ISC dynamics of two Cu(I) dimers, finding significant variation between them.[179] Correlations between structure and photophysical properties suggest potential for predicting ISC trends, aiding in the development of faster ISC processes for OLEDs. Yao and co-workers presented copper–iodide cluster hybrids with improved solubility and stability, enabling smooth solution-processed thin films with high photoluminescence quantum yields (>70%).[180] These films serve as efficient emissive layers in warm-white LEDs, achieving a maximum external quantum efficiency of 19.1% and high brightness exceeding 40,000 cdm^{-2}, with a

good operational lifetime. Additionally, large-area LEDs and color-tunable LEDs demonstrate the practical potential of these materials for panel displays and solid-state lighting.

1.4.3. Cu(I)-iodide coordination polymers

Cu(I)-iodide coordination polymers are primarily the polymeric form of the dinuclear complexes. The Cu(I)-iodide coordination chain is coordinated with π* acceptor ligands and forms 1D crystalline polymers. The ligands with multiple coordination sites can also simultaneously bind with the Cu(I) centers of two adjacent polymer chains, thereby forming a 2D network. In these polymeric frameworks, the (M+X)LCT nature is retained, and the origin of emission mostly emerges from these states. There are several other polymeric structures have also been reported other than the coordination polymer, which could be collectively designated as organic-inorganic hybrid metal halides. These polymers are structurally rigid, highly crystalline, stable, and solution-processable. In 2015, Li and co-workers developed Cu(I)-iodide-based network structures with strong luminescence and enhanced thermal stability by connecting Cu(I)-iodide rhomboid dimers into robust networks (**Figure 1.9a**).[181] These materials exhibit high photoluminescence (up to 95% quantum yield) and tunable emission energy and color through organic component modifications. Cost-effective, scalable synthesis and high quantum efficiency make these materials promising alternatives for RE-free phosphors in lighting applications. Lang and co-workers synthesized ((pyridinyl)-1H-pyrazolyl)pyridine ligands and reacted them with Cu(I)-iodide, producing eleven diverse complexes with binuclear, 1D, and 2D structures.[182] These complexes, characterized by IR, elemental analysis, X-ray diffraction, and crystallography, exhibit solid-state luminescence. The study shows how different ligand coordination sites affect the structures and luminescence of the Cu(I) complexes. Li and co-workers again in 2017, applied mechanochemical synthesis to synthesize Cu(I)-iodide rhombic complex-based polymers, which exhibit strong luminescence with high internal quantum yields, mostly above 66% and up to 92%.[183] This scalable, cost-effective method reduces the need for auxiliary substances, advancing these materials towards commercialization. In 2018, Zamora and co-workers reported one-pot reactions between Cu(I)-iodide and methyl or methyl 2-amino-isonicotinate create coordination polymers with double zig-zag Cu_2I_2 chains.[184] These polymers, influenced by NH_2 groups, exhibit semiconductor properties and reversible thermo/mechanoluminescence. Nanofibers formed through fast precipitation enable thin-film composites for optoelectronic devices. Kato and co-workers reported two luminescent Cu(I)-iodide coordination polymers, featuring one-dimensional chains with rhombic $\{Cu_2I_2(PPh_3)_2\}$ cores and 1,3,5-tris(m-

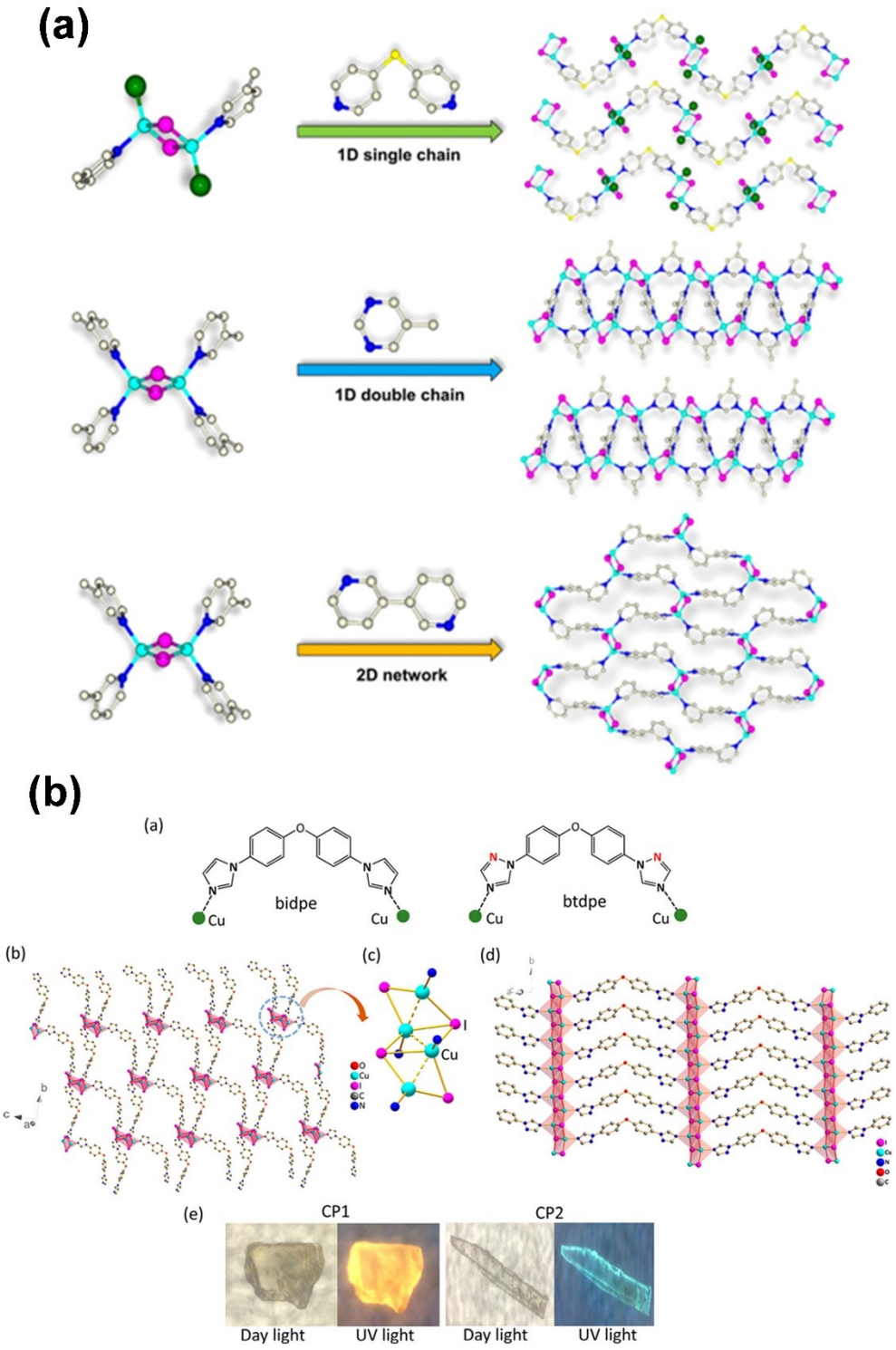

Figure 1.9. (a) Different 1D and 2D network of polymers formed by Cu_2I_2 complexes. *Reprinted with permission from ref.*[181]*; Copyright (2015) American Chemical Society.* (b) Closed staircase polymer and Cu(I)-iodide coordination polymer from two different imidazole-based ligands. The difference in the emission color is also evident. *Reprinted with permission from ref.*[189]*; Copyright (2021) American Chemical Society.*

pyridyl)benzene (m = 3, 4) ligands.[172] They exhibit blue-to-yellow TADF and moderate quantum yields (0.29 and 0.27). Both also show mechanochromic luminescence, switching

from TADF to phosphorescence upon grinding. Li and co-workers developed a novel class of inorganic-organic hybrid semiconductors with multiple-stranded one-dimensional (1D) structures, promising for energy applications.[185] These structures, formed by coordinating copper iodide units with strong-binding organic ligands, exhibit enhanced thermal and photostability and efficient blue excitability. With high internal quantum yields (IQYs), they represent a significant advancement in rare-earth element-free phosphors for energy-efficient lighting devices. Seshadri and co-workers presented three Cu(I) and Ag(I) hybrid iodides with 1,5-naphthyridine and additional triphenylphosphine (PPh_3) ligands, exhibiting intense and adjustable luminescence.[186] By substituting Cu with Ag and adding PPh_3 ligands, the emission color shifts from red to yellow with significantly improved quantum yield. DFT calculations reveal the distinct effects of the inorganic module and organic ligand on electronic structure, offering systematic tuning of bandgap and optical properties. This understanding facilitates the design of new compounds for general lighting applications. In 2020, Wu and co-workers reported a Cu(I)-iodide-based polymer with negative thermal quenching (NTQ) driven by fluctuations in its imidazole ligand .[187] The effect is reversible with temperature changes, opening possibilities for NTQ-based light-emitting diodes and new studies in coordination networks. Zou and co-workers synthesized a zero-dimensional organic copper bromide hybrid with isolated $[CuBr_2]^-$ units encircled by tetrabutylammonium cations, showing bright cyan emission and exceptional antiwater stability.[188] This highlights Cu(I)'s potential for stable, luminescent materials using suitable organic ligands. Wu and co-workers studied TADF in Cu(I) coordination polymers (CP1 and CP2) with imidazole or triazole derivatives (**Figure 1.9b**).[189] CP1 exhibited negative thermal quenching (NTQ) from 77−238 K and zero thermal quenching (ZTQ) from 238−318 K, while CP2 did not. This emphasizes the importance of ligand electronic structure in optimizing luminescent materials. Yao and co-workers presented quasi-2D hybrid crystals with Cu_2I_2-dimer/bidentate ligand clusters, emitting near-unity linearly polarized light.[190] Calculations reveal superaligned transition dipole moments as the key. Additionally, Cu_2I_2-dimer-based hybrid nanobelts exhibit high PL quantum yield (up to 64%) and ultrahigh PL polarization degree (~0.99), promising for quantum optics applications. Ochoa and co-workers synthesized two coordination polymers, $[CuI(dapym)]_n$ and $[Cu_2I_2(dapym)]_n$, forming 1D and 2D structures with Cu_2I_2 double chains in water at room temperature.[191] Their high insolubility enables nanoscale formation, with interesting optoelectronic properties responsive to pressure and temperature, suitable for sensors. Experimental and theoretical studies reveal different emission mechanisms due to structural differences, with semiconductor behavior observed. The 1D compound exhibits UV absorption

and intense room temperature emission, suitable for solar cells. In 2022, Seshadri and co-workers presented ten diverse hybrid Cu(I)-iodides emitting in the green to red region, offering promising prospects for next-generation lighting technologies without rare-earth elements.[192] These compounds feature various structures, including 1D Cu(I)-iodide chains, Cu_2I_2 rhomboid dimers, and Cu_4I_4 tetramers. Those with Cu_2I_2 or Cu_4I_4 structures exhibit higher photoluminescence quantum yields due to optimal inorganic motif condensation, suppressing nonradiative processes. Electronic structure calculations highlight the influence of inorganic motifs and organic ligands on band gaps and excitation characteristics. Temperature-dependent photoluminescence spectra provide insights into luminescence behavior, guiding the rational design of hybrid phosphors for general lighting applications. Ochoa and co-workers synthesized a luminescent and semiconducting coordination polymer based on $[CuI(PyzBr)]_n$ chains using 2-bromopyrazine ligands and copper iodide.[193] The polymer exhibits reversible luminescent response to temperature and pressure, with emission increasing as temperature decreases. Perruchas and co-workers prepared photoluminescent materials by adding multinuclear copper iodide complexes to a polyurethane matrix, retaining the polymer's benefits.[194] These materials exhibit room-temperature phosphorescence with emission-switching properties, such as luminescence thermochromism and solvatochromism, making them suitable for LED applications. This approach offers enhanced functionalities with low cost and sustainability. Using 2-(alkylsulfonyl)pyridines, Li and co-workers created 1D Cu(I)-iodide-based coordination polymers with unique $(CuI)_n$ chains.[195] These polymers show efficient TADF, phosphorescence, or dual emission with short decay times (0.4–2.0 μs) and strong X-ray radioluminescence up to 55% quantum efficiency, advancing TADF and triplet emitter designs.

1.5. Photon up-conversion properties: Importance and non-linear optical properties of Cu(I)-iodide-based systems

Photon up-conversion is an optical process where the low-energy photons (typically fall under NIR and IR region) are applied, and consequently, high-energy photons (typically fall under UV to visible green region) are obtained as the output. The energy of a photon can be up-converted by photophysical means as well as by employing non-linear optical techniques. Researchers have recently explored triplet-triplet annihilation (TTA) as a photophysical tool in photon up-conversion (TTA-UC). Here, the TTA molecule is sensitized by a triplet sensitizer

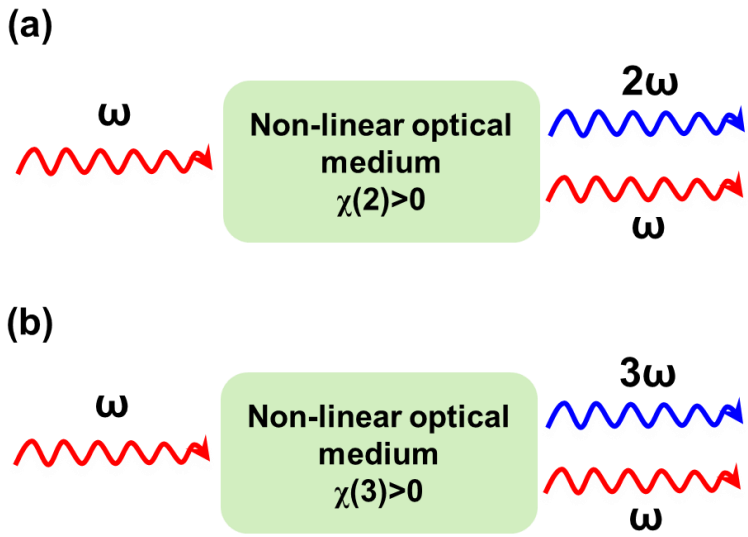

Figure 1.10. Schematic representations of (a) second-harmonic generation and (b) third-harmonic generation.

which absorbs in the visible region (< 400 nm). The sensitizer molecule then transfers its energy to the TTA molecule by the triplet-triplet energy transfer (TTET) process, and finally, the TTA molecule emits through a higher energy singlet state by the TTA process. Several phosphorescent metal complexes and organic TADF molecules have been used to develop efficient TTA-UC and eventually applied in photocatalytic applications.[196–199] Another way to increase the energy of photons is by employing non-linear optical techniques. Non-linear optics is the study of the optical properties of matter (refractive index, polarizability, etc.) upon application of sufficiently intense laser light. Under exposure to lower-intensity light, the induced polarization in a dielectric material is directly proportional to the applied electric field. However, when the intensity is extremely high (obtained from the laser exposure), the induced polarization is given by a power series of the applied electric field as follows[200],

$$P = \chi^{(1)}E + \chi^{(2)}E^2 + \chi^{(3)}E^3 + \cdots\cdots\cdots \quad \text{Eq. 1.7}$$

where P is the polarizability per unit volume, E is the external electric field, and $\chi^{(1)}, \chi^{(2)}, \chi^{(3)}$ represent first-order, second-order, and third-order non-linear susceptibilities, respectively. Depending upon the quadratic and cubic dependence of polarizability on the external electric field, the effects are called second-order and third-order optical non-linearity, respectively. The frequency of a laser can thus be doubled by applying it to a material where second-order non-linearity is reasonably high and this is called second-harmonic generation (SHG) (**Figure 1.10a**). Similarly, the frequency of a laser can also be tripled by applying it to a material with high third-order non-linearity, which is called third-harmonic generation (THG) (**Figure 1.10b**). These two phenomena are extremely important and useful in upconverting the photon

energy. Since its discovery, several materials have been found to exhibit excellent SHG and THG activities. Perovskite structures are particular to mention amongst them, which show high non-linear susceptibility values and sustainability towards laser-induced damage. Other metal-halide structures are comparatively underexplored. In 2005, Cariati and co-workers investigated new CuI adducts with para-substituted trans-stilbazolic and pyridinic ligands, revealing that different para-substituents significantly alter the structural motifs, resulting in novel polymeric and oligomeric forms.[201] These complexes exhibit discrete second harmonic generation observed in the noncentrosymmetric CuI adduct of trans-4'-(dimethylamino)stilbazole. Stoll and co-workers reported Cu(I)-halide coordination polymers with mono- and bidentate N-heteroaromatic ligands, forming double-stranded ladder or single-stranded zigzag structures.[202] These polymers exhibit exceptionally strong second harmonic generation. He and co-workers synthesized chiral hybrid copper halides with (R)- or (S)-methylbenzylamine, showing promising applications in optoelectronics due to their unique optical and electronic properties.[203] These materials demonstrated highly efficient second harmonic generation (SHG). DFT calculations explain the giant optical activity, offering insights into designing chiral materials for advanced photonic device applications. Mao and co-workers reported three pairs of 2D chiral hybrid Cu(I) halides using (R/S)-piperidine-3-carboxylic acid, forming noncentrosymmetric structures with tunable optical properties.[204] These materials exhibit strong second harmonic generation, making them promising candidates for photonic applications.

1.6. Motivation and objectives of the thesis

Despite the reasonable progress in optoelectronics, photosensitization, and non-linear optics, Cu(I)-based emitters require attention to improve tunable emission and high emission yield. Emission yield typically decreases with increasing red-shift in the emission, making it challenging to achieve both broadband tunability and high emission yield simultaneously. Segregated Cu nanoclusters, which are mostly emissive in solution, are prone to aerial oxidation, necessitating stability improvements. Aggregation-induced emission in self-assembled Cu nanoclusters addresses this by enhancing stability and emission yield through suppression of non-radiative decay pathways. However, this strategy has drawbacks: random aggregation forms non-uniform assemblies with high surface energy, making them unstable, and weak interactions among clusters cannot withstand thermal fluctuations, leading to disintegration. In this context, triplet-state harvesting offers a solution by potentially enhancing emission yield through the efficient use of triplet excitons. Research on Cu(I)- and Cu(I)-

halide-based emitters has demonstrated that incorporating triplet states can lead to useful properties like thermochromism and TADF, thereby increasing emission yield.

The aims and objectives of this thesis are as follows,

1. Achieving broadband emission tunability from a single SLCuNC system remains challenging due to synthetic complexities and the absence of facile methods. The mechanisms underlying emission band shifts are poorly understood, and distinguishing metal-centered from ligand-centered excited states is essential for future applications. Additionally, large fluctuations in luminescence intensity during emission shifts restrict the use of many CuNC systems in optoelectronics. Thus, developing straightforward protocols that enable broadband tunability with high quantum yield is crucial.
2. TADF active Cu(I)-iodide dinuclear complexes have been reasonably successful in avoiding the undesired Jahn-Teller distortions in the Cu(I)-based emitters. Strong Cu-Cu bonding interactions in these complexes can result in the formation of cluster-centered emissive states, which reduces the emission yield due to significant excited state distortions. This particular issue needs to be resolved.
3. Despite the high charge-transfer nature and bulk phase polarizability of these complexes, their non-linear photon up-conversion properties have not been adequately explored and warrant further investigation. These properties can be characterized by harmonic generations and multi-photon luminescence.

Bibliography

1 B. Valeur and M. N. Berberan-Santos, *J. Chem. Educ.*, 2011, **88**, 731–738.

2 A. Jablonski, *Nature*, 1933, **131**, 839–840.

3 G. G. Stokes, *Philos. Trans. R. Soc. London*, 1997, **142**, 463–562.

4 R. F. Ziolo, S. Lipton and Z. Dori, *J. Chem. Soc. D Chem. Commun.*, 1970, 1124–1125.

5 H. Amouri, *Chem. Rev.*, 2023, **123**, 230–270.

6 J. Hossain, R. Akhtar and S. Khan, *Polyhedron*, 2021, **201**, 115151.

7 H. Yersin, R. Czerwieniec, M. Z. Shafikov and A. F. Suleymanova, *ChemPhysChem*, 2017, **18**, 3508–3535.

8 J. Zheng, C. Zhang and R. M. Dickson, *Phys. Rev. Lett.*, 2004, **93**, 5–8.

9 J. Zheng, P. R. Nicovich and R. M. Dickson, *Annu. Rev. Phys. Chem.*, 2007, **58**, 409–

431.

10 L. Liu and A. Corma, *Chem. Rev.*, 2018, **118**, 4981–5079.

11 S. Palmal, S. K. Basiruddin, A. R. Maity, S. C. Ray and N. R. Jana, *Chem. – A Eur. J.*, 2013, **19**, 943–949.

12 I. Díez and R. H. A. Ras, *Nanoscale*, 2011, **3**, 1963–1970.

13 N. K. Pal and C. Kryschi, *Phys. Chem. Chem. Phys.*, 2015, **17**, 21423–21431.

14 A. Ghosh, T. Udayabhaskararao and T. Pradeep, *J. Phys. Chem. Lett.*, 2012, **3**, 1997–2002.

15 Q.-F. Zhang, P. G. Williard and L.-S. Wang, *Small*, 2016, **12**, 2518–2525.

16 R. Jin, C. Zeng, M. Zhou and Y. Chen, *Chem. Rev.*, 2016, **116**, 10346–10413.

17 M. Matulionyte, D. Dapkute, L. Budenaite, G. Jarockyte and R. Rotomskis, *Int. J. Mol. Sci.* , 2017, 18.

18 X. Le Guével, V. Trouillet, C. Spies, K. Li, T. Laaksonen, D. Auerbach, G. Jung and M. Schneider, *Nanoscale*, 2012, **4**, 7624–7631.

19 Y. Yu, J. Geng, E. Y. X. Ong, V. Chellappan and Y. N. Tan, *Adv. Healthc. Mater.*, 2016, **5**, 2528–2535.

20 J. Xie, Y. Zheng and J. Y. Ying, *J. Am. Chem. Soc.*, 2009, **131**, 888–889.

21 U. Anand, S. Ghosh and S. Mukherjee, *J. Phys. Chem. Lett.*, 2012, **3**, 3605–3609.

22 F. Gröhn, B. J. Bauer, Y. A. Akpalu, C. L. Jackson and E. J. Amis, *Macromolecules*, 2000, **33**, 6042–6050.

23 Y. Yu, C. Lin, B. Li, P. Zhao and S. Zhang, *Green Chem.*, 2016, **18**, 3647–3655.

24 Y. Negishi, K. Nobusada and T. Tsukuda, *J. Am. Chem. Soc.*, 2005, **127**, 5261–5270.

25 B. Nieto-Ortega and T. Bürgi, *Acc. Chem. Res.*, 2018, **51**, 2811–2819.

26 Y. Chen, W. Li, Y. Wang, X. Yang, J. Chen, Y. Jiang, C. Yu and Q. Lin, *J. Mater. Chem. C*, 2014, **2**, 4080–4085.

27 K. Durairaj, D. D. Than, A. T. Nguyen, H. S. Kim, S.-J. Yeo and H. Park, *Int. J. Mol. Sci.*, 2022, 23.

28 Y. Yang, A. Han, R. Li, G. Fang, J. Liu and S. Wang, *Analyst*, 2017, **142**, 4486–4493.

29 Y. Wang and T. Bürgi, *Nanoscale Adv.*, 2021, **3**, 2710–2727.

30 A. Amiri-Sadeghan, A. Dinari, S. Mohammadi, T. Zohrabi, R. Khodarahmi, S. Hosseinkhani and J. Yoon, *Sci. Rep.*, 2022, **12**, 2235.

31 R. Ho-Wu, K. Sun and T. Goodson, *J. Phys. Chem. C*, 2018, **122**, 2315–2329.

32 P. J. Herbert, C. Yi, W. S. Compel, C. J. Ackerson and K. L. Knappenberger, *J. Phys. Chem. C*, 2018, **122**, 19251–19258.

33 X. Wen, P. Yu, Y.-R. Toh, X. Ma, S. Huang and J. Tang, *Nanoscale*, 2013, **5**, 10251–10257.

34 Y. Liu, D. Yao and H. Zhang, *ACS Appl. Mater. Interfaces*, 2018, **10**, 12071–12080.

35 M. J. Barthel, I. Angeloni, A. Petrelli, T. Avellini, A. Scarpellini, G. Bertoni, A. Armirotti, I. Moreels and T. Pellegrino, *ACS Nano*, 2015, **9**, 11886–11897.

36 H. Cao, Z. Chen, H. Zheng and Y. Huang, *Biosens. Bioelectron.*, 2014, **62**, 189–195.

37 M. Zhao, L. Sun and R. M. Crooks, *J. Am. Chem. Soc.*, 1998, **120**, 4877–4878.

38 L. Balogh and D. A. Tomalia, *J. Am. Chem. Soc.*, 1998, **120**, 7355–7356.

39 P. N. Floriano, Noble, J. M. Schoonmaker, E. D. Poliakoff and R. L. McCarley, *J. Am. Chem. Soc.*, 2001, **123**, 10545–10553.

40 H. Zhang, X. Huang, L. Li, G. Zhang, I. Hussain, Z. Li and B. Tan, *Chem. Commun.*, 2012, **48**, 567–569.

41 H. Wu, G. Wang, Z. Cai, D. Li, F. Xiao, D. Lei, Z. Dai and X. Dou, *Anal. Methods*, 2022, **14**, 4485–4494.

42 Z. Wang, A. S. Susha, B. Chen, C. Reckmeier, O. Tomanec, R. Zboril, H. Zhong and A. L. Rogach, *Nanoscale*, 2016, **8**, 7197–7202.

43 A. Rotaru, S. Dutta, E. Jentzsch, K. Gothelf and A. Mokhir, *Angew. Chemie Int. Ed.*, 2010, **49**, 5665–5667.

44 Q. Song, Y. Shi, D. He, S. Xu and J. Ouyang, *Chem. – A Eur. J.*, 2015, **21**, 2417–2422.

45 Z. Qing, X. He, D. He, K. Wang, F. Xu, T. Qing and X. Yang, *Angew. Chemie Int. Ed.*, 2013, **52**, 9719–9722.

46 S. Pramanik, L. Khamari, S. Nandi and S. Mukherjee, *J. Phys. Chem. C*, 2019, **123**, 29047–29056.

47 N. Goswami, A. Giri, M. S. Bootharaju, P. L. Xavier, T. Pradeep and S. K. Pal, *Anal. Chem.*, 2011, **83**, 9676–9680.

48 L. Xiaoqing, L. Ruiyi, L. Zaijun, S. Xiulan, W. Zhouping and L. Junkang, *New J. Chem.*, 2015, **39**, 5240–5248.

49 C. Wang, C. Wang, L. Xu, H. Cheng, Q. Lin and C. Zhang, *Nanoscale*, 2014, **6**, 1775–1781.

50 L. Jin, Z. Zhang, A. Tang, C. Li and Y. Shen, *Biosens. Bioelectron.*, 2016, **79**, 108–113.

51 W. Wang, F. Leng, L. Zhan, Y. Chang, X. X. Yang, J. Lan and C. Z. Huang, *Analyst*, 2014, **139**, 2990–2993.

52 Y. Qiao, T. Xu, Y. Zhang, C. Zhang, L. Shi, G. Zhang, S. Shuang and C. Dong, *Sensors Actuators B Chem.*, 2015, **220**, 1064–1069.

53 M. Das, U. Goswami, S. Bhattacharyya, R. Kandimalla, A. Chattopadhyay and S. S. Ghosh, *ACS Appl. Bio Mater.*, 2020, **3**, 227–238.

54 R. Ghosh, A. K. Sahoo, S. S. Ghosh, A. Paul and A. Chattopadhyay, *ACS Appl. Mater. Interfaces*, 2014, **6**, 3822–3828.

55 W. Wei, Y. Lu, W. Chen and S. Chen, *J. Am. Chem. Soc.*, 2011, **133**, 2060–2063.

56 X. Jia, X. Yang, J. Li, D. Li and E. Wang, *Chem. Commun.*, 2014, **50**, 237–239.

57 A. Ganguly, I. Chakraborty, T. Udayabhaskararao and T. Pradeep, *J. Nanoparticle Res.*, 2013, **15**, 1522.

58 J.-Y. Ma, P.-C. Chen and H.-T. Chang, *Nanotechnology*, 2014, **25**, 195502.

59 S. M. Lin, S. Geng, N. Li, N. B. Li and H. Q. Luo, *Talanta*, 2016, **151**, 106–113.

60 T. Zhou, Q. Yao, T. Zhao and X. Chen, *Talanta*, 2015, **141**, 80–85.

61 Y.-J. Lin, P.-C. Chen, Z. Yuan, J.-Y. Ma and H.-T. Chang, *Chem. Commun.*, 2015, **51**, 11983–11986.

62 M. Cui, G. Song, C. Wang and Q. Song, *Microchim. Acta*, 2015, **182**, 1371–1377.

63 T. Zhou, W. Xu, Q. Yao, T. Zhao and X. Chen, *Methods Appl. Fluoresc.*, 2015, **3**, 44002.

64 X. Yang, Y. Feng, S. Zhu, Y. Luo, Y. Zhuo and Y. Dou, *Anal. Chim. Acta*, 2014, **847**, 49–54.

65 S. Zhou, Y. Li, F. Wang and C. Wang, *RSC Adv.*, 2016, **6**, 38897–38905.

66 X.-J. Zheng, R.-P. Liang, Z.-J. Li, L. Zhang and J.-D. Qiu, *Sensors Actuators B Chem.*, 2016, **230**, 314–319.

67 J.-S. Shen, Y.-L. Chen, Q.-P. Wang, T. Yu, X.-Y. Huang, Y. Yang and H.-W. Zhang, *J. Mater. Chem. C*, 2013, **1**, 2092–2096.

68 N. K. Das, S. Ghosh, A. Priya, S. Datta and S. Mukherjee, *J. Phys. Chem. C*, 2015, **119**, 24657–24664.

69 S. Ghosh, N. K. Das, U. Anand and S. Mukherjee, *J. Phys. Chem. Lett.*, 2015, **6**, 1293–1298.

70 S. Bhunia, S. Kumar and P. Purkayastha, *ACS Omega*, 2019, **4**, 2523–2532.

71 S. Bhunia, S. K. Seth, P. Gupta, M. Karmakar, P. K. Datta and P. Purkayastha, *ChemistrySelect*, 2019, **4**, 8568–8573.

72 T. Yang, B. Shan, F. Huang, S. Yang, B. Peng, E. Yuan, P. Wu and K. Zhang, *Commun. Chem.*, 2019, **2**, 132.

73 T.-Q. Yang, B. Peng, B.-Q. Shan, Y.-X. Zong, J.-G. Jiang, P. Wu and K. Zhang, *Nanomaterials*, 2020, 10.

74 Z. Wang, B. Chen and A. L. Rogach, *Nanoscale Horizons*, 2017, **2**, 135–146.

75 R. K. Koninti, S. Satpathi and P. Hazra, *J. Phys. Chem. C*, 2018, **122**, 5742–5752.

76 T. Yang, J. Zhou, B. Shan, B. Peng, L. Li, H. Gao, G. Chen and K. Zhang, *ACS Appl. Nano Mater.*, 2023, **6**, 17924–17931.

77 T. Yang, S. Dai, H. Tan, Y. Zong, Y. Liu, J. Chen, K. Zhang, P. Wu, S. Zhang, J. Xu and Y. Tian, *J. Phys. Chem. C*, 2019, **123**, 18638–18645.

78 Z. Wu and R. Jin, *Nano Lett.*, 2010, **10**, 2568–2573.

79 A. Singh, T. Rai and D. Panda, *RSC Adv.*, 2016, **6**, 55539–55545.

80 S. Maity, D. Bain and A. Patra, *J. Phys. Chem. C*, 2019, **123**, 2506–2515.

81 J.-H. Huang, L.-Y. Liu, Z.-Y. Wang, S.-Q. Zang and T. C. W. Mak, *ACS Nano*, 2022, **16**, 18789–18794.

82 Y. Zhang, J. Zhang, Z. Li, Z. Qin, S. Sharma and G. Li, *Commun. Chem.*, 2023, **6**, 24.

83 L. Ai, W. Jiang, Z. Liu, J. Liu, Y. Gao, H. Zou, Z. Wu, Z. Wang, Y. Liu, H. Zhang and B. Yang, *Nanoscale*, 2017, **9**, 12618–12627.

84 S. Kolay, S. Maity, D. Bain, S. Chakraborty and A. Patra, *Nanoscale Adv.*, 2021, **3**, 5570–5575.

85 L. Ai, Z. Liu, D. Zhou, J. Liu, H. Zou, Z. Wu, Y. Liu, H. Zhang and B. Yang, *Nanoscale*, 2017, **9**, 18845–18854.

86 J. Yuan, L. Wang, Y. Wang and J. Hao, *Chem. – A Eur. J.*, 2020, **26**, 3545–3554.

87 Z. Wu, J. Liu, Y. Gao, H. Liu, T. Li, H. Zou, Z. Wang, K. Zhang, Y. Wang, H. Zhang and B. Yang, *J. Am. Chem. Soc.*, 2015, **137**, 12906–12913.

88 X. Su and J. Liu, *ACS Appl. Mater. Interfaces*, 2017, **9**, 3902–3910.

89 Z. Wu, J. Liu, Y. Li, Z. Cheng, T. Li, H. Zhang, Z. Lu and B. Yang, *ACS Nano*, 2015, **9**, 6315–6323.

90 M. Sugiuchi, J. Maeba, N. Okubo, M. Iwamura, K. Nozaki and K. Konishi, *J. Am. Chem. Soc.*, 2017, **139**, 17731–17734.

91 Q. Yao, X. Yuan, Y. Yu, Y. Yu, J. Xie and J. Y. Lee, *J. Am. Chem. Soc.*, 2015, **137**, 2128–2136.

92 M. A. Baldo, D. F. O'Brien, Y. You, A. Shoustikov, S. Sibley, M. E. Thompson and S. R. Forrest, *Nature*, 1998, **395**, 151–154.

93 H. Uoyama, K. Goushi, K. Shizu, H. Nomura and C. Adachi, *Nature*, 2012, **492**, 234–238.

94 C. M. Marian, *WIREs Comput. Mol. Sci.*, 2012, **2**, 187–203.

95 C. M. Marian, *Annu. Rev. Phys. Chem.*, 2021, **72**, 617–640.

96 T.-Y. Li, S.-J. Zheng, P. I. Djurovich and M. E. Thompson, *Chem. Rev.*, 2024, **124**, 4332–4392.

97 J. A. Gareth Williams, S. Develay, D. L. Rochester and L. Murphy, *Coord. Chem. Rev.*, 2008, **252**, 2596–2611.

98 M. Cocchi, D. Virgili, V. Fattori, D. L. Rochester and J. A. G. Williams, *Adv. Funct. Mater.*, 2007, **17**, 285–289.

99 A. Tsuboyama, H. Iwawaki, M. Furugori, T. Mukaide, J. Kamatani, S. Igawa, T. Moriyama, S. Miura, T. Takiguchi, S. Okada, M. Hoshino and K. Ueno, *J. Am. Chem. Soc.*, 2003, **125**, 12971–12979.

100 D. Tanaka, H. Sasabe, Y.-J. Li, S.-J. Su, T. Takeda and J. Kido, *Jpn. J. Appl. Phys.*,

2007, **46**, L10.

101 H. Sasabe, J. Takamatsu, T. Motoyama, S. Watanabe, G. Wagenblast, N. Langer, O. Molt, E. Fuchs, C. Lennartz and J. Kido, *Adv. Mater.*, 2010, **22**, 5003–5007.

102 J. Lee, H.-F. Chen, T. Batagoda, C. Coburn, P. I. Djurovich, M. E. Thompson and S. R. Forrest, *Nat. Mater.*, 2016, **15**, 92–98.

103 J. Briffa, E. Sinagra and R. Blundell, *Heliyon*, 2020, **6**, e04691.

104 P. B. Tchounwou, C. G. Yedjou, A. K. Patlolla and D. J. Sutton, ed. A. Luch, Springer Basel, Basel, 2012, pp. 133–164.

105 W.-P. To, G. Cheng, G. S. M. Tong, D. Zhou and C.-M. Che, *Front. Chem.*, , DOI:10.3389/fchem.2020.00653.

106 Y. Zhang, J. Lee and S. R. Forrest, *Nat. Commun.*, 2014, **5**, 5008.

107 K. P. Klubek, C. W. Tang and L. J. Rothberg, *Org. Electron.*, 2014, **15**, 1312–1316.

108 I. R. de Moraes, S. Scholz, B. Lüssem and K. Leo, *Org. Electron.*, 2011, **12**, 341–347.

109 C. A. Parker and C. G. Hatchard, *Trans. Faraday Soc.*, 1961, **57**, 1894–1904.

110 Y. Tao, K. Yuan, T. Chen, P. Xu, H. Li, R. Chen, C. Zheng, L. Zhang and W. Huang, *Adv. Mater.*, 2014, **26**, 7931–7958.

111 A. Szabo and N. S. Ostlund, *Modern Quantum Chemistry: Introduction to Advanced Electronic Structure Theory*, Dover Publications, 1996.

112 L. Yu, Z. Wu, G. Xie, C. Zhong, Z. Zhu, H. Cong, D. Ma and C. Yang, *Chem. Commun.*, 2016, **52**, 11012–11015.

113 C. Adachi, *Jpn. J. Appl. Phys.*, 2014, **53**, 60101.

114 Z. Yang, Z. Mao, Z. Xie, Y. Zhang, S. Liu, J. Zhao, J. Xu, Z. Chi and M. P. Aldred, *Chem. Soc. Rev.*, 2017, **46**, 915–1016.

115 M. Y. Wong and E. Zysman-Colman, *Adv. Mater.*, , DOI:10.1002/adma.201605444.

116 Q. Zhang, J. Li, K. Shizu, S. Huang, S. Hirata, H. Miyazaki and C. Adachi, *J. Am. Chem. Soc.*, 2012, **134**, 14706–14709.

117 S. Hirata, Y. Sakai, K. Masui, H. Tanaka, S. Y. Lee, H. Nomura, N. Nakamura, M. Yasumatsu, H. Nakanotani, Q. Zhang, K. Shizu, H. Miyazaki and C. Adachi, *Nat. Mater.*, 2015, **14**, 330–336.

118 M. Yang, I. S. Park and T. Yasuda, *J. Am. Chem. Soc.*, 2020, **142**, 19468–19472.

119 Y. Tsuchiya, S. Diesing, F. Bencheikh, Y. Wada, P. L. dos Santos, H. Kaji, E. Zysman-Colman, I. D. W. Samuel and C. Adachi, *J. Phys. Chem. A*, 2021, **125**, 8074–8089.

120 X. Wu, B.-K. Su, D.-G. Chen, D. Liu, C.-C. Wu, Z.-X. Huang, T.-C. Lin, C.-H. Wu, M. Zhu, E. Y. Li, W.-Y. Hung, W. Zhu and P.-T. Chou, *Nat. Photonics*, 2021, **15**, 780–786.

121 F. B. Dias, *Philos. Trans. R. Soc. A Math. Phys. Eng. Sci.*, 2015, **373**, 20140447.

122 N. Haase, A. Danos, C. Pflumm, A. Morherr, P. Stachelek, A. Mekic, W. Brütting and A. P. Monkman, *J. Phys. Chem. C*, 2018, **122**, 29173–29179.

123 C. Li, L. Duan, D. Zhang and Y. Qiu, *ACS Appl. Mater. Interfaces*, 2015, **7**, 15154–15159.

124 B. van der Zee, Y. Li, G.-J. A. H. Wetzelaer and P. W. M. Blom, *Adv. Opt. Mater.*, 2021, **9**, 2100249.

125 M. Hasan, S. Saggar, A. Shukla, F. Bencheikh, J. Sobus, S. K. M. McGregor, C. Adachi, S.-C. Lo and E. B. Namdas, *Nat. Commun.*, 2022, **13**, 254.

126 N. C. Giebink and S. R. Forrest, *Phys. Rev. B*, 2008, **77**, 235215.

127 S. Reineke, K. Walzer and K. Leo, *Phys. Rev. B*, 2007, **75**, 125328.

128 C. Murawski, K. Leo and M. C. Gather, *Adv. Mater.*, 2013, **25**, 6801–6827.

129 V. W.-W. Yam, V. K.-M. Au and S. Y.-L. Leung, *Chem. Rev.*, 2015, **115**, 7589–7728.

130 M. Wallesch, D. Volz, D. M. Zink, U. Schepers, M. Nieger, T. Baumann and S. Bräse, *Chem. – A Eur. J.*, 2014, **20**, 6578–6590.

131 R. Czerwieniec and H. Yersin, *Inorg. Chem.*, 2015, **54**, 4322–4327.

132 J. C. Deaton, S. C. Switalski, D. Y. Kondakov, R. H. Young, T. D. Pawlik, D. J. Giesen, S. B. Harkins, A. J. M. Miller, S. F. Mickenberg and J. C. Peters, *J. Am. Chem. Soc.*, 2010, **132**, 9499–9508.

133 C. T. Cunningham, J. J. Moore, K. L. H. Cunningham, P. E. Fanwick and D. R. McMillin, *Inorg. Chem.*, 2000, **39**, 3638–3644.

134 R. Czerwieniec, J. Yu and H. Yersin, *Inorg. Chem.*, 2011, **50**, 8293–8301.

135 R. Czerwieniec, M. J. Leitl, H. H. H. Homeier and H. Yersin, *Coord. Chem. Rev.*, 2016, **325**, 2–28.

136 T. Hofbeck, U. Monkowius and H. Yersin, *J. Am. Chem. Soc.*, 2015, **137**, 399–404.

137 M. Z. Shafikov, A. F. Suleymanova, R. Czerwieniec and H. Yersin, *Chem. Mater.*, 2017, **29**, 1708–1715.

138 M. Z. Shafikov, A. F. Suleymanova, R. Czerwieniec and H. Yersin, *Inorg. Chem.*, 2017, **56**, 13274–13285.

139 L. X. Chen, G. B. Shaw, I. Novozhilova, T. Liu, G. Jennings, K. Attenkofer, G. J. Meyer and P. Coppens, *J. Am. Chem. Soc.*, 2003, **125**, 7022–7034.

140 D. Di, A. S. Romanov, L. Yang, J. M. Richter, J. P. H. Rivett, S. Jones, T. H. Thomas, M. Abdi Jalebi, R. H. Friend, M. Linnolahti, M. Bochmann and D. Credgington, *Science*, 2017, **356**, 159–163.

141 R. Hamze, J. L. Peltier, D. Sylvinson, M. Jung, J. Cardenas, R. Haiges, M. Soleilhavoup, R. Jazzar, P. I. Djurovich, G. Bertrand and M. E. Thompson, *Science (80-.).*, 2019, **363**, 601–606.

142 A. S. Romanov, C. R. Becker, C. E. James, D. Di, D. Credgington, M. Linnolahti and M. Bochmann, *Chem. – A Eur. J.*, 2017, **23**, 4625–4637.

143 A. S. Romanov, S. T. E. Jones, L. Yang, P. J. Conaghan, D. Di, M. Linnolahti, D. Credgington and M. Bochmann, *Adv. Opt. Mater.*, 2018, **6**, 1801347.

144 A. S. Romanov, S. T. E. Jones, Q. Gu, P. J. Conaghan, B. H. Drummond, J. Feng, F. Chotard, L. Buizza, M. Foley, M. Linnolahti, D. Credgington and M. Bochmann, *Chem. Sci.*, 2020, **11**, 435–446.

145 R. Tang, S. Xu, T.-L. Lam, G. Cheng, L. Du, Q. Wan, J. Yang, F.-F. Hung, K.-H. Low, D. L. Phillips and C.-M. Che, *Angew. Chemie Int. Ed.*, 2022, **61**, e202203982.

146 C. R. Hall, A. S. Romanov, M. Bochmann and S. R. Meech, *J. Phys. Chem. Lett.*, 2018, **9**, 5873–5876.

147 A.-P. M. Reponen, F. Chotard, A. Lempelto, V. Shekhovtsev, D. Credgington, M. Bochmann, M. Linnolahti, N. C. Greenham and A. S. Romanov, *Adv. Opt. Mater.*, 2022, **10**, 2200312.

148 P. Li, Z. Wang, S. Wang, C. Zhou, Y. Zhang, C. Zheng and R. Chen, *J. Phys. Chem. C*, 2021, **125**, 26770–26777.

149 F. Chotard, V. Sivchik, M. Linnolahti, M. Bochmann and A. S. Romanov, *Chem. Mater.*, 2020, **32**, 6114–6122.

150 S. Shi, M. C. Jung, C. Coburn, A. Tadle, D. Sylvinson M. R., P. I. Djurovich, S. R. Forrest and M. E. Thompson, *J. Am. Chem. Soc.*, 2019, **141**, 3576–3588.

151 T. Li, D. S. Muthiah Ravinson, R. Haiges, P. I. Djurovich and M. E. Thompson, *J. Am. Chem. Soc.*, 2020, **142**, 6158–6172.

152 T. Li, J. Schaab, P. I. Djurovich and M. E. Thompson, *J. Mater. Chem. C*, 2022, **10**, 4674–4683.

153 J. P. Zobel, A. M. Wernbacher and L. González, *Angew. Chemie Int. Ed.*, 2023, **62**, e202217620.

154 R. Hamze, S. Shi, S. C. Kapper, D. S. Muthiah Ravinson, L. Estergreen, M.-C. Jung, A. C. Tadle, R. Haiges, P. I. Djurovich, J. L. Peltier, R. Jazzar, G. Bertrand, S. E. Bradforth and M. E. Thompson, *J. Am. Chem. Soc.*, 2019, **141**, 8616–8626.

155 J. Li, L. Wang, Z. Zhao, X. Li, X. Yu, P. Huo, Q. Jin, Z. Liu, Z. Bian and C. Huang, *Angew. Chemie Int. Ed.*, 2020, **59**, 8210–8217.

156 X. Feng, J.-G. Yang, J. Miao, C. Zhong, X. Yin, N. Li, C. Wu, Q. Zhang, Y. Chen, K. Li and C. Yang, *Angew. Chemie Int. Ed.*, 2022, **61**, e202209451.

157 A. S. Romanov, L. Yang, S. T. E. Jones, D. Di, O. J. Morley, B. H. Drummond, A. P. M. Reponen, M. Linnolahti, D. Credgington and M. Bochmann, *Chem. Mater.*, 2019, **31**, 3613–3623.

158 D. Volz, D. M. Zink, T. Bocksrocker, J. Friedrichs, M. Nieger, T. Baumann, U. Lemmer and S. Bräse, *Chem. Mater.*, 2013, **25**, 3414–3426.

159 E. Bichoutskaia and N. C. Pyper, *J. Phys. Chem. C*, 2007, **111**, 9548–9561.

160 S. Perruchas, C. Tard, X. F. Le Goff, A. Fargues, A. Garcia, S. Kahlal, J.-Y. Saillard, T. Gacoin and J.-P. Boilot, *Inorg. Chem.*, 2011, **50**, 10682–10692.

161 Q. Benito, X. F. Le Goff, G. Nocton, A. Fargues, A. Garcia, A. Berhault, S. Kahlal, J.-Y. Saillard, C. Martineau, J. Trébosc, T. Gacoin, J.-P. Boilot and S. Perruchas, *Inorg. Chem.*, 2015, **54**, 4483–4494.

162 B. Huitorel, H. El Moll, R. Utrera-Melero, M. Cordier, A. Fargues, A. Garcia, F. Massuyeau, C. Martineau-Corcos, F. Fayon, A. Rakhmatullin, S. Kahlal, J.-Y. Saillard, T. Gacoin and S. Perruchas, *Inorg. Chem.*, 2018, **57**, 4328–4339.

163 F. De Angelis, S. Fantacci, A. Sgamellotti, E. Cariati, R. Ugo and P. C. Ford, *Inorg. Chem.*, 2006, **45**, 10576–10584.

164 M. Vitale, W. E. Palke and P. C. Ford, *J. Phys. Chem.*, 1992, **96**, 8329–8336.

165 M. Xie, C. Han, J. Zhang, G. Xie and H. Xu, *Chem. Mater.*, 2017, **29**, 6606–6610.

166 C. Chen, R.-H. Li, B.-S. Zhu, K.-H. Wang, J.-S. Yao, Y.-C. Yin, M.-M. Yao, H.-B. Yao and S.-H. Yu, *Angew. Chemie Int. Ed.*, 2018, **57**, 7106–7110.

167 M. Xie, C. Han, Q. Liang, J. Zhang, G. Xie and H. Xu, *Sci. Adv.*, 2024, **5**, eaav9857.

168 A. Tsuboyama, K. Kuge, M. Furugori, S. Okada, M. Hoshino and K. Ueno, *Inorg. Chem.*, 2007, **46**, 1992–2001.

169 D. M. Zink, M. Bächle, T. Baumann, M. Nieger, M. Kühn, C. Wang, W. Klopper, U. Monkowius, T. Hofbeck, H. Yersin and S. Bräse, *Inorg. Chem.*, 2013, **52**, 2292–2305.

170 C. Sun, L. Llanos, P. Arce, A. Oliver, R. Wannemacher, J. Cabanillas-Gonzalez, L. Lemus and D. Aravena, *Chem. Mater.*, 2021, **33**, 6383–6393.

171 J.-J. Wang, H.-T. Zhou, J.-N. Yang, L.-Z. Feng, J.-S. Yao, K.-H. Song, M.-M. Zhou, S. Jin, G. Zhang and H.-B. Yao, *J. Am. Chem. Soc.*, 2021, **143**, 10860–10864.

172 A. Kobayashi, Y. Yoshida, M. Yoshida and M. Kato, *Chem. – A Eur. J.*, 2018, **24**, 14750–14759.

173 A. Schinabeck, M. J. Leitl and H. Yersin, *J. Phys. Chem. Lett.*, 2018, **9**, 2848–2856.

174 M. J. Leitl, F.-R. Küchle, H. A. Mayer, L. Wesemann and H. Yersin, *J. Phys. Chem. A*, 2013, **117**, 11823–11836.

175 J. M. Busch, D. S. Koshelev, A. A. Vashchenko, O. Fuhr, M. Nieger, V. V Utochnikova and S. Bräse, *Inorg. Chem.*, 2021, **60**, 2315–2332.

176 Y. Okano, H. Ohara, A. Kobayashi, M. Yoshida and M. Kato, *Inorg. Chem.*, 2016, **55**, 5227–5236.

177 S. K. Gibbons, R. P. Hughes, D. S. Glueck, A. T. Royappa, A. L. Rheingold, R. B. Arthur, A. D. Nicholas and H. H. Patterson, *Inorg. Chem.*, 2017, **56**, 12809–12820.

178 D. Volz, Y. Chen, M. Wallesch, R. Liu, C. Fléchon, D. M. Zink, J. Friedrichs, H. Flügge, R. Steininger, J. Göttlicher, C. Heske, L. Weinhardt, S. Bräse, F. So and T. Baumann, *Adv. Mater.*, 2015, **27**, 2538–2543.

179 H. Yersin, R. Czerwieniec, U. Monkowius, R. Ramazanov, R. Valiev, M. Z. Shafikov, W.-M. Kwok and C. Ma, *Coord. Chem. Rev.*, 2023, **478**, 214975.

180 J.-J. Wang, L.-Z. Feng, G. Shi, J.-N. Yang, Y.-D. Zhang, H. Xu, K.-H. Song, T. Chen,

G. Zhang, X.-S. Zheng, F. Fan, Z. Xiao and H.-B. Yao, *Nat. Photonics*, 2024, **18**, 200–206.

181 W. Liu, Y. Fang, G. Z. Wei, S. J. Teat, K. Xiong, Z. Hu, W. P. Lustig and J. Li, *J. Am. Chem. Soc.*, 2015, **137**, 9400–9408.

182 J.-C. Li, H.-X. Li, H.-Y. Li, W.-J. Gong and J.-P. Lang, *Cryst. Growth Des.*, 2016, **16**, 1617–1625.

183 W. Liu, K. Zhu, S. J. Teat, B. J. Deibert, W. Yuan and J. Li, *J. Mater. Chem. C*, 2017, **5**, 5962–5969.

184 J. Conesa-Egea, N. Nogal, J. I. Martínez, V. Fernández-Moreira, U. R. Rodríguez-Mendoza, J. González-Platas, C. J. Gómez-García, S. Delgado, F. Zamora and P. Amo-Ochoa, *Chem. Sci.*, 2018, **9**, 8000–8010.

185 Y. Fang, C. A. Sojdak, G. Dey, S. J. Teat, M. Li, M. Cotlet, K. Zhu, W. Liu, L. Wang, D. M. ÓCarroll and J. Li, *Chem. Sci.*, 2019, **10**, 5363–5372.

186 S. Wang, E. E. Morgan, P. Vishnoi, L. Mao, S. M. L. Teicher, G. Wu, Q. Liu, A. K. Cheetham and R. Seshadri, *Inorg. Chem.*, 2020, **59**, 15487–15494.

187 T. Wu, S. Jiang, P. N. Samanta, Y. Xie, J. Li, X. Wang, M. Devashis, X. Gu, Y. Wang, W. Huang, Q. Zhang, J. Leszczynski and D. Wu, *Chem. Commun.*, 2020, **56**, 12057–12060.

188 H. Peng, Y. Tian, Z. Zhang, X. Wang, T. Huang, T. Dong, Y. Xiao, J. Wang and B. Zou, *J. Phys. Chem. C*, 2021, **125**, 20014–20021.

189 M. Li, Z. Cheng, X. Wang, Z. Yu, M. Zhou, H. Miao, W. Zhaxi, W. Huang, X. Ma, Q. Chen, S. Jiang, Q. Zhang and D. Wu, *J. Phys. Chem. Lett.*, 2021, **12**, 8237–8245.

190 J.-J. Wang, X. Mao, J.-N. Yang, Y.-C. Yin, J.-S. Yao, L.-Z. Feng, F. Zhu, C. Ma, C. Yang, G. Zou, G. Zhang, H. Zeng and H.-B. Yao, *Nano Lett.*, 2021, **21**, 4115–4121.

191 J. López, J. G. Platas, U. R. Rodríguez-Mendoza, J. I. Martínez, S. Delgado, G. Lifante-Pedrola, E. Cantelar, R. Guerrero-Lemus, C. Hernández-Rodríguez and P. Amo-Ochoa, *Inorg. Chem.*, 2021, **60**, 1208–1219.

192 S. Wang, E. E. Morgan, S. Panuganti, L. Mao, P. Vishnoi, G. Wu, Q. Liu, M. G. Kanatzidis, R. D. Schaller and R. Seshadri, *Chem. Mater.*, 2022, **34**, 3206–3216.

193 M. Murillo, J. Álvarez-Conde, R. Wannemacher, J. Cabanillas-González, J. González-Platas, U. R. Rodríguez-Mendoza, A. Liang, R. Turnbull, D. Errandonea, J. I. Martínez

and P. Amo-Ochoa, *J. Mater. Chem. C*, 2022, **10**, 18004–18016.

194 S. Stal, B. Huitorel, T. Coustham, N. Stephant, F. Massuyeau, T. Gacoin, L. Bouteiller and S. Perruchas, *ACS Appl. Mater. Interfaces*, 2022, **14**, 47931–47940.

195 A. V Artem'ev, E. P. Doronina, M. I. Rakhmanova, X. Hei, D. V Stass, O. A. Tarasova, I. Y. Bagryanskaya, D. G. Samsonenko, A. S. Novikov, N. A. Nedolya and J. Li, *Dalt. Trans.*, 2023, **52**, 4017–4027.

196 W. Zhao and F. N. Castellano, *J. Phys. Chem. A*, 2006, **110**, 11440–11445.

197 B. Pfund, D. M. Steffen, M. R. Schreier, M.-S. Bertrams, C. Ye, K. Börjesson, O. S. Wenger and C. Kerzig, *J. Am. Chem. Soc.*, 2020, **142**, 10468–10476.

198 N. Harada, Y. Sasaki, M. Hosoyamada, N. Kimizuka and N. Yanai, *Angew. Chemie Int. Ed.*, 2021, **60**, 142–147.

199 T. J. B. Zähringer, J. A. Moghtader, M.-S. Bertrams, B. Roy, M. Uji, N. Yanai and C. Kerzig, *Angew. Chemie Int. Ed.*, 2023, **62**, e202215340.

200 R. W. Boyd, *Nonlinear Optics*, Academic Press, 2003.

201 E. Cariati, D. Roberto, R. Ugo, P. C. Ford, S. Galli and A. Sironi, *Inorg. Chem.*, 2005, **44**, 4077–4085.

202 N. M. Khatri, M. H. Pablico-Lansigan, W. L. Boncher, J. E. Mertzman, A. C. Labatete, L. M. Grande, D. Wunder, M. J. Prushan, W. Zhang, P. S. Halasyamani, J. H. S. K. Monteiro, A. de Bettencourt-Dias and S. L. Stoll, *Inorg. Chem.*, 2016, **55**, 11408–11417.

203 Z. Guo, J. Li, C. Wang, R. Liu, J. Liang, Y. Gao, J. Cheng, W. Zhang, X. Zhu, R. Pan and T. He, *Angew. Chemie Int. Ed.*, 2021, **60**, 8441–8445.

204 X. Ji, S. Geng, S. Zhang, Y. Gong, X. Zhang, R. Li, Y. Liu, J. Chen, R. Chen, Z. Xiao and L. Mao, *Chem. Mater.*, 2022, **34**, 8262–8270.

Chapter 2:

Intrinsic-to-Extrinsic Emission Tuning in Luminescent Cu Nanoclusters by *in-situ* Ligand Engineering

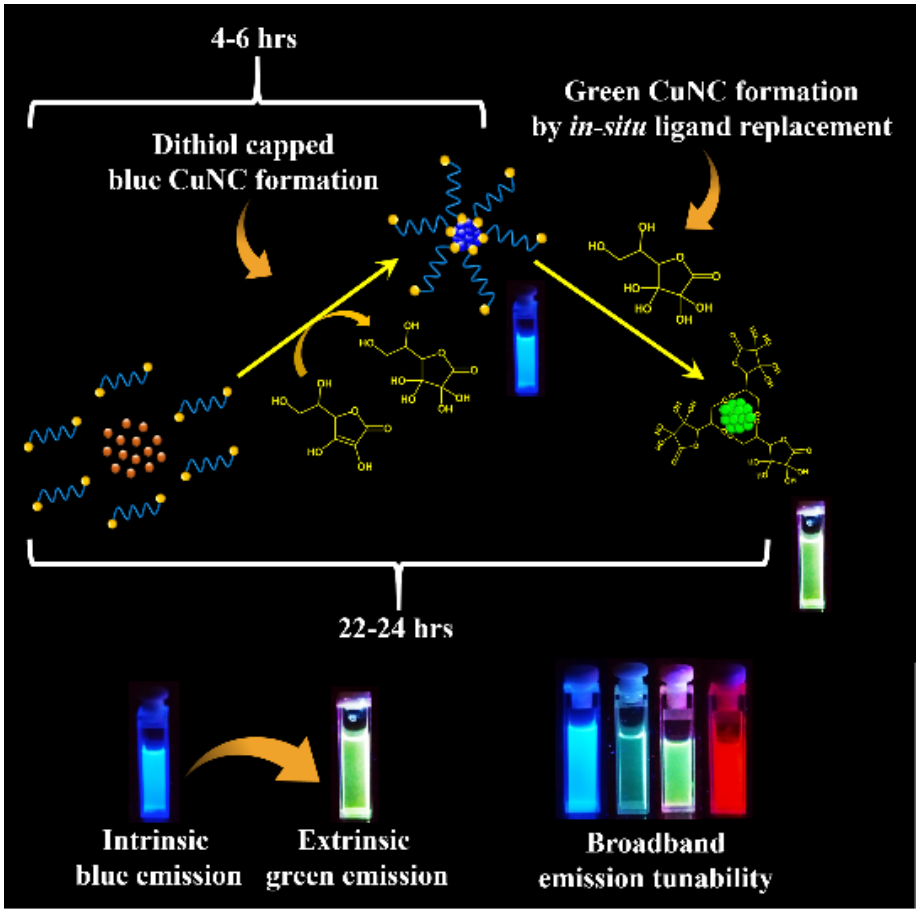

The work is published in the following article,

J. Chatterjee, A. Chatterjee and P. Hazra, *Phys. Chem. Chem. Phys.* 2021, **23**, 25850-25865.

DOI: 10.1039/D1CP03596G.

Abstract: Enhancement in the emission quantum yield and expansion of the emission tunability spectrum are the key incentive aspects of an emitter, which directs the evolution of future generation light harvesting materials. In this regard, small molecular ligand-protected Cu nanoclusters (SLCuNCs) have emerged as a prospective candidate. Herein, we report broadband emission tunability in a SLCuNC system, mediated by *in-situ* ligand replacement. 1,6-hexanedithiol-protected blue emissive discrete Cu nanoclusters (CuNC) and red emissive CuNC assemblies have been synthesized in one pot. Red emissive CuNC assemblies were characterized and found to be covalently linked nanocluster superstructures. The blue emissive CuNC was further converted to green-yellow emissive CuNC over the time by a ligand replacement process, which was mediated by the oxidized form of the reducing agent, used for synthesizing the blue emissive nanocluster. Steady-state emission results and fluorescence dynamics studies were used to elucidate that the ligand replacement process not only modulates the emission color but also alters the nature of the emission from metal-centered intrinsic to ligand-centered extrinsic emission. Moreover, time-dependent blue to green-yellow emission tunability was demonstrated in an optimized reaction condition.

2.1. Introduction

Light is one of the prevalent forms of energy which decides the advancement of the human civilization. More than 20% of the electrical energy output of the world is invested for light harvesting.[1] Phosphor based light emitting diodes (LEDs) are one of the key participants to play the pronounced role in this regard. Performance of an LED is principally dictated by the luminescence efficiency of its emissive layer. Considerable attention has been paid to increase its luminescence efficiency in recent decades by fabricating the emissive layer with several semiconductor materials and quantum dots.[2–8] Regarding this aspect, small molecular ligand protected luminescent copper nanoclusters (SLCuNC) have emerged as one of the prospective candidates owing to its potential applicability over the field of optoelectronics and photosensitization.[9–17] Structural and conformational diversity of the protecting ligands have provided additional rigidity to this potential by enhancing its luminescence output and by enlarging the spectrum of luminescence tunability.[18–24] In early period, the photoemission from all noble metal nanoclusters were believed to be generated only from the metal core due to quantum confinement effect[25,26] until, it was unraveled that enormous shift in emission band can be achieved by tailoring metal atoms or the protecting ligands.[27–32] These results eventually tempted researchers to look for necessary amendments in traditional mechanistic models for nanocluster emission which was also applied to explain emission mechanism of SLCuNCs.

Sequential studies have disclosed that, electronic effects of the surface bound ligands have a promising role to dictate the nature and color of the emission in SLCuNCs.[16,32,33] Moreover, it was also unveiled that, along with the electronic effects, the ligand directed self-assembly can lead to the modulation of its emissive properties including emergence of aggregation induced emission (AIE).[34] For instance, several polymers[35], DNA-nanoribbons[22] proteins[36], peptides[37], thiolates[13], amino acids[38] etc. have been utilized as templates and ligands to synthesize highly luminescent CuNC assemblies with AIE properties.

Along with emission enhancement, emission tunability in noble metal nanocluster systems has gained prominent directional signatures in the field of photosensitization, white LEDs, future-generation multi-color display technology and photo-printing technology.[39–41] In this regard, worthwhile recognition has been offered to the gold and silver nanoclusters[42–46], nevertheless, the applicability of copper nanoclusters has recently gathered reasonable attention in these fields. Researchers have used several methodologies to tune the emission of SLCuNC such as, by tailoring the metal atoms[19], applying surface engineering techniques[47], modulation of self-assembly processes[38], regulating intra and inter-cluster cuprophilic interactions[13,48], modulating the electronic effect of ligands by altering their substituents[16] etc. Despite of reasonable progress, broadband emission tunability from a single SLCuNC system became one of the major challenges because of several synthetic complications, lack of facile methods and so on. The respective mechanisms and underlying processes during the shift in emission band are still unexplored. Moreover, the indistinguishable contributions of the metal-centered and ligand-centered excited states to the resultant emission also need to be unraveled to expand further applications of SLCuNCs. Furthermore, drastic oscillations in the luminescence intensity during the emission shift make several CuNC systems ineffective for further optoelectronic applications. Therefore, it is very crucial to introduce alternative facile protocols that can manifest broadband tunability in emission as well as reasonably high quantum yield in the maximum range.

Herein, we introduce in-situ ligand engineering as a medium for tuning the emission color of a SLCuNC system from blue to green-yellow and explored the versatility in the excited state properties of the system. Two novel synthetic protocols have been established in this regard. Protocol 1 (P1) involves the synthesis of SLCuNCs where the protecting ligand itself acts as reducing agent; on the contrary, in protocol 2 (**P2**), additional reducing agent was added to synthesize the nanoclusters. In P1, 1,6-hexanedithiol (1,6-HDT) protected blue emissive SLCuNC (BCuNC) and red emissive CuNC assemblies (RCuNC) were synthesized in one-pot via a novel protocol (**Scheme 2.1**). In P2, we followed the same protocol as we used in case of

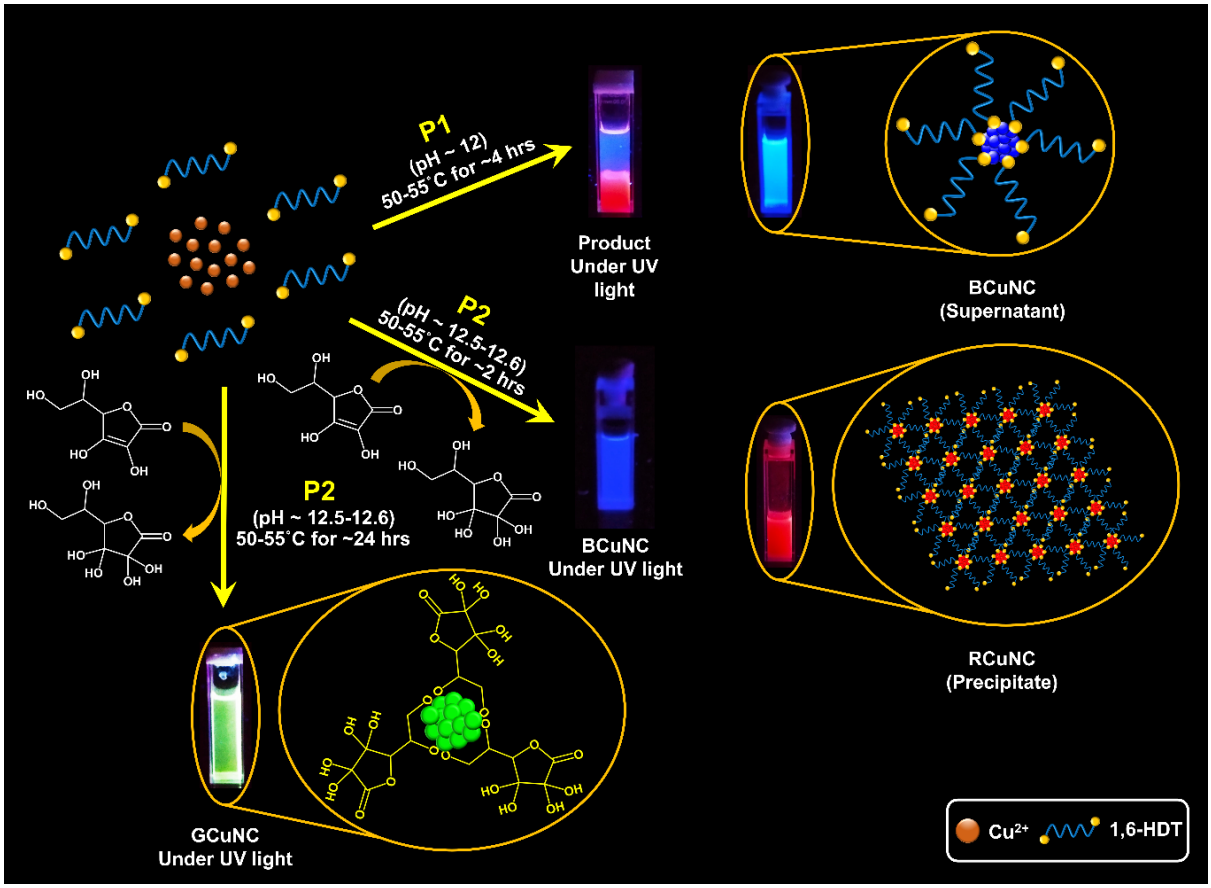

Scheme 2.1. Schematic representation for the synthesis of BCuNC, GCuNC and RCuNC.

P1, additionally, L-ascorbic acid (AA) was used as a reducing agent and the reaction was carried out at slightly higher pH. We monitored the reaction in two pots with different reaction times, one is up to 2 hrs and another till 24 hrs. In the first pot (with 2 hrs of reaction time), we obtained similar blue emission like BCuNC as supernatant, but in the second pot (with 24 hrs of reaction time), surprisingly it led to the formation of green-yellow emissive supernatant (**Scheme 2.1**). We have determined this unusual event to be the consequence of an in-situ ligand replacement process which leads to the formation of green-yellow emissive Cu nanoclusters (GCuNC). Several experiments were performed to figure out that the ligand replacement is mediated by the reducing agent added for synthesizing BCuNC. Moreover, we have demonstrated this process as a unique strategy to alter the nature of emission from metal centered (intrinsic) to ligand centered (extrinsic). The reaction condition was optimized in such a way that, reaction time becomes the only determinant factor to generate different emission colors including blue, cyan and green-yellow; which along with the RCuNC, cover the whole visible spectrum.

2.2. Experimental Section

2.2.1. Materials

Copper (II) sulphate pentahydrate ($CuSO_4.5H_2O$), 1,6-hexanedithiol (97%), L-ascorbic acid (99%), L-dehydroascorbic acid, 1-octanethiol (98.5%), 3-mercaptopropionic acid (99%), 1,3-propanedithiol (99%), 1,9-nonanedithiol (95%), single side polished silicon wafers were purchased from Sigma-Aldrich and the chemicals were used without further purification. Cu grids with 200 mesh for electron microscopy measurements were purchased from Ted Pella, Inc. NaOH beads and HPLC grade methanol (99.8%) were purchased from Avantor Performance Materials India Ltd.

2.2.2. Characterization techniques

HRTEM samples were prepared by drop-casting the diluted CuNC solutions on 200 mesh carbon coated Cu grids, and then allowed to be dried under vacuum for overnight. Images were recorded in JEM2200FS, JEOL (200 keV) transmission electron microscope. FESEM samples were prepared by drop-casting the diluted RCuNC disperse on a small piece of single side polished silicon wafer, and then allowed to be dried under vacuum for overnight. Images were recorded in a ZEISS Ultra Plus scanning electron microscope. EDX spectra of RCuNC were recorded during FESEM analysis in a ZEISS Ultra Plus scanning electron microscope. MALDI-TOF mass spectra were collected in 4800 Plus MALDI TOF analyzer from Applied Biosystems by using α-Cyano-4-hydroxycinnamic acid (CHCA) as matrix. Zeta potential and DLS measurements were performed in Zetasizer Nano series, Nano-2590 (Malvern instruments, U.K.) with a 655 nm laser. All the samples were passed through 0.2 micron syringe filter before measurements. Fourier transform infra-red (FT-IR) spectroscopy was carried out by using solid KBr discs in a NICOLET 6700 FT-IR spectrometer. Raman spectra were recorded in a Raman microscope (LabRAM HR, HORIBA, Jobin Yvon) with a 50X objective lens loading solid CuNC samples on glass-slide. X-ray photoelectron spectroscopy (XPS) characterization was performed with an ESCALAB spectrometer having the Al K_α X-ray source ($h\nu$ = 1486.6 eV) operating at 150 W (using a Physical Electronics 04-548 dual Mg/Al anode) and in a UHV system with a base pressure of $\leq 5\times10^{-9}$ Torr.

2.2.3. Steady-state and time-resolved spectroscopic studies

Steady-state absorption measurements in liquid state were carried out in UV-2600 UV-Vis spectrophotometer, Shimadzu, and solid state absorption measurements of RCuNC were done using UV-3600 UV-Vis-NIR spectrophotometer, Shimadzu. Steady-state fluorescence measurements in liquid state were carried out using a FluoroMax-4 spectrofluorometer

(HORIBA Jobin Yvon, USA). Fluorescence decays (pico- to nanosecond) were collected using a TCSPC setup from HORIBA Jobin Yvon. Diode lasers (NanoLED-375L and NanoLED-402L, IBH, UK) having a FWHM of <100 ps were used as excitation sources for lifetime studies. The fluorescence transients were collected at the magic angle using an MCP-PMT (Hamamatsu, Japan) detector. The analysis of lifetime (TCSPC) data was done by IBH DAS6 analysis software. Lifetime (TCSPC) data were fitted with a minimum number of exponentials. The quality of fitting was evaluated by the χ^2 value, and the value close to 1 was considered as a good fit. Solid-state fluorescence measurements (including lifetime) of RCuNC were carried out in FLS 980 spectrofluorometer, Edinburgh Instruments. For microsecond lifetime measurements of RCuNC, EPL-405 nanosecond pulsed laser (Edinburgh Instruments) with FWHM of ~ 4 ns was used as the excitation source.

2.2.4. Femtosecond fluorescence up-conversion measurements

The samples were excited at 375 and 420 nm using the second harmonic of a mode-locked Ti-sapphire laser (Mai Tai, Spectra-Physics). The fundamental beams (750 nm or 840 nm) were frequency doubled in a nonlinear crystal of β-barium borate (BBO). Samples were loaded in a 1 mm thick rotating sample chamber. Fluorescence emitted from the sample was upconverted in another nonlinear crystal (BBO) using a gate pulse (750 nm or 840 nm) of the fundamental beam and passed through a variable delay line before up-conversion. The sum frequency of the fluorescence and gate pulse was detected as a function of the time delay between excitation and gate pulses. The angle between the polarization of the pump and gate pulses was maintained at the magic angle to eliminate effects from rotational diffusion. The upconverted signal was dispersed in a monochromator and detected using photon-counting electronics. A cross-correlation function obtained using the Raman scattering from ethanol provided a full width at half-maximum (FWHM) of ~300 fs. Estimated uncertainties in the up-conversion measurements are ~15−20%. The average excitation power was varied but was around 8 ± 0.5 mW, and an average collection time of 2.5 s was used. No degradation of the sample was observed as the traces overlapped after each repetition, and the optical absorption measurements did not show any change before and after the measurements. The fluorescence decays were deconvoluted using a Gaussian-shaped excitation pulse by Igor Pro 6.0 analysis

software. The long component lifetime obtained from TCSPC was kept fixed during the analysis of upconverted decay profiles.

2.2.5. Quantum yield determination of BCuNC, GCuNC and RCuNC.

Relative quantum yield of BCuNC and GCuNC were calculated using the following equation[49],

$$\phi_s = \phi_r \frac{I_s}{I_r} \cdot \frac{A_r}{A_s} \cdot \frac{\eta_s^2}{\eta_r^2} \qquad \text{Eq 2.1}$$

Where, ϕ_s = relative quantum yield of the sample, ϕ_r = relative quantum yield of the reference, I_s = Integrated PL intensity of the sample, I_r = Integrated PL intensity of the reference, A_r = absorbance value of the reference at excitation wavelength, A_s = absorbance value of the sample at excitation wavelength, η_s = refractive index of the solvent for the sample (in our case methanol), η_r = refractive index of the solvent for the reference (in our case ethanol).

The calculated relative quantum yield of BCuNC was found to be 0.10 (10%), and relative quantum yield of GCuNC was found to be 0.30 (30%). Where quantum yield of references are as following, POPOP (for BCuNC) = 0.97 (97%)[50]

Coumarin 30 (for GCuNC) = 0.67 (67%)[51].

Absolute quantum yield of RCuNC was measured by using integrating sphere method and found to be 3% (absolute error $\pm$ 0.047, relative error $\pm$ 0.02625).

2.2.6. Calculation of macroscopic rate constant for the formation of GCuNC

Figure 2.9f was plotted by collecting fluorescence intensities at corresponding time from **Figure A2 in Appendix**. where, F = fluorescence intensities at reaction time of 2, 6, 10, 14, 18, 22, 26 hrs respectively, collected at 520 nm and F_0 = fluorescence intensity at reaction time of 2 hrs. F/F_0 vs. reaction time (hrs) was plotted and fitted with a sigmoid function (eq. 2) by using Igor Pro 6.0 software.

$$y = b + \frac{y_{max}}{1 + e^{\frac{x_{half} - x}{k}}} \qquad \text{Eq 2.2}$$

Where, k is the macroscopic rate constant of the corresponding process, b is the base value of y, y_{max} is the maximum value of y and x_{half} is the value of x at $y = \frac{y_{max} - b}{2}$.

The parameters obtained from fitting are

$(F/F_0)_{base}$ = 0.68579 $\pm$ 0.346 $\quad$ k = 2.1421 $\pm$ 0.241 hrs^{-1}

$(F/F_0)_{max}$ = 12.055 $\pm$ 0.443

$(\text{Reaction time})_{half}$ = 10.686 $\pm$ 0.262 hrs

2.3. Results and discussion

2.3.1. Protocol 1 (P1): Synthesis of BCuNC and RCuNC

In a typical experiment, 4 mL of 10 mM $CuSO_4.5H_2O$ solution was prepared in methanol and was taken in a 25 mL round bottom (RB) flask. 18.2 µL of 1,6-hexanedithiol (1,6-HDT) was dissolved in ~150 µL of 0.6 M methanolic NaOH, and was added to the Cu^{2+} solution, which resulted into instantaneous formation of a yellowish precipitate (The concentration of OH^- ions and 1,6-HDT in the final mixture were ~20 mM and ~30 mM, respectively). The mixture was kept under inert and constant stirring condition at ~50-55˚C temperature for 4-6 hrs, followed by centrifugation at 12000 rpm for 10 min. Resulting colorless supernatant appeared as blue emissive under UV light and the precipitate was red emissive under UV light.

2.3.2. Protocol 2 (P2): Synthesis of green-yellow emissive CuNC (GCuNC)

Two sets of following reaction were prepared. 4 mL of 10 mM $CuSO_4.5H_2O$ solution was taken in a 25 mL RB flask. 18.2 µL of 1,6-hexanedithiol was dissolved in 300 µL of 0.6 M methanolic NaOH and added to the solution in RB flask, so that the concentration of OH^- ions and 1,6-HDT in the resulting solution were ~40 mM and ~30 mM, respectively. A yellowish precipitate was formed instantaneously, and then we have added 14 mg of solid L-ascorbic acid into the mixture. The first set of reaction was kept under inert condition and constant stirring at 50-55 ˚C temperature for 2 hrs, and the second set of reaction was kept under same reaction condition for 24 hrs. The mixtures were then centrifuged at 12000 rpm for 10 min. In the first set, resulting colorless supernatant appeared as blue emissive under UV light and the precipitate was red emissive similar to protocol 1 (**P1**). On the other hand, in second set, resultant supernatant was found to be bright green emissive and the precipitate was non-emissive.

2.3.3. Characterization of BCuNC, GCuNC and RCuNC

The blue, green-yellow, and red emitting products were characterized by several techniques. High-resolution transmission electron microscopy (HRTEM) of the blue fluorescent supernatant reveals the ultra-small nature of synthesized BCuNC with a size of 2-3 nm and an inter-planar distance of 0.23 nm, which corresponds to the (111) crystal plane of Cu nanocluster (**Figure 2.1a, 2.1b, 2.1c**). Dynamic light scattering (DLS) studies further show the size distribution of BCuNC with a maximum at 3.7 nm (**Figure 2.1d**). XPS measurement was performed to determine the oxidation states of Cu inside BCuNC, where binding energy of electrons for Cu $2p_{3/2}$ and Cu $2p_{1/2}$ states was obtained at 934.78 and 954.78 eV (**Figure 2.1e**), which confirms the oxidation states of Cu inside the cluster to be 0 and +1. No satellite peak at

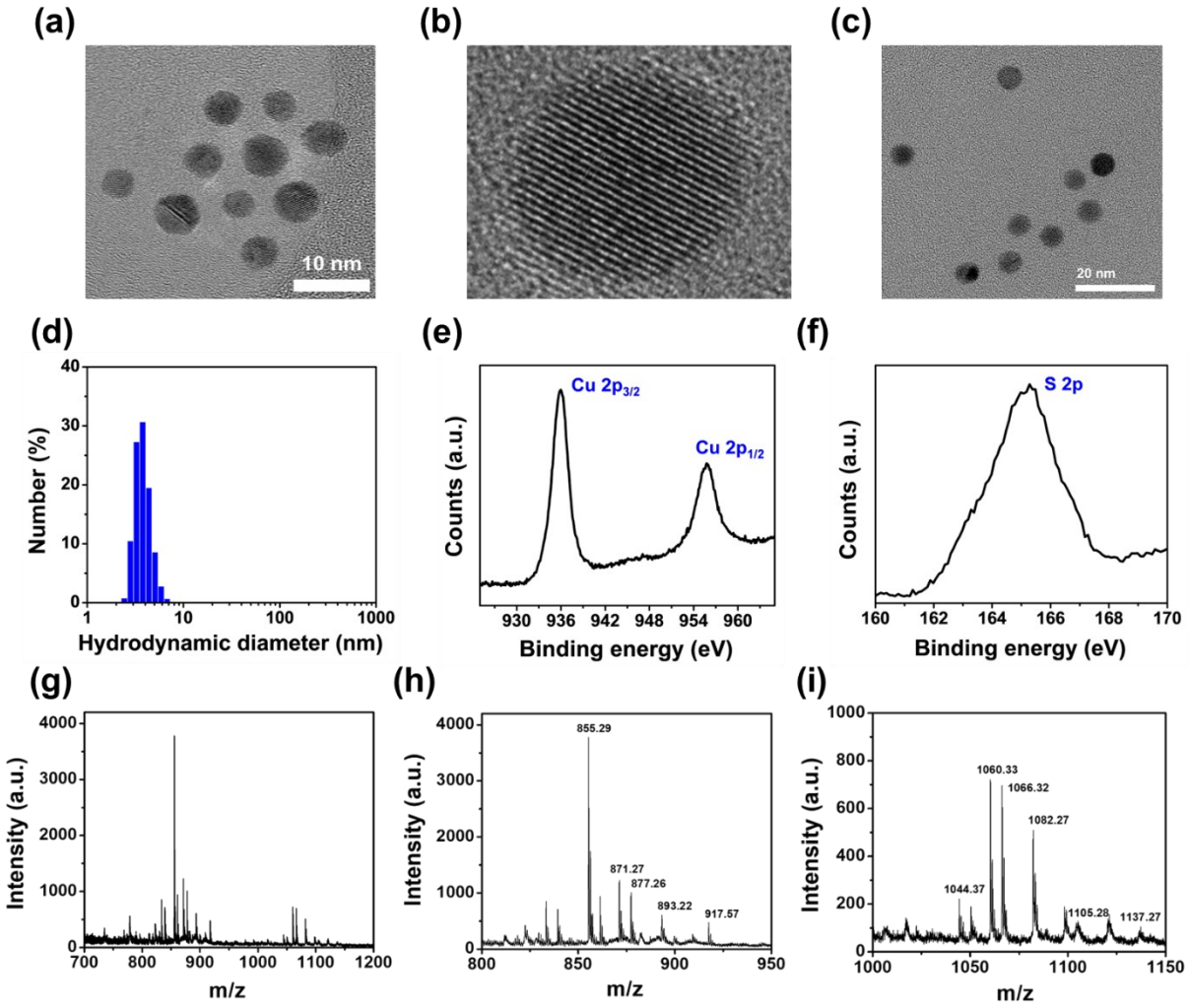

Figure 2.1. (a), (b), (c) HRTEM images of BCuNCs, (d) DLS particle size distribution of BCuNCs, XPS spectra of BCuNC for (e) Cu 2p electrons, (f) S 2p electrons. (g), (h), (i) MALDI-TOF mass spectrum of BCuNC. Assigned peaks have been shown in (h) and (i). Estimated compositions of BCuNC, 855.29 = $[Cu_6(1,6\text{-}HDT)_3 + Na^+]^+$, 871.27 = $[Cu_6(1,6\text{-}HDT)_3 + K^+]^+$, 877.26 = $[Cu_6(1,6\text{-}HDT)_3 + 2Na^+ - H^+]^+$, 893.22 = $[Cu_7(1,6\text{-}HDT)_3 - 2H^+]^+$, 917.57 = $[Cu_7(1,6\text{-}HDT)_3 + Na^+ - H^+]^+$, 1044.37 = $[Cu_9(1,6\text{-}HDT)_3 + Na^+ - H^+]^+$, 1060.33 = $[Cu_9(1,6\text{-}HDT)_3 + K^+ - H^+]^+$, 1082.27 = $[Cu_9(1,6\text{-}HDT)_3 + Na^+ + K^+ - 2H^+]^+$, 1105.28 = $[Cu_8(1,6\text{-}HDT)_4 - 4H^+]^+$, 1137.27 = $[Cu_8(1,6\text{-}HDT)_4 + Na^+ + 5H^+]^+$.

~942 eV also corroborates the absence of Cu(II) in the cluster. Additionally, another peak at 165.28 eV (**Figure 2.1f**) corresponds to the binding energy of S 2p electrons, which confirms the presence of Cu-S bond in the cluster. To determine the number of Cu atoms present in the cluster, we performed MALDI-TOF mass spectrometry in the positive ion mode, which shows major peaks at 855, 871, 877, 893, 917, 1044, 1060, 1066, 1082, 1105, 1137 m/z (**Figure 2.1g, 2.1h, 2.1i**). These m/z values clearly indicate the composition of BCuNC to be $Cu_{(6\text{-}9)}(1,6\text{-}HDT)_{(3\text{-}4)}$. Further, the FT-IR spectra shows that the -SH stretching band of 1,6-HDT at ~2550 cm^{-1} was divided into two small bands (**Figure 2.2a**) upon formation of BCuNC indicating vibrational coupling between two -SH groups. This suggests that one -SH end of the dithiol

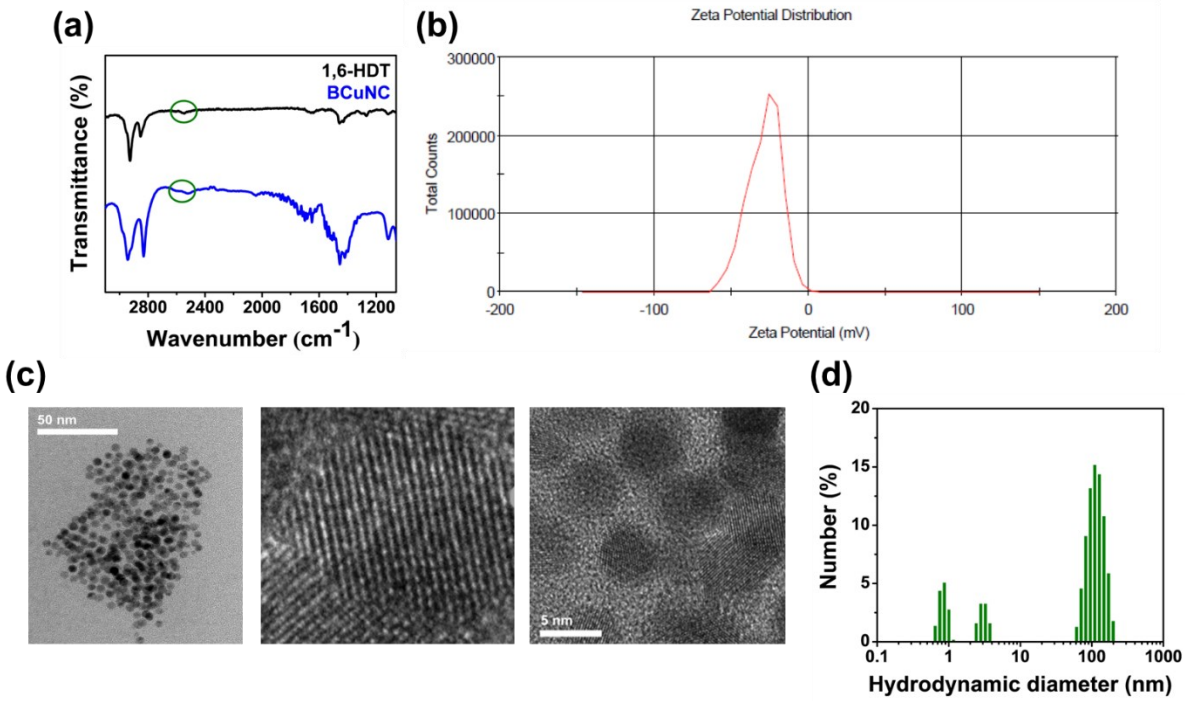

Figure 2.2. (a) FT-IR spectra of BCuNC (S-H stretching frequency of thiol is indicated under green circles), (b) Zeta potential distribution of BCuNC, (c) HRTEM images of GCuNCs, and (d) DLS particle size distribution of GCuNCs.

ligands bind to the nanocluster surface and the -SH groups at the other end remains free. The doublet in the vibrational band arises due to coupling of those adjacent free -SH groups. Zeta potential measurement of BCuNC shows a value of -28.5 mV (**Figure 2.2b**) which arises due to accumulation of negative charge on the nanocluster surface. The accumulation of the negative charge is due to free -SH groups present on the nanocluster surface, which also supports the FT-IR results. A reasonably large negative value of zeta potential also accounts for the colloidal stability of BCuNC. Alongside, to address the distinct observation of the formation of green-yellow emissive supernatant, it was characterized under the transmission electron microscope where the size, inter-planer distance and shape of GCuNC remain similar as in case of BCuNC. However, the particles were found to be in a contiguous state, which was not observed in the case of BCuNC (**Figure 2.2c**). DLS experiment of GCuNC further indicates the formation of polydisperse phase, comprised of particle size distributions with maxima at 0.6, 1.8 and 147 nm (**Figure 2.2d**), where the size distribution around 147 nm further signifies the formation of aggregates of nanoclusters. RCuNC was characterized by scanning electron microscopy (FESEM) (**Figure 2.3a, 2.3b**) and energy dispersive X-ray (EDX) techniques (**Figure 2.3c**), which reveals fibrillar morphology of the precipitate along with estimation of Cu, C and S contents (**Table 2.1**). HRTEM images of RCuNC further show the distribution of ultrasmall clusters, which act as the basic constituting unit for the fibril shaped precipitate

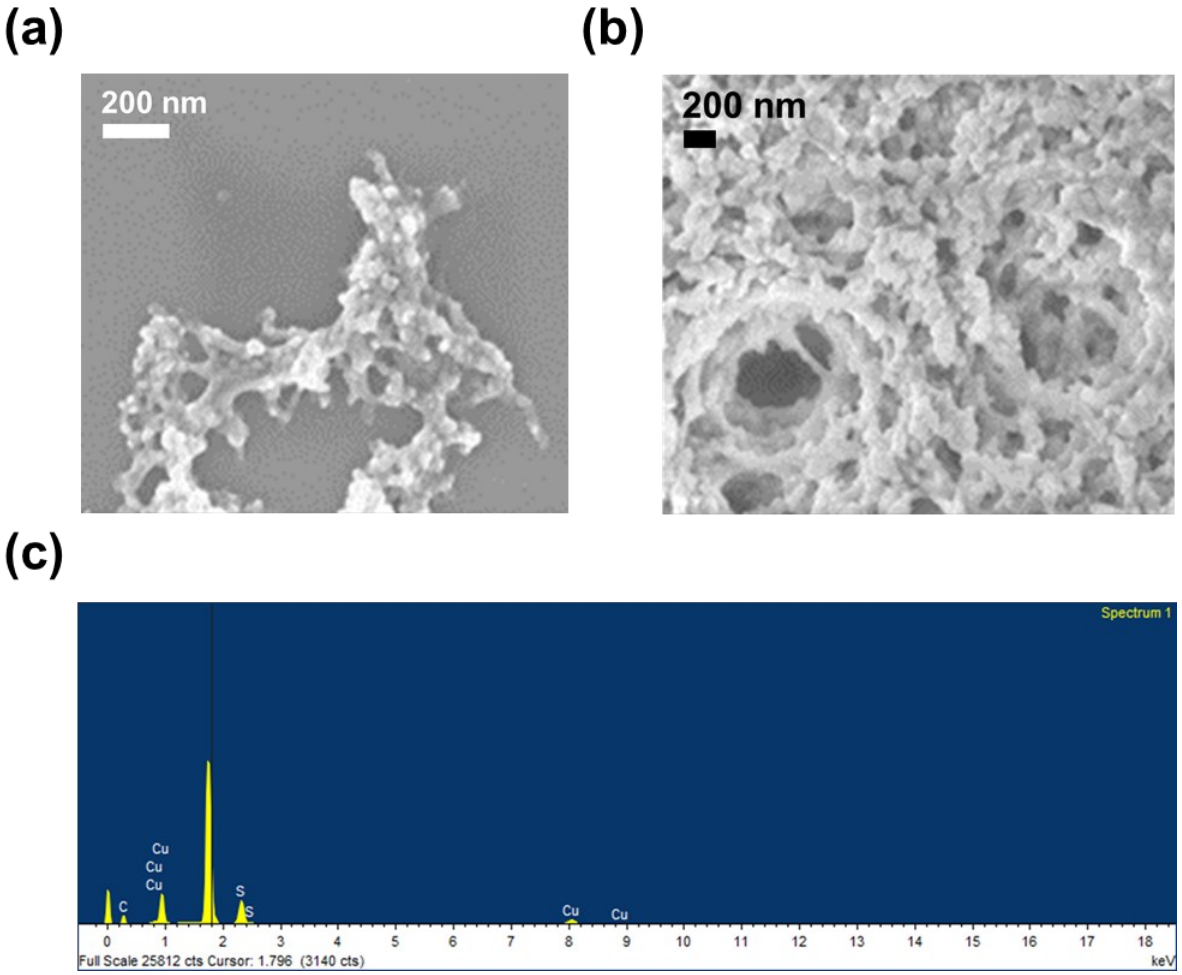

Figure 2.3. (a), (b) FESEM images, and (c) EDX spectrum of RCuNC

Table 2.1. Atomic and weight percentages of Cu, C and S in RCuNC, obtained from EDX analysis at the time of FESEM measurements.

Element	Weight%	Atomic%
C K	59.08	84.66
S K	16.02	8.60
Cu K	24.90	6.74
Totals	100.00	

(**Figure 2.4a, 2.4b**). All these results indicate that the red precipitate is mainly comprised of assembled ultrasmall nanoclusters. Additionally, we have recorded FT-IR spectra of RCuNC which shows complete disappearance of thiol stretching frequency at ~2550 cm^{-1} (**Figure 2.4c**). It confirms that both the thiol ends participate in the bonding with the nanocluster surface of RCuNC, unlike in the case of BCuNC, where only one thiol group was attached to the

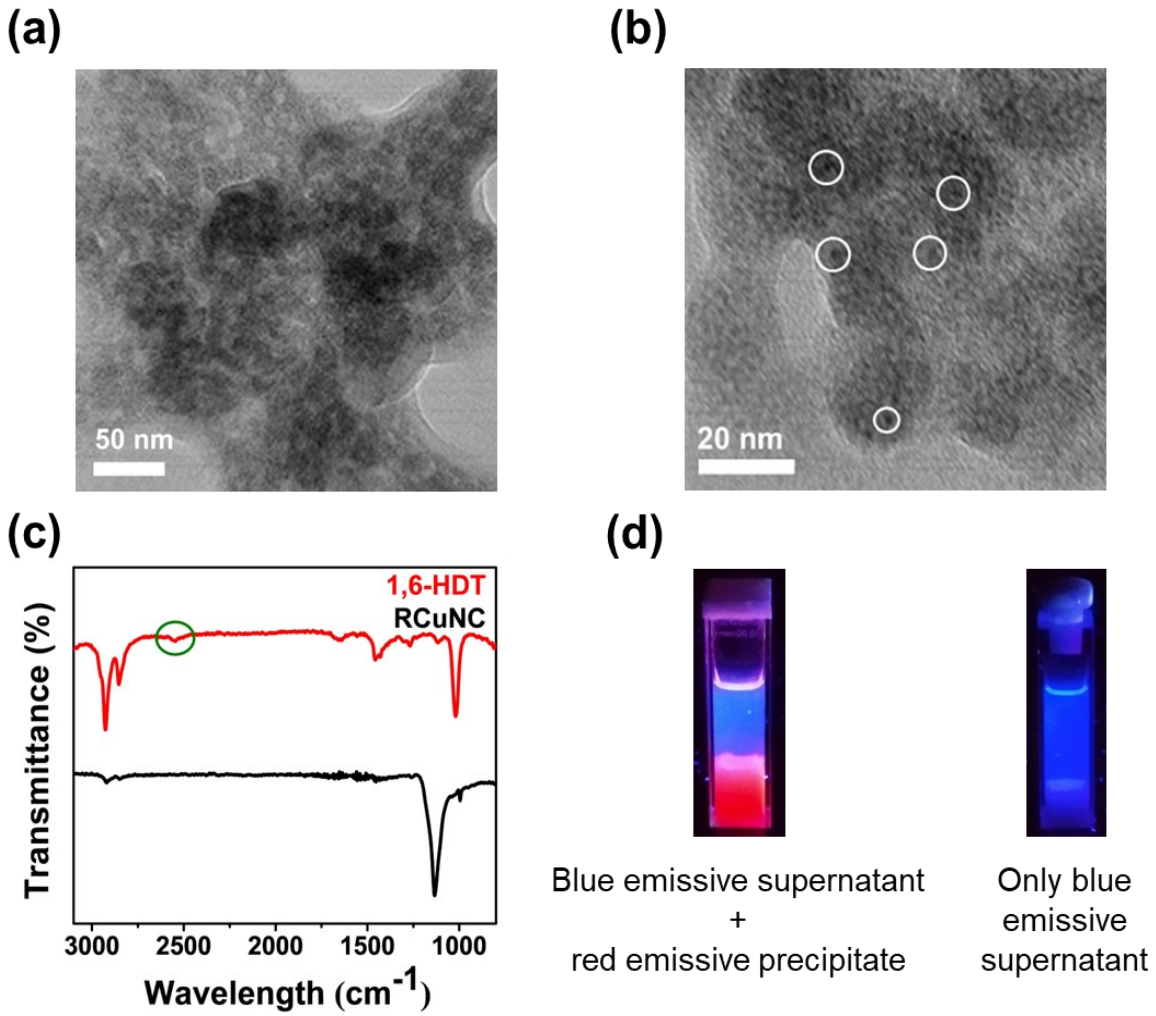

Figure 2.4. (a), (b) HRTEM images of RCuNC. Small nanoclusters are marked under white circles, (c) FT-IR spectra of RCuNC (S-H stretching frequency of thiol is indicated under green circle), and (d) Blue emissive supernatant and red emissive precipitate when synthesized by using 1,6-HDT. Only blue emissive supernatant when synthesized by using 1-octanethiol.

nanocluster. FT-IR results also justify the formation of the strongly correlated nanostructure where the dithiol can simultaneously bind to two nanocluster moieties, and the sequential binding of these ligands ultimately leads to the formation of fibril-shaped nanocluster assemblies. To validate the role of dithiol for the formation of RCuNC, we further repeated the protocol 1 (P1) by using 1-octanethiol as ligand, but only blue supernatant was formed without formation of any red emissive precipitate (**Figure 2.4d**).

2.3.4. Steady-state absorption and emission results: metal-centered and ligand-centered emission

Absorption spectra of BCuNC in methanol exhibited a broad absorption feature along with two distinct humps at around 310 nm and 345 nm (**Figure 2.5a**). On the other hand, GCuNC

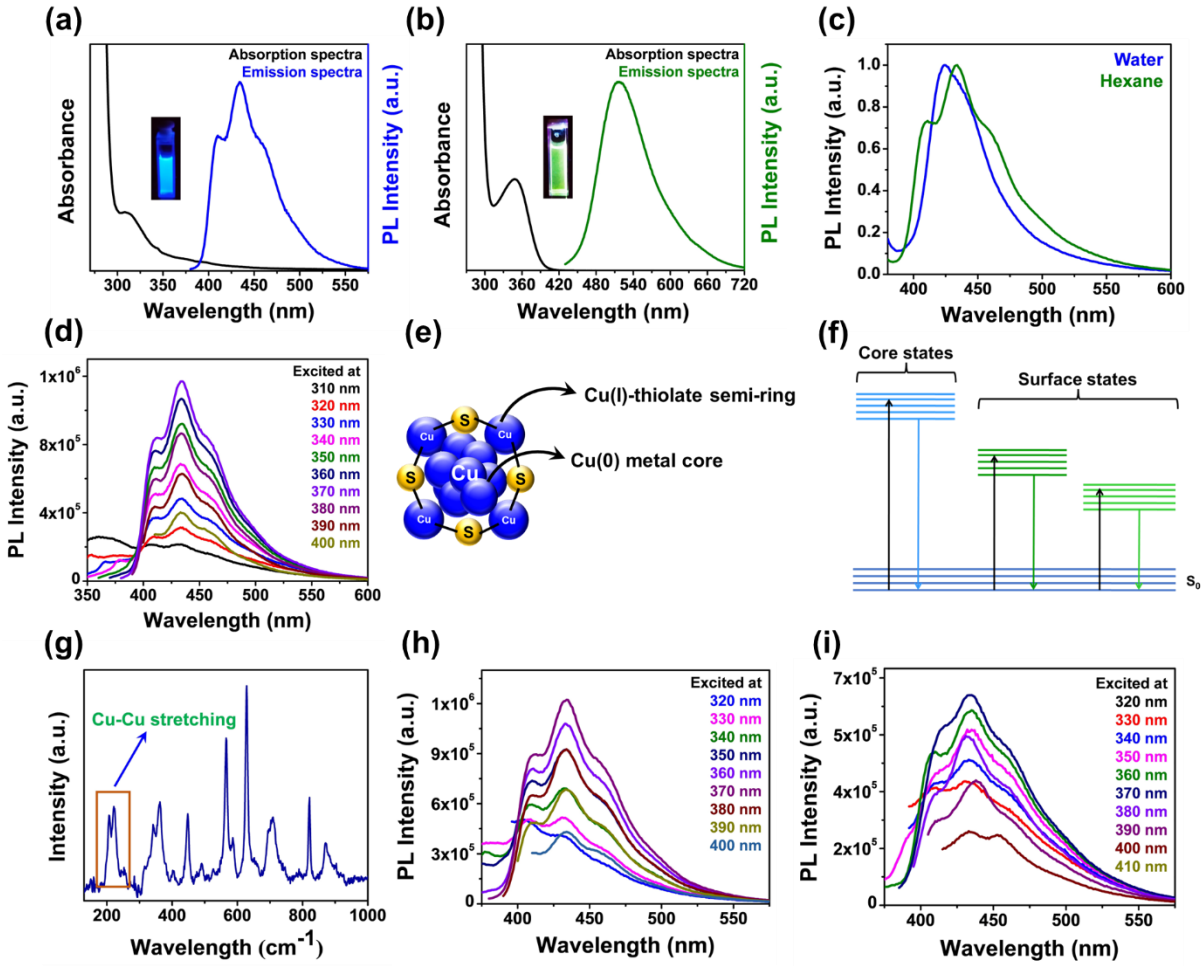

Figure 2.5. Absorption and emission spectra of (a) BCuNC, (b) GCuNC. (c) Emission spectra of BCuNC in n-hexane and water. (d) Excitation-independent emission spectra of BCuNCs. (e) Schematic diagram of Cu(0) metal core and Cu(I)-thiolate semi-ring. (f) Energy level diagram of core and surface states. (g) Raman spectra of BCuNC. (h) Emission spectra of 1-OT templated CuNC, (i) 3-MPA templated CuNC.

displays similar broad absorption features with a peak at ~350 nm (**Figure 2.5b**). This kind of broad absorption spectra is one of the key characteristics of noble metal nanoclusters where inter-band transition takes place from d-band to sp-band.[52] Absence of broad absorption peak in 560-600 nm region for both the nanoclusters confirm that no plasmonic Cu nanoparticles have been formed.[53] Emission spectra of BCuNC in methanol shows three equidistant peaks at 410 nm, 435 nm and 460 nm with a FWHM of ~71 nm (**Figure 2.5a**). To find out the origin of the structured emission features, we recorded emission spectra of BCuNC in a non-polar and a polar solvent along with methanol. Emission spectra in *n*-hexane remains similar to that of methanol but in polar solvent like water the structured feature of spectra disappeared and a broad spectrum was obtained with a maxima at~ 425 nm (**Figure 2.5c**). This broadening is due to several electrostatic interactions of cluster with the solvent molecules that causes the broadening of individual vibronic bands, and ultimately a broad structureless emission band is

generated. This kind of modulation in the emission feature with increasing solvent polarity indicates that three equidistant peaks are originated from the excited state relaxation to different vibrational levels of the ground state. However, the individual nanoclusters and their interactions also have an appreciable extent of correlation with the polarity and H-bonding parameters of the dispersing solvent.[54] The vibrational coarse structures in the emission band are usually obtained from aromatic fluorophores, which are rarely reported in metal nanocluster systems.[55] Emergence of vibrational coarse structures also suggests the formation of discrete nanoclusters having minimal electronic interaction with each other. Notably, when BCuNC was excited in the range of 320-400 nm, no emission band shift was observed (**Figure 2.5d**); therefore, the system displays excitation-independent emission characteristics and follows Kasha's rule. The thiolate-protected noble metal nanoclusters are usually composed of an M(0) core and an M(I)-thiolate semi-ring structure surrounding the core part (**Figure 2.5e**).[56] Excitation-independent emission typically evolves from the non-protected or weakly protected nanoclusters where emission from the metal core is predominant. Here, the quantum confinement effect is the sole governing factor to control over the luminescence; and the electronic states are principally comprised of metal orbitals, which results into minimal spectroscopic heterogeneity in these states. As a result, the emission band exhibits dependence on the size of the metal core rather than the excitation wavelength (**Figure 2.5f**). Additionally, for long-chain alkyl ligand-protected nanoclusters like BCuNC, the electrons might get trapped into the semi-ring-centered surface states. These electrons undergo non-radiative decay because of the unbound conformational mobilities in long alkyl chain of 1,6-HDT ligand; therefore, no ligand-centered emission is observed. Consequentially, the quantum yield of BCuNC was found out to be 10% (**Experimental section 2.2.5**). In the context of metal-centered emission, it is also necessary to show the presence of Cu-Cu bond in the cluster. Thus, we have recorded Raman spectra of BCuNC, where, Raman peak at 206.6 and 221.2 cm^{-1} (**Figure 2.5g**) corresponds to Cu-Cu stretching mode[57,58] in the cluster core. Moreover, to demonstrate the ligand independence over the BCuNC emission, Cu nanoclusters were synthesized using ligands, such as, 1-octanethiol (1-OT), and 3-mercaptopropionic acid (3-MPA) (**Appendix 2.5.1.1 and 2.5.1.2**). Interestingly, all these ligand-capped CuNCs exhibited the same excitation-independent blue emission band with vibrational coarse structures in methanol (**Figure 2.5h, 2.5i**). Steady state emission features of GCuNC follow exactly the opposite trend as that of BCuNC. At different excitation wavelengths ranging from 390-500 nm, the emission maxima of GCuNC became pervaded over the range of 500-564 nm (**Figure 2.6b**). The span of excitation-dependent emission band shift reflects the extent of spectroscopic

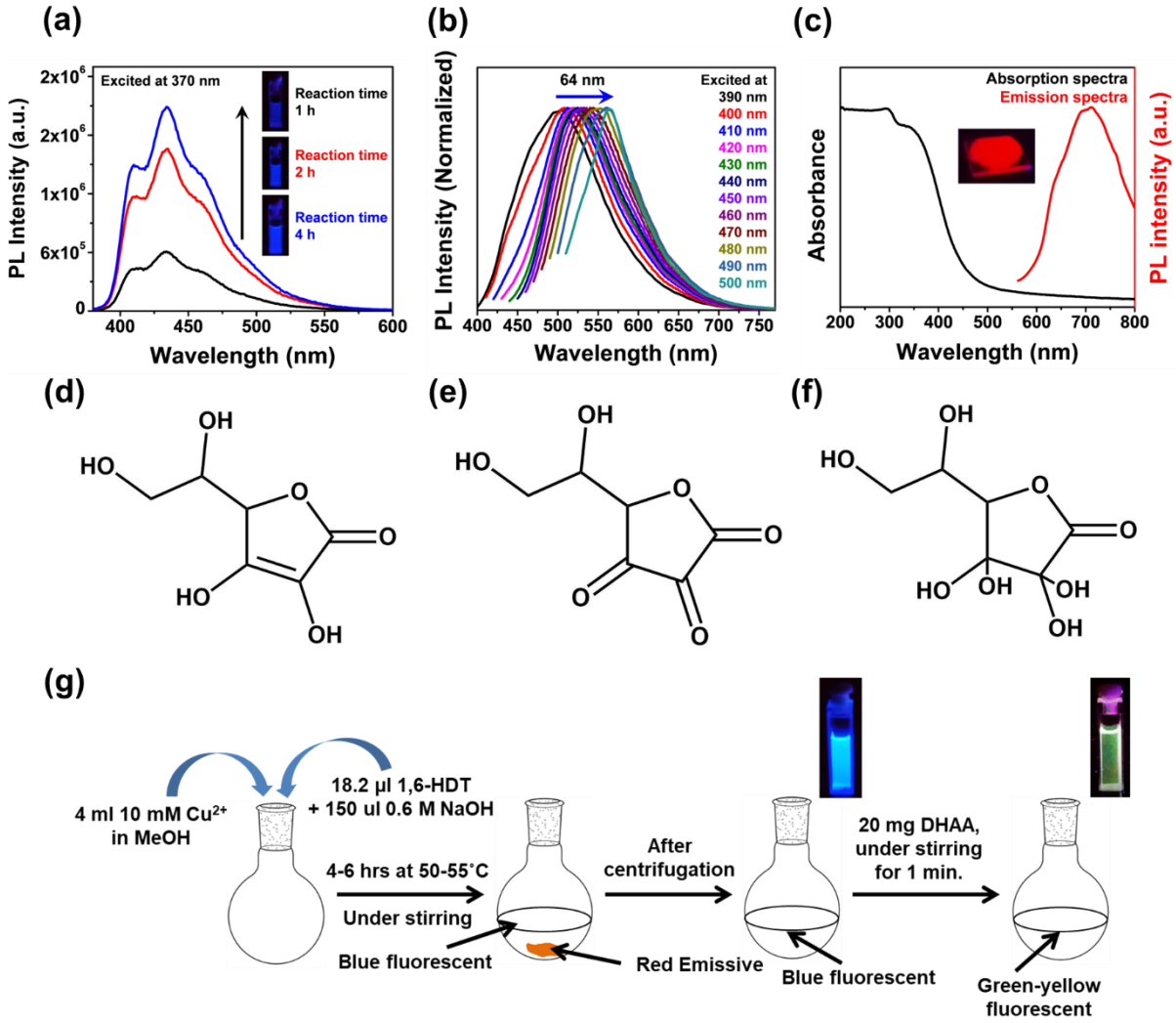

Figure 2.6. (a) Time dependent evolution of BCuNC in P1, (b) Excitation-dependent emission spectra of GCuNCs, (c) Absorption and emission spectra of RCuNC (Excited at 360 nm). Structure of (d) L-ascorbic acid (AA), (e) L-dehydroascorbic acid (DHAA), (f) L-dehydroascorbic acid dihydrate. (g) Schematic representation of the cross-check experiment.

heterogeneity present in the bright excited states of GCuNC. This kind of heterogeneity in photoemission mainly arises from the ligand-centered excited states or surface states, and it indicates the formation of self-assembled or aggregated nanoclusters. The surface states consist of several unpassivated metal orbitals, which lead to the formation of trap states as well.[33] Presence of these trap states are mostly responsible for the emergence of excitation-dependent or extrinsic emission. In aggregated or self-assembled state, restricted mobilities of the protecting ligands drive the electrons to undergo radiative relaxation by suppressing the non-radiative decay processes. As a result, it produces relatively larger quantum yield of 30% ($\lambda_{Excitation}$ = 420 nm) compared to BCuNC (**Experimental section 2.2.5**). In addition to that, HRTEM and DLS results of GCuNC also suggest the formation of nanocluster aggregates (**Figure 2.2c, 2.2d**). However, the photo-physical properties of RCuNC aggregates are much

distinct, where it exhibits larger Stokes' shift as compared to BCuNC and GCuNC. The solid-state absorption spectra of RCuNC shows broad absorption band with peaks around 300 nm and 350 nm (**Figure 2.6c**) and the emission spectra exhibits a red shifted emission band which has a peak at 710 nm (**Figure 2.6c**). The exceptionally large stokes' shift also indicates this red emission to be generated from highly stabilized triplet states. The emission band was found to be excitation-independent unlike GCuNC, which indicates that the emission emerges from specific triplet states (**Figure A1 in Appendix 3**). M(I)-thiolate complexes of noble metals (M=Cu, Au) are found to exhibit phosphorescence due to presence of bright triplet states in their aggregated state.[59,60] The stability of these triplet state depends upon intra and inter-cluster metalophillic interactions and electron-donating properties of ligand. These triplet states possess larger contributions from metal orbitals and originate due to ligand-to-metal charge transfer (LMCT) or ligand-to-metal-metal charge transfer (LMMCT) through sulphur atom of 1,6-HDT. We also believe that in these aggregates, due to decrement in Cu(I)…Cu(I) distance inter and intra-cluster metalophillic interaction also increases[13], which causes a large extent of stabilization of the triplet states, resulting into a ~360 nm Stokes' shift. Notably, the absolute quantum yield of RCuNC was found to be 3% (**Experimental section 2.2.5**). Furthermore, generation of the two marginal emission bands from supernatant (BCuNC) and precipitate part (RCuNC) from a single pot synthesis (**P1**) is an indication of aggregation induced emission (AIE) type behaviour of individual monomeric clusters in RCuNC. Here it is necessary to mention that it is not possible to demonstrate AIE behaviour of RCuNC in a solvent mixture (such as, 0-90% water/ethanol mixture), as the precipitates cannot be solubilized in common solvents.

2.3.5. Mechanism for the formation of GCuNC: *in-situ* ligand replacement

In order to investigate the mechanism of GCuNC formation, we revisited the synthetic protocol 2 (**P2**), where AA was used as the reducing agent. AA or vitamin C, an environmentally friendly and mild reducing agent, has been successfully utilized in synthesizing several nanoparticle and nanocluster systems (**Figure 2.6d**).[61–63] AA reduces Cu(II) to Cu(I) and Cu(0), and is itself oxidized to L-dehydroascorbic acid (DHAA) (**Figure 2.6e**). Due to the presence of three adjacent carbonyl groups, the molecule is highly electrophilic and becomes unstable in nucleophilic environment such as in water and alcohols. As a result, it forms a dihydrate structure (**Figure 2.6f**) in this kind of nucleophilic solvents.[64] Moreover, due to the presence of multiple hydroxyl groups, the molecule exhibits multidentate ligating behavior especially in an alkaline condition. In order to scrutinize the possible role of the DHAA which was formed *in-*

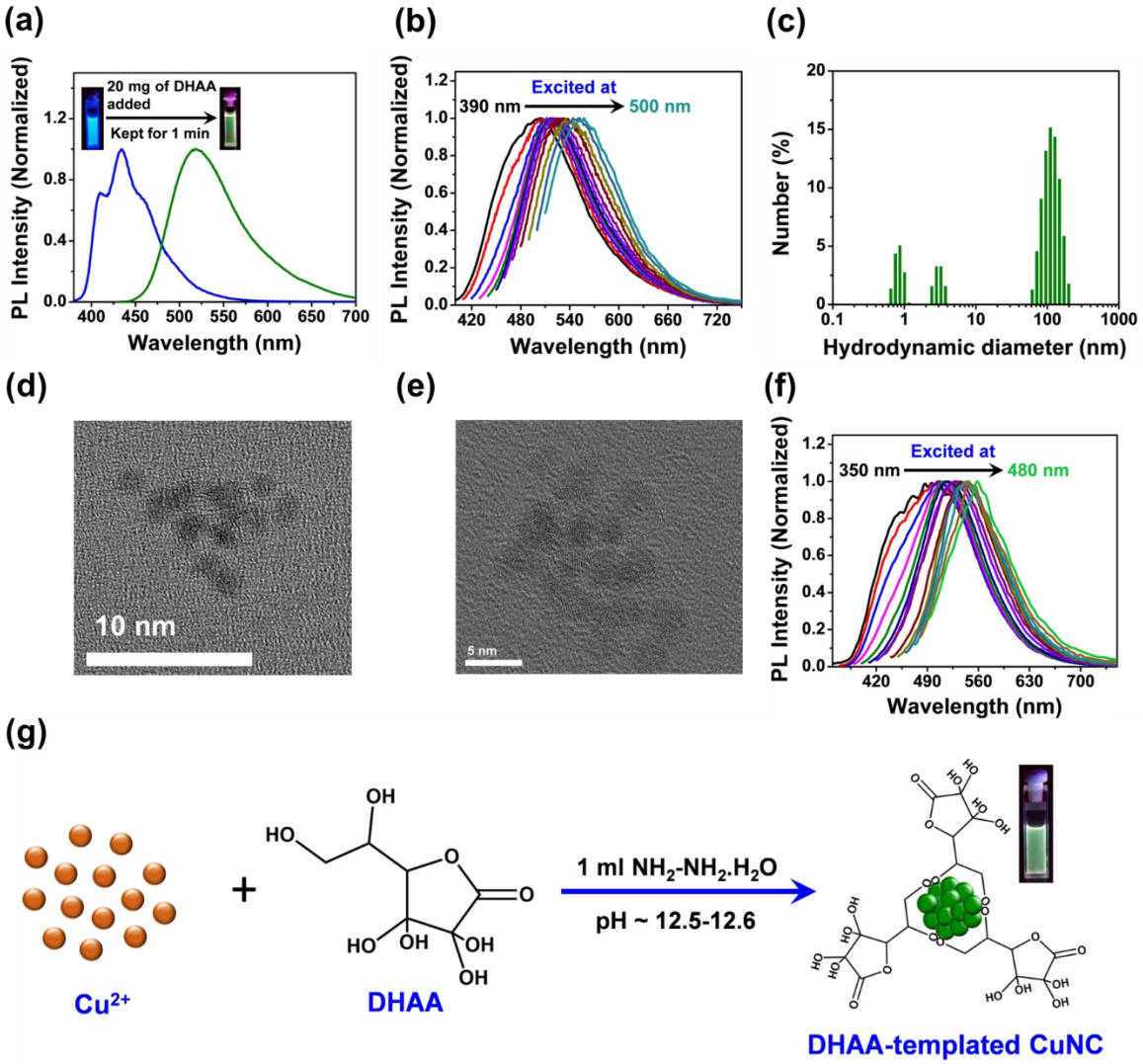

Figure 2.7. (a) Blue to green emission switching upon DHAA addition, (b) Emission spectra of green-yellow emissive CuNC from cross-check experiment, (c) DLS size distribution of green-yellow emissive CuNC from cross-check experiment, (d), (e) HRTEM images of green-yellow emissive CuNC from cross-check experiment, (f) Emission spectra of DHAAtemplated CuNC, (g) synthesis of DHAA-templated CuNCs.

situ as a side product, we performed a cross-check experiment. We synthesized BCuNC separately by using the same protocol as that of **P1**, followed by the addition of 20 mg of DHAA at an elevated pH of ~12.5 under constant stirring condition (**Figure 2.6g**). Surprisingly, the solution promptly turned into yellowish green within 1 minute and exhibited bright green-yellow emission under UV light (**Figure 2.7a**). However, no blue emission was observed, signifying a complete transformation of emission from blue to green-yellow, mediated by DHAA (**Figure 2.7a**). Furthermore, the emission characteristics of the resultant solution was excitation dependent (with almost 60 nm of emission band shift) (**Figure 2.7b**) similar to what was observed in the case of GCuNC. The DLS study of the sample shows the similar emergence

of a size distribution (**Figure 2.7c**) like GCuNC. Additionally, HRTEM results exhibit that the size of individual nanoclusters remains unaltered in the blue-to-green transformation, but they are closely assembled with each other (**Figure 2.7d, 2.7e**). This clearly states that in **P2**, the GCuNC was formed from BCuNC which was mediated by the *in-situ* formed DHAA. To elucidate the mechanism further, we have designed another protocol where Cu nanocluster was synthesized by using DHAA as capping agent and hydrazine monohydrate as the reducing agent (**Figure 2.7g**). Interestingly, these DHAA-capped CuNCs also exhibited the similar excitation-dependent green-yellow emission (**Figure 2.7f**) resembling the emission properties of GCuNC. We have also characterized the product with DLS technique, HRTEM and FT-IR spectroscopy. DLS experiment reveals the nature of the nanocluster aggregates with a size >100 nm (**Figure 2.8a**), which are compatible with the nature of GCuNC. HRTEM images of DHAA-capped CuNC (**Figure 2.8b, 2.8c**) also corroborate with the TEM results of GCuNC as well. Raman spectra of GCuNC and DHAA capped nanoclusters also show similar features with peaks at ~430 cm^{-1} and ~500 cm^{-1} corresponding to the stretching frequency of Cu-O bond[65] (**Figure 2.9a**), which indicates that oxygen is the binding site for both the nanoclusters. These results clearly indicate that DHAA itself can act as a protecting ligand and lead to the successful formation of luminescent Cu nanoclusters, which are structurally and photo-physically similar to GCuNC. We have also collected MALDI-TOF mass spectrum of GCuNC (**Figure 2.8d**), where the derived composition is $Cu_{7-9}(DHAA)_{2-3}$, which confirms that GCuNC is basically the *in-situ* formed DHAA capped CuNC. To confirm the oxidation states of Cu in GCuNC, XPS measurement was performed which exhibits two peaks at 934.78 and 954.78 eV (**Figure 2.9b**) corresponding to binding energy of electrons for Cu $2p_{3/2}$ and Cu $2p_{1/2}$, respectively. The data confirms the presence of Cu(0) and Cu(I) in the GCuNC similar as BCuNC, which also proves that the metallic counterpart is similar for both BCuNC and GCuNC. In addition to that, another peak at 534.48 eV (**Figure 2.9c**) corresponding to the binding energy of O 1s electrons confirms the presence of Cu-O bond. The collected insights of all mechanistic investigations culminate that the GCuNC is formed from the BCuNC upon delaying reaction time in **P2**, via an *in-situ* ligand replacement process by the oxidized form of the reducing agent (AA) present in the reaction medium. In this regard, the formation of nanocluster aggregates as reflected in the DLS and HRTEM results may be assigned to the multidentate nature of the DHAA molecule. It has a pair of hydroxyl groups at one end and a quartet of hydroxyl groups at the other end in its dihydrate structure (**Figure 2.6f**). Therefore, it can bind to two nanoclusters simultaneously with its two ends,[66] and can form bigger nanocluster aggregates (**Figure 2.9d**). The formation of these aggregates leads to the restriction

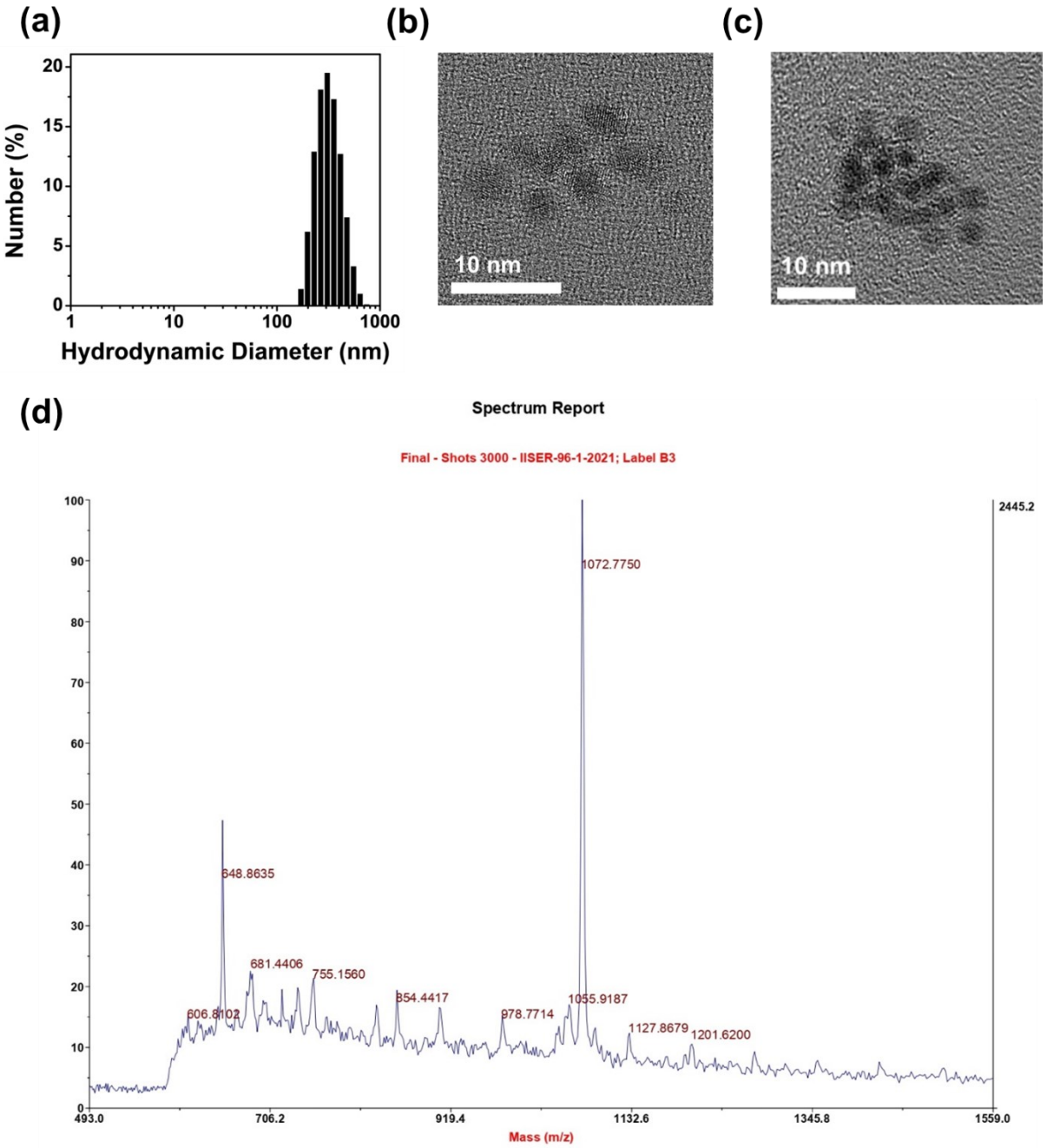

Figure 2.8. (a) DLS size distribution, and (b), (c) HRTEM images of DHAA capped CuNC. (d) MALDI-TOF mass spectrum of GCuNC. Estimated compositions of GCuNC, 1072.77 = $[Cu_7(DHAA)_3 - 3H^+]^+$, 1201.62 = $[Cu_9(DHAA)_3 - H^+]^+$, 904.46 = $[Cu_7(DHAA)_2 + K^+]^+$, 1127.86 = $[Cu_8(DHAA)_3 - 10H^+]^+$.

in ligand mobilities, which results in the evolution of ligand-centered emission in GCuNC. Notably, ligand replacement process, a well-known ligand engineering technique, which has been utilized in the modulation of several properties and functionalities of nanomaterials,[67–70] is severely influenced by pH of the medium and the ligand concentration. To elucidate the pH dependence, at first, we synthesized BCuNC following **P2** with a reaction time of 2 hrs and monitored the change in emission intensity at 520 nm with sequential addition of methanolic

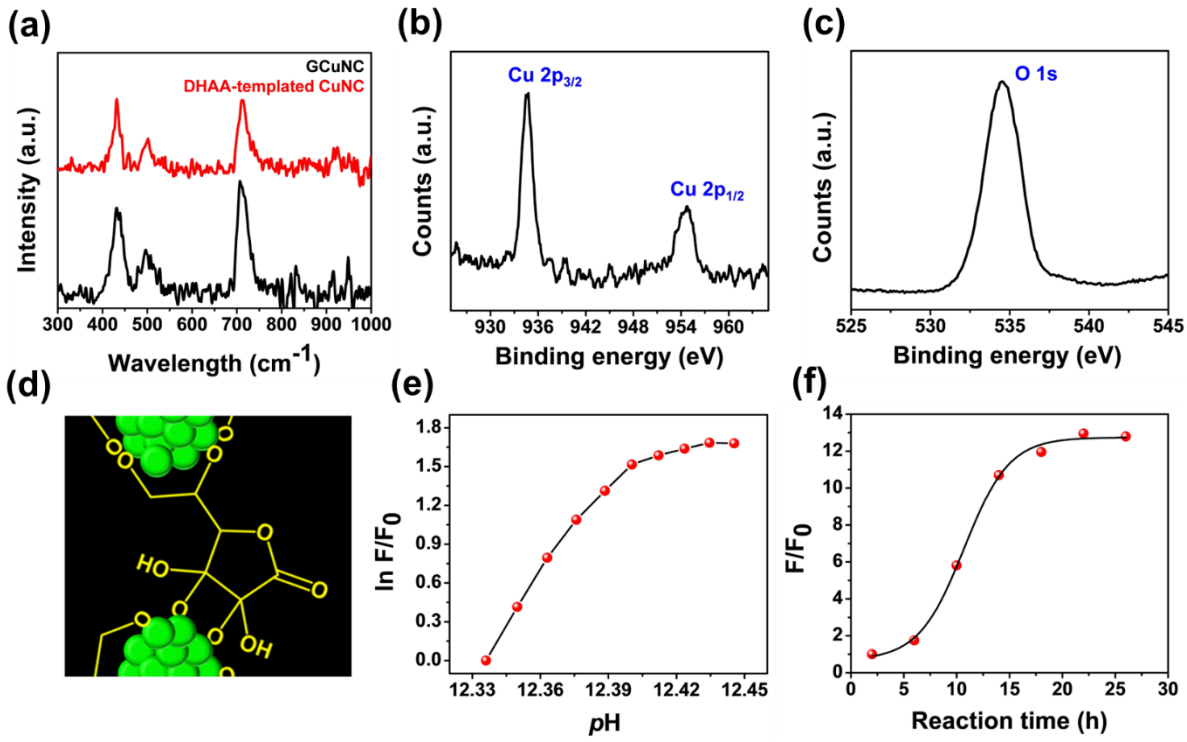

Figure 2.9. (a) Raman spectra of GCuNC and DHAA capped CuNC, (b) XPS spectra of GCuNC for Cu 2p electrons, (c) XPS spectra of GCuNC for O 1s electrons, (d) Plausible coordination of DHAA with two CuNC, (e) $\ln(F/F_0)$ vs. pH plot (emission collected at 520 nm), (f) F/F_0 vs. reaction time plot of protocol 2 (**P2**) (emission collected at 520 nm).

NaOH. $\ln(F/F_0)$ vs. pH plot (**Figure 2.9e**, **Table A1 in Appendix 4**) shows that with increasing the pH of the BCuNC solution, the $\ln(F/F_0)$ increased sharply and gradually became saturated when pH increased after ~12.4. With the increase in pH, the concentration of the deprotonated DHAA molecules (which are responsible for the GCuNC formation) increases, thus accelerating the ligand exchange rate, and thereby results into the emission enhancement at 520 nm. To monitor the evolution kinetics of GCuNC, we have recorded the emission intensity (at 520 nm) of GCuNC samples (synthesized by following **P2**) at different reaction time periods. The F/F_0 vs. reaction time (hrs) plot was fitted with a sigmoid function, and the macroscopic rate constant of ligand exchange process was found to be 2.14 ± 0.241 hrs^{-1} (**Figure 2.9f, Table A2 in Appendix 4**). To clarify the role of ligand concentration, we synthesized GCuNC with different AA concentration by following **P2** and plotted F/F_0 (emission collected at 520 nm) against respective concentrations of AA (**Figure 2.10a, Table A3 in Appendix 4**). The observed linear dependence of the plot suggests that the ligand replacement process also depends on concentration of DHAA, which is directly proportional to the concentration of AA added to the reaction mixture. We believe the principal driving force behind the ligand exchange process to be the thermodynamics of chelation effect. Ligand associated with BCuNC is a dithiol, which binds to the nanocluster surface with one -SH end, thus behaves as a

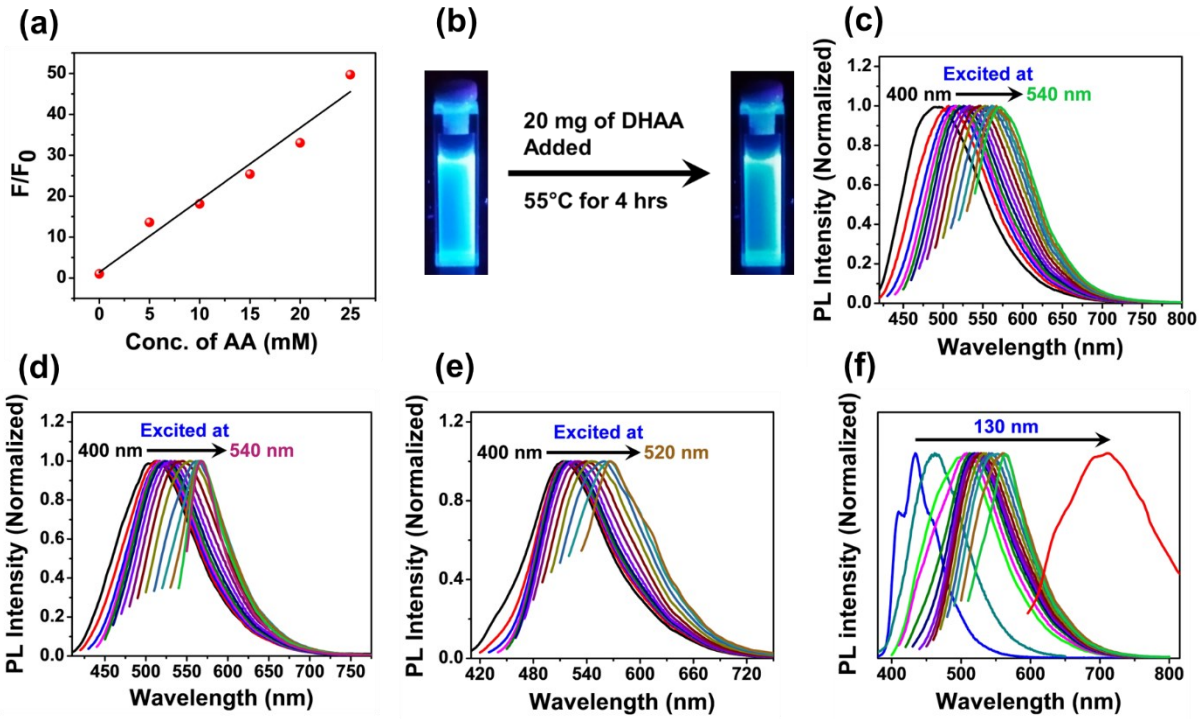

Figure 2.10. (a) F/F_0 vs. conc. of AA plot (emission collected at 520 nm), (b) AA capped CuNC under UV light and after addition of DHAA. Emission spectra of green yellow emissive CuNC by following P2 and using (c) 1-OT as capping ligand; (d) 1,3-PDT as capping ligand and (e) 1,9-NDT as capping ligand, (f) Time dependent emission spectra of the supernatant (P2) and emission spectra of RCuNC.

monodentate ligand. On the other hand, DHAA has multiple -OH residues, which is responsible for the multidentate behaviour of the DHAA. Therefore, during the ligand exchange process, a single DHAA ligand binds to the nanocluster surface at the cost of dissociation of multiple dithiol ligands, which leads to the drastic elevation in the entropy of the system, and thus making the ligand exchange process favorable in terms of thermodynamic parameters. To support our speculation, we have synthesized blue emissive AA capped CuNC exhibiting similar emission characteristics like BCuNC and added 20 mg of DHAA into it. Consequentially, no blue to green-yellow emission switching was observed from the solution (**Figure 2.10b**). As AA and DHAA both are multidentate ligands, therefore, ligand exchange process would have led to negligible change in the entropy, thus making the process thermodynamically forbidden. Whereas, 1-OT, 1,3-propanedithiol (1,3-PDT), 1,9-nonanedithiol (1,9-NDT) capped CuNCs, synthesized separately by following the **P2** protocol exhibited the same green-yellow emission (**Figure 2.10c, 2.10d, 2.10e**), where these three ligands manifested monodentate behaviour like 1,6-HDT exhibited in case of BCuNC.

2.3.6. Demonstration of broadband emission tunability

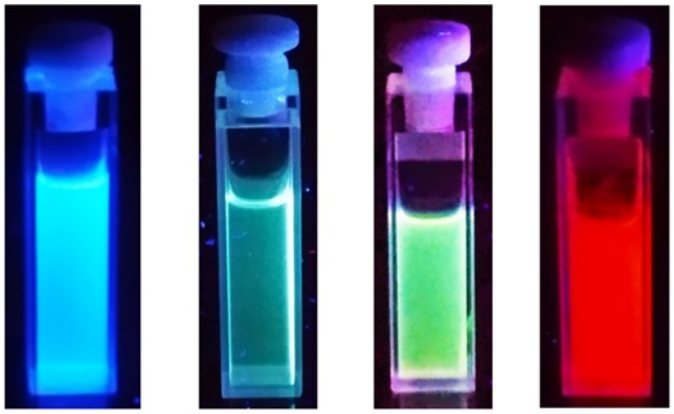

Figure 2.11. Reaction time dependent emission tuning by resolving GCuNC formation reaction along with RCuNC.

This dual nanocluster system composed of BCuNC and GCuNC also exhibits broadband emission tunability in the visible spectrum, where time appears to be the only determining factor to generate different colors from blue to green-yellow. As, the GCuNC formation requires longer reaction time, hence, we quenched the reaction (**P2**) at different time intervals and collected corresponding emission spectra (**Figure 2.10f**). Eventually, monitoring the protocol 2 with time led to the formation of blue, cyan and green-yellow emissive CuNC assemblies at 4, 10 and 20 hrs of reaction time, respectively (**Figure 2.11**), which shows an emission tunability of ~130 nm (**Figure 2.10f**). To investigate the origin of cyan emission, we synthesized DHAA-capped CuNC using the previously mentioned procedure (**Appendix 2.5.1.4.**) with a reaction time of 10-12 hrs. Interestingly, the cyan emission was observed from the synthesized CuNCs (**Figure A2 in Appendix 3**), and this observation suggests that the cyan emission is appeared from the DHAA capped CuNCs in the intermediate reaction time. The reason of the emergence of two different emissions (cyan and green-yellow) from both the DHAA capped CuNC and GCuNC is believed to be due to the formation of aggregates having different dimensions and structures in two different reaction times. To investigate the effect of AA concentration on emission tuning process we followed the protocol 2 at two different concentrations of AA, (i) 20 mM and (ii) 50 mM. We observed that emission tuning is reasonably faster in the reaction mixture with 50 mM AA concentration than that of the reaction with 20 mM AA concentration (**Figure A3 in Appendix 3**). This particular observation corroborates with the evolution kinetics of GCuNC. The rate of GCuNC formation is gradually enhanced with increasing AA concentration, hence $t_{1/2}$ of the sigmoidal curve (**Figure 2.9f, Experimental Section 2.2.6.**) decreases and emission tuning process becomes faster. Thus, our

experimental results eventually generalize the ligand replacement mediated emission tuning model and also prove its applicability in broader aspects.

2.3.7. Excited state dynamics of BCuNC, GCuNC and RCuNC

The ligand exchange process on the surface of BCuNC not only changes its emission colour but also changes the nature of the emission. We have previously discussed about the origin of the vibronically resolved intrinsic emission band of BCuNC, which was mainly attributed to the metal centered excited states or core states. On the other hand, the excitation dependent extrinsic emission band of GCuNC was assigned to be generated mainly from the ligand centered semi-ring surface states. To elucidate several processes associated with metal and ligand centered excited states, we have investigated the fluorescence dynamics with the help of TCSPC and femtosecond fluorescence up-conversion techniques. TCSPC decay transients of BCuNC at 410, 435 and 460 nm are bi-exponential in nature with components of 60-80 ps and 1.35-1.4 ns (**Figure 2.12a, Table 2.2**). In case of the ideal intrinsic emission, the core state electrons sequentially undergo decay through vibrational relaxation followed by radiative recombination. Therefore, ideally, the emission decay transients should be single exponential which is usually found in highly luminescent metal nanoclusters.[71] But in real scenario, a significant population of the excitons undergo decay through several non-radiative pathways from the core to surface states or ground state, which leads to the emergence of bi-exponential fluorescent transients. The longer nanosecond component (1.35-1.4 ns) is assigned to the radiative relaxation from the core states, relative contribution of which increases with the ascending collection wavelength from 410 to 460 nm (**Table 2.2**). This component also remains almost constant with increasing emission wavelength (410-460 nm) because of the higher spectroscopic homogeneity in the blue emissive core states. In case of intrinsic emission, the depopulation of the core states at 60-80 ps time scale originated from several non-radiative relaxations of excitons from the core to surface states or ground state. Conversely, the effect of spectroscopic heterogeneity becomes prominent in GCuNCs with multi-emissive surface states, leading to evolution of tri-exponential emission transient at 520 nm with components of 82 ps, 875 ps and 3.0 ns (**Figure 2.12b**, **Table 2.2**). To elucidate the processes associated with these three components, we collected wavelength dependent fluorescent transients of GCuNC from 450 nm to 590 nm (**Figure 2.12c**, **Table 2.3**). Two long components of ~0.8-1 ns and ~2-3 ns represent the radiative recombination process from two different surface states. The relatively shorter component gradually decreases from ~1 ns to 0.8 ns with a declining relative contribution while collected the emission from 450 nm to 590 nm wavelength (**Table 2.3**),

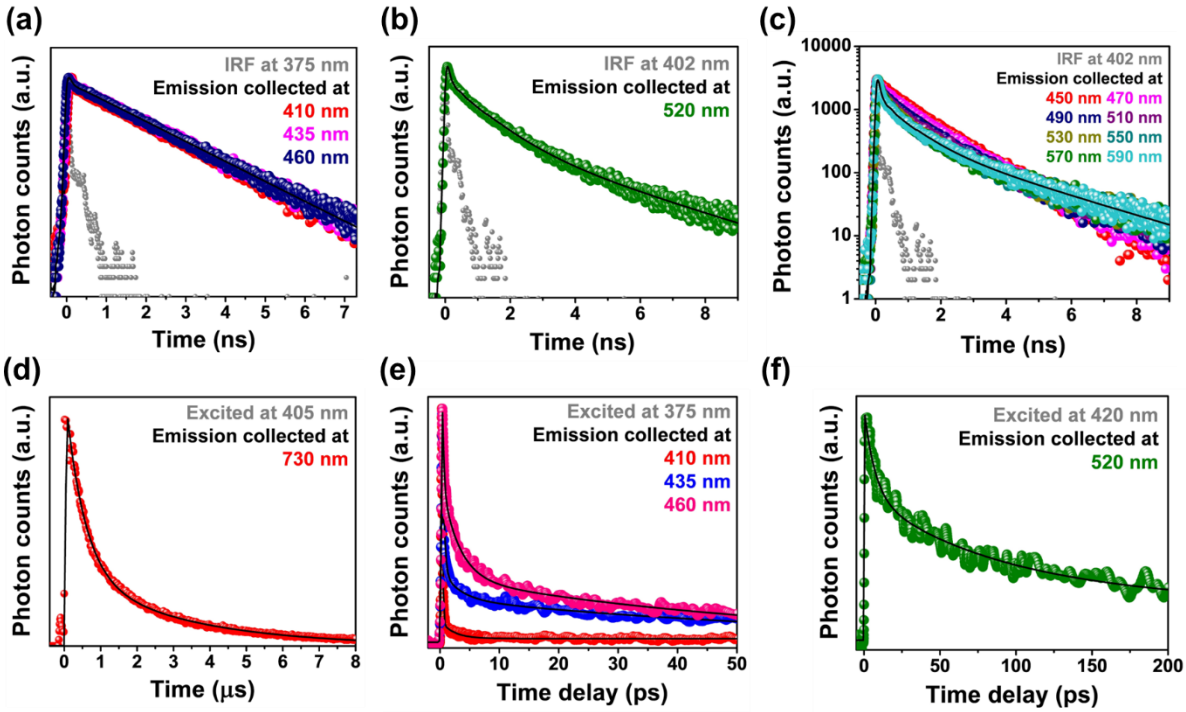

Figure 2.12. Emission decay transients of (a) BCuNCs and (b) GCuNCs obtained from TCSPC technique. (c) Emission dependent fluorescence transients of GCuNC by TCSPC. (d) microsecond photoluminescence decay of RCuNC. Femtosecond fluorescence up-conversion decay transients of (e) BCuNCs and, (f) GCuNC.

indicating that the respective relaxation belongs to the excited states, which are relatively higher in energy. The ~2-3 ns component is attributed to the ligand-centered surface states residing in the lowest energy regime. This component increases with ascending emission wavelength due to the participation of more numbers of lower energy surface states. The quenching of lifetime in the case of ~0.8-1 ns component may be attributed to the increasing non-radiative decay processes, as the collection wavelength approaches the emission from the lower energy surface state. The increase in non-radiative processes is mainly attributed to two factors. Firstly, in the case of the lower energy surface states, the cross-section between the excited state and ground state potential energy surfaces increases, which results in enhancement in the non-radiative decay. Secondly, lower energy surface states face enhanced non-radiative decay pathways due to increased vibrational and rotational mobilities in the ligands associated with the surface states. We anticipate these two radiative recombination time scales to be generated due to the presence of aggregates with miscellaneous dimensions, which is also evident from DLS and HRTEM results discussed earlier. Interestingly, another shorter component of ~80-90 ps arises in the lifetime profile having an inclining relative contribution with increasing collection wavelength (**Table 2.3**). The inclining relative contribution clearly indicates that the component is sensitive towards the influence of the lower energy surface

states, and it may be attributed to the carrier trapping onto the surface states due to the presence of several unpassivated metal orbitals on the surface of nanoclusters which are often regarded as surface defects[33]. We also observe an increase in average lifetime from 450-590 nm wavelength (**Table 2.3**), which is attributed to the increasing relative contribution of the carrier trapping timescale (~80-90 ps) onto the surface states and increase in the long component (~2-3 ns) with ascending emission wavelength. To look into the ultrafast behaviour of the excited states, femtosecond fluorescence up-conversion technique was utilized and the ultrafast components derived out from the BCuNC are of <500 fs, 2-3 ps (**Figure 2.12e**, **Table 2.4**). The relative contribution of <500 fs component decreases with increasing wavelength (**Table 2.4**), which indicates that it is associated with the core state dynamics. This ultrafast component may be attributed to the intra-band relaxation in the core states. The intra-band relaxation in the core states is followed by solvent relaxation, and thereby, stabilizing the core states before excitons undergo a non-radiative transfer onto the surface states.[72] In a polar solvent like methanol, this kind of solvent relaxation occurs at ultrafast time scales which can be attributed to the observed 2-3 ps components. However, 2-3 ps time scale may also include the excited state redistribution of axial and equatorial Cu-Cu bond lengths.[73] Up-conversion transient of GCuNC reveals a component of ~7 ps (**Figure 2.12f**, **Table 2.4**), which may be attributed to the non-radiative relaxations from core states to Cu(I)-thiolate semi-ring surface state. Contrary to BCuNC and GCuNC, the red emissive RCuNC exhibits much long lifetime components in micro-second timescale. The decay transient of RCuNC collected at 730 nm shows two components with 0.51 μs and 3.0 μs lifetime (**Figure 2.12d**, **Table 2.5**), indicating the phosphorescent nature of the emission. In these aggregates, due to decrement in Cu(I)…Cu(I) distance inter and intra-cluster cuprophilic interaction also increases,[13] and increase in cuprophilic interaction leads to generation of stable triplet states with longer lifetime in microsecond timescale. We believe that the triplet states of the system corresponding to the observed decay components become stabilized with increasing extent of aggregation in the precipitates, and the observed two decay components may be attributed to the radiative relaxation from two separate triplet states having distinct charge transfer characters.

Table 2.2. Lifetime fitting parameters of BCuNC and GCuNC, obtained from TCSPC.

Sample	λ_{Em}	τ_1	α_1	τ_2	α_2	τ_3	α_3	$<\tau>$
BCuNC	410 nm	70.2 ps	0.62	1.39 ns	0.38	-	-	1.28 ns
BCuNC	435 nm	68.2 ps	0.54	1.39 ns	0.46	-	-	1.31 ns
BCuNC	460 nm	82.3 ps	0.51	1.4 ns	0.49	-	-	1.32 ns
GCuNC	520 nm	82.0 ps	0.76	0.875 ns	0.20	3.0 ns	0.04	1.45 ns

Table 2.3. Wavelength-dependent lifetime fitting parameters of GCuNC obtained from TCSPC.

λ_{Em}	τ_1	α_1	τ_2	α_2	τ_3	α_3	$<\tau>$
450 nm	87.0 ps	0.53	997 ps	0.36	1.8 ns	0.11	1.19 ns
470 nm	84.5 ps	0.60	962 ps	0.32	2.1 ns	0.08	1.24 ns
490 nm	77.5 ps	0.71	952 ps	0.25	2.6 ns	0.05	1.34 ns
510 nm	85.9 ps	0.74	908 ps	0.22	2.8 ns	0.04	1.33 ns
530 nm	78.6 ps	0.78	852 ps	0.18	3.1 ns	0.04	1.53 ns
550 nm	81.9 ps	0.78	815 ps	0.17	3.0 ns	0.04	1.48 ns
570 nm	78.1 ps	0.79	798 ps	0.16	3.0 ns	0.04	1.50 ns
590 nm	80.3 ps	0.80	800 ps	0.16	3.0 ns	0.04	1.49 ns

Table 2.4. Lifetime fitting parameters of BCuNC and GCuNC obtained from femtosecond fluorescence up-conversion.

Sample	λ_{Em}	τ_1	α_1	τ_2	α_2	τ_3	α_3
BCuNC	410 nm	99 fs	97.40%	2.24 ps	2.51%	-	-
BCuNC	435 nm	297.4 fs	79.80%	2.98 ps	8.05%	67.4 ps	12.08%
BCuNC	460 nm	220 fs	56.96%	2.89 ps	25.94%	57.4 ps	17.08%
GCuNC	520 nm	7.0 ps	38.29%	82 ps	42.22%	875 ps	24.10%

Table 2.5. Lifetime fitting parameters of RCuNC obtained from TCSPC.

Sample	λ_{Em}	τ_1	α_1	τ_2	α_2	$<\tau>$
RCuNC	730 nm	0.51 μs	0.7	3.0 μs	0.3	2.29 μs

2.4. Conclusions

In summary, we have been able to develop a unique system where the emission can be tuned from blue to green-yellow by in situ ligand replacement process. The process has been mediated by the oxidized form of the reducing agent itself, therefore, in our proposed protocol, no external agent is required to drive this blue to green-yellow emission tuning. Moreover, blue and red emitting CuNCs have been synthesized in one-pot which was not reported earlier to the best of our knowledge. Along with red emission from RCuNC, the emission band of the whole system covers almost the visible spectrum thus manifests excellent emission tunability from a single nanocluster system. A significant role of L-ascorbic acid has been explored in our study, and it has been proved that it can be used to modulate the emission properties of nanomaterials. This property of L-ascorbic acid can be further extended to several nano-systems, which may contribute to the field of ligand engineering of nanomaterials. We have also synthesized a covalently linked CuNC superstructures, which are red emissive in nature and can be utilized in LED applications. The blue emissive nanocluster exhibits excitation independent emission which implies it to be originated from metal centered core states. In contrast, the green-yellow emissive nanocluster shows excitation dependent emission which signifies that ligand centered surface states are predominantly involved in this process. The excited state dynamics in nano- and sub-nanosecond regime, along with the ultrafast spectroscopy further differentiate between these two excited state emissions with contrasting nature. In case of BCuNC, the emission is originated mainly from the metal centered core states. The fluorescence dynamics studies also deciphered the involvement of two distinct surface states in the excited state relaxation of GCuNC. Authors hope that, this particular nanocluster system along with the developed protocol shall pave the way forward to fabricate highly efficient future generation LED devices with broadband color tunability and will be useful to develop multi-color printing technology.

2.5. Appendices

2.5.1. Appendix 1: Synthesis of 1-OT capped CuNC, 3-MPA capped CuNC and AA capped CuNC

2.5.1.1. Synthesis of 1-OT capped CuNC

In a typical experiment, 4 mL of 10 mM $CuSO_4.5H_2O$ solution was prepared in methanol solvent and was taken in a 25 mL round bottom (RB) flask. 20.8 µL of 1-OT was dissolved in ~150 µL of 0.6 M methanolic NaOH and the resulting disperse was sonicated and added to the Cu^{2+} solution. It resulted into the formation of a white turbid solution (The conc. of OH^- ions and 1-OT in the final mixture becomes ~20 mM and ~30 mM respectively). The mixture was kept under inert condition and constant stirring at ~50-55˚C temperature for 4-5 hrs. followed by centrifugation at 12000 rpm for 10 min. Resulting colourless supernatant appeared as blue emissive under UV light.

2.5.1.2. Synthesis of 3-MPA capped CuNC

In a typical experiment, 4 mL of 10 mM $CuSO_4.5H_2O$ solution was prepared in methanol solvent and was taken in a 25 mL round bottom (RB) flask. 10.4 µL of 3-MPA was dissolved in ~150 µL of 0.6 M methanolic NaOH and the resulting disperse was sonicated and added to the Cu^{2+} solution. It resulted into the formation of a white turbid solution (The conc. of OH^- ions and 3-MPA in the final mixture becomes ~20 mM and ~30 mM respectively). The mixture was kept under inert condition and constant stirring at ~50-55˚C temperature for 4-5 hrs. followed by centrifugation at 12000 rpm for 10 min. Resulting colourless supernatant appeared as blue emissive under UV light.

2.5.1.3. Synthesis of AA capped CuNC

In a typical experiment, 4 mL of 10 mM $CuSO_4.5H_2O$ solution was prepared in methanol solvent and was taken in a 25 mL round bottom (RB) flask. 21.1 mg of AA was dissolved in ~150 µL of 0.6 M methanolic NaOH and the resulting disperse was sonicated and added to the Cu^{2+} solution. It resulted into the formation of a deep brown precipitate (The conc. of OH^- ions and AA in the final mixture becomes ~20 mM and ~30 mM respectively). The mixture was kept under inert condition and constant stirring at ~50-55˚C temperature for 4-5 hrs. followed by centrifugation at 12000 rpm for 10 min. Resulting colourless supernatant appeared as blue emissive under UV light.

2.5.1.4. Synthesis of DHAA capped CuNCs

In a typical experiment, 4 mL of 10 mM $CuSO_4.5H_2O$ solution was prepared in methanol solvent and was taken in a 25 mL round bottom (RB) flask. 20.8 mg of DHAA was dissolved in ~250 µL of 0.6 M methanolic NaOH and the resulting disperse was sonicated and added to the Cu^{2+} solution resulting into instantaneous formation of a yellowish precipitate (The conc. of OH^- ions and DHAA in the final mixture becomes ~20 mM and ~30 mM respectively). 1 ml of hydrazine monohydrate was dropwise added to the mixture. The mixture was kept under inert condition and constant stirring at ~50-55˚C temperature for 24 hrs. Bigger particles and aggregates were removed by centrifugation at 8000 rpm for 10 min. Resulting yellowish green supernatant appeared as green emissive under UV light.

2.5.2. Appendix 2: Synthesis of green-yellow emissive CuNC by following P2 and using 1-OT, 1,3-PDT and 1,6-NDT as capping ligands

2.5.2.1. Synthesis of green-yellow emissive CuNC from 1-OT capped CuNC.

4 mL of 10 mM $CuSO_4.5H_2O$ solution was prepared in methanol solvent and was taken in a 25 mL RB flask. 20.8 µL of 1-OT was dissolved in 250 µL of 0.6 M methanolic NaOH and added to the solution in RB flask so that conc. of OH^- ions and 1-OT in the resulting solution becomes ~40 mM and ~30 mM respectively. White precipitate was formed instantaneously, followed by an addition of 14 mg (20 mM) of solid L-ascorbic acid into the mixture. The mixture was kept under inert condition and constant stirring at 50-55˚C temperature for 24 hrs. After that, the mixture was centrifuged at 12000 rpm for 10 min. and resulting yellowish green supernatant appeared as bright green emissive under UV light.

2.5.2.2. Synthesis of green-yellow emissive CuNC from 1-PDT capped CuNC.

4 mL of 10 mM $CuSO_4.5H_2O$ solution was prepared in methanol solvent and was taken in a 25 mL RB flask. 12 µL of 1,3-PDT was dissolved in 250 µL of 0.6 M methanolic NaOH and added to the solution in RB flask so that conc. of OH^- ions and 1,3-PDT in the resulting solution becomes ~40 mM and ~30 mM respectively. White precipitate was formed instantaneously, followed by an addition of 14 mg (20 mM) of solid L-ascorbic acid into the mixture. The mixture was kept under inert condition and constant stirring at 50-55˚C temperature for 24 hrs. After that, the mixture was centrifuged at 12000 rpm for 10 min. and resulting yellowish green supernatant appeared as bright green emissive under UV light.

2.5.2.3. Synthesis of green-yellow emissive CuNC from 1,9-NDT capped CuNC.

4 mL of 10 mM $CuSO_4.5H_2O$ solution was prepared in methanol solvent and was taken in a 25 mL RB flask. 24.2 µL of 1,9-NDT was dissolved in 250 µL of 0.6 M methanolic NaOH and added to the solution in RB flask so that conc. of OH^- ions and 1,9-NDT in the resulting solution becomes ~40 mM and ~30 mM respectively. White precipitate was formed instantaneously, followed by an addition of 14 mg (20 mM) of solid L-ascorbic acid into the mixture. The mixture was kept under inert condition and constant stirring at 50-55˚C temperature for 24 hrs. After that, the mixture was centrifuged at 12000 rpm for 10 min. and resulting yellowish green supernatant appeared as bright green emissive under UV light.

2.5.3. Appendix 3: Excitation-independent emission from RCuNC.

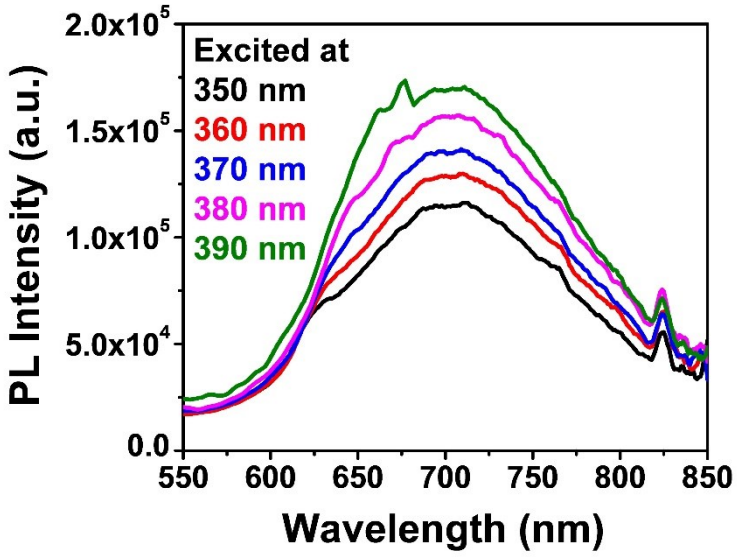

Figure A1. Emission spectra of RCuNC at different excitation wavelengths.

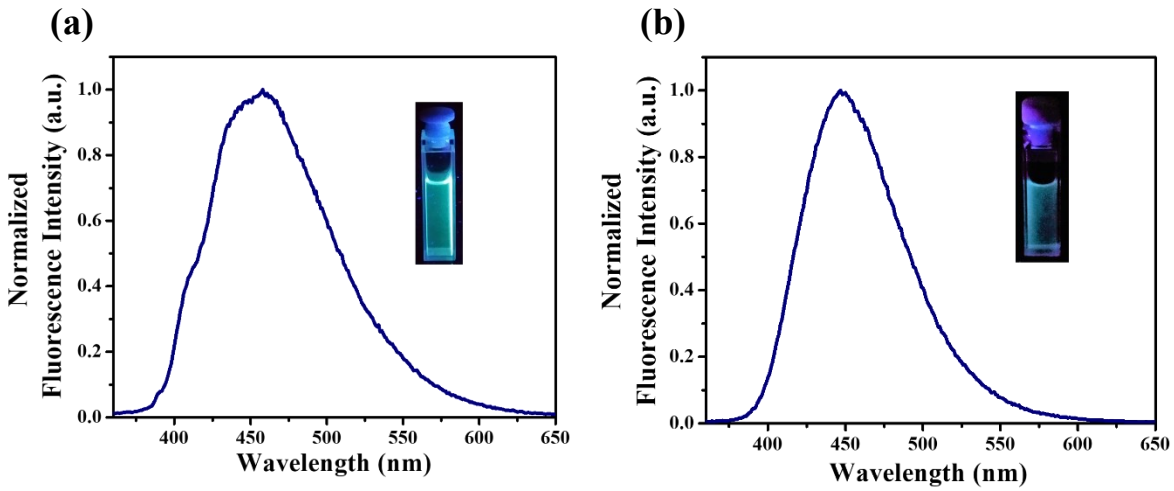

Figure A2. Emission spectra of (a) cyan emissive CuNC by following P2 at 10 hrs of reaction time, (b) cyan emissive CuNC by capping with DHAA with a reaction time of 10-12 hrs by using the same protocol as Appendix 2.5.1.4.

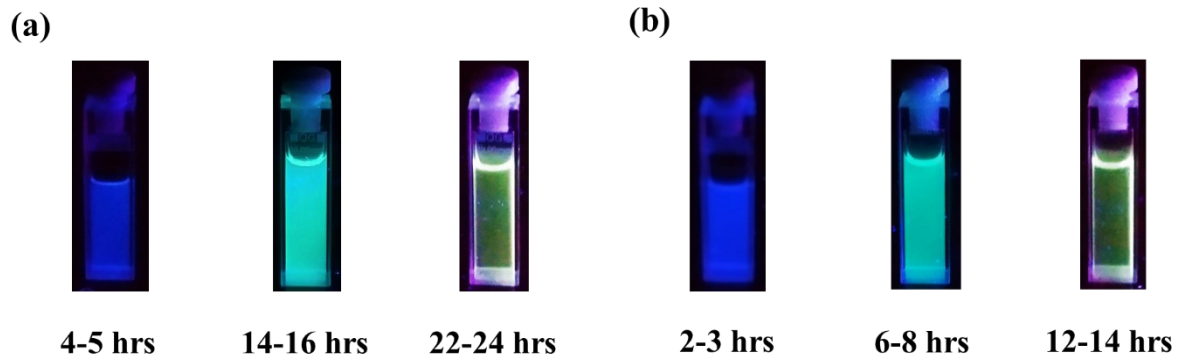

Figure A3. (a) Sample images under UV light at different reaction times when concentration of AA was 20 mM. (b) Sample images under UV light at different reaction times when concentration of AA was 50 mM.

2.5.4. Appendix 4: Tables.

Table A1. Plot for $\ln(F/F_0)$ vs. pH.

pH	$\ln(F/F_0)$
12.33606	0
12.34986	0.41479
12.36305	0.79452
12.37585	1.08885
12.38846	1.3118
12.40037	1.51603
12.41212	1.58661
12.42357	1.63756
12.43457	1.68362
12.44545	1.67931

Table A2. Plot for F/F_0 vs. reaction time (h).

Reaction time (h)	F/F_0
2	1
6	1.74812
10	5.80902
14	10.69835
18	11.94964
22	12.94954
26	12.7899

Table A3. Plot for F/F_0 vs. conc. of AA (mM).

Conc. of AA (mM)	F/F_0
0	1
5	13.6018
10	18.10731
15	25.38834
20	33.03889
25	49.67453

Bibliography

1 I. E. Agency, *Light's labour's lost*, 2006.

2 M. K. Choi, J. Yang, D. C. Kim, Z. Dai, J. Kim, H. Seung, V. S. Kale, S. J. Sung, C. R. Park, N. Lu, T. Hyeon and D.-H. Kim, *Adv. Mater.*, 2018, **30**, 1703279.

3 Y. Fang, K. Ding, Z. Wu, H. Chen, W. Li, S. Zhao, Y. Zhang, L. Wang, J. Zhou and B. Hu, *ACS Nano*, 2016, **10**, 10023–10030.

4 K. Qasim, B. Wang, Y. Zhang, P. Li, Y. Wang, S. Li, S.-T. Lee, L.-S. Liao, W. Lei and Q. Bao, *Adv. Funct. Mater.*, 2017, **27**, 1606874.

5 V. L. Colvin, M. C. Schlamp and A. P. Alivisatos, *Nature*, 1994, **370**, 354–357.

6 J. Zhao, J. A. Bardecker, A. M. Munro, M. S. Liu, Y. Niu, I.-K. Ding, J. Luo, B. Chen, A. K.-Y. Jen and D. S. Ginger, *Nano Lett.*, 2006, **6**, 463–467.

7 S. Coe, W.-K. Woo, M. Bawendi and V. Bulović, *Nature*, 2002, **420**, 800–803.

8 B. S. Mashford, M. Stevenson, Z. Popovic, C. Hamilton, Z. Zhou, C. Breen, J. Steckel, V. Bulovic, M. Bawendi, S. Coe-Sullivan and P. T. Kazlas, *Nat. Photonics*, 2013, **7**, 407–412.

9 Z. Wang, A. S. Susha, B. Chen, C. Reckmeier, O. Tomanec, R. Zboril, H. Zhong and A. L. Rogach, *Nanoscale*, 2016, **8**, 7197–7202.

10 J. Liu, Z. Wu, Y. Tian, Y. Li, L. Ai, T. Li, H. Zou, Y. Liu, X. Zhang, H. Zhang and B. Yang, *ACS Appl. Mater. Interfaces*, 2017, **9**, 24899–24907.

11 D. Li, G. Wang, Y. Peng, Z. Chen, X. Gao, L. Cheng and X. Mei, *Nanoscale Adv.*, 2019, **1**, 1086–1095.

12 S. Bhunia, M. Mukherjee and P. Purkayastha, *Langmuir*, 2021, **37**, 3500–3507.

13 Z. Wu, J. Liu, Y. Gao, H. Liu, T. Li, H. Zou, Z. Wang, K. Zhang, Y. Wang, H. Zhang and B. Yang, *J. Am. Chem. Soc.*, 2015, **137**, 12906–12913.

14 Z. Wang, B. Chen, A. S. Susha, W. Wang, C. J. Reckmeier, R. Chen, H. Zhong and A. L. Rogach, *Adv. Sci.*, 2016, **3**, 1600182.

15 Y. Wang, Y. Shi, T. Li, H. Wang, Y. Li, Y. Xiong, S. Peng and Z. Wang, *Nanoscale Adv.*, 2019, **1**, 834–839.

16 L. Ai, W. Jiang, Z. Liu, J. Liu, Y. Gao, H. Zou, Z. Wu, Z. Wang, Y. Liu, H. Zhang and

B. Yang, *Nanoscale*, 2017, **9**, 12618–12627.

17 H.-H. Deng, Q.-Q. Zhuang, K.-Y. Huang, P. Balasubramanian, Z. Lin, H.-P. Peng, X.-H. Xia and W. Chen, *Nanoscale*, 2020, **12**, 15791–15799.

18 K. Pyo, V. D. Thanthirige, K. Kwak, P. Pandurangan, G. Ramakrishna and D. Lee, *J. Am. Chem. Soc.*, 2015, **137**, 8244–8250.

19 U. Anand, S. Ghosh and S. Mukherjee, *J. Phys. Chem. Lett.*, 2012, **3**, 3605–3609.

20 X. Jia, X. Yang, J. Li, D. Li and E. Wang, *Chem. Commun.*, 2014, **50**, 237–239.

21 L. Kong, X. Chu, C. Wang, H. Zhou, Y. Wu and W. Liu, *Nanoscale*, 2018, **10**, 1631–1640.

22 X. Ouyang, M. Wang, L. Guo, C. Cui, T. Liu, Y. Ren, Y. Zhao, Z. Ge, X. Guo, G. Xie, J. Li, C. Fan and L. Wang, *Angew. Chemie Int. Ed.*, 2020, **59**, 11836–11844.

23 T. Jiang, G. Qu, J. Wang, X. Ma and H. Tian, *Chem. Sci.*, 2020, **11**, 3531–3537.

24 Z. Wu, Q. Yao, O. J. H. Chai, N. Ding, W. Xu, S. Zang and J. Xie, *Angew. Chemie Int. Ed.*, 2020, **59**, 9934–9939.

25 J. Zheng, C. Zhang and R. M. Dickson, *Phys. Rev. Lett.*, 2004, **93**, 5–8.

26 J. Zheng, P. R. Nicovich and R. M. Dickson, *Annu. Rev. Phys. Chem.*, 2007, **58**, 409–431.

27 Z. Wu and R. Jin, *Nano Lett.*, 2010, **10**, 2568–2573.

28 T. Yang, S. Dai, H. Tan, Y. Zong, Y. Liu, J. Chen, K. Zhang, P. Wu, S. Zhang, J. Xu and Y. Tian, *J. Phys. Chem. C*, 2019, **123**, 18638–18645.

29 T. Udaya Bhaskara Rao and T. Pradeep, *Angew. Chemie Int. Ed.*, 2010, **49**, 3925–3929.

30 S. Basu, M. W. Nawaj, C. Gayen and A. Paul, *Phys. Chem. Chem. Phys.*, 2019, **21**, 21776–21781.

31 T. Yang, S. Dai, S. Yang, L. Chen, P. Liu, K. Dong, J. Zhou, Y. Chen, H. Pan, S. Zhang, J. Chen, K. Zhang, P. Wu and J. Xu, *J. Phys. Chem. Lett.*, 2017, **8**, 3980–3985.

32 H. Li, H. Zhai, C. Zhou, Y. Song, F. Ke, W. W. Xu and M. Zhu, *J. Phys. Chem. Lett.*, 2020, **11**, 4891–4896.

33 Z. Wu, H. Liu, T. Li, J. Liu, J. Yin, O. F. Mohammed, O. M. Bakr, Y. Liu, B. Yang and H. Zhang, *J. Am. Chem. Soc.*, 2017, **139**, 4318–4321.

34 Q. Yao, Z. Wu, Z. Liu, Y. Lin, X. Yuan and J. Xie, *Chem. Sci.*, 2021, **12**, 99–127.

35 T. Zhou, J. Zhu, L. Gong, L. Nong and J. Liu, *J. Am. Chem. Soc.*, 2019, **141**, 2852–2856.

36 J. Feng, Y. Chen, Y. Han, J. Liu, S. Ma, H. Zhang and X. Chen, *ACS Omega*, 2017, **2**, 9109–9117.

37 X. Jia, J. Li and E. Wang, *Small*, 2013, **9**, 3873–3879.

38 X. Su and J. Liu, *ACS Appl. Mater. Interfaces*, 2017, **9**, 3902–3910.

39 A. Aires, V. Fernández-Luna, J. Fernández-Cestau, R. D. Costa and A. L. Cortajarena, *Nano Lett.*, 2020, **20**, 2710–2716.

40 J. V Rival, P. Mymoona, R. Vinoth, A. M. V. Mohan and E. S. Shibu, *ACS Appl. Mater. Interfaces*, 2021, **13**, 10583–10593.

41 T. Kawawaki, Y. Negishi and H. Kawasaki, *Nanoscale Adv.*, 2020, **2**, 17–36.

42 S. Kundu, B. Ghosh, S. Nandi, M. Ghosh, A. Pyne, J. Chatterjee and N. Sarkar, *ACS Appl. Bio Mater.*, 2020, **3**, 4282–4293.

43 D. Mishra, V. Lobodin, C. Zhang, F. Aldeek, E. Lochner and H. Mattoussi, *Phys. Chem. Chem. Phys.*, 2018, **20**, 12992–13007.

44 I. Díez, M. Pusa, S. Kulmala, H. Jiang, A. Walther, A. S. Goldmann, A. H. E. Müller, O. Ikkala and R. H. A. Ras, *Angew. Chemie Int. Ed.*, 2009, **48**, 2122–2125.

45 X. Kang, S. Wang and M. Zhu, *Chem. Sci.*, 2018, **9**, 3062–3068.

46 J. M. Pettibone and J. W. Hudgens, *J. Phys. Chem. Lett.*, 2010, **1**, 2536–2540.

47 T.-A. D. Nguyen, Z. R. Jones, D. F. Leto, G. Wu, S. L. Scott and T. W. Hayton, *Chem. Mater.*, 2016, **28**, 8385–8390.

48 R. K. Koninti, S. Satpathi and P. Hazra, *J. Phys. Chem. C*, 2018, **122**, 5742–5752.

49 J. R. Lakowicz, *Principles of Fluorescence Spectroscopy*, Springer US, 2007.

50 M. Mardelli and J. Olmsted, *J. Photochem.*, 1977, **7**, 277–285.

51 G. Jones, W. R. Jackson, C. Y. Choi and W. R. Bergmark, *J. Phys. Chem.*, 1985, **89**, 294–300.

52 S. Link, A. Beeby, S. FitzGerald, M. A. El-Sayed, T. G. Schaaff and R. L. Whetten, *J. Phys. Chem. B*, 2002, **106**, 3410–3415.

53 G. H. Chan, J. Zhao, E. M. Hicks, G. C. Schatz and R. P. Van Duyne, *Nano Lett.*, 2007,

7, 1947–1952.

54 P. Yuan, R. Zhang, E. Selenius, P. Ruan, Y. Yao, Y. Zhou, S. Malola, H. Häkkinen, B. K. Teo, Y. Cao and N. Zheng, *Nat. Commun.*, 2020, **11**, 2229.

55 N. Vilar-Vidal, M. C. Blanco, M. A. López-Quintela, J. Rivas and C. Serra, *J. Phys. Chem. C*, 2010, **114**, 15924–15930.

56 M. S. Devadas, J. Kim, E. Sinn, D. Lee, T. Goodson and G. Ramakrishna, *J. Phys. Chem. C*, 2010, **114**, 22417–22423.

57 R. Nivetha, A. Sajeev, A. Mary Paul, K. Gothandapani, S. Gnanasekar, P. Bhardwaj, G. Jacob, R. Sellappan, V. Raghavan, K. C. N, S. Pitchaimuthu, S. K. Jeong and A. Nirmala Grace, *Mater. Res. Express*, 2020, **7**, 114001.

58 A. Al-Obaidi, G. Baranovič, J. Coyle, C. G. Coates, J. J. McGarvey, V. McKee and J. Nelson, *Inorg. Chem.*, 1998, **37**, 3567–3574.

59 S. Maity, D. Bain and A. Patra, *J. Phys. Chem. C*, 2019, **123**, 2506–2515.

60 Z. Luo, X. Yuan, Y. Yu, Q. Zhang, D. T. Leong, J. Y. Lee and J. Xie, *J. Am. Chem. Soc.*, 2012, **134**, 16662–16670.

61 P. Suchomel, L. Kvitek, R. Prucek, A. Panacek, A. Halder, S. Vajda and R. Zboril, *Sci. Rep.*, 2018, **8**, 4589.

62 X. Zhang, R. Gallagher, D. He and G. Chen, *Chem. Mater.*, 2020, **32**, 5626–5633.

63 L. Malassis, R. Dreyfus, R. J. Murphy, L. A. Hough, B. Donnio and C. B. Murray, *RSC Adv.*, 2016, **6**, 33092–33100.

64 R. C. Kerber, *J. Chem. Educ.*, 2008, **85**, 1237.

65 Q. Li, Y. Li, H. Li, X. Yan, G. Han, F. Chen, Z. Song, J. Zhang, W. Fan, C. Yi, Z. Xu, B. Tan and W. Yan, *Nanomater.* , 2020, 10.

66 C. Ünaleroğlu, Y. Mert and B. Zümreoğlu-Karan, *Synth. React. Inorg. Met. Chem.*, 2001, **31**, 1531–1543.

67 Y. Song, Y. Lv, M. Zhou, T.-Y. Luo, S. Zhao, N. L. Rosi, H. Yu, M. Zhu and R. Jin, *Nanoscale*, 2018, **10**, 12093–12099.

68 A. D. Merg, Y. Zhou, A. M. Smith, J. E. Millstone and N. L. Rosi, *ChemNanoMat*, 2017, **3**, 745–749.

69 X. Kang and M. Zhu, *Chem. Mater.*, 2019, **31**, 9939–9969.

70 X. Wang, X. Wang, X. Bai, L. Yan, T. Liu, M. Wang, Y. Song, G. Hu, Z. Gu, Q. Miao and C. Chen, *Nano Lett.*, 2019, **19**, 8–18.

71 X. Wen, P. Yu, Y.-R. Toh, X. Ma, S. Huang and J. Tang, *Nanoscale*, 2013, **5**, 10251–10257.

72 M. Zhou, S. Long, X. Wan, Y. Li, Y. Niu, Q. Guo, Q.-M. Wang and A. Xia, *Phys. Chem. Chem. Phys.*, 2014, **16**, 18288–18293.

73 S. Maity, D. Bain, K. Bhattacharyya, S. Das, R. Bera, B. Jana, B. Paramanik, A. Datta and A. Patra, *J. Phys. Chem. C*, 2018, **122**, 13354–13362.

Chapter 3:

Activation of TADF in Photon Up-converting Crystals of Dinuclear Cu(I)-iodide Complexes by Ligand Engineering

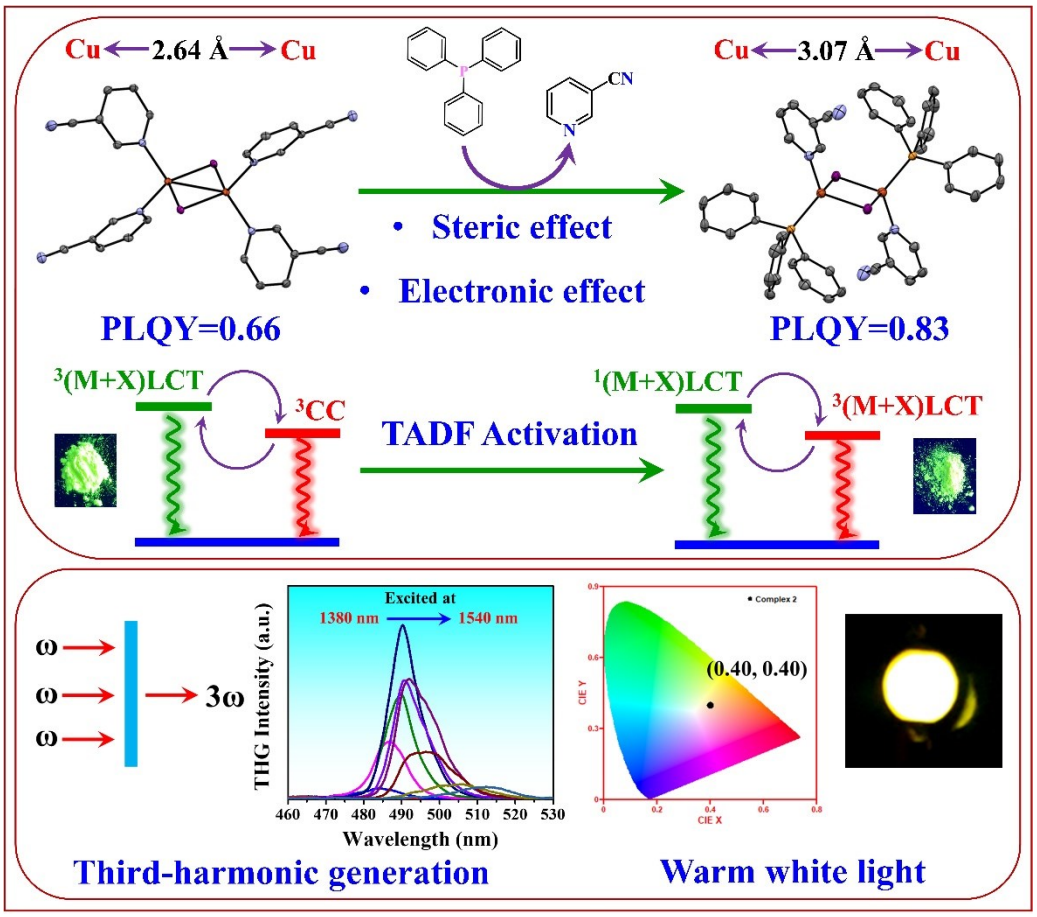

The work is published in the following article,

J. Chatterjee, A. Chatterjee, R. Tanwar, P. Panwaria, S. Saikia, M. D. Ambhore, P. Mandal, and P. Hazra, *J. Phys. Chem. Lett.* 2024, **15**, 6069−6080.

DOI: 10.1021/acs.jpclett.4c01122.

Abstract: In this work, we have reported a novel approach, where ligand engineering can modulate the triplet harvesting mechanism in iodide-bridged rhombic Cu_2I_2 complexes. Complex-1, with a smaller Cu-Cu distance (2.64 Å), exhibits phosphorescence from ^{3}(M+X)LCT and ^{3}CC states with 66% quantum yield; whereas an increased Cu-Cu distance (3.07 Å) in complex-2 results in a switch of the emission from phosphorescence to TADF, which takes place via $^{1/3}$(M+X)LCT states with 83% quantum yield. The TADF property of complex-2 has been utilized for the fabrication of pc-LED in order to examine the scope of its utilization in OLED devices, and the designed pc-LED emits efficient warm white light. Moreover, the high charge transfer nature of these complexes leads to the emergence of several non-linear photon up-conversion properties, like, third harmonic generation (THG) and two-photon excited luminescence. Interestingly, complex-1 exhibits efficient third harmonic generation with a $\chi^{(3)}$ value of $1.15 \times 10^{-18}\ m^2V^{-2}$ and LIDT value of 14.73 GW/cm^2. In summary, this work provided a structure-property relationship to achieve an effective harvest of triplet excitons in iodide-bridged rhombic Cu_2I_2 complexes, and their effective utilization in OLED device fabrication and non-linear photon up-conversion processes.

3.1. Introduction

Ligand-coordinated Cu(I) and Cu(I)-iodide frameworks have made a revolutionary impact on triplet state harvesting, thereby expanding the horizon of applications in optoelectronics, polarized emission and photosensitization.[1–9] Thanks to its structural diversity, facile synthesis, high crystallinity, and plenty of different radiative decay pathways.[10–16] Particularly, (metal+halide)-to-ligand charge transfer ($^{1/3}$(M+X)LCT), and cluster-centered (^{3}CC) emissive states of Cu(I)-iodide frameworks having different electronic configurations give rise to multiple radiative decay pathways that can be effectively utilized in triplet state harvesting.[10,11,17,18] Additionally, because of the closed-shell d^{10} configuration of Cu(I), non-radiative decay via low-lying metal-centered (MC) states is restricted in these systems, producing a higher quantum yield.[7,16,19] Several of these excited states have previously been identified and studied in closed cubane-type Cu_4I_4 clusters coordinated with a wide range of ligands having low-lying π* orbitals, such as pyridine, triphenylphosphine, and their derivatives.[15,17,20–23] Stability of the ^{3}CC states plays a crucial role in the radiative decay process of these clusters which is highly dependent on Cu···Cu bonding interactions. These states are comprised of metal-centered 3d→4s,4p transitions and halide-to-metal charge transfer (XMCT) transitions.[11,24–26] A small contraction in the Cu-Cu distance can sufficiently stabilize the ^{3}CC state, resulting in a substantial red-shift of the emission band; therefore, these clusters

stand out to exhibit long-range mechanochromic and rigidochromic behavior.[23,27,28] These states undergo high degree of geometry distortion compared to (M+X)LCT states, thereby exhibiting lower energy emission with broad bandwidth. Furthermore, the thermal equilibrium of the population between the ^{3}(M+X)LCT and ^{3}CC states gives rise to intriguing thermochromic properties in these clusters.[11,15] Consequently, they find broad applications in developing external stimuli-responsive materials and OLED devices.[17,20,23,28,29]

The high charge transfer nature of the low-lying $^{1/3}$(M+X)LCT states also creates spatially well-separated electron and hole, opening the possibility of thermally activated delayed fluorescence (TADF).[30,31] TADF is unequivocally known to be one of the most competent luminescence pathways, reaching a maximum of 100% internal efficiency.[7,32] However, in Cu_4I_4 clusters, ^{3}CC states are populated at the expense of ^{3}(M+X)LCT via thermal energy barrier, and ^{3}CC states becomes most emissive at room temperature, thereby making (M+X)LCT emission negligible.[11,15] Therefore, the attempt to utilize the triplet excitons through TADF becomes unworkable in these clusters. In this regard, the iodide-bridged Cu_2I_2 complexes stand out to bring about a potential solution owing to its strong (M+X)LCT emission as well as high quantum yield due to lesser flexibility and higher degree of structural rigidity.[10,12,18,30,33,34] The iodide-bridges also prevents the (M+X)LCT states to undergo large Jahn-Teller flattening distortion which is observed in mononuclear Cu(I) complexes.[31,35] Consequently, $^{1/3}$(M+X)LCT states of these complexes have emerged as the center of interest for the scientific community in the past few years. Several complexes have been reported where these excited states were extensively characterized, and the TADF mechanisms were investigated using plenty of theoretical and experimental methodologies.[10,12,18,30,33,34] However, in Cu_2I_2 complexes with shorter Cu-Cu distance, ^{3}CC states have also been reported to take part in the emission process due to the presence of bonding interactions between two Cu atoms.[10,18,36] Nevertheless, the strong (M+X)LCT nature of these complexes can exhibit TADF properties, but, shorter Cu-Cu distances can increase the contribution of ^{3}CC emission, thereby enhancing the radiative decay through phosphorescence. Additionally, ^{3}CC states can suffer from reasonable amount of non-radiative decay owing to their higher degree of geometry distortion, which can reduce the emission yield to a greater extent. Therefore, it is an urgent requirement to establish structure-property relationship, where the selection of appropriate π*-acceptor ligands can direct the luminescence pathway exclusively via TADF mechanism from $^{1/3}$(M+X)LCT states. Systematic modulation of the Cu-Cu distance can play a pivotal role in this regard. In addition, the high charge transfer character of these complexes can give rise to several non-linear optical (NLO) properties that remain underexplored.[37,38] NLO processes are extremely important for

the up-conversion of photon energy, which is utilized in photosensitization, light manipulation, laser manufacturing, and other optical technologies.[39–42] Since non-linear susceptibilities in the bulk phase mostly depend on the polarizability of molecules, charge transfer-based push-pull luminogens are considered as suitable candidates in this context.[37,38]

Here in, we report two rhombic iodide-bridged Cu_2I_2 complexes, where regulation of the Cu-Cu distance can dictate the triplet harvesting mechanism. At first, the complex-1 was synthesized by using 3-cyanopyridine as the ligand, where Cu-Cu distance is 2.64 Å. This was followed by the replacement of two 3-cyanopyridines by PPh_3 ligands, which results in the elongation of the Cu-Cu distance from 2.64 Å to 3.07 Å in the newly formed complex-2. The two complexes have almost overlapping emission bands. Interestingly, the emission mechanisms of these two complexes are completely different in nature. Complex-1 undergoes predominant phosphorescence decay with contributions from ^{3}(M+X)LCT and ^{3}CC states, whereas complex-2 decays through TADF mechanism associated with $^{1/3}$(M+X)LCT states. Most importantly, considering nearly overlapping emission bands of two complexes, triplet harvesting through the TADF process was found to be the most efficient, with an absolute quantum yield of 83% in complex-2. Additionally, high charge transfer nature of these complexes prompted us to explore their non-linear photon up-conversion properties. Complex-1 was found to exhibit efficient third harmonic generation with a non-linear susceptibility ($\chi^{(3)}$) value of 1.15 x 10^{-18} m^2V^{-2} and a laser-induced damage threshold (LIDT) value of 14.73 GW/cm^2. Due to high third-order susceptibility, both complexes are two-photon active in the crystalline phase, confirming their potential in various two-photon imaging applications. A phosphor-converted light-emitting diode (pc-LED) was also fabricated with complex-2, which emits warm white light.

3.2. Experimental Section

3.2.1. Materials and general protocol for synthesis

Copper(I) iodide powder, 3-cyanopyridine, and triphenylphosphine were purchased from Sigma Aldrich and used as received. Ethanol, dichloromethane, acetonitrile, toluene, and *n*-pentane were purchased from Neelchem Corporation. All syntheses were carried out under an argon atmosphere and using Schlenk glass apparatus (except those with ethanol). All solvents were purified and distilled under an inert atmosphere and stored under argon.

3.2.2. Characterization techniques

^{1}H NMR (at 400 MHz) and ^{13}C NMR (at 100 MHz) data characterizations of all the synthesized compounds were conducted by using JEOL ECS-400 and Bruker Ascend ^{TM} 400 spectrometer, taking deuterated chloroform ($CDCl_3$) as solvent (having residual chloroform) and tetramethylsilane (TMS) as the internal standard. Chemical shift (δ) values were measured in ppm downfield from $CDCl_3$ (δ = 7.26 ppm) for ^{1}H NMR, and relative to central $CDCl_3$ resonance (δ = 77.16 ppm) for ^{13}C NMR. A solution of H_3PO_4 85% weight was used as an external standard for recording ^{31}P NMR. Thermogravimetric analyses were carried out by using Perkin-Elmer STA 6000 TGA analyzer and the samples were heated from 30 to 800 °C under N_2 atmosphere with a heating rate of 10 °C min^{-1}. Elemental analyses were carried out in a vario EL cube (Elementar) instrument. Single-crystal diffraction analysis data were collected at 100K with a BRUKER KAPPA APEX II CCD Duo diffractometer (operated at 1500 W power: 50 kV, 30 mA) using graphite monochromatic Mo Kα radiation (λ = 0.71073 Å). The structures were solved by direct methods and refined by least-squares against F2 utilizing the software package SHELXL-97.[43,44] More information on crystal structures can also be obtained from the Cambridge Crystallographic Data Centre under the CCDC deposition number (2272091). Powder XRD experiments were performed using BRUKER D8 advanced X-ray diffractometer with a Cu-K_α radiation source.

3.2.3. Steady-state and time-resolved spectroscopic studies

Solid-state absorption spectra were measured by using a Shimadzu, UV-3600 UV-NIR spectrophotometer. Steady-state solution-based absorption spectra were recorded on Shimadzu, UV-2600 UV spectrophotometer. Steady-state emission spectra and time-gated emission spectra of all the samples in solution and solid state were recorded in Fluoromax-4C (HORIBA) and Fluorolog-3 (HORIBA), respectively. Absolute quantum yields were measured in Fluoromax-4C (HORIBA) instrument by using an integrating sphere. Time-resolved PL decay profiles have been recorded either using a diode-laser source (for a total time window <50 μs) or a microsecond flash lamp source (of 1.5-2.5 μs bandwidth and in cases where the total time window > 50 μs) in an Edinburgh FLS980 instrument. Temperature-dependent PL and PL decay profiles were recorded in an Edinburgh FLS980 Instrument coupled with a cryostat. The solid samples were placed between two sapphire plates and fixed in a gold-coated copper sample holder. The sample holder is fixed in a closed cycle He cryostat (Advanced Research Systems) attached with a Lake Shore 335 temperature controller. A mode-locked Ti-sapphire laser (Mai-Tai, Spectra-Physics) was used for the two-photon excited luminescence imaging experiment as the excitation source. Two-photon excited luminescence spectra and

corresponding excitation spectra were collected by using a multiphoton microscope (Leica, Germany) at 10X objectives. Complex-1 undergoes polymerization in solution phase starting at around several μM concentration. Therefore, the photophysical studies in solution phase was carried out at 60 nM concentration, where it was confirmed that no polymerization takes place.

3.2.4. Synthesis of complex-1

Complex-1 was synthesized by following a reported method[45] with slight modification in the crystallization process, which yielded a crystal structure similar to the reported one,[45] and can be found against the CCDC number 1990789. 832 mg 3-cyanopyridine (4 eq., 8 mmol) was taken in a 50 mL RB flask and dissolved into 20 mL of CH_3CN. 380 mg of CuI powder (1 eq., 2 mmol) was added to it and kept under stirring condition at room temperature for 2 h. The green-yellow precipitate was filtered and washed with excess CH_3CN, *n*-pentane subsequently dried under vaccuum for 3 h. The obtained green-yellow powder was then taken in a 100 mL conical flask, dispersed in 15 mL CH_3CN and stirred well. The disperse was filtered and green rhombus-shaped crystals were obtained from the filtrate by keeping it overnight at room temperature. Yield: 43.06%. The complex was characterized by using ^{1}H NMR, powder X-ray diffraction (PXRD) analysis, and thermogravimetric analysis (**Appendix 1**).

^{1}H NMR (400 MHz, $CDCl_3$): δ 8.99 (d, J = 27.7 Hz, 8H), 8.02 (d, J = 7.9 Hz, 4H), 7.50 (dd, J = 7.5, 5.2 Hz, 4H).

Elemental analysis: Calculated % of C, 36.15; H, 2.02; N, 14.05. Experimental % of C, 36.16; H, 1.83; N, 13.93.

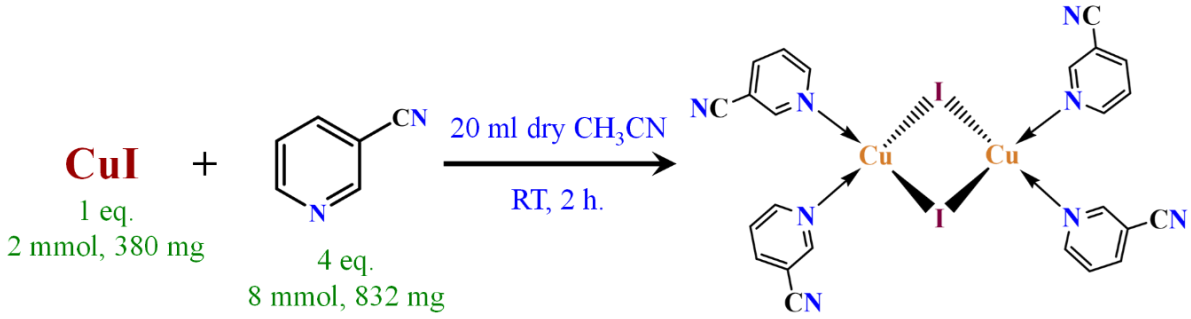

Scheme 3.1. Synthesis of complex-1

3.2.5. Synthesis of complex-2

832 mg 3-cyanopyridine (4 eq., 8 mmol) was taken in a 50 ml RB flask and dissolved into 20 mL of CH_3CN. 380 mg of CuI powder (1 eq., 2 mmol) was added to it and kept under stirring condition at room temperature for 2 h. The green-yellow precipitate was filtered and washed with excess CH_3CN, *n*-pentane, and subsequently dried under vaccuum for 3 h. The obtained green-yellow powder was then taken in a 100 mL RB flask and dispersed in 40 mL CH_2Cl_2.

448 mg PPh_3 (2 eq.) was added to it and kept under stirring conditions at room temperature for 24 h. The white precipitate was filtered out, and the filtrate solution was slowly diffused with *n*-pentane to get single crystals. Yield: 10.45%. The complex was characterized by using ^{1}H NMR, ^{13}C NMR, ^{31}P NMR, single-crystal X-ray diffraction (SCXRD) analysis, PXRD analysis, and thermogravimetric analysis (**Appendix 1**).

^{1}H NMR (400 MHz, $CDCl_3$): δ 8.91 (d, J = 1.5 Hz, 2H), 8.85 (dd, J = 5.0, 1.5 Hz, 2H), 7.97 (dt, J = 7.9, 1.8 Hz, 2H), 7.53 (t, J = 8.7 Hz, 12H), 7.44 (dd, J = 7.9, 5.1 Hz, 2H), 7.37 (t, J = 7.2 Hz, 6H), 7.29 (d, J = 7.2 Hz, 12H).

$^{13}C\{^{1}H\}$ NMR (100 MHz, $CDCl_3$): δ 153.78, 153.30, 140.03, 134.82, 134.69, 133.45, 133.14, 130.19, 128.89, 128.80, 124.43, 116.67, 110.94.

^{31}P NMR (161.976 MHz, $CDCl_3$): δ -13.34.

Elemental analysis: Calculated % of C, 51.77; H, 3.44; N, 5.03. Experimental % of C, 51.6; H, 3.27; N, 4.85.

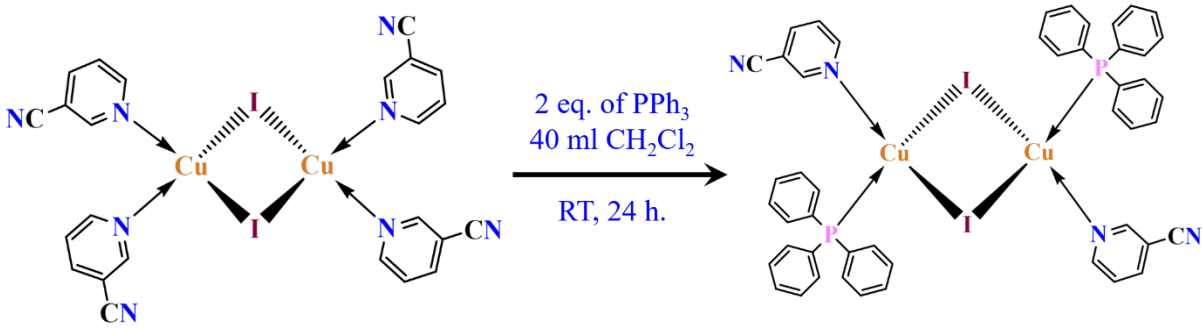

Scheme 3.2. Synthesis of complex-2.

3.2.6. DFT calculations

Crystal structures of both complexes were chosen as the initial geometries for obtaining the coordinates of the local minima of these complexes. These geometries were optimized employing the integral equation formalism variant polarizable continuum model (IEFPCM) in chloroform solvent using the Gaussian09 program package.[46–48] Ground state geometries of both the complexes were optimized at the Grimmes dispersion corrected B3LYP functional with def2-SVP basis set with the ultrafine numerical integration grid and tight convergence criteria. The absence of imaginary harmonic frequency confirms the local minima of these optimized complexes. The singlet and triplet excited state (S_1/T_1) geometries of the complexes were optimized at the TD-B3LYP-D3/def2-SVP level using the respective ground state geometries of the complexes. Franck-Condon excitation calculations were also performed using ground-state geometries of the respective complexes. Steric repulsion energy and

electron delocalization energy between two ligands covalently linked to a single copper atom of these complexes was calculated using natural steric analysis implemented in the NBO7.0 program.[49]

Spin-orbit coupling matrix element (SOCME) calculation: The spin-orbit coupling matrix between different excited singlet and triplet states was calculated using the zeroth-order regular approximation (ZORA) to the Dirac equation. In this approximation, the SOC operator, $\widehat{H}_{SOC}$, is expressed as following,[50]

$$\widehat{H}_{SOC} = \frac{c^2}{(2c^2 - v)^2}\sigma \cdot (\nabla v \times p)$$

Where c, v, σ, and p signify the speed of light, Kohn-Sham potential, Pauli spin-matrix vector, and linear momentum operator, respectively. The first-order perturbation is applied on scalar relativistic orbitals after the self-consistent field (SCF) and TD-DFT calculations to obtain SOC effects. Grimmes dispersion corrected B3LYP functional with def2-SVP basis set with the ultrafine numerical integration grid, and tight convergence criteria were used to calculate SOCME values. All these calculations were done using the PYSOC program[51].

3.2.7. Calculation of absolute quantum yields

Complex-1:

Φ = 66%. Absolute error = 0.068, relative error = 0.001.

Complex-2:

Φ = 83%. Absolute error = 0.052, relative error = 6.22×10^{-4}.

20% emitter-doped PMMA film for complex-2:

Φ = 77%. Absolute error = 0.175, relative error = 0.00226.

3.2.8. Determination of TADF and phosphorescence proportions in complex-2 at variable temperatures.

$$\tau_{obs} = \frac{3 + e^{-\frac{\Delta E_{ST}}{k_B T}}}{\frac{3}{\tau(T_1)} + \frac{1}{\tau(S_1)} e^{-\frac{\Delta E_{ST}}{k_B T}}} \qquad \text{Eq. 3.1}$$

By fitting the lifetime vs. temperature plot with equation 1, we get the parameters as $\Delta E_{ST} = 0.076\ eV$, $\tau_{T_1} = 91.63\ \mu s$, $\tau_{S_1} = 164\ ns$, $k_r(S_1) = 6.09 \times 10^6\ s^{-1}$, and $k_r(T_1) = 1.09 \times 10^4\ s^{-1}$.

3.2.9. Calculation of fractional quantum yields of complex-2.

At room temperature, the percentage of TADF in total emission = 90.5%, and the percentage of phosphorescence in total emission = 9.5%.

Absolute quantum yield (Φ) = 83%.

Φ_{DF} = 75.1%

Φ_{Phos} = 7.8%

3.2.10. Fabrication of emitter-doped PMMA films for complex-2

100 mg of PMMA particles were dissolved in chloroform by heating at 50°C for 10 minutes under stirring conditions. Thereafter, ~20 mg of complex-2 was added to the PMMA solution, and 0.2 mL of the resulting solution was used for drop-casting on a quartz substrate. The quartz substrate was then kept under high vacuum for another 20 minutes prior to photophysical studies.

3.2.11. Third-harmonic generation

3.2.11.1. Experimental setup for third harmonic generation

The third-harmonic generation in the crystals was investigated by using ultrafast (~50 fs) pulses of different wavelengths from an optical parametric amplifier (OPA) as the excitation source, with the 400 μm beam spot size. An ultrafast regenerative amplifier (Spitfire Pro XP, Spectra-Physics) with a pulse width of ~45 fs (FWHM), 1 kHz repetition rate, and 800 nm center wavelength was used as a pump for the OPA (TOPAS-C, Light Conversion). The amplifier was seeded with the ~35 fs pulses from a mode-locked Ti:Sapphire oscillator (Tsunami, Spectra-Physics) of 80 MHz repetition rate and 800 nm central wavelength. The pump beam produced by the OPA passes through an 800 nm long pass filter for the purity of the pump beam. The filtered beam was then passed through a neutral density (N.D.) filter for power-dependent measurements. The incident laser beam passes through an assembly of Glan polarizer and a half-wave plate for polarization-dependent NLO measurements. The sample was mounted on a rotating mount with an axis orthogonal to the polarization of the incident source. The pump pulses upon passing through a half-wave plate focus onto the sample using a 200 mm plano-convex lens. In the collection path, a 25 mm plano-convex lens was used, followed by a 750 nm short pass filter to filter out the pump beam. The filtered collimated signal was then routed towards a miniature spectrometer (USB4000, Ocean Optics) coupled to a 400 μm optical fiber.

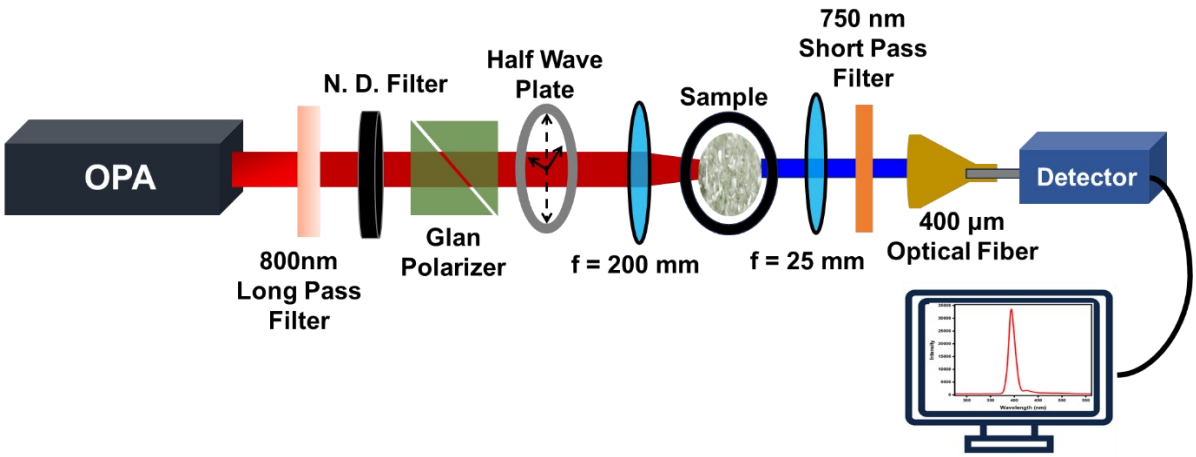

Scheme 3.3. Schematic of the third harmonic generation setup.

3.2.11.2. Calculation of third-order nonlinear susceptibility and LIDT

The third-order nonlinear susceptibility was calculated by exploiting a relative intensity method based on nonlinear Maxwell's equations[52–56]:

$$\chi_S^{(3)} = \chi_R^{(3)} \sqrt{\frac{I_S(3\omega)}{I_R(3\omega)}} \qquad \text{Eq 3.2}$$

$$\chi_{\omega_1}^{(3)} = \chi_{\omega_2}^{(3)} \left(\frac{3\omega_2}{3\omega_1}\right) \sqrt{\frac{I(3\omega_1)}{I(3\omega_2)}} \qquad \text{Eq 3.3}$$

Where $\chi_S^{(3)}$ and $\chi_R^{(3)}$ are the third-order NLO susceptibilities of the sample and reference, $I_S(3\omega)$ and $I_R(3\omega)$ are the relative THG emission intensities of the sample and the reference, $\chi_{\omega_1}^{(3)}$ and $\chi_{\omega_2}^{(3)}$ are the third-order susceptibilities at fundamental pump frequencies ω_1 and ω_2, and $I(3\omega_1)$and $I(3\omega_2)$ are the respective THG intensities. Using $PyPbI_3$ as a reference for $\chi^{(3)}$ and relying on the above two equations (Eq. 3.2 and 3.3), we obtained a $\chi^{(3)}$ value of 1.15 x 10^{-18} m^2V^{-2} for complex-1 at pump wavelength of 1470 nm.[53]

Laser-induced damage threshold (LIDT) is the optical power at which the nonlinear optical response of a material starts to deviate from its cubic behavior. For determining the laser-induced damage threshold (LIDT) of our sample, we have used Eq. 3.4, which gives us the LIDT of around 14.73 GW/cm^2.

$$Peak\ Intensity = \frac{Energy\ \ per\ pulse}{Pulse\ width \times Effective\ Spot\ Area} \quad \ldots\ldots\ldots\ldots \text{ Eq. 3.4}$$

$$Where,\quad Energy\ per\ pulse = \frac{Average\ Power}{Repetition\ Rate}$$

$$LIDT = \ Peak\ Intensity = \frac{Average\ Power}{Repetition\ Rate \times Pulse\ Width \times Effective\ Spot\ Area}$$

$$LIDT = \ Peak\ Intensity = \frac{3.7 \times 10^{-3}\ W}{1000\ Hz \times 50 \times 10^{-15}\ s \times \pi \times (400 \times 10^{-6} m)^2}$$

LIDT = Peak Intensity = 14.73 GW/cm^2

3.2.11.3. Polarization dependence of third harmonic generation

The intense electric field, when applied to a dielectric material, induces a nonlinear polarization in the material. The well-known power series is used to express the polarization of the sample, where the third-order nonlinear polarization is related to the incident electric field by the equation[57]:

$P_i^{(3)} = \varepsilon_0 \sum_{jkl} \chi_{ijkl}^{(3)} E_j E_k E_l$ …… Eq. 3.5

where i, j, k, l are the Cartesian indices.[57] Here, we have recorded the polarization-dependent THG response of pump light to understand the structural anisotropy of the material. In **Figure 3.13.c**, the four-lobed pattern represents the THG response with respect to the pump polarization angle.[54] This nearly equal distribution of intensity of the THG and sudden drop to near zero value can be due to the high nonlinearity along both axes. This behavior of crystal lattice with polarized light suggests a high anisotropy of the complex-1 crystal. The polarization ratio of the complex-1 crystal was found to be 87.4 % using the equation[58]:

$\rho = (I_{max} - I_{min})/(I_{max} + I_{min})$ …… Eq. 3.6

3.3. Results and discussion

3.3.1. Design strategy

Steric effect and σ-donor effects of the coordinating ligands were harnessed to regulate the Cu-Cu distance in the complexes (**Scheme 3.4**). We first synthesized complex-1 by following a reported protocol with slight modification[45], where 3-cyanopyridine was used as coordinating ligand (**Experimental section 3.2.4**). This was followed by the replacement of one 3-cyanopyrdine attached to each Cu atom with PPh_3, resulting in the formation of a heteroleptic complex named complex-2 (**Experimental section 3.2.5**). The crystallographic details of complex-1 were previously reported[45] and can be found against the CCDC number 1990789. We mention a few parameters here that are relevant to this particular work. ∠N-Cu-N is significantly shorter compared to heteroleptic di-nuclear Cu_2I_2 complexes[10,12,18,30,33,34], with a value of 108.10°. In order to minimize the electronic repulsion, ∠I-Cu-I becomes relatively wider with a value of 120.20°, which results in a significant shortening of the Cu-Cu distance (2.64 Å). The crystallographic data of complex-2 is listed in **Table A1** of **Appendix 1**, and the crystal structure is given in **Scheme 3.4**. Interestingly in this case, the ∠N-Cu-P was found to be 121.18°, which is much higher compared to the ∠N-Cu-N (108.10°) of complex-1. Consequently, ∠I-Cu-I becomes much shorter than that of complex-1 with a value of 109.85°.

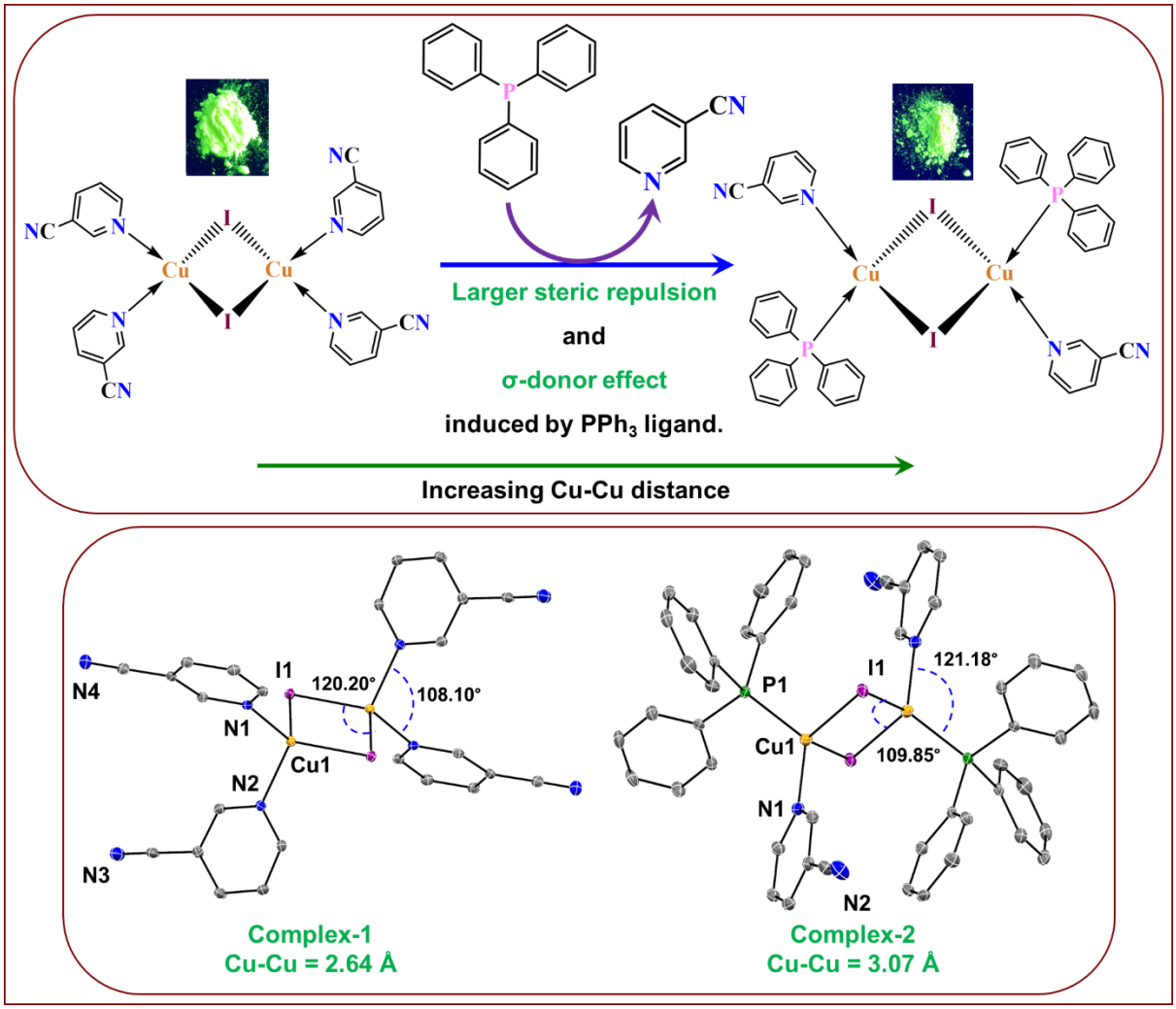

Scheme 3.4. Design strategy for complex-1, and complex-2, along with the corresponding crystal structures (below).

This contraction in the bond angle further led to an increase in the Cu-Cu distance, which was found to be 3.07 Å. In the case of complex-1, all ligands are 3-cyanopyridine; therefore, a minimum amount of steric hindrance is obtained. In complex-2, the insertion of two PPh_3 ligands leads to a significant increase in steric hindrance. Due to the enhanced steric factor, the ∠N-Cu-P increases; therefore, in order to neutralize the excess electronic repulsions, ∠I-Cu-I undergoes a consequential decrease. The steric effect and σ-donor effects were further quantified for both complexes by performing natural bonding orbital (NBO) calculations (**Experimental section 3.2.6**). NBO calculations shows that Cu···Cu distance was increased from complex-1 to complex-2, as similar to observed in the crystal structures. Steric repulsion between the two ligands attached to the Cu center increases from 4.49 kcal/mol (complex-1) to 13.60 kcal/mol (complex-2). At the same time, the delocalization of the electron density from the nitrogen lone-pair of the cyanopyridine ligands to the lone vacant orbital of the Cu center was found to be similar in both these complexes with the second-order perturbative energy

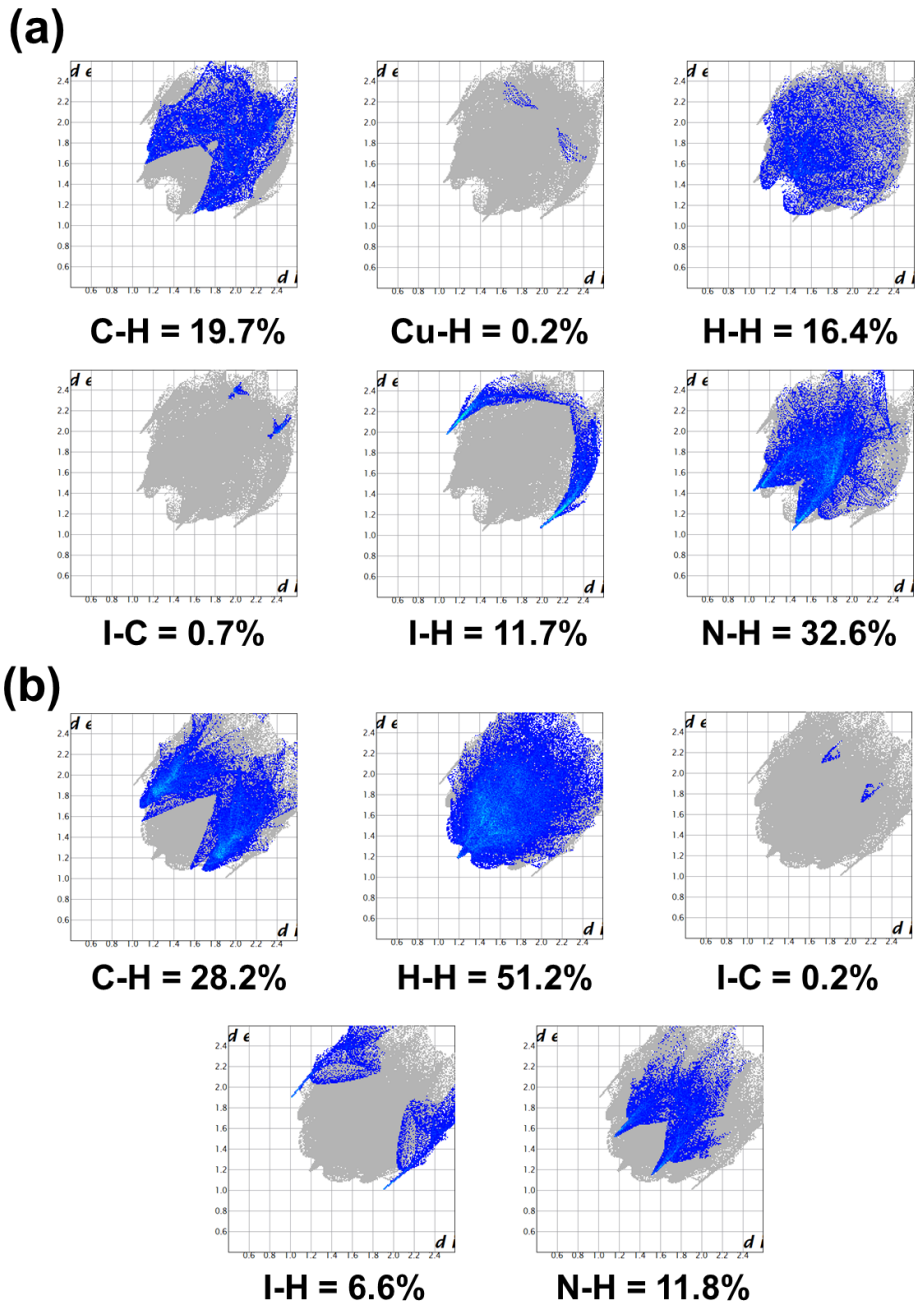

Figure 3.1. Hirshfeld surface analysis[85–87] of the complexes. Fingerprint plots revealing quantitative description of several non-covalent interactions were quantified by using crystal explorer 3.1 software[88]. Fingerprint plots from normalized distance (d_{norm}) mapped over Hirshfeld surface to calculate the percentage of each non-covalent interaction for (a) complex-1, (b) complex-2.

[$E^{(2)}$] of ~25-27 kcal/mol. However, the $E^{(2)}$ values of the delocalization of the phosphorus lone-pair of the triphenylphosphine ligand to the lone vacant orbital of the Cu center was found to be ~51 kcal/mol, almost two-folds of the delocalization observed in case of 3-cyanopyridine ligand. The enhancement in this delocalization can substantially increase the steric repulsion between the Cu centers in complex-2, thereby increasing the Cu···Cu distance to avoid the steric

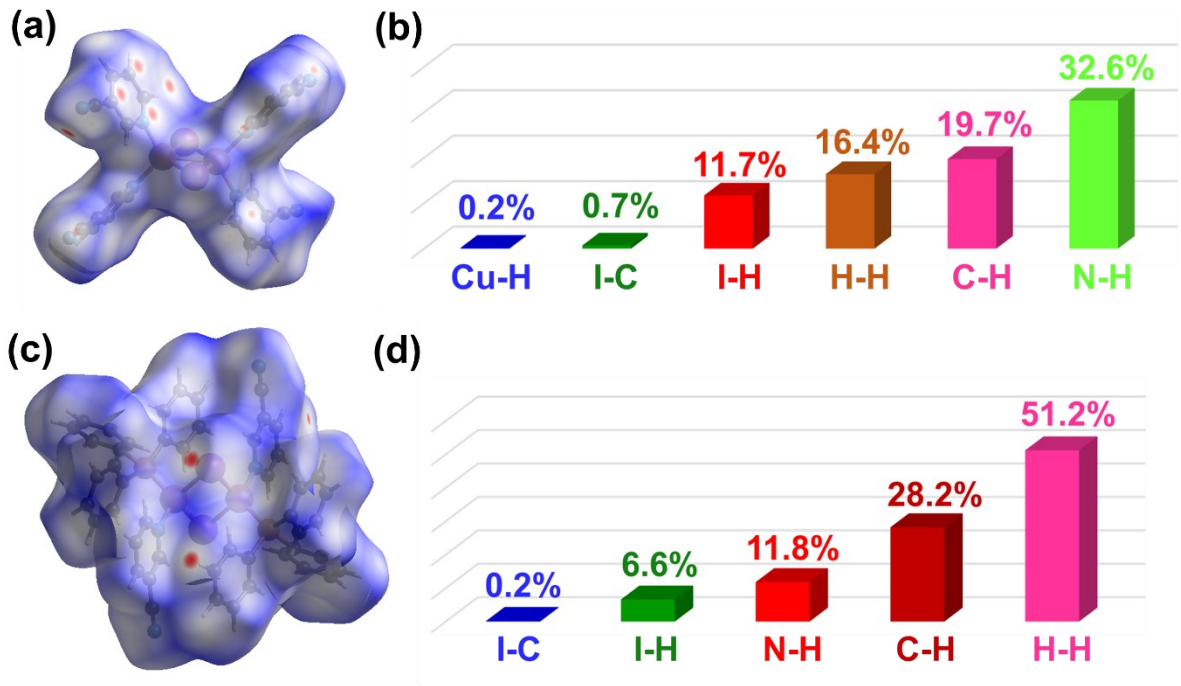

Figure 3.2. Normalized distance (d_{norm}) mapped over Hirshfeld surface for (a) complex-1, and (c) complex-2. Histogram of the percentage contributions of different non-covalent interactions in (b) complex-1 and (d) complex-2.

repulsion between Cu centers. This clearly corroborates our experimentally derived variation of the Cu-Cu distance from the crystal structure (**Scheme 3.4**).

3.3.2. Non-covalent interactions in the bulk phase

The triplet harvesting pathways of two complexes were explored in solid-state, therefore it is worth noting that several non-covalent interactions with high enthalpy values can moderately increase the ISC processes in the solid phase. To identify some of these interactions, Hirshfeld surface analysis calculations were carried out using the crystal structures (**Figure 3.1**). The normalized distance (d_{norm}) mapped over the Hirshfeld surface for both complexes is given in **Figures 3.2a** and 3.**2c**. The histogram containing the percentage contributions of several interactions is shown in **Figures 3.2b** and **3.2d**. We observe that in both complexes, strong interactions such as N···H (enthalpy ~2.97 kJ/mol)[59], C···H (enthalpy ~10.3 kJ/mol)[60], and I···H (enthalpy ~16-25 kJ/mol)[61] are present in the bulk phase. These strong non-covalent interactions not only influence the photophysical processes but also dictate the direction of the polarizability in bulk condensed phase, which has large impact on the NLO properties of the complexes.[62,63] The polarizability in the bulk phase is dictated by the charge transfer properties. Non-covalent interactions with high enthalpy can induce through-space charge transfer in the bulk phase.[64,65] NLO properties of the material depend on the polarizability in the bulk phase.

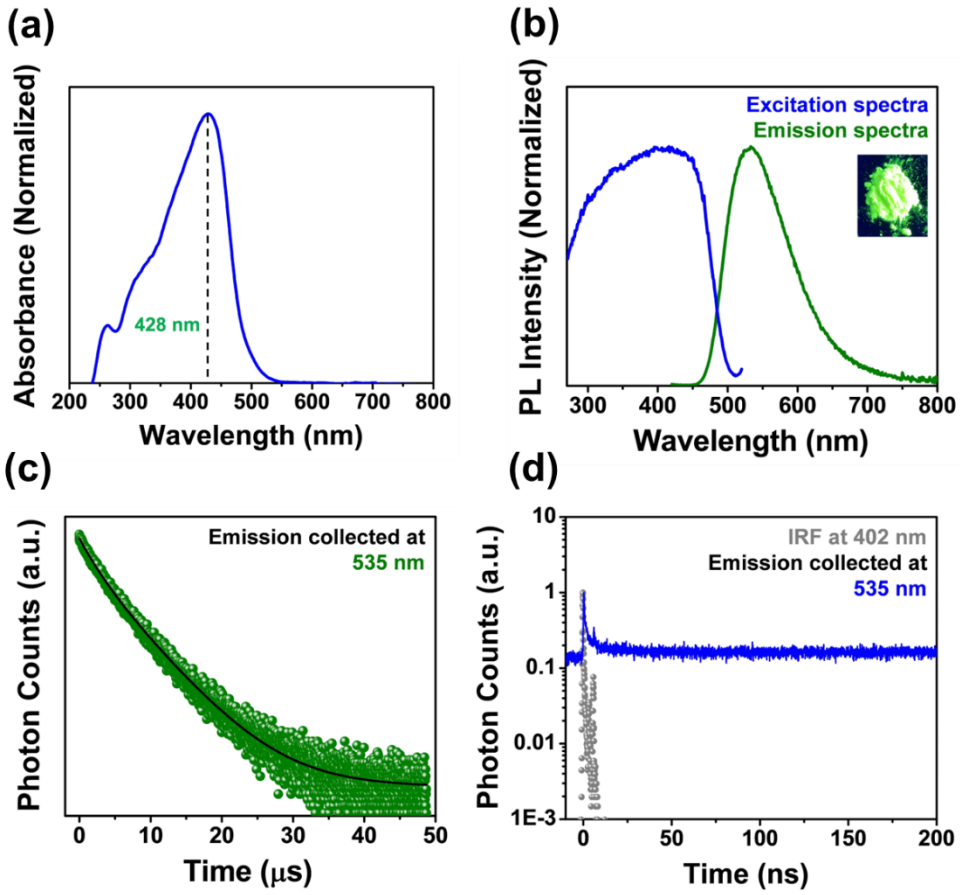

Figure 3.3. (a) Solid-state absorption spectra of complex-1, (b) excitation and emission spectra of complex-1, (c) PL decay profile for complex1, and (d) Nanosecond luminescence decay profile for complex-1.

The non-covalent interactions along a particular direction within the crystal can decide the direction of the polarizability. As a result, it can induce directional features in the NLO properties of the material.

3.3.3. Phosphorescence emission from complex-1

Complex-1 manifests green color under UV light in the solid state along with an absorption peak at 428 nm (**Figure 3.3a**). It displays a broad emission band having a maximum at ~535 nm (**Figure 3.3b**), along with an absolute quantum yield of 66% (**Experimental section 3.2.7**). Moreover, the PL decay profile exhibits biexponential decay having long lifetime components of 2.27 μs and 6.43 μs (**Figure 3.3c**, **Table A3 in Appendix 4**). Spin-orbit coupling matrix elements (SOCME) calculations (**Experimental section 3.2.6**) derived from DFT methods (B3LYP-D3/def2svp level) show reasonably high values in the excited states for S_1-T_n pairs (~3-130 cm^{-1}) (**Table A2 in Appendix 4**). It suggests the presence of strong spin-orbit coupling, which subsequently enhances the ISC rate between singlet and triplet states. This is further supported by the PL decay profile, which consists of only microsecond components and is

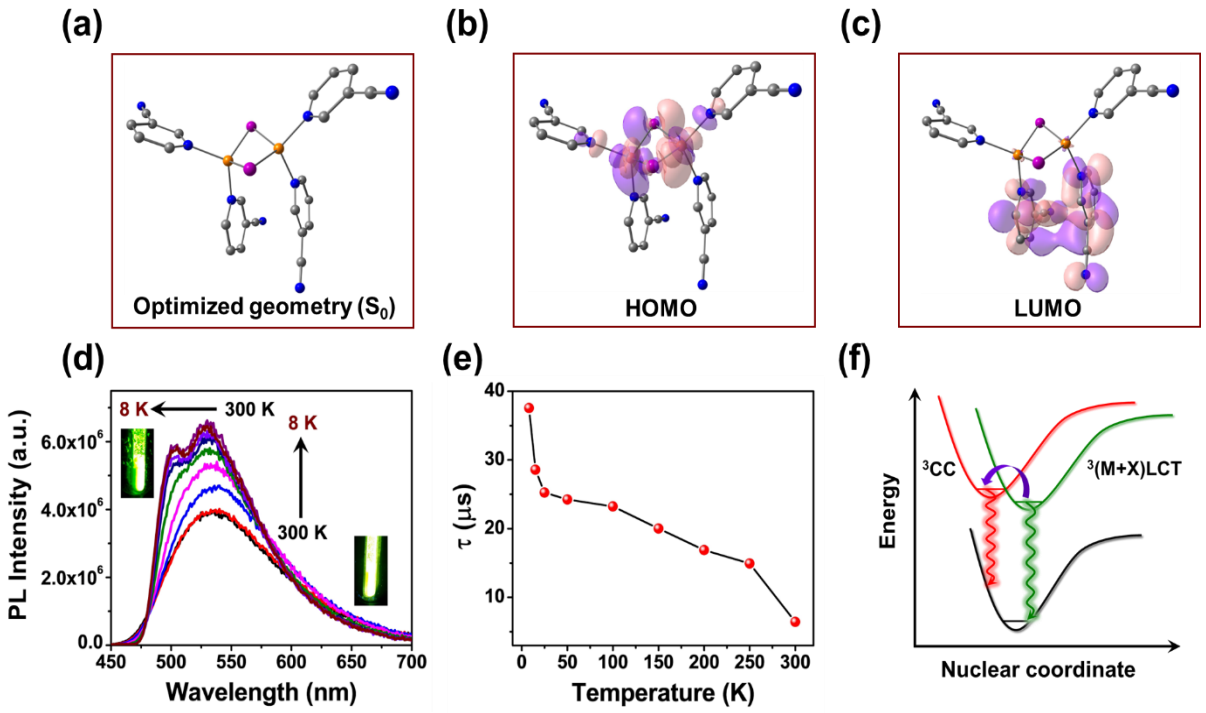

Figure 3.4. (a) Ground state optimized geometry of complex-1 in chloroform along with corresponding (b) HOMO and (c) LUMO of complex-1, (d) temperature-dependent emission spectra of complex-1(excited at 400 nm), (e) lifetime vs. temperature plot of complex-1 (lifetime collected by exciting at 405 nm), and (f) schematic Jablonski diagram for complex-1.

devoid of any prompt fluorescence (PF) owing to the high ISC rate (**Figure 3.3d**). Interestingly, a significantly high SOCME value between T_1 and S_0 (91.34 cm^{-1}) (**Table A2** in **Appendix 4**) indicates a higher rate of phosphorescence decay in this complex. DFT calculations (B3LYP-D3/def2svp level) (**Experimental section 3.2.6**) also reveal that the HOMO is located over Cu (3d), I (5p) orbitals (Figure 4b) and LUMO is distributed over the π* orbital of the 3-cyanopyridine ligand (Figure 4c), unveiling the (M+X)LCT character of the complex. In order to identify the character of each triplet level, natural transition orbital (NTO) analysis was carried out for some of the low-lying singlet and triplet states (S_1-S_3 and T_1-T_3) (**Figure A3**, **A4** in **Appendix 3**) which shows (M+X)LCT nature of low-lying states. However, a much shorter Cu-Cu distance of 2.64 Å (less than the van der Waals distance of Cu atom) in solid state is likely to give rise to a strong Cu···Cu bonding character in higher energy excited states, which can eventually lead to the formation of ^{3}CC excited states with low-energy emission. Notably, the higher analogues of the Cu_2I_2 framework, such as cubane-type Cu_4I_4 clusters coordinated with suitable ligands with low-lying π* orbitals, exhibit emission characteristics derived from a thermal equilibrium between ^{3}(M+X)LCT and ^{3}CC states.[11,15] At room temperature, the emission comes mostly from the ^{3}CC state at the expense of the population from the ^{3}(M+X)LCT state.[11,15] As the temperature decreases, insufficient thermal energy does

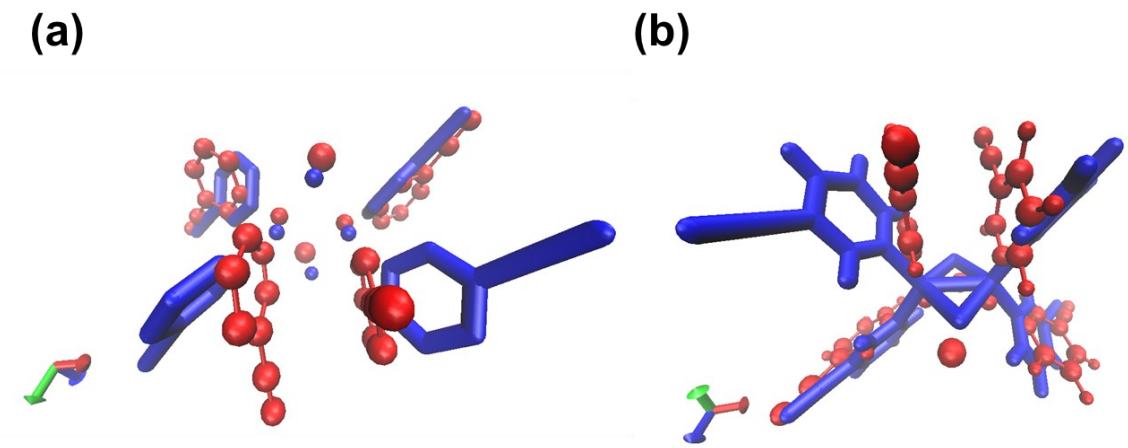

Figure 3.5. Root-mean square deviation (RMSD) of the ground state geometry in crystalline phase with (a) the ground state geometry in $CHCl_3$ (depicted in red) and (b) in THF (depicted in red) for complex-1, calculated and plotted using VMD software. RMSD in case of both solvents was found to be much higher with a value of ~1.96 Å.

not allow the ^{3}(M+X)LCT state population to overcome the energy barrier for transition to ^{3}CC state. As a result, the emission intensity of the high-energy ^{3}(M+X)LCT band undergoes an enormous enhancement at lower temperatures.[11,15] Upon lowering the temperature to 150 K, the emission intensity of complex-1 was sequentially enhanced, accompanied by a continuous blue-shift of the spectra (**Figure 3.4d**). When the temperature was reduced below 150 K, another hump emerged at ~500 nm (**Figure 3.4d**). Upon further lowering the temperature to 8 K, the band-splitting became progressively prominent with the emergence of two shoulder peaks at 500 nm and 530 nm (**Figure 3.4d**). The extent of enhancement in the emission intensity was comparatively lower in the 50-8 K temperature range. The sequential blue-shift and intensity enhancement of the emission band is indicative of an increase in the emission from ^{3}(M+X)LCT state and simultaneous suppression of ^{3}CC emission at lower temperatures. The origin of the band-splitting at lower temperatures can be attributed to the activation of ligand-centered (LC) states showing vibrational progression in the emission band. The lifetime of complex-1 was found to increase from ~6.43 µs to ~37.56 µs when the sample was cooled down from 300 K to 8 K (**Figure A5** in **Appendix 3** and **Table A4** in **Appendix 4**). By virtue of a high ISC rate, fast thermalization can be assumed to take place in this complex. However, the lifetime *vs.* temperature plot shows a sequential increment of the lifetime with temperature and does not represent any Boltzmann-like thermal distribution of the excited state population (**Figure 3.4e**). Hence, the possibility of TADF is effectively ruled out in this case and confirms the presence of phosphorescence. Previously, Ford and Toriumi reported that ^{3}(M+X)LCT and ^{3}CC states do not exhibit large variations in lifetime with temperature.[24,66] Therefore, the comparatively lesser variation in the lifetime with temperature can be attributed to thermal

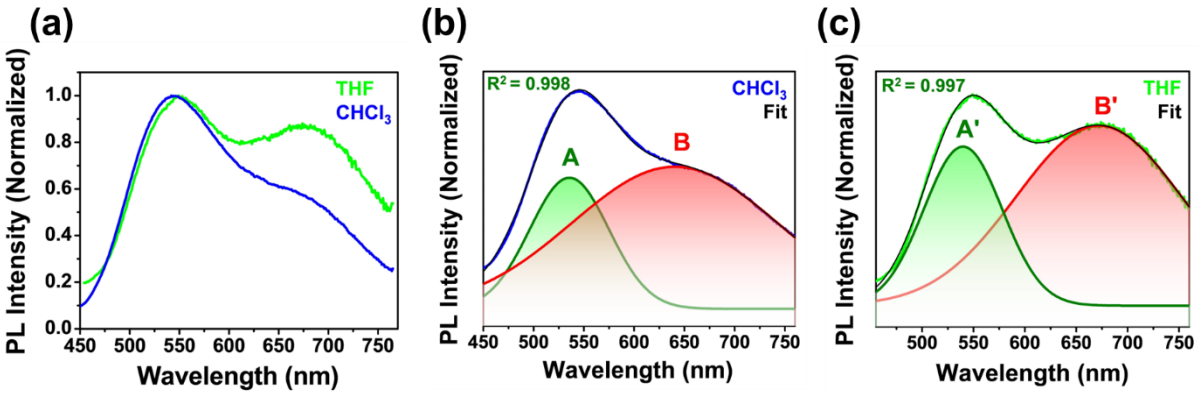

Figure 3.6. (a) Emission spectra of complex-1 in $CHCl_3$ and THF (excited at 390 nm). (b) Deconvoluted emission bands of complex-1 in $CHCl_3$. (c) Deconvoluted emission bands of complex-1 in THF. (The concentration of the solution is 60 nM).

equilibrium between ^{3}(M+X)LCT and ^{3}CC states (**Figure 3.4f**). As (M+X)LCT states are majorly associated with HOMO to LUMO transition, electron-withdrawing group like -CN can sufficiently stabilize the LUMO energy, and the (M+X)LCT emission gets shifted to longer wavelength. As a result, the emission energies of ^{3}(M+X)LCT and ^{3}CC state become much closer to each other making them spectrally unresolvable. Interestingly, the stabilization in LUMO energies leads to a larger energetic barrier between these two states which results in a strong ^{3}(M+X)LCT emission at room temperature coexisting with ^{3}CC emission.[15] This fact also explains the occurrence of simultaneous ^{3}(M+X)LCT and ^{3}CC emission in complex-1 at room temperature. The presence of ^{3}(M+X)LCT and ^{3}CC emission is further supported by the solvent-based theoretical and experimental analysis. DFT calculations in $CHCl_3$ and THF reveal that the ground-state optimized geometry is much distorted in solution compared to that of the crystalline phase with a large RMSD value of ~1.96 Å (**Figures 3.5a, 3.5b**). In both $CHCl_3$ and THF, complex-1 exhibited a broad emission band with the maximum located at ~550 nm, which is slightly red-shifted compared to the solid-state emission spectrum owing to the solvation effect (**Figure 3.6a**). In addition, another hump was observed in $CHCl_3$ solution with the maximum at ~650 nm, which emerged as a peak with a maximum at ~675 nm in case of THF (**Figure 3.6a**). To completely resolve the emission bands, the emission spectra were deconvoluted by using minimum number of Gaussian peaks (**Figures 3.6b, 3.6c**). The additional emission peaks in $CHCl_3$ and THF are comprised of bands with reasonably high bandwidths (B and B' in **Figures 3.6b, 3.6c**), which significantly differ from the bandwidth of the other two high-energy bands (A and A'). The difference in emission bandwidths indicates the presence of different emissive states based on orbital contributions and relaxation energies. The previous theoretical and experimental approaches have shown that in Cu_4I_4-type cubane clusters, ^{3}CC state is formed by exciting one electron from HOMO to a high energy vacant

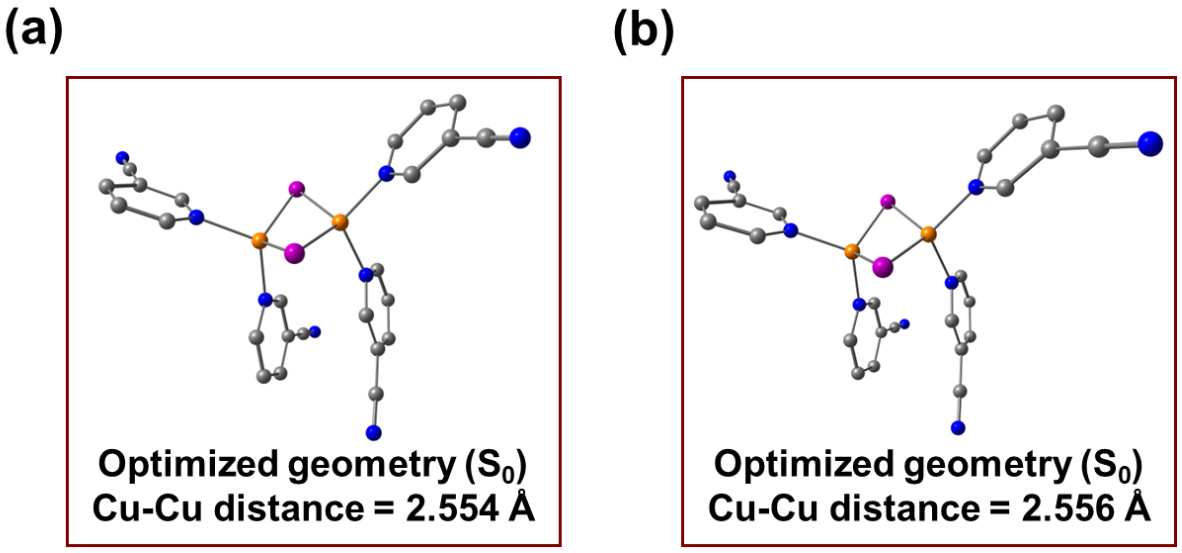

Figure 3.7. Ground state optimized geometry with Cu-Cu distance of complex-1 in (a) $CHCl_3$, and in (b) THF.

orbital (LUMO+24), which has a sufficient Cu-Cu bonding character.[11,25,67] This state undergoes a greater extent of geometry relaxation than ^{3}(M+X)LCT states. As a result, the extent of band-broadening is much greater in the case of ^{3}CC emission compared to ^{3}(M+X)LCT emission. Therefore, the exceptionally large bandwidth of B and B' in our case can be directly correlated to higher relaxation energy of ^{3}CC states. Interestingly, in this complex, a high energy vacant orbital (LUMO+19) was identified with a strong Cu···Cu bonding interaction which has similar characteristics to LUMO+24 of Cu_4I_4 clusters (**Figure A6** in **Appendix 3**). In addition, the ground-state optimized geometry of complex-1 in $CHCl_3$ and THF shows a Cu-Cu distance of 2.554 Å and 2.556 Å, respectively, which are significantly shorter than the distance in the solid phase (2.64 Å) (**Figure 3.7a, 3.7b, Scheme 3.4**). It suggests that in solution, the Cu···Cu bonding interaction undergoes an enormous increment compared to the solid state and the LUMO+19 can be further stabilized. The enhanced bonding interaction can lead to significant stabilization of the ^{3}CC state, resulting in a major red-shift in the corresponding emission band. Therefore, the emergence of red-shifted emission peaks (B and B') in the solution phase can be attributed to a further stabilized ^{3}CC state compared to the solid-phase. Alongside, the high-energy A and A' bands are ascribed to ^{3}(M+X)LCT emission. As a result, we observe a dual-band emission from complex-1 in the solution phase, but in the solid state, the individual spectral contributions of these two emissive states are unresolvable. The dual emissive nature also substantiates the temperature-dependent emission spectra in solid-phase, where the blue-shift at lower temperatures confirms the presence of thermal equilibrium between ^{3}(M+X)LCT and ^{3}CC states. Therefore, a shorter Cu-Cu distance plays a key role in dictating emission pathways of (M+X)LCT active Cu_2I_2 complexes.

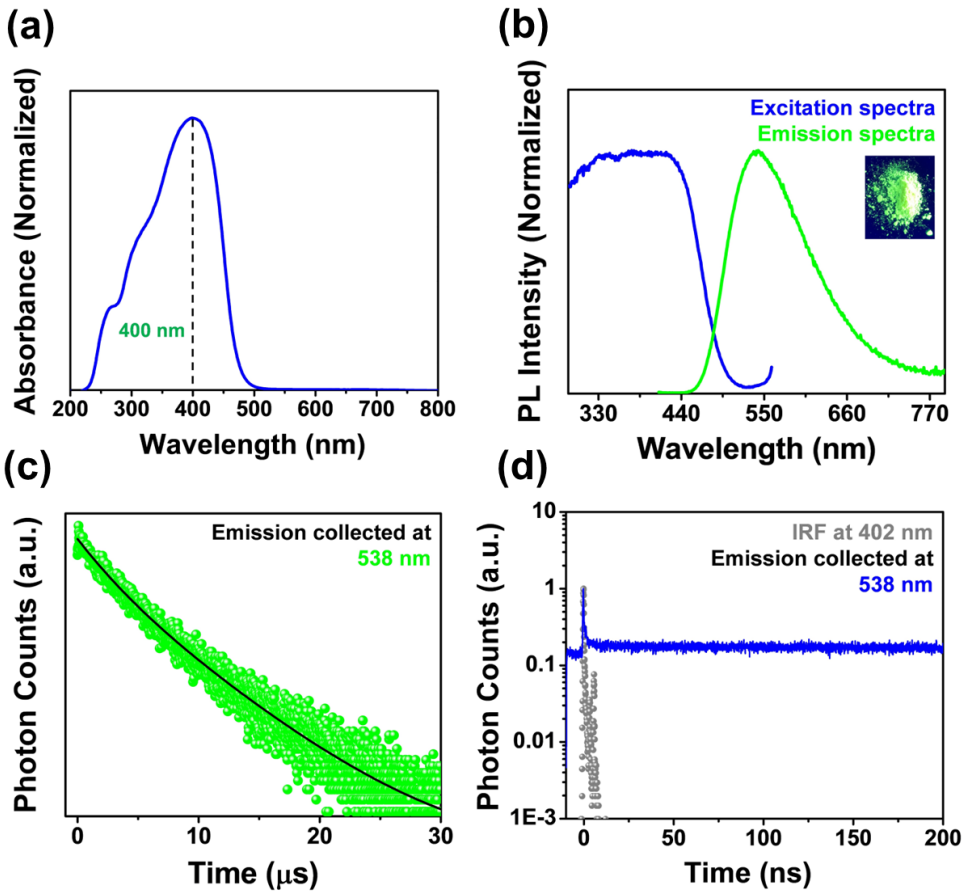

Figure 3.8. (a) Solid-state absorption spectra of complex-2, (b) excitation and emission spectra of complex-2, (c) PL decay profile for complex-2, and (d) Nanosecond luminescence decay profile for complex-2.

3.3.4. TADF emission from complex-2

Following the ligand replacement in complex-1, the complex-2 exhibits green-yellow color under UV light, with an absorption peak at 400 nm (**Figure 3.8a**) and emission maximum at ~538 nm in the solid phase (**Figure 3.8b**). DFT calculations show the low-lying excited states to be (M+X)LCT in nature, where the HOMO and LUMO are spatially well-separated (**Figure 3.10b, 3.10c**). The absorption peak of complex-2 (at 400 nm) lies at higher energy compared to complex-1 (at 428 nm). This can be attributed to the larger number of 3-cyanopyridine ligands in complex-1, where the strong electron-withdrawing effect of four -CN groups reduces the energy of low-lying excited states of complex-1 compared to that of complex-2. The single-point TDDFT calculation shows that the low-lying excited states are energetically close with a reasonably small ΔE_{ST} value of 0.03 eV (**Figure 3.9b**). Additionally, high SOCME values between S_1-T_n pairs (~7-14 cm^{-1}) (**Table A2** in **Appendix 4**) indicate a high ISC rate in the excited states. In addition, the ground-state optimized geometry of complex-2 significantly overlaps with the geometry in the crystal phase, unlike complex-1 (**Figure 3.10a**). However, the crystal structure suggests that the Cu-Cu distance (3.07 Å) (**Scheme 3.4**) is much larger

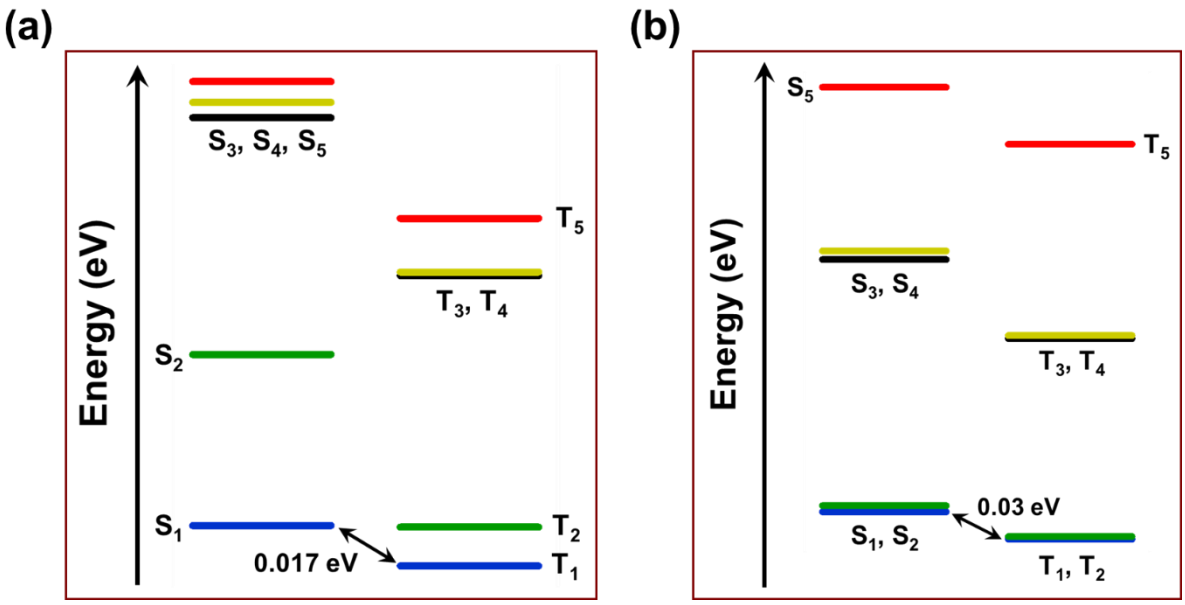

Figure 3.9. TDDFT single-point energy diagram (in $CHCl_3$, using IEFPCM model) of (a) complex-1, and (b) complex-2 for S_1-S_5 and T_1-T_5.

than the van der Waals radius of the Cu atom, which is indicative of the absence of any Cu···Cu bonding interaction in the solid phase. The temperature-dependent emission study shows a sequential red-shift in the emission band along with an increment in intensity upon lowering the temperature from 300 K to 8 K (**Figure 3.10d**). The observation of the red-shift is in complete contrast with complex-1, which can also be realized from the images of the sample at room temperature and low temperature (**Figure 3.4d, 3.10d**). The lifetime at room temperature for this complex was determined to be 6.98 µs (**Figure 3.8c**, **Table A3** in **Appendix 4**) in solid phase. Interestingly, the emission lifetime of this sample inclined enormously to ~94 µs upon lowering the temperature to 50 K (**Figure 3.10e**, **Table A5** in **Appendix 4**). In 50-100 K region the lifetime distribution forms a plateau with high lifetime, which indicates that the emission exclusively comes from the triplet state as phosphorescence. Above 100 K, a sharp decrease in lifetime takes place, which indicates that a higher lying state with a shorter lifetime is thermally activated at higher temperatures. Under the assumption of a fast thermalization process, the lifetime vs. temperature plot represents a Boltzmann-type thermal distribution of the population, and fitted with Eq 3.7,[31,34,68] (**Figure 3.10f**).

$$\tau_{obs} = \frac{3 + e^{-\frac{\Delta E_{ST}}{k_B T}}}{\frac{3}{\tau(T_1)} + \frac{1}{\tau(S_1)} e^{-\frac{\Delta E_{ST}}{k_B T}}} \qquad \text{Eq 3.7}$$

where, $\tau_{obs}, k_B, \tau(T_1)$, and $\tau(S_1)$ denotes experimentally observed lifetime, Boltzmann constant, intrinsic lifetime of triplet state and singlet state, respectively. The particular feature

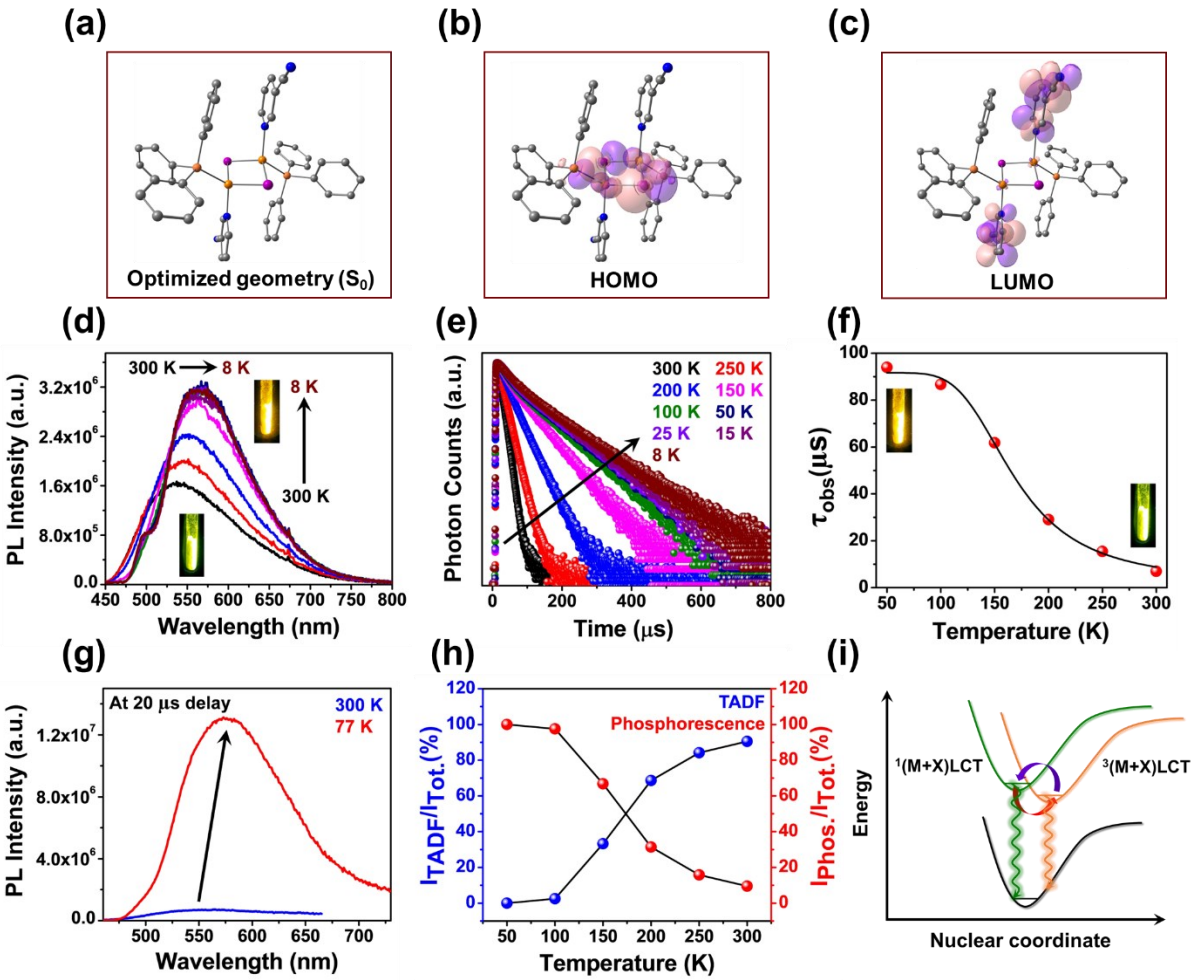

Figure 3.10. (a) Ground state optimized geometry of complex-2 in chloroform. Corresponding (b) HOMO and (c) LUMO of complex-2. (d) Temperature-dependent emission spectra of complex-2 (excited at 400 nm), (e) temperature-dependent variation in the lifetime of complex-2 (lifetime collected by exciting at 405 nm), (f) lifetime vs. temperature plot for complex-2, (g) gated emission spectra of complex-2 at 300 K and 77 K (excited at 400 nm), (h) proportions of TADF and phosphorescence at different temperatures, and (i) schematic Jablonski diagram for complex-2.

of temperature-dependent lifetime variation is related to the thermal equilibrium between singlet and triplet state population and confirms the presence of TADF in complex-2 within three-state model. At room temperature, a much shorter lifetime suggests that the emission yield is predominantly derived from the delayed fluorescence process. The intrinsic lifetimes of singlet and triplet states were obtained from the fitting parameters of eq. 1 and were calculated to be 164 ns and 91.63 μs, respectively (**Experimental section 3.2.8**). The ΔE_{ST} was obtained from the fitting parameters and calculated to be 0.076 eV (**Experimental section 3.2.8**). Such a lower ΔE_{ST} clearly shows that following the ISC process, the singlet state can be thermally repopulated at the cost of the triplet state population at room temperature. The occurrence of the red-shift in the emission spectra is attributed to the increased triplet emission

at lower temperature, which has a lower energy than the singlet state. As both states are (M+X)LCT in nature, therefore, no vibrational structure is observed in this case as is shown by complex-1. Additionally, the absence of vibrational structure also indicates that the whole emission is derived from the thermal equilibrium between $^{1/3}$(M+X)LCT states and no ligand-centered emission is involved. Due to a reasonably high ISC rate, prompt fluorescence (PF) is severely quenched to several picoseconds in this kind of moieties, where strong spin-orbit coupling is present.[31,69] As a result, no detectable PF was present within the nanosecond decay profiles of this complex (**Figure 3.8d**). In this case, ISC rate (k_{ISC}) can be qualitatively estimated to be in the order of 10^{11}-10^{12} s^{-1}, given that the PF lifetime is in the order of several picoseconds. The increase in the triplet population at lower temperatures can also be demonstrated by comparing the gated emission spectra at 300 K and 77 K. At 300 K, the intensity of the emission band is quenched to a significant extent upon applying a 20 μs detector delay, which suggests that the emissive state has a shorter lifetime at room temperature (**Figure 3.10g**), which corresponds to predominant delayed fluorescence. Surprisingly, upon lowering the temperature to 77 K, an immense boost in intensity took place at the same detector delay (**Figure 3.10g**). The exceptional increment in the emission intensity clearly shows that at low temperature, the emissive state has a much longer lifetime corresponding to phosphorescence emission. Furthermore, we have calculated the temperature-dependent contributions of delayed fluorescence and phosphorescence to the total emission along with delayed fluorescence lifetime by using Eq 3.8, 3.9, and 3.10, respectively[34,70].

$$\frac{I(T_1)}{I_{Tot}} = \left[1 + \frac{k_r(S_1)}{3k_r(T_1)} e^{\frac{-\Delta E_{ST}}{k_B T}}\right]^{-1} \qquad \text{Eq 3.8}$$

$$\frac{I(S_1)}{I_{Tot}} = 1 - \left[1 + \frac{k_r(S_1)}{3k_r(T_1)} e^{\frac{-\Delta E_{ST}}{k_B T}}\right]^{-1} \qquad \text{Eq 3.9}$$

$$\tau_{DF} = \frac{\Phi_{DF}}{\frac{1}{\tau_{obs}} - \frac{1}{\tau_{T_1}}} \qquad \text{Eq 3.10}$$

where, $k_r(S_1)$ and $k_r(T_1)$ denote rate of prompt fluorescence and rate of phosphorescence, respectively. The temperature dependence of the TADF and phosphorescence attributes were found to follow a similar nature as the lifetime variation, which is complementary to each other (**Figure 3.10h**). At room temperature, the contributions of TADF and phosphorescence were found to be 90.5% and 9.5% of the total emission yield, respectively (**Table A6** in **Appendix 4**). As a result, the majority of triplet excitons are easily recoverable through the delayed fluorescence process, which gives rise to a high absolute quantum yield of 83% (**Experimental section 3.2.7**). The percentage contribution of TADF was sequentially decreased with

decreasing temperature, along with a simultaneous inclination in phosphorescence contribution (**Figure 3.10h**, **Table A6** in **Appendix 4**). Finally, at 50 K, only phosphorescence emission was observed (**Figure 3.10h**). The fractional quantum yields for TADF and phosphorescence were found to be 75.1% and 7.8%, respectively (**Experimental section 3.2.9**) at room temperature. The delayed fluorescence lifetime of the complex was found to be 5.6 µs, which is significantly lower and comparable to other reported Cu(I) TADF complexes.[31,68] A high quantum yield value, along with a shorter delayed fluorescence lifetime, make this complex a suitable candidate to be utilized in fabricating OLED devices. The exceptionally high delayed fluorescence yield in this complex is further supported by a feeble SOCME value of 0.0014 cm^{-1} between T_1 and S_0 (**Table A2** in **Appendix 4**). As a result, the phosphorescence decay rate becomes reasonably lower in this complex, thereby enhancing the RISC rate from T_1 to S_1. Additionally, it should be noted that the quantum yield of this complex is reasonably higher compared to complex-1. In complex-1, along with the ^{3}(M+X)LCT states, the ^{3}CC states act as an additional radiative pathway through which a significant portion of excitons can be recovered. The loss in emission yield in complex-1 can be significantly attributed to the enhanced non-radiative decay owing to the higher reorganization energy of ^{3}CC states. Therefore, considering the rudimentary structural framework for both complexes to be the same, triplet harvesting was found to be more efficient in case of complex-2, which is a $^{1/3}$(M+X)LCT active TADF complex (**Figure 3.10i**). The photophysical parameters of two complexes, along with Cu-Cu distances are summarized in **Table 3.1**. Evidently, a significant increase in Cu-Cu distance can lead to a complete transition in the emission pathway and activates TADF in (M+X)LCT complexes with high quantum yield.

Table 3.2. Photophysical parameters of complex-1 and complex-2 in solid phase.

Complex name	Cu-Cu distance [Å]	Emission maxima [nm]	Lifetime [µs]	Quantum yield
Complex-1	2.64	535	6.43	66%
Complex-2	3.07	538	6.98	83%

3.3.5. Fabrication of emitter-doped PMMA film and warm white light emitting pc-LED with complex-2.

As complex-2 exhibits TADF, we further went on to fabricate emitter-doped polymethyl methacrylate (PMMA) films of this complex in order to examine the scope of its utilization in

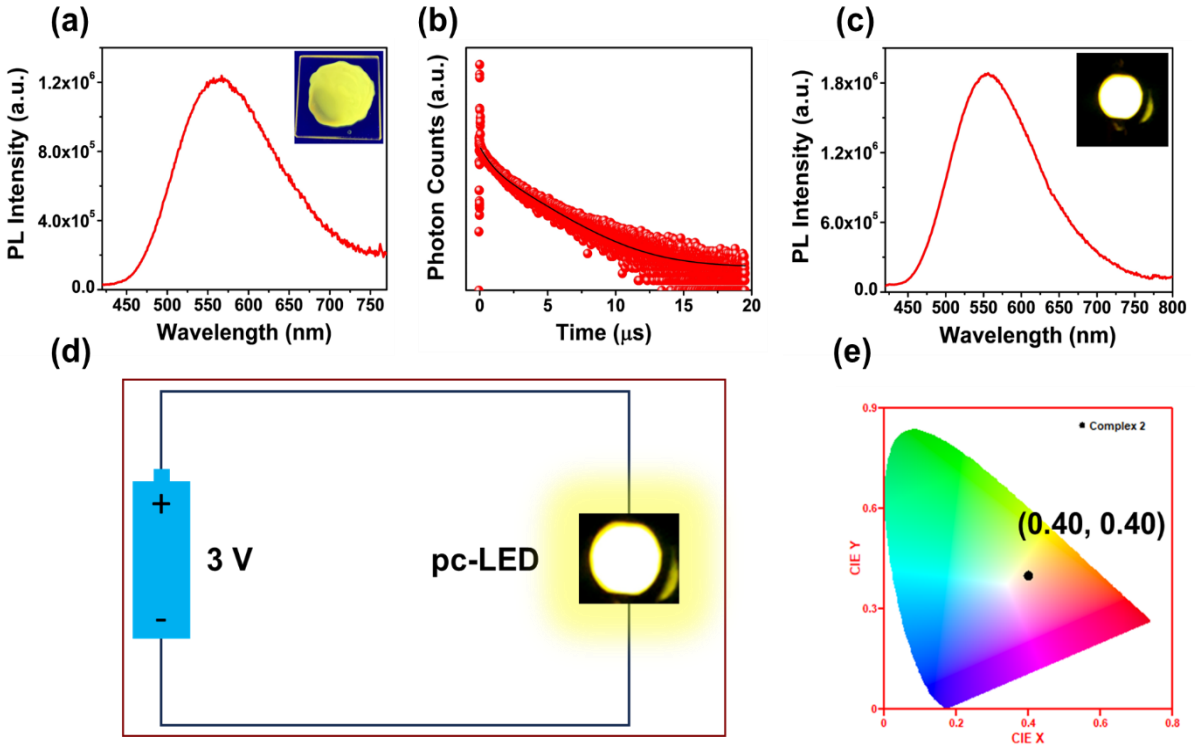

Figure 3.11. (a) Emission spectra of 20% (w/w) emitter-doped PMMA film for complex-2 (excited at 400 nm), (b) PL decay profile of 20% (w/w) complex-2-doped PMMA film, (c) Emission spectra of the pc-LED fabricated with 20% (w/w) complex-2-doped PMMA film, (d) demonstration of the pc-LED set-up emitting warm white light, and (e) CIE color coordinate of the pc-LED fabricated with 20% (w/w) emitter-doped PMMA film for complex-2.

OLED devices (**Experimental section 3.2.10**). PMMA acts as a suitable host matrix with high-energy triplet states so that no energy transfer can take place between the emitter and PMMA.[71] It can also suppress the non-radiative decay rates in the bulk phase, thereby reducing the concentration-quenching effects in the emitter.[71] 20% (w/w) emitter-doped PMMA film for complex-2 shows a broad emission band with a maximum at ~560 nm (**Figure 3.11a**) with a quantum yield of 77% (**Experimental section 3.2.7**). Interestingly, the lifetime components of the emitter-doped film were found to be ~2.8 μs, which are much lower compared to the solid-state lifetime (**Figure 3.11b**, **Table A7** in **Appendix 4**). The decrement in the lifetime can be attributed to the increased reverse inter-system crossing (RISC) rate in the polymer matrix film. For an emitter k_{RISC} is given by[72],

$$k_{RISC} = \frac{\Phi_{DF}}{\tau_{PF}\tau_{DF}k_{ISC}\Phi_{PF}} \qquad \text{Eq. 3.11}$$

where, τ_{PF} and Φ_{PF} are PF lifetime and PF quantum yield, respectively. The τ_{DF} and k_{ISC} may undergo negligible changes as a consequence of the intrinsically strong spin-orbit coupling of the complex. From Eq. 3.11, it can be determined that if τ_{DF} decreases, the k_{RISC} would increase (or *vice versa*). PMMA matrix prevents the triplet excitons from undergoing non-radiative

decay by providing rigid environment to the emitter. PMMA has high energy triplet states, which prohibits the triplet-triplet energy transfer from the emitter. As a result, inside the polymer matrix availability of triplet excitons for RISC process increases compared to the emitter in solid phase, and eventually the RISC rate increases. As the quantum yield of complex-2 remains largely unchanged in the PMMA film, the faster RISC rate is reflected by a shorter emission lifetime. Copper(I) iodide-based phosphors can also be utilized in fabricating solution-processable pc-LED.[73–76] In our case we have further fabricated the pc-LED by using 20% emitter-doped PMMA matrix as described above. The $CHCl_3$ solution containing the polymer and emitter was coated over the InGaN LED chips (**Figure A7** in **Appendix 3**). It was connected to a battery which resulted in the emission of warm white light from the pc-LED (**Figure 3.11d**) with a CIE coordinate of (0.40, 0.40) (**Figure 3.11e**). The emission spectra was collected, and the band maximum was found to be at ~560 nm (**Figure 3.11c**). These results further uphold the potential utility of this complex in fabricating OLED devices.

3.3.6. Photon up-conversion properties

3.3.6.1. Third harmonic generation

Consequently, the high charge-transfer nature and strong non-covalent interactions in bulk phase further prompted us to explore non-linear photon up-conversion properties of these complexes. Despite the presence of high (M+X)LCT character, exploration of NLO responses of these materials is rarely found in the literature. Second harmonic generation (SHG) is a second-order nonlinear process and intrinsically most efficient for photon up-conversion. However, only non-centrosymmetric materials can produce SHG. In contrast, the third harmonic generation (THG) has no such symmetry limitations.[77] THG is a third-order nonlinear process where the photon energy can be upconverted three-fold in a single step. As these complexes have a charge-transfer state as the excited electronic state, we anticipate them to have large polarizability, a requirement for efficient third-order nonlinearity. Hence, we have investigated the third-order NLO properties of our samples by conducting extensive THG measurements at a wide range of excitation wavelengths. We used ~50 femtosecond pulses produced from an ultrafast optical parametric amplifier as the excitation source for all THG measurements. The experimental details are provided in the **Experimental section 3.2.11**. We examined the THG responses of the centrosymmetric crystals of both complex-1 & complex-2 at various excitation wavelengths ranging from 1380 – 1580 nm at a constant power of 3 mW for complex-1 and 8 mW for complex-2 (**Figures 3.12a, 3.12b**). The THG response is dependent on the excitation wavelength, and we observe a resonance enhancement of THG

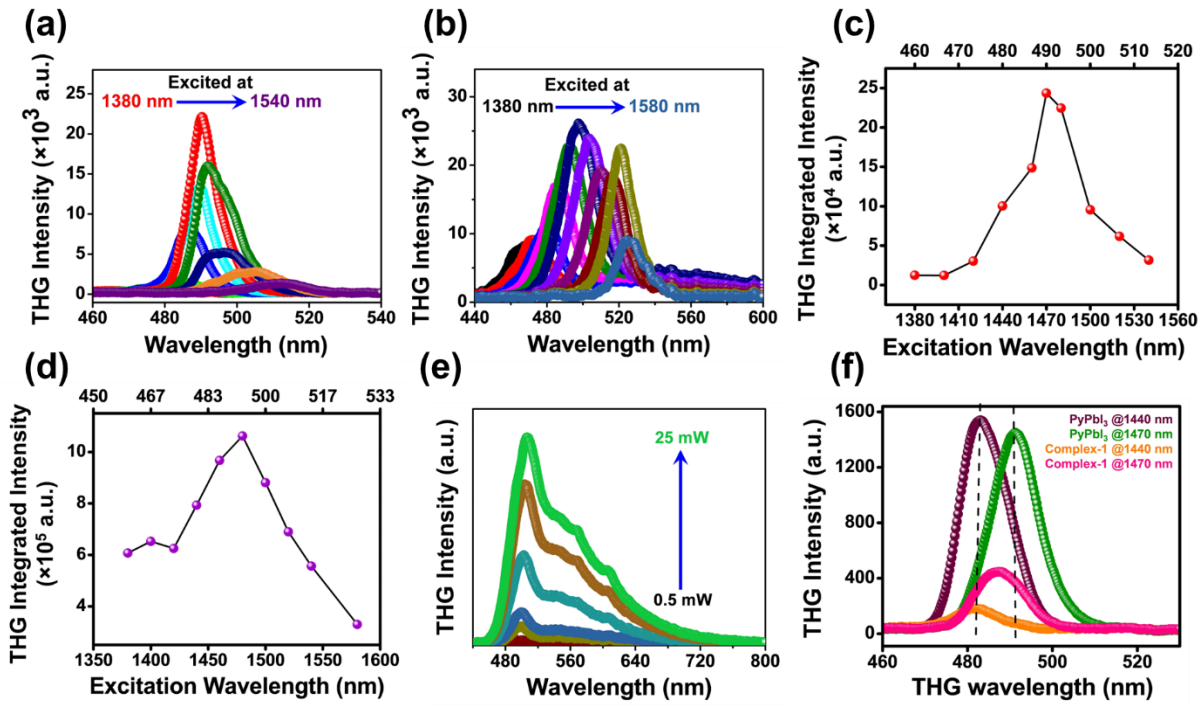

Figure 3.12. Excitation wavelength-dependent THG response of (a) complex-1 and (b) complex-2. Excitation wavelength was varied from 1380 nm to 1540 nm keeping the average power of 3 mW for complex-1, and 8 mW for complex-2. THG response (integrated intensity) vs the excitation pump wavelength for (c) Complex-1 and (d) Complex-2. Maximum THG response is observed at excitation wavelength of 1470 nm and 1480 nm for complex-1 and complex-2, respectively. (e) Excitation power-dependent spectra of the THG response at the excitation pump wavelength of 1470 nm for complex-2, and (f) comparison of THG response of reference $PyPbI_3$ at excitation wavelengths 1440 nm and 1470 nm with the THG response of the complex-1 at the similar wavelengths.

intensity corresponding to the edge of the absorption spectra. The THG intensity maxima are at 490 and 495 nm for the complex-1 and complex-2, respectively (**Figure 3.12c**, **3.12d**). Complex-1 exhibits an order of magnitude higher resonance-enhanced THG response than that in complex-2. For complex-1, a dramatic enhancement of the THG is observed near the pump wavelength of 1470 nm, as it approaches the bandgap resonance.[53,78] The THG drops drastically upon further decrease in pump wavelength due to self-absorption.[53,79] Complex-2 shows an intriguing THG response. An equally strong spectrally-overlapping 3-photon absorption-induced fluorescence accompanies the THG spectra (**Figure 3.12e**). An efficient three-photon absorption (a fifth-order nonlinear process) and subsequent fluorescence compete with the THG process resulting overall lower THG intensity compared to the complex-1 where such a competition is absent. Due to the complication of deconvoluting the THG intensities from the complex THG-fluorescence spectra, we could not quantitatively determine the THG efficiency for complex-2.

We quantitatively assessed the THG efficiency and the optical stability of complex-1 at the excitation wavelength corresponding to the maximum THG response. We determined the third-order nonlinear susceptibility ($\chi^{(3)}$) using a modified relative method derived from nonlinear Maxwell's equation[53,54] (**Experimental section 3.2.11.2**). To determine $\chi^{(3)}$, we have used pyridinium lead iodide ($PyPbI_3$) as the reference as it shows maximum THG response at a nearby excitation wavelength (1440 nm).[53] $PyPbI_3$ has a $\chi^{(3)}$ value of 1.96×10^{-18} m^2V^{-2} at 1440 nm. The $\chi^{(3)}$ value of complex-1 is obtained to be about 0.79×10^{-18} m^2V^{-2} at 1440 nm. From the relative THG response of the reference and complex-1 at identical condition (**Figure 3.12f**), we determined the $\chi^{(3)}$ value of complex-1 to be 1.15×10^{-18} m^2V^{-2} at pump wavelength 1470 nm, exhibiting the highest THG response. Complex-1 shows a comparable THG response at 490 nm to $PyPbI_3$ and other lower-order metal-halide perovskites which are in the limelight for their efficient NLO properties.[53,54,79]

Optical stability is another important factor for any material for potential NLO applications. Laser-induced damage threshold (LIDT) is the quantitative measure of optical stability of a material and corresponds to the optical damage limit of the material at a source wavelength.[80] To determine the LIDT, we recorded the THG response of complex-1 at varied excitation power at the resonant condition of maximum THG (λ_{pump} = 1470 nm) with the laser spot size of 400 μm. **Figure 3.13a** depicts the excitation power-dependent THG spectra at the resonance excitation condition, whereas **Figure 3.13b** plots the integrated THG intensities vs the excitation power. It is evident from **Figure 3.13b** that the THG response deviates from its usual cubic dependence beyond excitation power of ~3.7 mW and corresponds to LIDT of complex-1. This sudden loss in THG is due to the saturation effects such as local heating.[79] We obtain a LIDT value of 14.73 GW/cm^2 for complex-1 (**Experimental section 3.2.11.2**), which is almost comparable to the reported benchmark NLO materials or even higher than that (~11600 × LIDT of $AgGaS_2$, which is a conventional NLO material for comparison of LIDT measurements).[80,81] Therefore, it is a promising material that shows a satisfactory response in third-order susceptibility and optical stability and should be further explored.

In addition to higher NLO efficiency and optical stability, intrinsic structural anisotropy is envisioned as another crucial factor for any material to be used as a potential NLO source.[82] This structural anisotropy is examined by the change in polarization of the excitation source. Here, we determined the THG response with respect to different polarization angles under the resonant conditions where we observed the maximum THG. **Figure 3.13c** shows the four-lobed distribution of THG intensity, and the maximum THG corresponds to the orthogonal direction of the polarization concerning the axis of the crystal.[54] On the contrary, there is a negligible

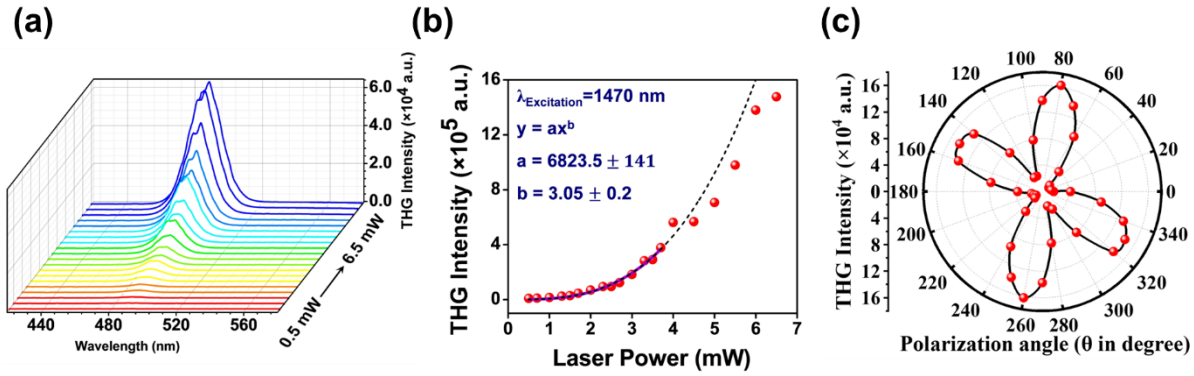

Figure 3.13. (a) Excitation power-dependent spectra of the THG response at the excitation pump wavelength of 1470 nm for complex-1, (b) integrated THG intensity vs. excitation power for complex-1 at pump wavelength of 1470 nm. THG response deviates from its cubic-dependence on excitation power at ~3.7 mW, and (c) variation of normalized THG intensity with respect to the change in the polarisation angle of the excitation source.

THG response when the incident pump polarization is parallel to the axis of the crystal. Thus, we conclude that the THG emission pattern is highly sensitive to the crystal symmetry of the material.

3.3.6.2. Two-photon excited luminescence properties

Two-photon absorption (TPA) is a prodigious photon up-conversion phenomenon that can generate high energy photons by using near-IR or IR light sources.[83,84] TPA is a non-linear optical process where the material with high energy band-gap is excited from ground state to excited state by simultaneous absorption of two low energy photons.[84] The excitation source is typically a laser beam in this case, having high density of photons which is required in simultaneous absorption of multiple photons. Therefore, in case of two-photon active luminogens, this optical excitation leads to luminescence with an energy that is much higher than the excitation source. π-conjugated push-pull type luminogens having high charge transfer nature in their excited state can exhibit strong TPA properties. In this particular work, complex-1 and complex-2 were found to exhibit efficient two-photon excited luminescence owing to their high charge transfer character, polarizability, and dipole moments. The dipole moment and polarizability of complex-1 was found to be 1.71 D and 500.24, respectively; and that of the complex-2 was calculated 0 D and 860.29, respectively. Although the complex-2 has zero dipole moment, but the higher polarizability can impart two-photon absorption properties. The corresponding PL spectra, excitation spectra and microscope images for both complexes were collected by using multi-photon excitation luminescence set-up. The two-photon excited PL spectra of both complexes significantly resemble the single-photon excited PL spectra of the complexes (**Figures 3.14a**, **3.14b**). PL intensity vs. incident laser power plot (**Figures 3.14e,**

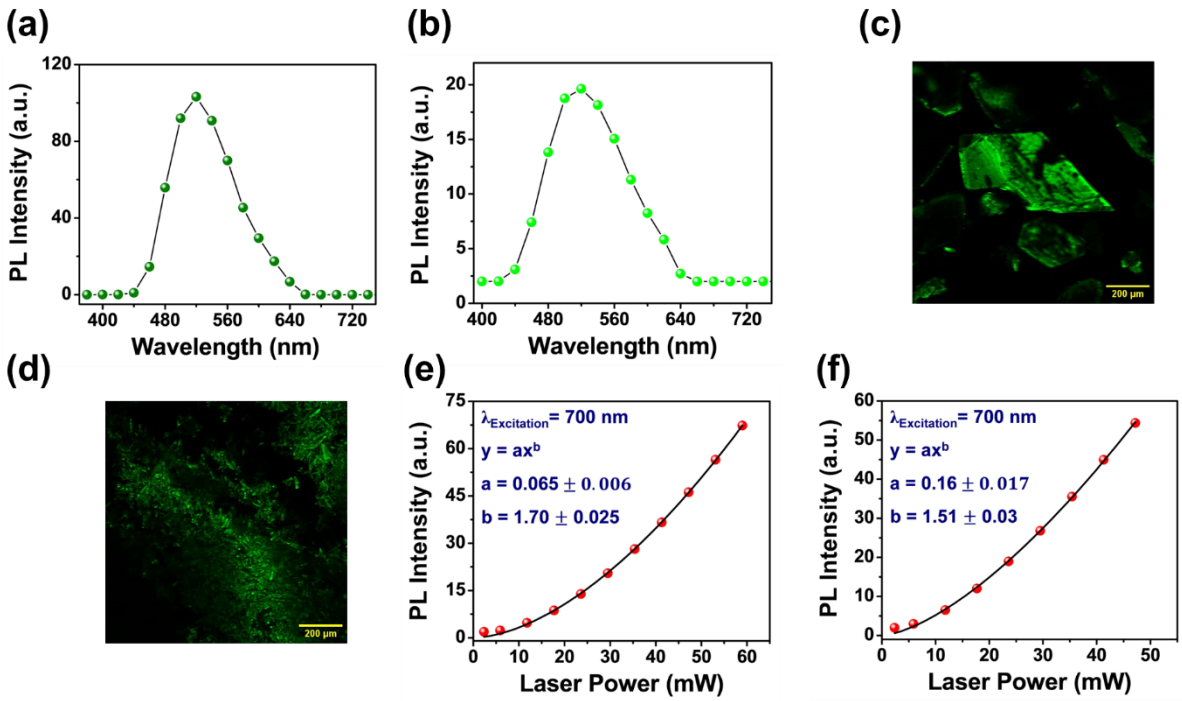

Figure 3.14. Two-photon excited PL spectra of (a) complex-1 and (b) complex-2 in their crystalline phases. Two-photon excited luminescence microscopy images of (c) complex-1 and (d) complex-2 in their crystalline phases. PL intensity vs. laser power plot for (e) complex-1, and (f) complex-2.

3.14f) for both samples were fitted by using power equation and the order was evaluated from the fitting parameters. The orders were found to be 1.70 and 1.51 for complex-1 and complex-2, respectively, which shows that the PL intensity is slightly deviated from the quadratic relationship with the input laser power (**Figures 3.14e, 3.14f**). It signifies that the anti-Stokes emission has a small contribution from the first-order emission, therefore the resultant emission is a mixture of two-photon excited luminescence and some residual first-order emission. The excitation spectra show significant absorption in the range of 700-900 nm (**Figure 3.15a, 3.15b**) for both complexes. The two-photon excited PL images are given in **Figures 3.14c** and **3.14d**, where the single crystals are visible upon excitation at 700 nm and 690 nm, for the complex-1 and complex-2 respectively. The higher two-photon excited luminescence intensity of complex-1 than complex-2 can be explained by comparing their $\chi^{(3)}$ values. In THG section we have mentioned that $\chi^{(3)}$ of complex-2 is much lower than complex-1 due to a strong three-photon luminescence response of complex-2 in same excitation range of THG. As two-photon excited luminescence is also a $\chi^{(3)}$ process, therefore two-photon excited luminescence response of complex-1 is much higher than complex-2.

3.4. Conclusion

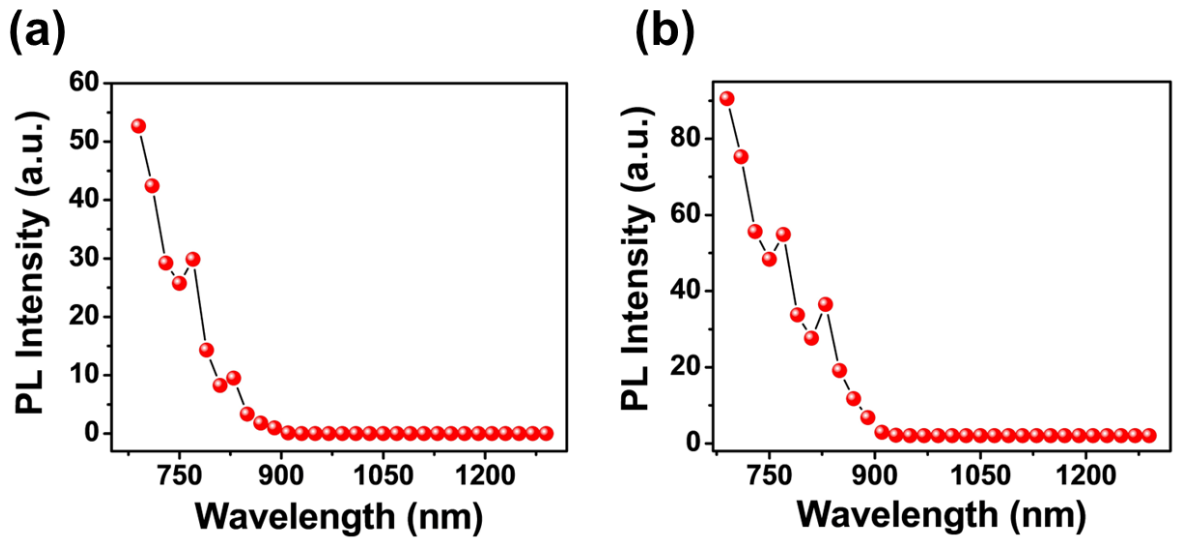

Figure 3.15. (a) Two-photon excited PL excitation spectra of (a) complex-1 and (b) complex-2. Emission window was as follows: 480 nm-540 nm for both complex-1 and complex-2. 20 nm step size was used during the measurements.

In summary, we have developed an approach where ligand engineering can modulate the triplet harvesting mechanism in iodide-bridged Cu_2I_2 complexes by keeping the emission energy almost intact. Replacement of two 3-cyanopyridine ligands in complex-1 with PPh_3 results in an enormous enhancement in the inter-ligand steric hindrance, which increases the Cu-Cu distance, thereby leading to activation of TADF in complex-2. Complex-1, having a Cu-Cu distance of 2.64 Å, undergoes excited state relaxation via ^{3}(M+X)LCT and ^{3}CC states, with an absolute QY of 66%. On the other hand, after replacing two 3-cyanopyridine ligands with PPh_3, the Cu-Cu distance increases to 3.07 Å in complex-2. This complex exhibits no sign of cluster-centered emission; rather, the thermal equilibrium between ^{1}(M+X)LCT and ^{3}(M+X)LCT states leads to radiative relaxation through the TADF process with a much higher absolute QY of 83%. Therefore, larger steric hindrance between ligands can increase the Cu-Cu distance in these complexes which results into eradication of ^{3}CC emission and improve the quantum yield of the system. Furthermore, complex-1 exhibits highly efficient third harmonic generation with a $\chi^{(3)}$ value of $1.15 \times 10^{-18}\ m^2V^{-2}$ and LIDT value of 14.73 GW/cm^2 owing to its high charge transfer nature and large number of strong non-covalent interactions in bulk phase. The producibility of the complex-2 in OLED devices was verified by fabricating emitter-doped PMMA films and the pc-LED, which emits an efficient warm white light. This work sheds light on an efficient design strategy for developing highly emissive Cu_2I_2 complexes and can pave the way towards development of efficient OLED devices and photon up-conversion systems.

3.5. Appendices

3.5.1. Appendix 1: Characterization

^{1}H NMR spectra of complex-1 at ~2 nM concentration

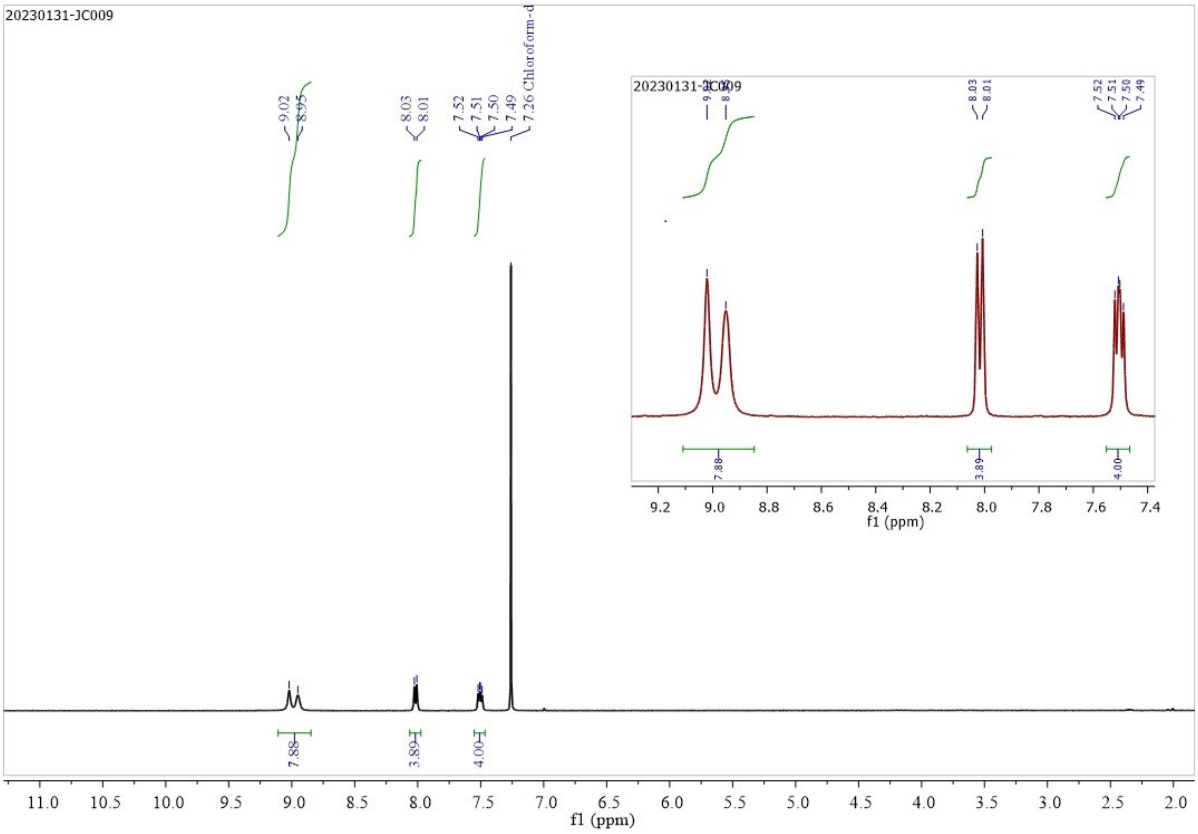

Complex-1 undergoes polymerization in solution phase at high concentration (even in the order of several µM concentration). Therefore the ^{1}H NMR spectra was collected at ~2 nM concentration, where it was confirmed that no polymerization takes place. At this reasonably lower concentration of the sample, collection of ^{13}C NMR is not feasible. Hence, we are not able to provide ^{13}C NMR spectra for complex-1.

^{1}H NMR spectrum of complex-1 upon polymerization (performed using 2 µM concentration)

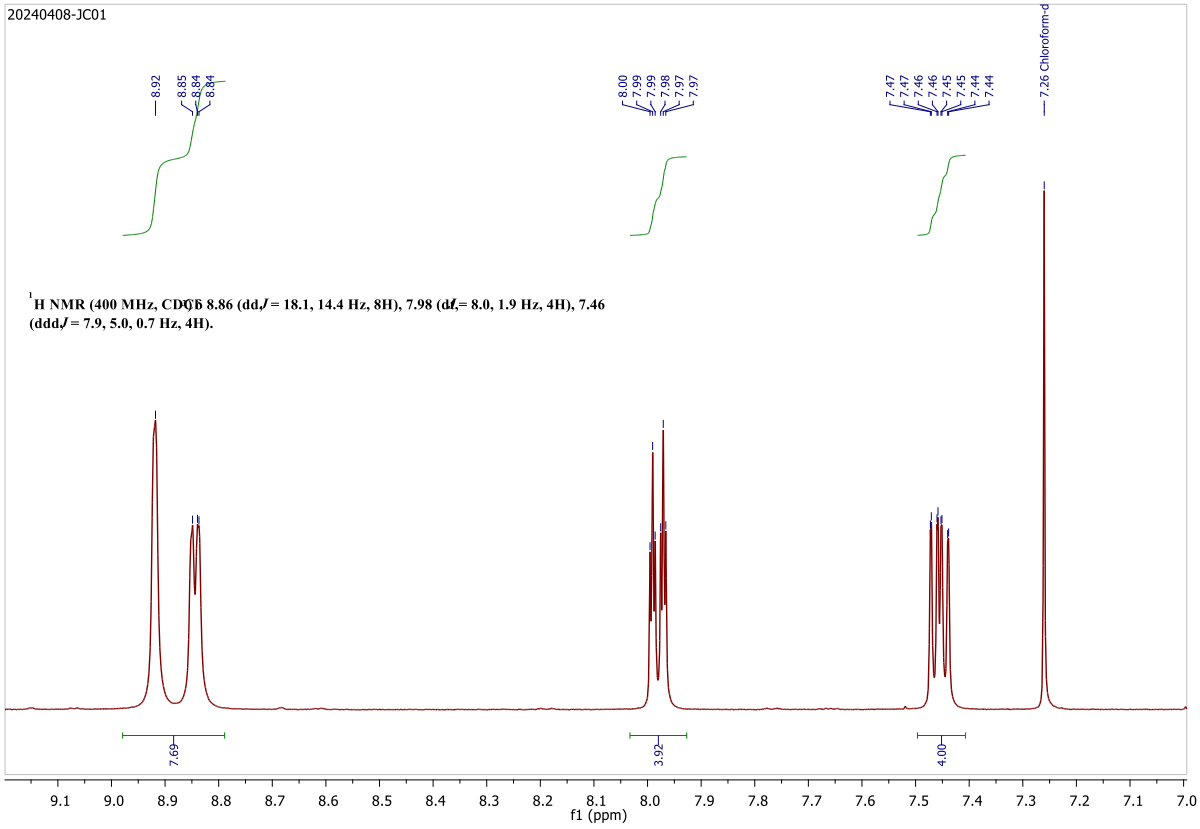

The dinuclear complex coordinated with pyridine may form copper iodide coordination polymer at higher concentrations. To prove whether there is any polymer formation even at very low concentrations, ^{1}H NMR studies were carried out. The interaction between the ligands would be different in monomeric di-nuclear complex and the coordination polymer, therefore, ^{1}H NMR is particularly useful to distinguish between two structures in solution. We compared the NMR data of two different samples- 1) the polymeric sample with high concentration (2 µM), and 2) the monomeric sample with 2 nM concentration of sample. We found a significant shift of peaks and J-values, suggesting a change in both the chemical environment and coupling patterns. Here is a summary of the results we obtained: a) For monomeric sample: ^{1}H NMR (400 MHz, $CDCl_3$) δ 8.99 (d, J = 27.7 Hz, 8H), 8.02 (d, J = 7.9 Hz, 4H), 7.50 (dd, J = 7.5, 5.2 Hz, 4H). The patterns here perfectly resemble the chemical environment and splitting pattern of the protons in the 3-cyano pyridine moiety. On the contrary, b) For polymeric sample: ^{1}H NMR (400 MHz, $CDCl_3$) δ 8.86 (dd, J = 18.1, 14.4 Hz, 8H), 7.98 (dt, J = 8.0, 1.9 Hz, 4H), 7.46 (ddd, J = 7.9, 5.0, 0.7 Hz, 4H), significantly differing from the predicted NMR pattern of monomeric species. From this study, therefore, we can confirm, that at low concentrations, we only observe the monomer, and there is no chance of polymerization.

^{1}H NMR spectra of complex-2.

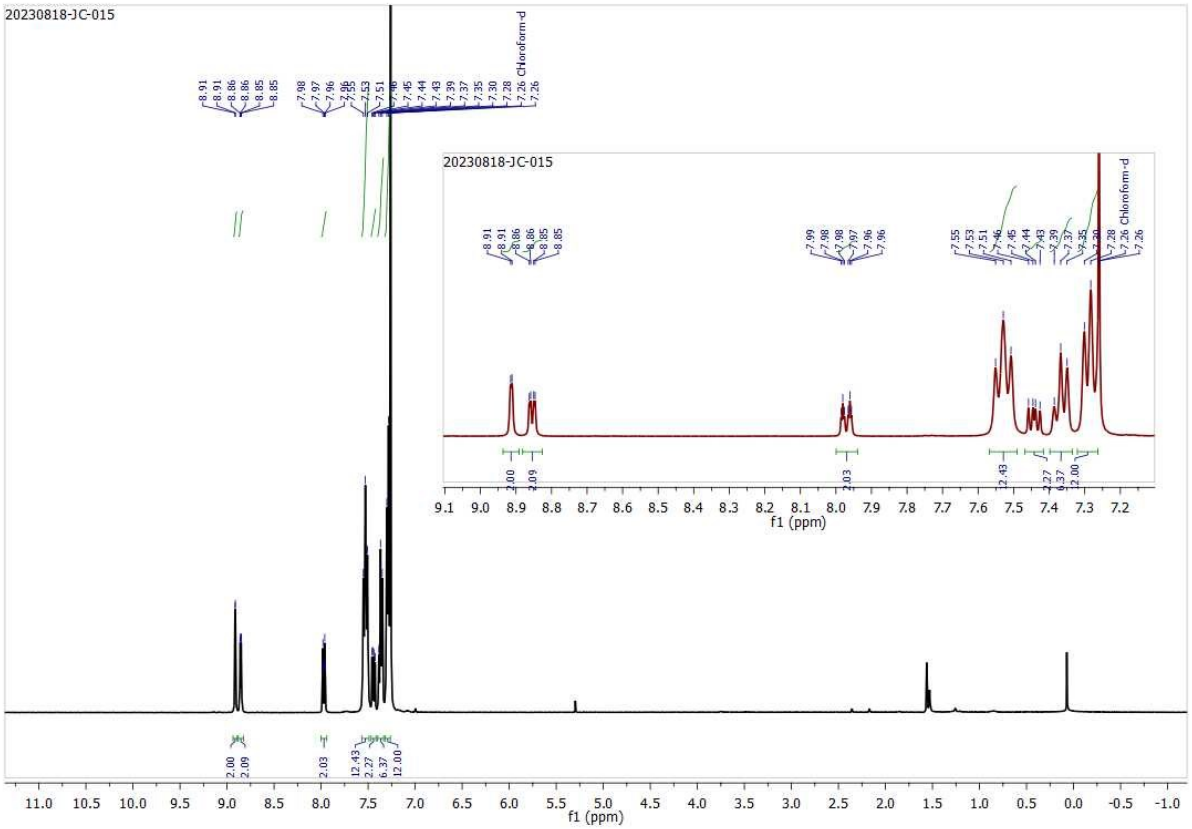

^{13}C{^{1}H} NMR spectra of complex-2.

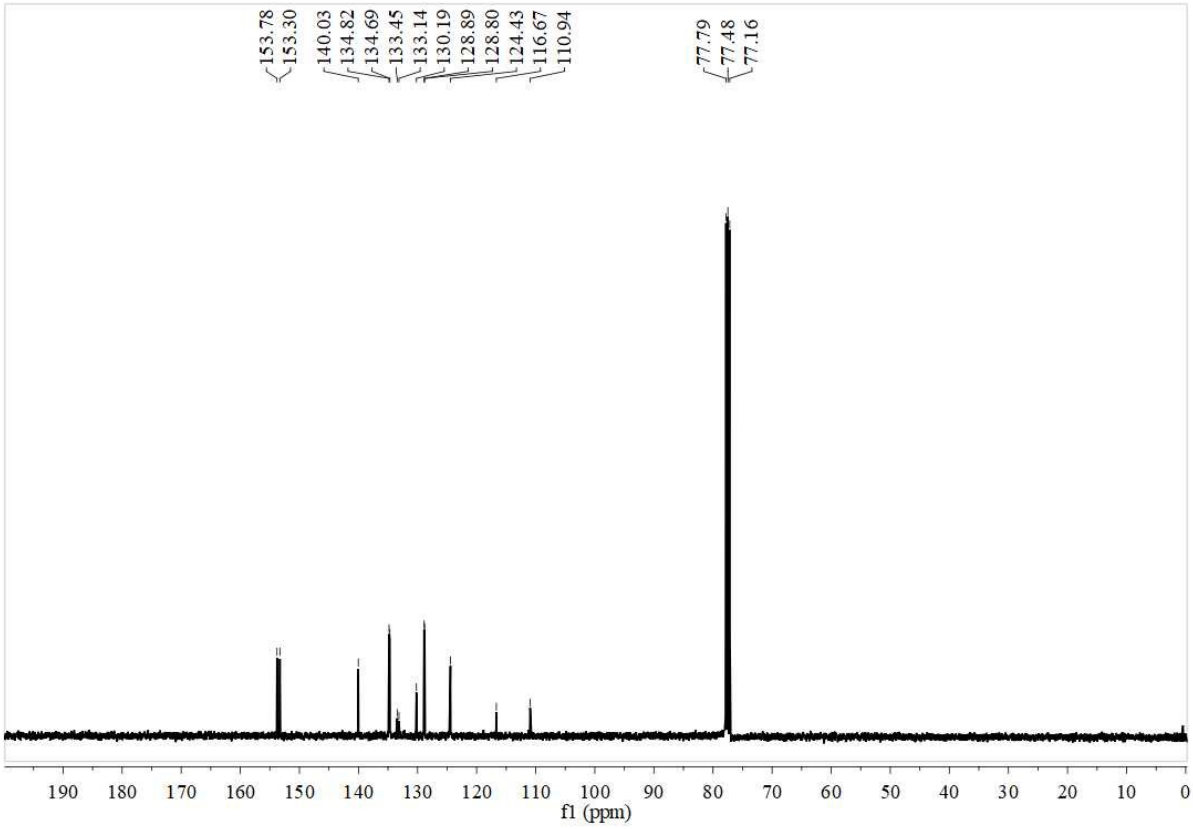

^{31}P NMR spectra of complex-2.

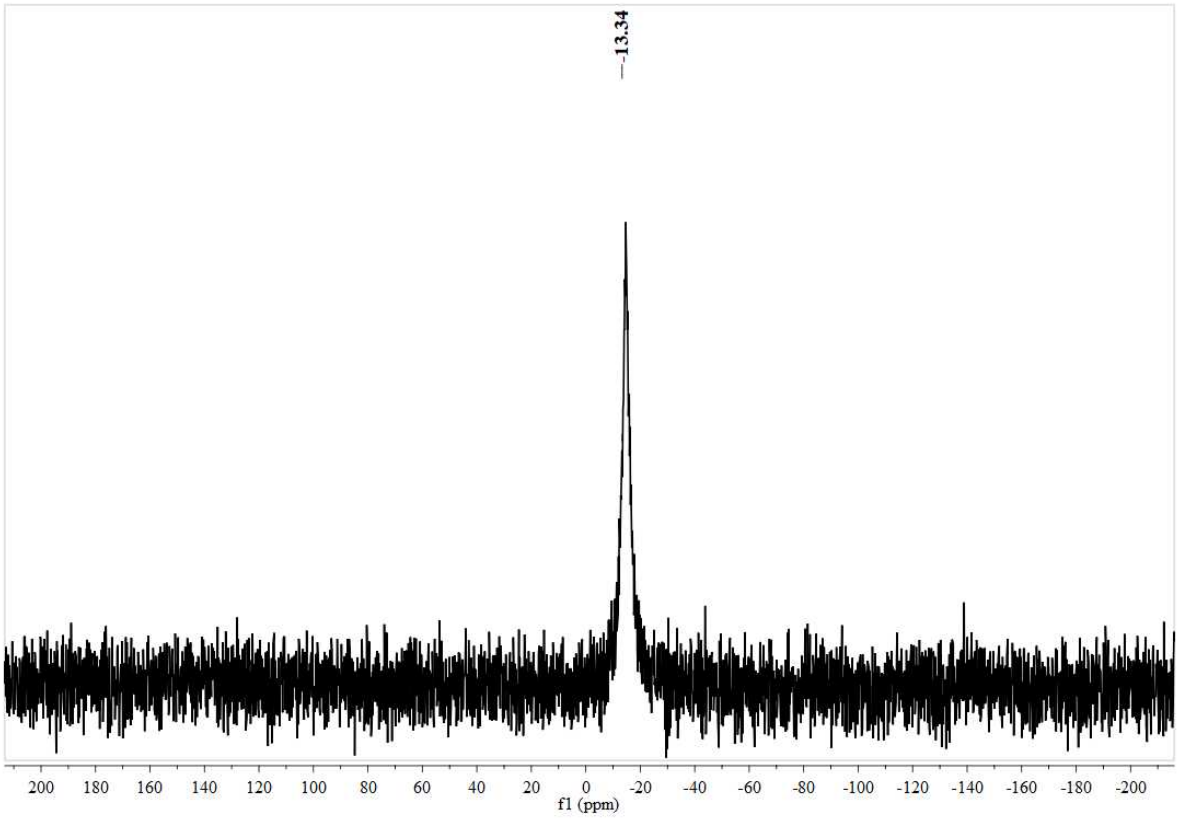

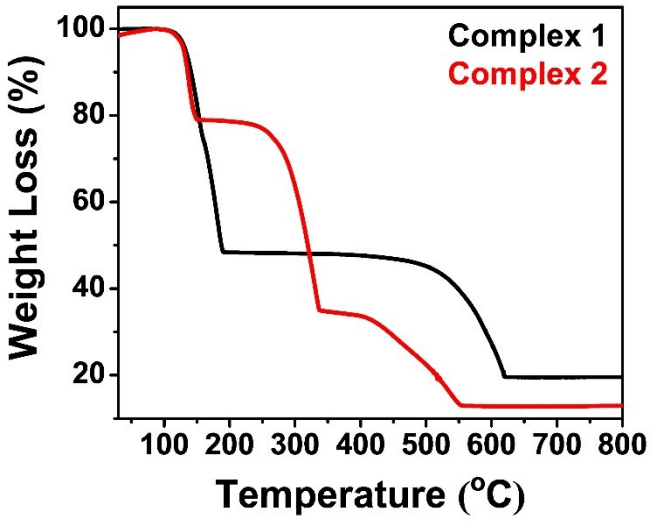

Figure A1. Thermogravimetric analysis (TGA) profile of complex-1 and complex-2.

Table A1. Crystallographic data of complex-2.

Identification code	3CPTCu2I2
CCDC	2272091
Empirical formula	$C_9H_9Cu_9I_9N_9P_9$
Formula weight	1113.66
Temperature/K	100(2)
Crystal system	monoclinic
Space group	$P2_1/n$
a/Å	8.6147(19)
b/Å	15.590(3)
c/Å	16.529(3)
α/°	90
β/°	93.103(7)
γ/°	90
Volume/Å^3	2216.7(8)
Z	2
ρ_{calc}g/cm^3	1.669
μ/mm^{-1}	2.463
F(000)	1996.0
Radiation	MoKα (λ = 0.71073)
2Θ range for data collection/°	4.936 to 56.754
Index ranges	$-11 \le h \le 11$, $-20 \le k \le 20$, $-22 \le l \le 22$
Reflections collected	71865
Independent reflections	5514 [R_{int} = 0.0920, R_{sigma} = 0.0482]
Data/restraints/parameters	5514/0/263
Goodness-of-fit on F^2	1.516
Final R indexes [I>=2σ (I)]	R_1 = 0.0511, wR_2 = 0.0448
Final R indexes [all data]	R_1 = 0.0800, wR_2 = 0.0476
Largest diff. peak/hole / e Å^{-3}	0.54/-0.56

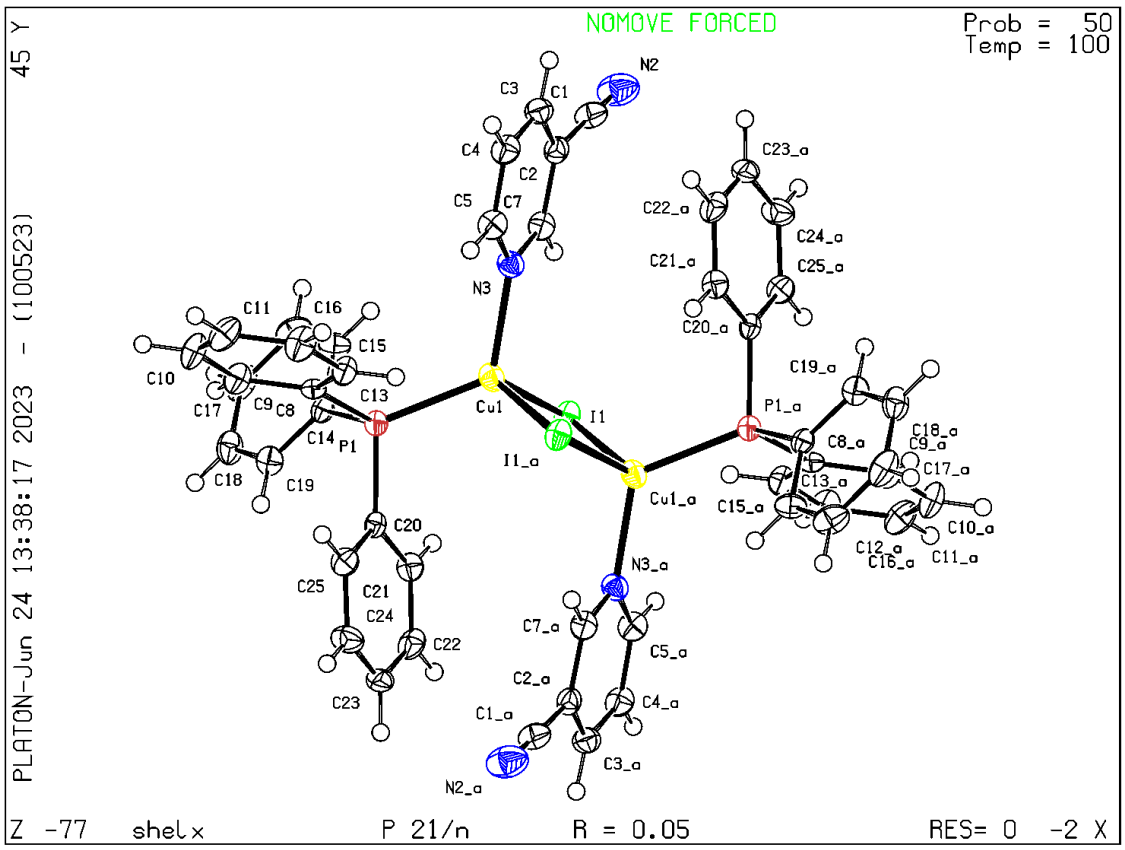

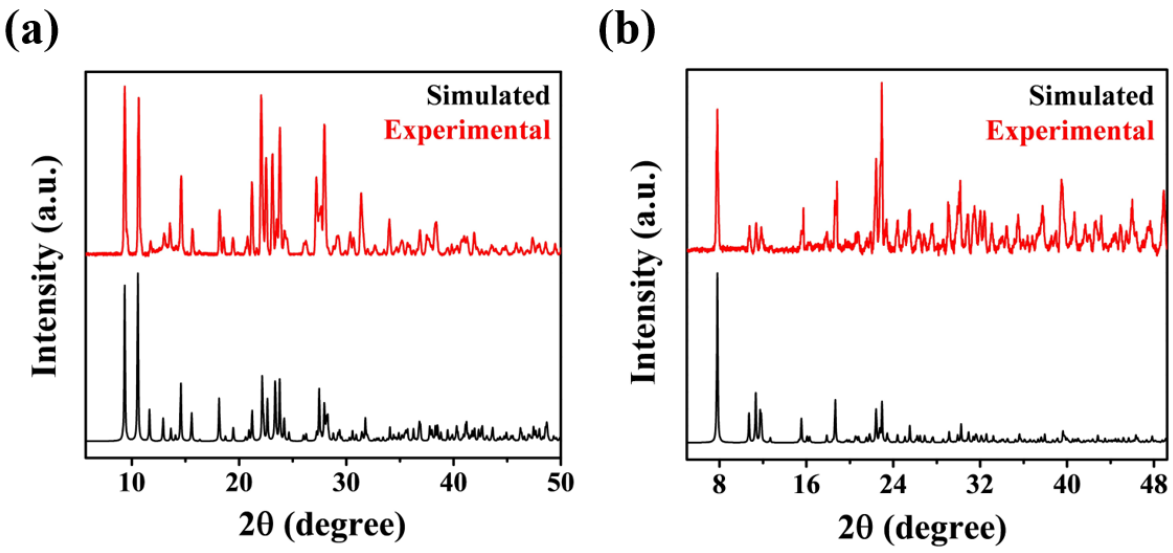

Figure A2. Powder XRD data of (a) complex-1, and (b) complex-2.

3.5.2. Appendix 2: Cartesian coordinates of the ground state optimized geometries

Complex-1

I	0.67293800	-0.84626700	-2.27502200
Cu	1.22466400	-0.35551300	0.36479600

N	1.57552200	1.69214600	0.55915300
N	1.66110800	5.33439400	-2.55975400
N	2.83559000	-1.57668400	0.79833800
N	6.60768700	-3.03731500	-1.78989800
C	1.69081700	3.62844400	1.97947900
H	1.70342900	4.03619400	2.99095300
C	1.60660000	2.24989000	1.78160100
H	1.53584900	1.55648900	2.62314000
C	4.10154800	-2.89517700	2.35941200
H	4.19325200	-3.29977600	3.36851200
C	5.83645900	-2.85049600	-0.94283200
C	1.62572300	2.48275800	-0.51607200
H	1.58446100	1.98540400	-1.48901400
C	1.73242900	4.46704000	0.86828400
H	1.77672400	5.55157200	0.98076000
C	5.06345000	-3.16279600	1.38850900
H	5.93495700	-3.78150100	1.60980800
C	1.68995200	4.68643600	-1.59720500
C	3.00582500	-2.09831700	2.02498700
H	2.22150300	-1.86906100	2.75136700
C	1.69517300	3.88193100	-0.40998000
C	4.88469000	-2.61606700	0.10492400
C	3.74960200	-1.82734100	-0.14475000
H	3.56414900	-1.39668700	-1.13198200
I	-0.67190700	-0.84686600	2.27511300
Cu	-1.22390200	-0.35684800	-0.36464600
N	-2.83382800	-1.57940700	-0.79823500
N	-6.60524500	-3.04244500	1.78962400
N	-1.57717400	1.69046800	-0.55919100
N	-1.66680900	5.33276300	2.55953600
C	-4.09867700	-2.89887300	-2.35938200

H	-4.18998100	-3.30359700	-3.36846800
C	-3.00355200	-2.10122300	-2.02487500
H	-2.21931700	-1.87142900	-2.75118100
C	-1.69491200	3.62654600	-1.97961200
H	-1.70809600	4.03422000	-2.99111000
C	-1.69495600	4.68473800	1.59701200
C	-3.74776900	-1.83065100	0.14475900
H	-3.56271700	-1.39983100	1.13199800
C	-5.06051000	-3.16710100	-1.38857900
H	-5.93156300	-3.78642100	-1.60994500
C	-1.73740900	4.46515300	-0.86846100
H	-1.78298400	5.54962700	-0.98098900
C	-5.83402600	-2.85518100	0.94264800
C	-1.60903500	2.24810100	-1.78166200
H	-1.53753600	1.55474200	-2.62317100
C	-4.88228600	-2.62017300	-0.10500400
C	-1.69934400	3.88016000	0.40983300
C	-1.62822000	2.48107900	0.51599600
H	-1.58627700	1.98382100	1.48895700

Complex-2

I	-1.72493300	0.03227900	-1.68619100
Cu	0.45304700	1.18215600	-0.39219300
P	-0.51504300	3.08701900	0.41665800
C	-1.69486100	2.74865700	1.78604600
C	-1.51054600	3.99319100	-0.83615400
C	0.61049600	4.37514100	1.10827800
C	1.66439700	0.96842800	-3.14544200
H	0.66090800	0.59382100	-3.36353700
C	2.62634900	1.11851100	-4.15744100
C	-1.34908700	2.96600100	3.12967400

H	-0.38576900	3.41427600	3.38199000
C	3.15257300	1.70119800	-1.54011700
H	3.31986900	1.89950700	-0.47915700
C	4.16475800	1.88654900	-2.48143300
H	5.14347600	2.25009500	-2.16499400
C	-2.93206400	2.14826800	1.48614800
H	-3.19795000	1.94071800	0.44735600
C	-3.81861000	1.81058400	2.50993000
H	-4.77855900	1.35063600	2.26287500
C	3.90292600	1.59704000	-3.81836900
H	4.66882200	1.72343300	-4.58553300
C	1.89557200	3.97105400	1.50525300
H	2.17954300	2.92139400	1.40309300
C	-1.10347000	3.86508400	-2.17455900
H	-0.26430700	3.20759100	-2.41436000
C	-2.62258800	4.79557800	-0.53201200
H	-2.96738300	4.88586400	0.50067000
C	-1.77737700	4.54803400	-3.18976800
H	-1.45170100	4.43899500	-4.22728900
N	2.04243400	0.45336800	-6.59644300
C	-3.47466000	2.04536000	3.84632300
H	-4.16501000	1.77224500	4.64809500
C	0.24250100	5.72388000	1.25250700
H	-0.74862800	6.06005300	0.94176700
C	-2.23505400	2.61344400	4.15345900
H	-1.95299300	2.78095000	5.19572000
C	-2.87873300	5.35276200	-2.87841700
H	-3.41347400	5.88040700	-3.67235900
C	1.14455400	6.64730000	1.78729300
H	0.84918700	7.69446900	1.89219700
C	-3.30265900	5.47122200	-1.54999800

H	-4.16836700	6.09170300	-1.30440300
C	2.30133500	0.75698200	-5.50648200
C	2.79479500	4.89514000	2.04737800
H	3.78926400	4.56500400	2.35845100
C	2.42166800	6.23517500	2.18718500
H	3.12450700	6.96010400	2.60585800
I	1.72493300	-0.03227900	1.68619100
Cu	-0.45304700	-1.18215600	0.39219300
P	0.51504300	-3.08701900	-0.41665800
C	1.69486100	-2.74865700	-1.78604600
C	1.51054600	-3.99319100	0.83615400
C	-0.61049600	-4.37514100	-1.10827800
C	-1.66439700	-0.96842800	3.14544200
H	-0.66090800	-0.59382100	3.36353700
C	-2.62634900	-1.11851100	4.15744100
C	1.34908700	-2.96600100	-3.12967400
H	0.38576900	-3.41427600	-3.38199000
C	-3.15257300	-1.70119800	1.54011700
H	-3.31986900	-1.89950700	0.47915700
C	-4.16475800	-1.88654900	2.48143300
H	-5.14347600	-2.25009500	2.16499400
C	2.93206400	-2.14826800	-1.48614800
H	3.19795000	-1.94071800	-0.44735600
C	3.81861000	-1.81058400	-2.50993000
H	4.77855900	-1.35063600	-2.26287500
C	-3.90292600	-1.59704000	3.81836900
H	-4.66882200	-1.72343300	4.58553300
C	-1.89557200	-3.97105400	-1.50525300
H	-2.17954300	-2.92139400	-1.40309300
C	1.10347000	-3.86508400	2.17455900
H	0.26430700	-3.20759100	2.41436000

C	2.62258800	-4.79557800	0.53201200
H	2.96738300	-4.88586400	-0.50067000
C	1.77737700	-4.54803400	3.18976800
H	1.45170100	-4.43899500	4.22728900
N	-2.04243400	-0.45336800	6.59644300
C	3.47466000	-2.04536000	-3.84632300
H	4.16501000	-1.77224500	-4.64809500
C	-0.24250100	-5.72388000	-1.25250700
H	0.74862800	-6.06005300	-0.94176700
C	2.23505400	-2.61344400	-4.15345900
H	1.95299300	-2.78095000	-5.19572000
C	2.87873300	-5.35276200	2.87841700
H	3.41347400	-5.88040700	3.67235900
C	-1.14455400	-6.64730000	-1.78729300
H	-0.84918700	-7.69446900	-1.89219700
C	3.30265900	-5.47122200	1.54999800
H	4.16836700	-6.09170300	1.30440300
C	-2.30133500	-0.75698200	5.50648200
C	-2.79479500	-4.89514000	-2.04737800
H	-3.78926400	-4.56500400	-2.35845100
C	-2.42166800	-6.23517500	-2.18718500
H	-3.12450700	-6.96010400	-2.60585800
N	-1.92539100	-1.26425200	1.86946000
N	1.92539100	1.26425200	-1.86946000

3.5.3. Appendix 3: Figures

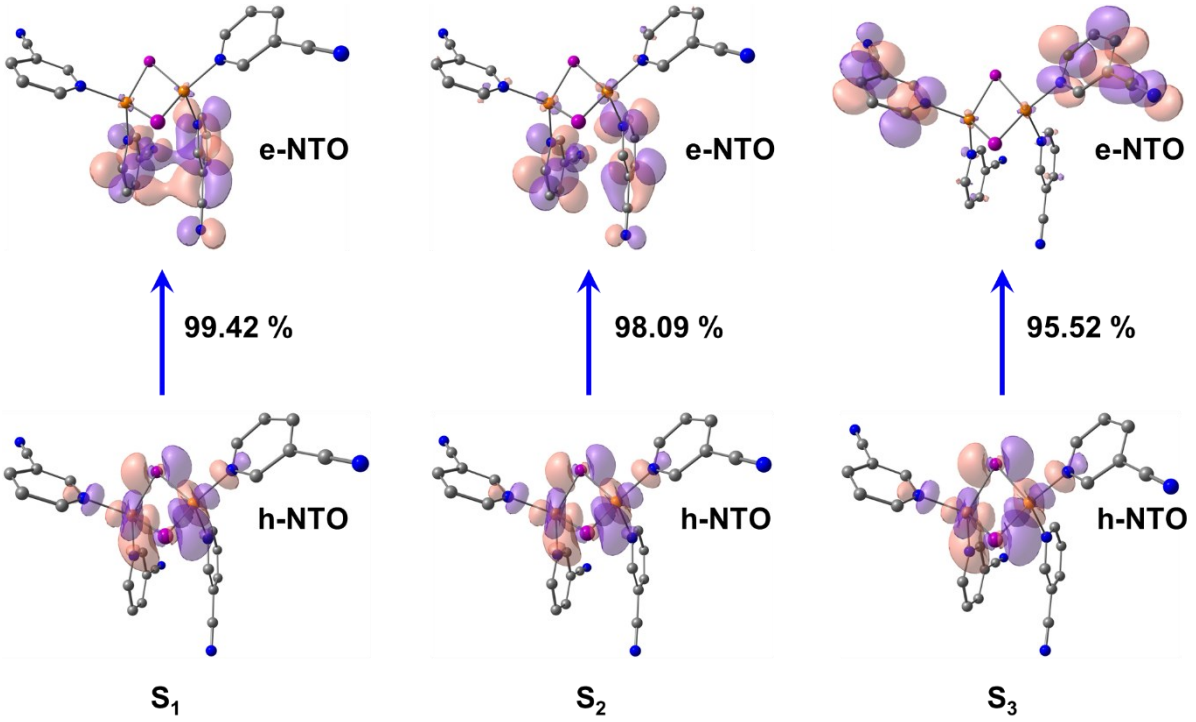

Figure A3. NTO images of S_1, S_2, and S_3.

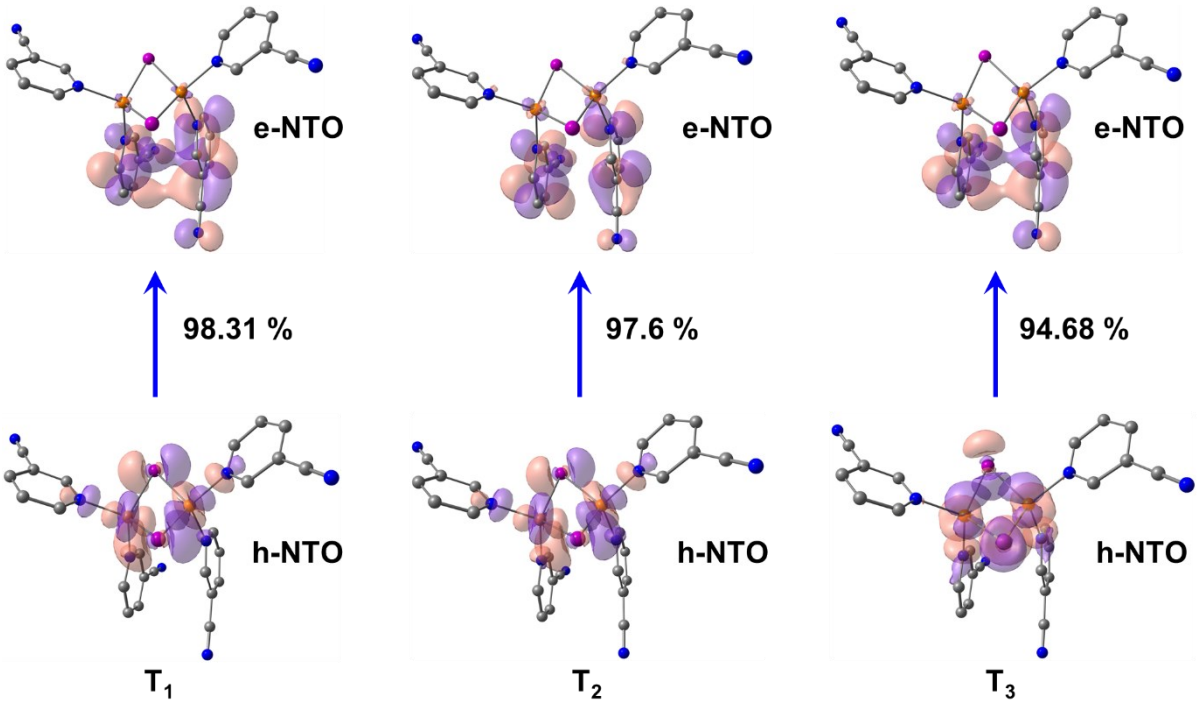

Figure A4. NTO images of T_1, T_2, and T_3.

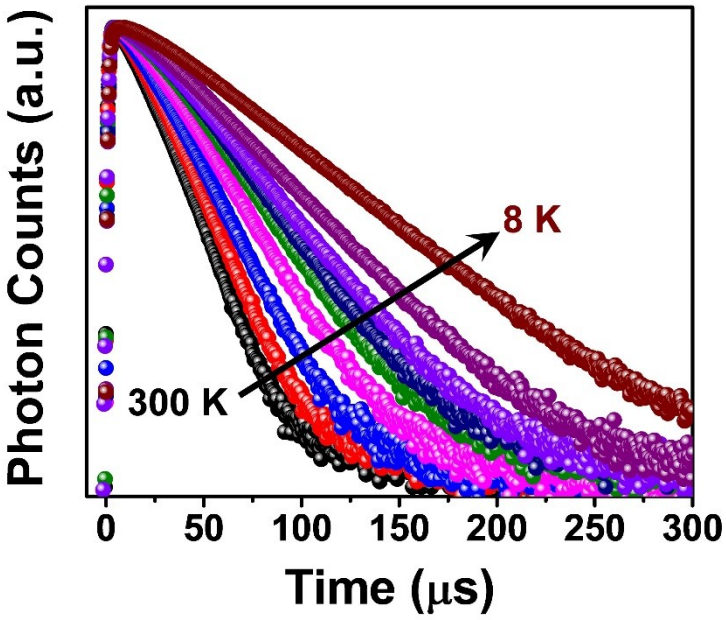

Figure A5. Temperature-dependent PL decay profile of complex-1.

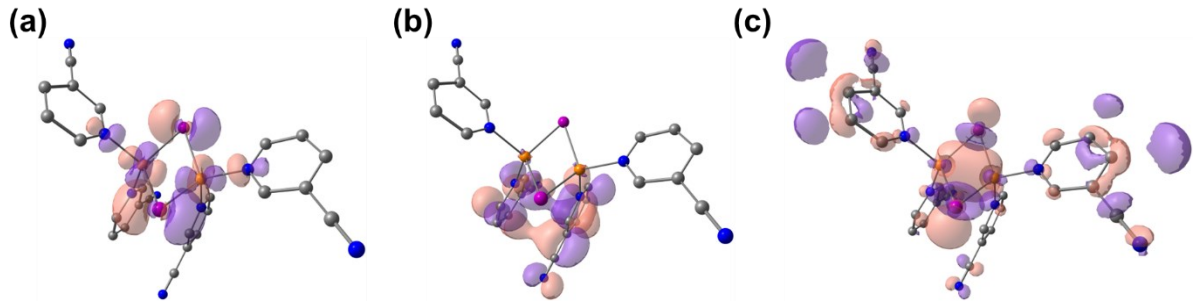

Figure A6. (a) HOMO, (b) LUMO, and (c) LUMO+19 of complex-1.

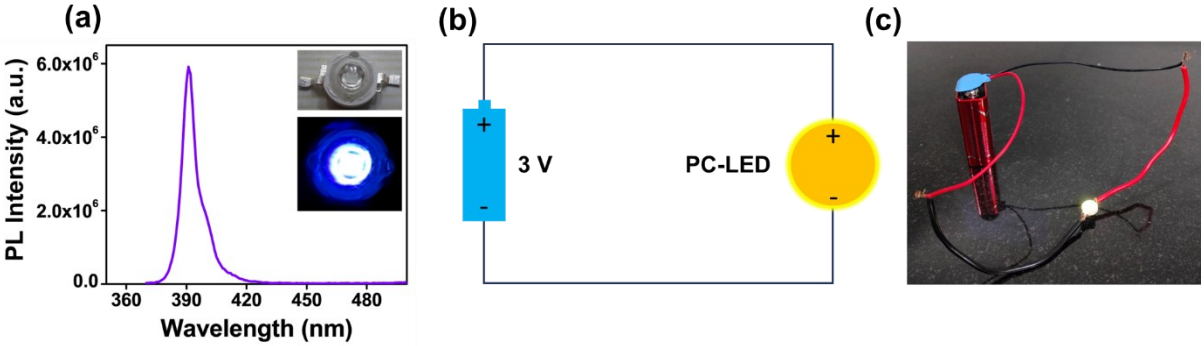

Figure A7. (a) Emission spectra of InGaN chip under 3 V, (b) Circuit diagram of pc-LED set-up, and (c) Image of the pc-LED set-up.

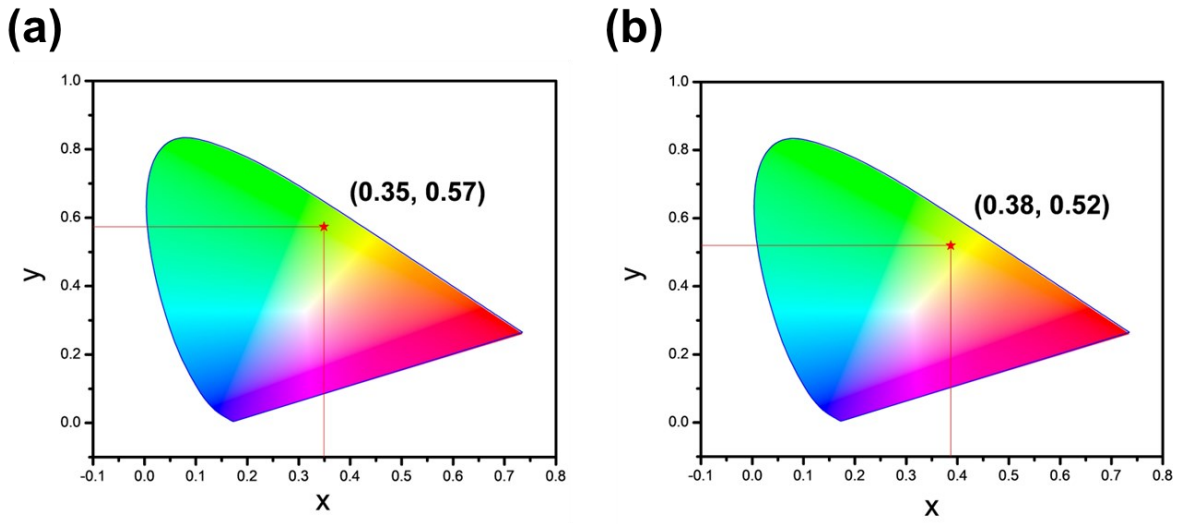

Figure A8. CIE coordinate of (a) complex-1, and (b) complex-2.

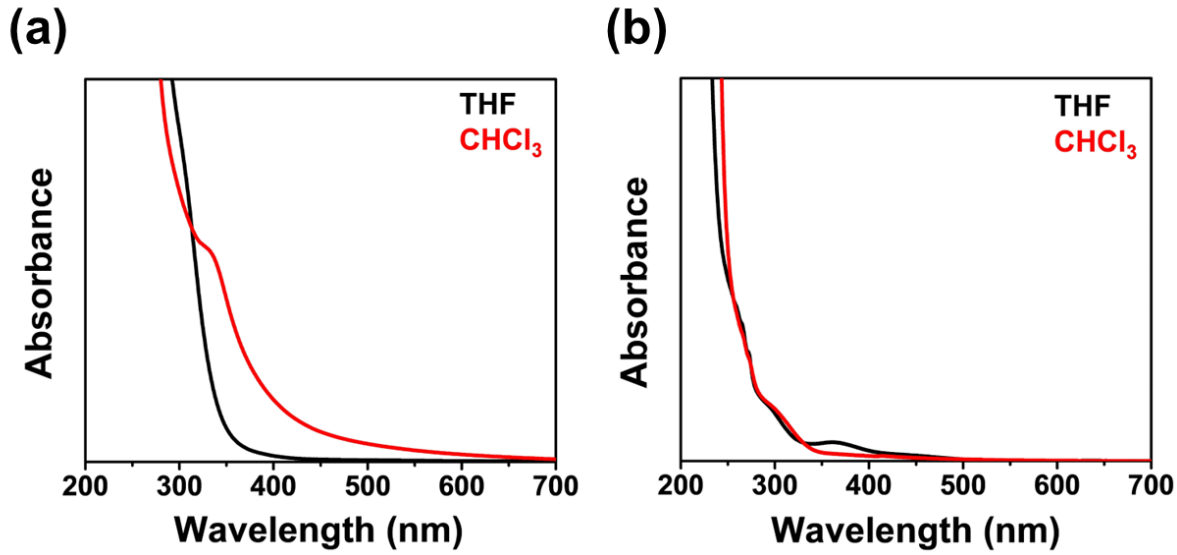

Figure A9. Absorption spectra of (a) complex-1, and (b) complex-2 in THF and $CHCl_3$.

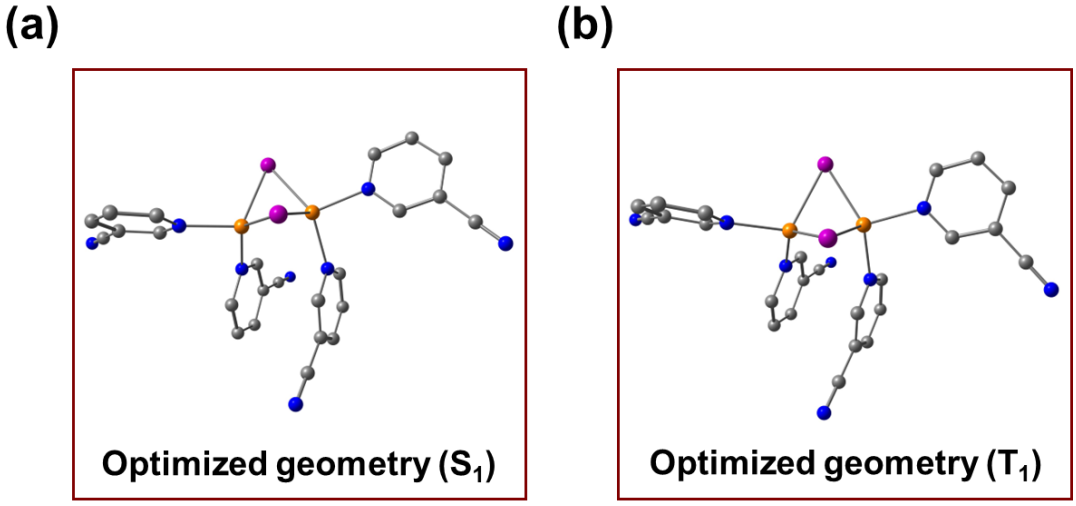

Figure A10. (a) Optimized geometry of S_1 states in complex-1, (a) Optimized geometry of T_1 state in complex-1.

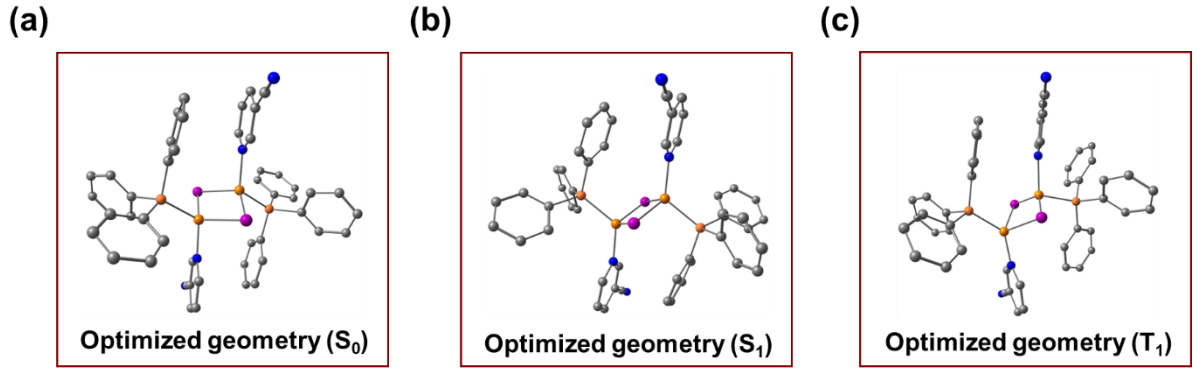

Figure A11. (a) Ground state optimized geometry of complex-2, (b) Optimized geometry of S_1 state in complex-2, (c) Optimized geometry of T_1 state in complex-2.

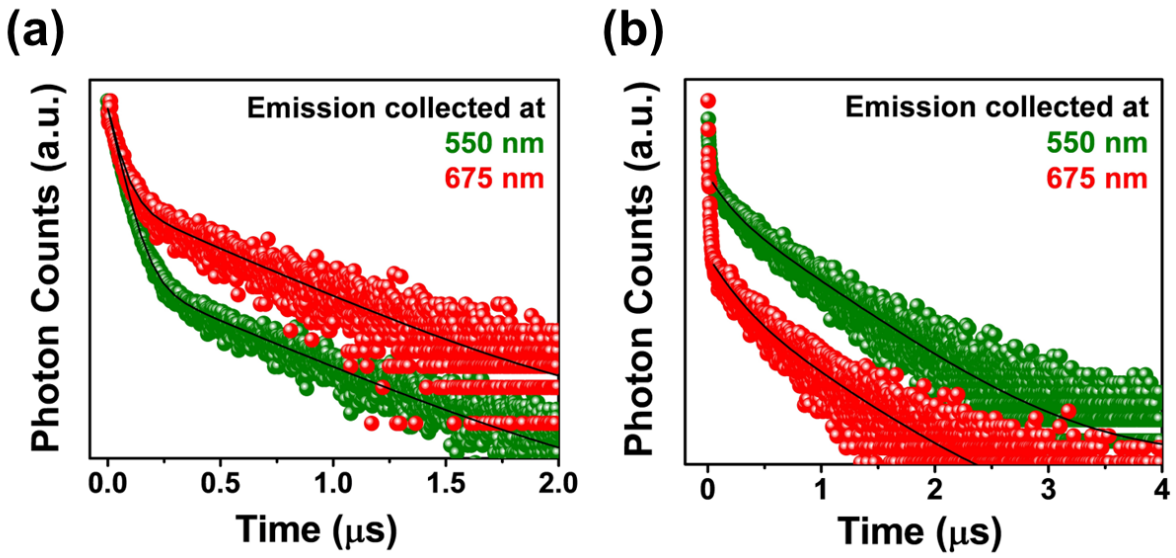

Figure A12. PL decay profile of complex-1 (a) in chloroform, and (b) in THF.

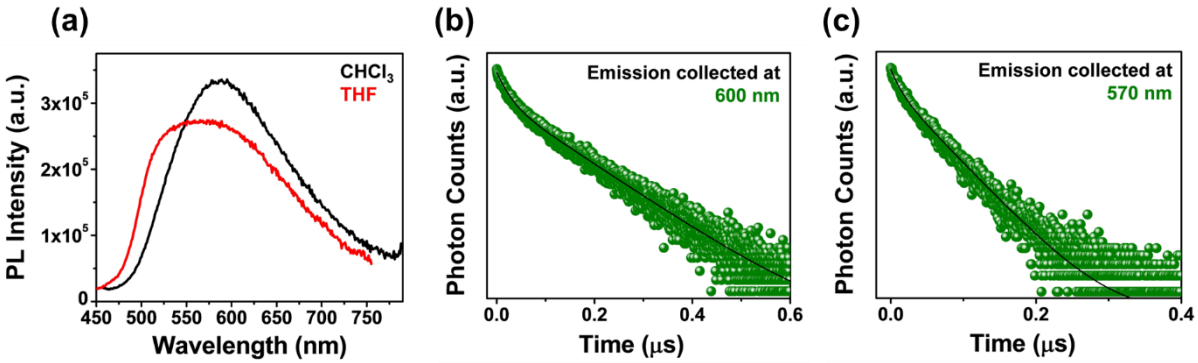

Figure A13. (a) Emission spectra of complex-2 in chloroform and THF. PL decay profile of complex-2 (b) in chloroform and (c) in THF.

3.5.4. Appendix 4: Tables

Table A2. Spin-orbit coupling matrix element (SOCME) values of complex-1 and complex-2 for S_0-T_n (n=1-5) and S_1-T_n (n=1-5).

Singlet-triplet pairs	Complex-1 (cm^{-1})	Complex-2 (cm^{-1})
S_0-T_1	91.34439	0.00143
S_0-T_2	8.57142	25.4254
S_0-T_3	12.6917	29.54617
S_0-T_4	114.6187	0.0001
S_0-T_5	80.37374	0.00394
S_1-T_1	25.52247	0.00021
S_1-T_2	4.43378	7.16585
S_1-T_3	17.92178	14.1312
S_1-T_4	129.6307	0.00023
S_1-T_5	3.38355	0.00276

Table A3. PL decay profiles of complex-1 and complex-2 in solid state.

Sample	Wavelength	α_1	τ_1	α_2	τ_2
Complex-1	535 nm	32.9%	2.27 μs	67%	6.43 μs
Complex-2	538 nm	40.0%	2.63 μs	60.0 %	6.98 μs

Table A4: Lifetime of complex-1 at different temperatures.

Temperature (K)	Lifetime (µs)
300	6.43
250	14.93
200	16.89
150	20.02
100	23.24
50	24.25
25	25.26
15	28.57
8	37.56

Table A5: Lifetime of complex-2 at different temperatures.

Temperature (K)	Lifetime (µs)
300	6.98
250	15.44
200	29.07
150	61.77
100	86.69
50	93.97
25	103.70
15	110.17
8	109.81

Table A6. Percentage of the TADF and phosphorescence in complex-2 at different temperatures.

Temperature (K)	TADF (%)	Phosphorescence (%)
300	90.5	9.5
250	84.19	15.81
200	68.62	31.38
150	33.2	66.8
100	2.5	97.5
50	0.01	99.99

Table A7. PL decay profiles of 20% (w/w) complex-2-doped PMMA film.

Sample	Wavelength	α_1	τ_1	α_2	τ_2
20% (w/w) complex-2-doped PMMA film	560 nm	51.8 %	0.6 µs	48.2%	2.8 µs

Table A8. PL decay profiles of complex-1 in solution.

Sample	Wavelength	α_1	τ_1	α_2	τ_2
Complex-1 in $CHCl_3$	550 nm	98%	51.6 ns	2%	0.54 µs
Complex-1 in $CHCl_3$	675 nm	87%	47 ns	13%	0.52 µs
Complex-1 in THF	550 nm	42.5%	0.15 µs	57.5%	0.66 µs
Complex-1 in THF	675 nm	51.6%	0.19 µs	48.4%	0.67 µs

Table A9. PL decay profiles of complex-2 in solution.

Sample	Wavelength	α_1	τ_1	α_2	τ_2
Complex-2 in $CHCl_3$	600 nm	55%	21.5 ns	44%	0.12 µs
Complex-2 in THF	570 nm	33%	11.3 ns	66%	52.2 ns

Bibliography

1 A. S. Romanov, S. T. E. Jones, Q. Gu, P. J. Conaghan, B. H. Drummond, J. Feng, F. Chotard, L. Buizza, M. Foley, M. Linnolahti, D. Credgington and M. Bochmann, *Chem. Sci.*, 2020, **11**, 435–446.

2 Y. Zhang, M. Schulz, M. Wächtler, M. Karnahl and B. Dietzek, *Coord. Chem. Rev.*, 2018, **356**, 127–146.

3 A. M. T. Muthig, O. Mrózek, T. Ferschke, M. Rödel, B. Ewald, J. Kuhnt, C. Lenczyk, J. Pflaum and A. Steffen, *J. Am. Chem. Soc.*, 2023, **145**, 4438–4449.

4 R. Tang, S. Xu, T.-L. Lam, G. Cheng, L. Du, Q. Wan, J. Yang, F.-F. Hung, K.-H. Low, D. L. Phillips and C.-M. Che, *Angew. Chemie Int. Ed.*, 2022, **61**, e202203982.

5 N. V Tzouras, E. A. Martynova, X. Ma, T. Scattolin, B. Hupp, H. Busen, M. Saab, Z. Zhang, L. Falivene, G. Pisanò, K. Van Hecke, L. Cavallo, C. S. J. Cazin, A. Steffen and S. P. Nolan, *Chem. – A Eur. J.*, 2021, **27**, 11904–11911.

6 D. Volz, Y. Chen, M. Wallesch, R. Liu, C. Fléchon, D. M. Zink, J. Friedrichs, H. Flügge, R. Steininger, J. Göttlicher, C. Heske, L. Weinhardt, S. Bräse, F. So and T. Baumann, *Adv. Mater.*, 2015, **27**, 2538–2543.

7 R. Hamze, J. L. Peltier, D. Sylvinson, M. Jung, J. Cardenas, R. Haiges, M. Soleilhavoup, R. Jazzar, P. I. Djurovich, G. Bertrand and M. E. Thompson, *Science (80-.).*, 2019, **363**, 601–606.

8 J. E. Barnsley, S. Ø. Scottwell, A. B. S. Elliott, K. C. Gordon and J. D. Crowley, *Inorg. Chem.*, 2016, **55**, 8184–8192.

9 C. Dutta, S. Maniappan and J. Kumar, *Chem. Sci.*, 2023, **14**, 5593–5601.

10 S. Wang, E. E. Morgan, S. Panuganti, L. Mao, P. Vishnoi, G. Wu, Q. Liu, M. G. Kanatzidis, R. D. Schaller and R. Seshadri, *Chem. Mater.*, 2022, **34**, 3206–3216.

11 S. Perruchas, C. Tard, X. F. Le Goff, A. Fargues, A. Garcia, S. Kahlal, J.-Y. Saillard, T. Gacoin and J.-P. Boilot, *Inorg. Chem.*, 2011, **50**, 10682–10692.

12 J.-J. Wang, C. Chen, W.-G. Chen, J.-S. Yao, J.-N. Yang, K.-H. Wang, Y.-C. Yin, M.-M. Yao, L.-Z. Feng, C. Ma, F.-J. Fan and H.-B. Yao, *J. Am. Chem. Soc.*, 2020, **142**, 3686–3690.

13 J. Troyano, F. Zamora and S. Delgado, *Chem. Soc. Rev.*, 2021, **50**, 4606–4628.

14 J.-J. Wang, H.-T. Zhou, J.-N. Yang, L.-Z. Feng, J.-S. Yao, K.-H. Song, M.-M. Zhou, S. Jin, G. Zhang and H.-B. Yao, *J. Am. Chem. Soc.*, 2021, **143**, 10860–10864.

15 B. Huitorel, H. El Moll, R. Utrera-Melero, M. Cordier, A. Fargues, A. Garcia, F. Massuyeau, C. Martineau-Corcos, F. Fayon, A. Rakhmatullin, S. Kahlal, J.-Y. Saillard, T. Gacoin and S. Perruchas, *Inorg. Chem.*, 2018, **57**, 4328–4339.

16 C. Wegeberg and O. S. Wenger, *JACS Au*, 2021, **1**, 1860–1876.

17 M. Xie, C. Han, Q. Liang, J. Zhang, G. Xie and H. Xu, *Sci. Adv.*, 2023, **5**, eaav9857.

18 A. Kobayashi, Y. Yoshida, M. Yoshida and M. Kato, *Chem. – A Eur. J.*, 2018, **24**, 14750–14759.

19 M. Klein, N. Rau, M. Wende, J. Sundermeyer, G. Cheng, C.-M. Che, A. Schinabeck and H. Yersin, *Chem. Mater.*, 2020, **32**, 10365–10382.

20 M. Xie, C. Han, J. Zhang, G. Xie and H. Xu, *Chem. Mater.*, 2017, **29**, 6606–6610.

21 C. Chen, R.-H. Li, B.-S. Zhu, K.-H. Wang, J.-S. Yao, Y.-C. Yin, M.-M. Yao, H.-B. Yao and S.-H. Yu, *Angew. Chemie Int. Ed.*, 2018, **57**, 7106–7110.

22 X.-C. Shan, F.-L. Jiang, L. Chen, M.-Y. Wu, J. Pan, X.-Y. Wan and M.-C. Hong, *J. Mater. Chem. C*, 2013, **1**, 4339–4349.

23 S. Perruchas, X. F. Le Goff, S. Maron, I. Maurin, F. Guillen, A. Garcia, T. Gacoin and J.-P. Boilot, *J. Am. Chem. Soc.*, 2010, **132**, 10967–10969.

24 K. R. Kyle, C. K. Ryu, P. C. Ford and J. A. DiBenedetto, *J. Am. Chem. Soc.*, 1991, **113**, 2954–2965.

25 M. Vitale, W. E. Palke and P. C. Ford, *J. Phys. Chem.*, 1992, **96**, 8329–8336.

26 Q. Benito, I. Maurin, T. Cheisson, G. Nocton, A. Fargues, A. Garcia, C. Martineau, T. Gacoin, J.-P. Boilot and S. Perruchas, *Chem. – A Eur. J.*, 2015, **21**, 5892–5897.

27 Q. Benito, X. F. Le Goff, S. Maron, A. Fargues, A. Garcia, C. Martineau, F. Taulelle, S. Kahlal, T. Gacoin, J.-P. Boilot and S. Perruchas, *J. Am. Chem. Soc.*, 2014, **136**, 11311–11320.

28 D. Tran, J. L. Bourassa and P. C. Ford, *Inorg. Chem.*, 1997, **36**, 439–442.

29 W.-T. Chen, L. Chen, Z.-Y. Liang, Z.-W. Mo, J.-W. Ye and X.-M. Chen, *Adv. Opt. Mater.*, 2023, **11**, 2202771.

30 A. Schinabeck, M. J. Leitl and H. Yersin, *J. Phys. Chem. Lett.*, 2018, **9**, 2848–2856.

31 H. Yersin, R. Czerwieniec, M. Z. Shafikov and A. F. Suleymanova, *ChemPhysChem*, 2017, **18**, 3508–3535.

32 H. Uoyama, K. Goushi, K. Shizu, H. Nomura and C. Adachi, *Nature*, 2012, **492**, 234–238.

33 D. M. Zink, D. Volz, T. Baumann, M. Mydlak, H. Flügge, J. Friedrichs, M. Nieger and S. Bräse, *Chem. Mater.*, 2013, **25**, 4471–4486.

34 M. J. Leitl, F.-R. Küchle, H. A. Mayer, L. Wesemann and H. Yersin, *J. Phys. Chem. A*, 2013, **117**, 11823–11836.

35 C. Sandoval-Pauker, M. Santander-Nelli and P. Dreyse, *RSC Adv.*, 2022, **12**, 10653–10674.

36 S. Wang, E. E. Morgan, P. Vishnoi, L. Mao, S. M. L. Teicher, G. Wu, Q. Liu, A. K. Cheetham and R. Seshadri, *Inorg. Chem.*, 2020, **59**, 15487–15494.

37 E. Cariati, D. Roberto, R. Ugo, P. C. Ford, S. Galli and A. Sironi, *Inorg. Chem.*, 2005, **44**, 4077–4085.

38 E. Cariati, M. Pizzotti, D. Roberto, F. Tessore and R. Ugo, *Coord. Chem. Rev.*, 2006, **250**, 1210–1233.

39 M. Uji, T. J. B. Zähringer, C. Kerzig and N. Yanai, *Angew. Chemie Int. Ed.*, 2023, **62**, e202301506.

40 M. Yu, X. Zhu, J. Zeng, H. Liu, R. Huang, Z. Zhuang, P. Shen, Z. Zhao and B. Z. Tang, *J. Mater. Chem. C*, 2021, **9**, 14808–14814.

41 G. Li, Y. Chen, H. Jiang and X. Chen, *Opt. Lett.*, 2017, **42**, 939–942.

42 M. Braune, M. Maiwald, B. Eppich, O. Brox, A. Ginolas, B. Sumpf and G. Tränkle, *IEEE Trans. Components, Packag. Manuf. Technol.*, 2017, **7**, 720–725.

43 G. M. Sheldrick, *Acta Crystallogr. Sect. A*, 2008, **64**, 112–122.

44 G. M. Sheldrick, *Acta Crystallogr. Sect. C Struct. Chem.*, 2015, **71**, 3–8.

45 M. D. Kessler, T. Duston, M. Parker and R. D. Pike, *Inorganica Chim. Acta*, 2020, **509**, 119706.

46 S. Miertuš, E. Scrocco and J. Tomasi, *Chem. Phys.*, 1981, **55**, 117–129.

47 J. Tomasi, B. Mennucci and R. Cammi, *Chem. Rev.*, 2005, **105**, 2999–3094.

48 M. J. Frisch, *http//www. gaussian. com/*.

49 E. D. Glendening, C. R. Landis and F. Weinhold, *J. Comput. Chem.*, 2019, **40**, 2234–2241.

50 S. V. K. Isukapalli, R. S. Lekshmi, P. K. Samanta and S. R. Vennapusa, *J. Chem. Phys.*, 2020, **153**, 124301.

51 X. Gao, S. Bai, D. Fazzi, T. Niehaus, M. Barbatti and W. Thiel, *J. Chem. Theory Comput.*, 2017, **13**, 515–524.

52 Y. Xie, F. Liang, B. Zhang, B. Ge, H. Yu, Z. Lin, Z. Wang, H. Zhang, B. Huang and J. Wang, *ACS Omega*, 2019, **4**, 1045–1052.

53 S. Maqbool, T. Sheikh, Z. Thekkayil, S. Deswal, R. Boomishankar, A. Nag and P. Mandal, *J. Phys. Chem. C*, 2021, **125**, 22674–22683.

54 S. Maqbool, Z. Thekkayil and P. Mandal, *Adv. Opt. Mater.*, 2023, **n/a**, 2202942.

55 R. C. Eckardt, H. Masuda, Y. X. Fan and R. L. Byer, *IEEE J. Quantum Electron.*, 1990, **26**, 922–933.

56 A. S. Haynes, A. Banerjee, F. O. Saouma, C. O. Otieno, J. I. Jang and M. G. Kanatzidis, *Chem. Mater.*, 2016, **28**, 2374–2383.

57 T. Fehn, T. Vogtmann, J. Hübner and M. Schwoerer, *Appl. Phys. B*, 1994, **59**, 203–209.

58 C. Yuan, X. Li, S. Semin, Y. Feng, T. Rasing and J. Xu, *Nano Lett.*, 2018, **18**, 5411–5417.

59 K. Wendler, J. Thar, S. Zahn and B. Kirchner, *J. Phys. Chem. A*, 2010, **114**, 9529–9536.

60 A. Chatterjee, J. Chatterjee, S. Sappati, T. Sheikh, R. M. Umesh, M. D. Ambhore, M. Lahiri and P. Hazra, *J. Phys. Chem. B*, 2021, **125**, 12832–12846.

61 D. A. Smith, L. Brammer, C. A. Hunter and R. N. Perutz, *J. Am. Chem. Soc.*, 2014, **136**, 1288–1291.

62 T. Viswanathan and N. Palanisami, *New J. Chem.*, 2021, **45**, 12509–12518.

63 C. L. Shiny, A. Rathika, J. D. D. Tarika, S. Alen and T. J. Beaula, *Polycycl. Aromat. Compd.*, 2023, **43**, 4621–4639.

64 S. Kumar, L. G. Franca, K. Stavrou, E. Crovini, D. B. Cordes, A. M. Z. Slawin, A. P. Monkman and E. Zysman-Colman, *J. Phys. Chem. Lett.*, 2021, **12**, 2820–2830.

65 R. T. Ayinla, M. Shiri, B. Song, M. Gangishetty and K. Wang, *Mater. Chem. Front.*, 2023, **7**, 3524–3542.

66 H. Kitagawa, Y. Ozawa and K. Toriumi, *Chem. Commun.*, 2010, **46**, 6302–6304.

67 F. De Angelis, S. Fantacci, A. Sgamellotti, E. Cariati, R. Ugo and P. C. Ford, *Inorg. Chem.*, 2006, **45**, 10576–10584.

68 H. Yersin, A. F. Rausch, R. Czerwieniec, T. Hofbeck and T. Fischer, *Coord. Chem. Rev.*, 2011, **255**, 2622–2652.

69 L. Bergmann, G. J. Hedley, T. Baumann, S. Bräse and I. D. W. Samuel, *Sci. Adv.*, 2024, **2**, e1500889.

70 G. Farias, C. A. M. Salla, J. Toigo, L. G. T. A. Duarte, A. J. Bortoluzzi, E. Girotto, H. Gallardo, T. D. Z. Atvars, B. de Souza and I. H. Bechtold, *Dalt. Trans.*, 2022, **51**, 1008–1018.

71 X. Yan, H. Peng, Y. Xiang, J. Wang, L. Yu, Y. Tao, H. Li, W. Huang and R. Chen, *Small*, 2022, **18**, 2104073.

72 A. Chatterjee, J. Chatterjee, S. Sappati, R. Tanwar, M. D. Ambhore, H. Arfin, R. M. Umesh, M. Lahiri, P. Mandal and P. Hazra, *Chem. Sci.*, , DOI:10.1039/D3SC04280D.

73 K.-H. Song, J.-J. Wang, L.-Z. Feng, F. He, Y.-C. Yin, J.-N. Yang, Y.-H. Song, Q. Zhang, X.-C. Ru, Y.-F. Lan, G. Zhang and H.-B. Yao, *Angew. Chemie Int. Ed.*, 2022, **61**, e202208960.

74 S. Zhou, S. Zhang, H. Li, D. Sun, J. Zhang and X. Xin, *ACS Appl. Nano Mater.*, 2021, **4**, 10911–10920.

75 Y. Fang, W. Liu, S. J. Teat, G. Dey, Z. Shen, L. An, D. Yu, L. Wang, D. M. O'Carroll and J. Li, *Adv. Funct. Mater.*, 2017, **27**, 1603444.

76 W. Liu, Y. Fang, G. Z. Wei, S. J. Teat, K. Xiong, Z. Hu, W. P. Lustig and J. Li, *J. Am.*

Chem. Soc., 2015, **137**, 9400–9408.

77 R. W. Boyd, *Nonlinear Optics*, Academic Press, 2003.

78 P. P. Markowicz, H. Tiryaki, H. Pudavar, P. N. Prasad, N. N. Lepeshkin and R. W. Boyd, *Phys. Rev. Lett.*, 2004, **92**, 83903.

79 I. Abdelwahab, G. Grinblat, K. Leng, Y. Li, X. Chi, A. Rusydi, S. A. Maier and K. P. Loh, *ACS Nano*, 2018, **12**, 644–650.

80 S.-F. Li, X.-M. Jiang, Y.-H. Fan, B.-W. Liu, H.-Y. Zeng and G.-C. Guo, *Chem. Sci.*, 2018, **9**, 5700–5708.

81 Z.-Z. Luo, C.-S. Lin, H.-H. Cui, W.-L. Zhang, H. Zhang, H. Chen, Z.-Z. He and W.-D. Cheng, *Chem. Mater.*, 2015, **27**, 914–922.

82 Z. Chen, Q. Zhang, M. Zhu, H. Chen, X. Wang, S. Xiao, K. P. Loh, G. Eda, J. Meng and J. He, *J. Phys. Chem. Lett.*, 2021, **12**, 7010–7018.

83 W. Chen, S. Zhang, M. Zhou, T. Zhao, X. Qin, X. Liu, M. Liu and P. Duan, *J. Phys. Chem. Lett.*, 2019, **10**, 3290–3295.

84 A. Picot, A. D'Aléo, P. L. Baldeck, A. Grichine, A. Duperray, C. Andraud and O. Maury, *J. Am. Chem. Soc.*, 2008, **130**, 1532–1533.

85 A. D. Martin, K. J. Hartlieb, A. N. Sobolev and C. L. Raston, *Cryst. Growth Des.*, 2010, **10**, 5302–5306.

86 J. J. McKinnon, D. Jayatilaka and M. A. Spackman, *Chem. Commun.*, 2007, 3814–3816.

87 A. D. Martin, J. Britton, T. L. Easun, A. J. Blake, W. Lewis and M. Schröder, *Cryst. Growth Des.*, 2015, **15**, 1697–1706.

88 P. R. Spackman, M. J. Turner, J. J. McKinnon, S. K. Wolff, D. J. Grimwood, D. Jayatilaka and M. A. Spackman, *J. Appl. Crystallogr.*, 2021, **54**, 1006–1011.

Chapter 4:

Ligand-mediated Staircase-to-Cubane Structural Switch in Photon Up-converting Crystals of Cu(I)-Iodide-based Polymers: From TADF to Self-trapped Excitonic Emission

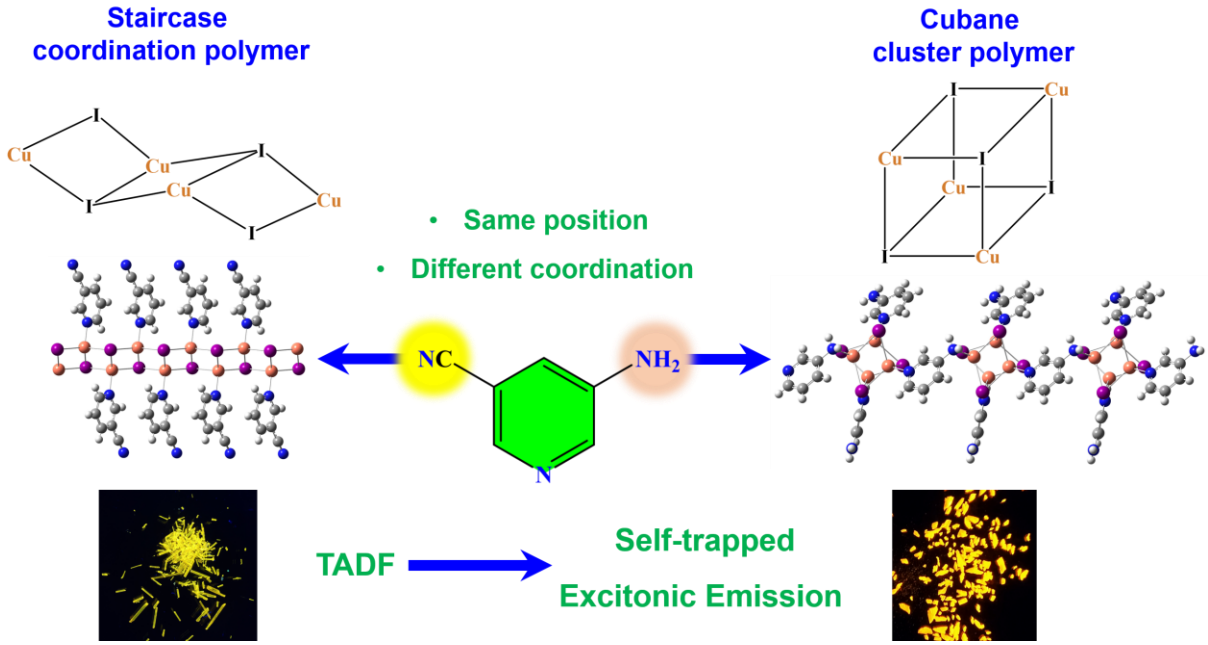

Abstract: Organic-inorganic hybrid metal-halides have gained enormous importance in the field of optoelectronics, sensing, photosensitization, and so on. In this study, we describe a structural transition from a staircase to a cubane configuration in Cu(I)-iodide-based polymers, influenced by the coordination behavior of two different π*-acceptor ligands. The staircase polymer structure, coordinated with 3-cyanopyridine, demonstrates efficient thermally activated delayed fluorescence (TADF) from (metal+halide)-to-ligand charge transfer ($^{1/3}$(M+X)LCT) states, with a singlet-triplet energy splitting of approximately 0.009 eV. Conversely, upon replacing the cyano with an amino group at the same position, the cubane polymer structure is formed, which shows strong cluster-centered (^{3}CC) orange emission at room temperature. Temperature-dependent photoluminescence studies indicate that the ^{3}CC state behaves as a self-trapped excitonic state with significant exciton-phonon coupling having a Huang-Rhys factor of 58.6. These polymer crystals also exhibit efficient third-order nonlinearity which is demonstrated by two-photon excited luminescence properties.

4.1. Introduction

Organic-inorganic hybrid metal-halides have attracted significant attention in the field of optoelectronics, sensing devices, and artificial photosynthesis owing to the versatility in the emission mechanisms, robust structural features, thermal stability, structural diversity, and so on.[1–4] Particularly, Cu(I)-iodide frameworks stand out to exhibit intriguing characteristics such as the stability of Cu(I)-iodide frameworks[5], as well as the suppression of non-radiative decay pathways resulting from the absence of d-d electronic transitions in Cu(I).[6] Consequently, the inclusion of Cu(I) in these hybrid structures results in intrinsically higher quantum yield.[7,8] These structures include Cu(I)-iodide staircase coordination polymers, Cu_4I_4 and associated clusters, Cu_2I_2 complexes and other heteronuclear complexes. The versatility of the emission mechanisms in these hybrids is largely attributed to the electronic properties of the coordinating ligands and the geometry of the Cu(I)-iodide framework.[9] Ligands with low-energy π*-orbitals can significantly contribute to the low-lying unoccupied orbitals of the hybrid system.[10] Since the highest occupied molecular orbital (HOMO) primarily consists of the filled d orbitals of Cu and the filled p orbitals of iodide, the low-lying excited states exhibit (metal+halide)-to-ligand charge transfer ((M+X)LCT) characteristics.[10] The 1D staircase coordination polymers exhibit significant charge-transfer properties[11], while the individual cubane-type Cu_4I_4 clusters form an additional distinct excited state known as the cluster-centered state (^{3}CC).[12,13] This excited state is particularly intriguing, formed by exciting one electron from the HOMO to a high-

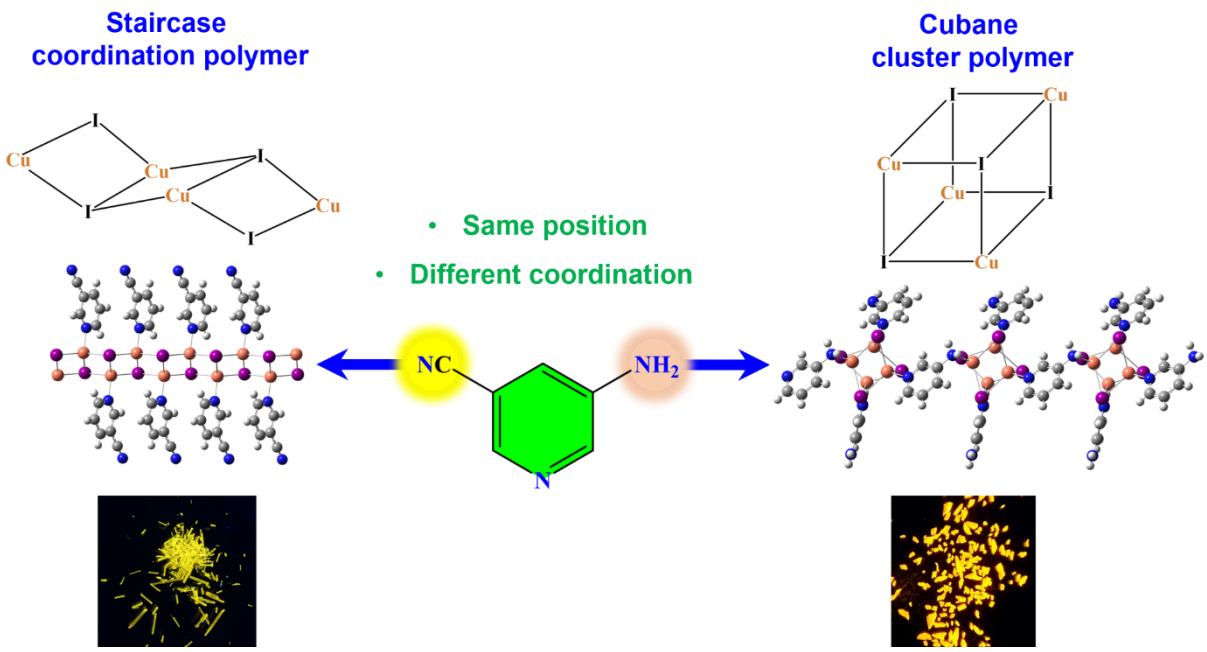

Scheme 4.1. Schematic representation of ligand-mediated structural modulation in Cu(I)-iodide-based polymeric frameworks and their emission.

energy vacant orbital with significant Cu···Cu bonding character.[12] The energy of the ^{3}CC states is highly dependent on the distance between Cu atoms and becomes more stable as the Cu-Cu distance decreases.[12] The thermal equilibrium of (M+X)LCT and ^{3}CC states in these Cu_4I_4 clusters gives rise to intriguing thermochromic emission features.[12,13]

The diversity in the excited states leads to the emergence of several different kinds of emission pathways in these materials, such as charge-transfer emission[9,14], self-trapped excitonic (STE) emission[15–17], dual emission[18–20], and so on. The charge-transfer states can also lead to the emergence of thermally activated delayed fluorescence (TADF) as a result of well-separated electrons and holes in these moieties.[10] The presence of TADF for these systems has been previously demonstrated in isolated copper iodide complexes and some polymeric systems where the distinct copper iodide moieties are linked by organic ligands with π*-orbitals.[21,22] Several of these complexes and clusters show excellent emission yield and have been utilized in fabricating high-performing OLED devices.[7,23–28] In these TADF active complexes, the spin-orbit coupling (SOC) is very strong, and consequently, the intersystem crossing (ISC) rate is reasonably higher than that of the organic luminophores.[29] The strong SOC gives rise to a significant shortening in the emission lifetime, thereby making this system more suitable for robust OLED applications. The efficiency of TADF in these systems has been monitored previously by modulating the electronic effects of the ligands, steric interactions, and so on.[30–36] However, despite the presence of sufficient charge-transfer character in the Cu(I)-iodide coordination polymers, the investigation of the TADF remains underexplored in this particular

framework. On the other hand, STE emission emerges from the spatial distortion of the lattice by the electron-hole pair.[37] STEs are typically known for their broadband emission characteristics and are widely utilized as phosphors in fabricating white/warm white light-emitting diodes (WLEDs), scintillators, and so on.[38,39] In a crystal lattice, electrons and holes are generated upon the photoexcitation, and they form a bound electron-hole pair by attracting each other through the Coulomb interaction.[40] The bound electron-hole pair is called exciton, and it is treated as a neutral quasiparticle. In a soft lattice, photogenerated electrons can strongly interact with phonon modes, causing excitons to become further stabilized as they get trapped within the distorted lattice.[38] This leads to a highly stabilized trapped state. Carrier recombination from this trapped state results in low-energy emission, known as STE emission.[37] The extent of electron-phonon coupling in a crystal lattice is generally quantified by determining a dimensionless quantity called Huang-Rhys factor (S).[37] S is a measurement of the non-radiative energy loss of the originally formed exciton upon the interaction with the vibrational modes of the crystal. STE emission band undergoes a distinctive broadening caused by the strong interaction of the emissive state with the crystal's phonon modes.[38] STE emission is prevalent in metal-halides and organic crystals where the presence of a soft lattice structure induces a strong interaction between the electron and phonon modes.[41–43] Several perovskite structures have been reported to exhibit exceptionally broad emission spectra owing to STE, which is tunable between cold white to warm white light.[37,44–47] STE emission has also been demonstrated in some Cu(I)-halide frameworks, along with quantifying the Huang-Rhys factor as medium to high.[15–17,48,49] However, in organic-inorganic hybrid, Cu(I)-iodide frameworks, the structure-property relationship largely depends upon the electronic effect and coordination behavior of the ligands. While various structural types have been reported independently, there is a lack of a well-established design strategy documented in previous literature.

Here in, we present a structural transition from staircase to cubane in Cu(I)-iodide-based polymers, influenced by the different coordination properties of two π*-acceptor ligands (**Scheme 4.1**). The staircase polymer coordinated with 3-cyanopyridine demonstrates efficient exciton recovery via TADF from $^{1/3}$(M+X)LCT states, with a singlet-triplet splitting of ~0.009 eV. Conversely, the cubane-cluster polymer coordinated with 3-aminopyridine shows strong ^{3}CC yellow-orange emission at room temperature. Temperature-dependent photoluminescence studies reveal that the ^{3}CC state in this structure acts as a self-trapped excitonic state with significant exciton-phonon coupling. At low temperatures, (M+X)LCT emission also appears, which is at higher energy compared to the staircase polymer. This indicates the amino group's much stronger electron-donating effect compared to the cyano group in modulating the

emission energy of the charge transfer state. The polymers also exhibit efficient third-order non-linearity which is reflected from their two-photon excited luminescence properties.

4.2. Experimental Section

4.2.1. Materials and general protocol for synthesis

Copper(I) iodide powder, 3-cyanopyridine, and 3-aminopyridine were purchased from Sigma Aldrich and used as received. Ethanol, acetonitrile, toluene, and *n*-pentane were purchased from Neelchem Corporation.

4.2.2. Characterization techniques

Single-crystal diffraction analysis data were collected at 100K with a BRUKER KAPPA APEX II CCD Duo diffractometer (operated at 1500 W power: 50 kV, 30 mA) using graphite monochromatic Mo Kα radiation (λ = 0.71073 Å). The structures were solved by direct methods and refined by least-squares against F^2 utilizing the software package SHELXL-97.[50,51] More information on crystal structures can also be obtained from the Cambridge Crystallographic Data Centre under the CCDC deposition number (2388009). Powder XRD experiments were performed using BRUKER D8 advanced X-ray diffractometer with a Cu-K_α radiation source.

4.2.3. Steady-state and time-resolved spectroscopic studies

Solid-state absorption spectra were measured by using a Shimadzu, UV-3600 UV-NIR spectrophotometer. Steady-state solution-based absorption spectra were recorded on Shimadzu, UV-2600 UV spectrophotometer. Steady-state emission spectra and time-gated emission spectra of all the samples in solution and solid state were recorded in Fluoromax-4C (HORIBA) and Fluorolog-3 (HORIBA), respectively. Absolute quantum yields were measured in Fluoromax-4C (HORIBA) instrument by using an integrating sphere. Time-resolved PL decay profiles have been recorded either using a diode-laser source (for a total time window <50 μs) or a microsecond flash lamp source (of 1.5-2.5 μs bandwidth and in cases where the total time window > 50 μs) in an Edinburgh FLS980 instrument. Temperature-dependent PL and PL decay profiles were recorded in an Edinburgh FLS980 Instrument coupled with a cryostat. The solid samples were placed between two sapphire plates and fixed in a gold-coated copper sample holder. The sample holder is fixed in a closed cycle He cryostat (Advanced Research Systems) attached with a Lake Shore 335 temperature controller. A mode-locked Ti-sapphire laser (Mai-Tai, Spectra-Physics) was used as the excitation source for the two-photon excited

luminescence imaging experiment. Two-photon excited luminescence spectra and corresponding excitation spectra were collected by using a multiphoton microscope (Leica, Germany) at 10X objectives.

4.2.4. Synthesis of polymer 1 (P1)

The single crystals were synthesized in a three-layer slow diffusion method. 95 mg of CuI (0.5 mmol) was dissolved in 1 mL saturated aqueous solution of KI. 52 mg (0.5 mmol) of 3-pyridinecarbonitrile was dissolved in 1 mL of acetone. The aqueous solution was placed in a glass tube with a diameter of 5 mm and became the bottom layer. 1 mL of pure acetonitrile was added slowly along the glass wall with a syringe, forming the middle layer. The ligand solution was added in a similar way over the middle layer. The tube was kept closed overnight, yielding needle-shaped yellow crystals in the middle layer. The product was characterized by using SCXRD and PXRD techniques.

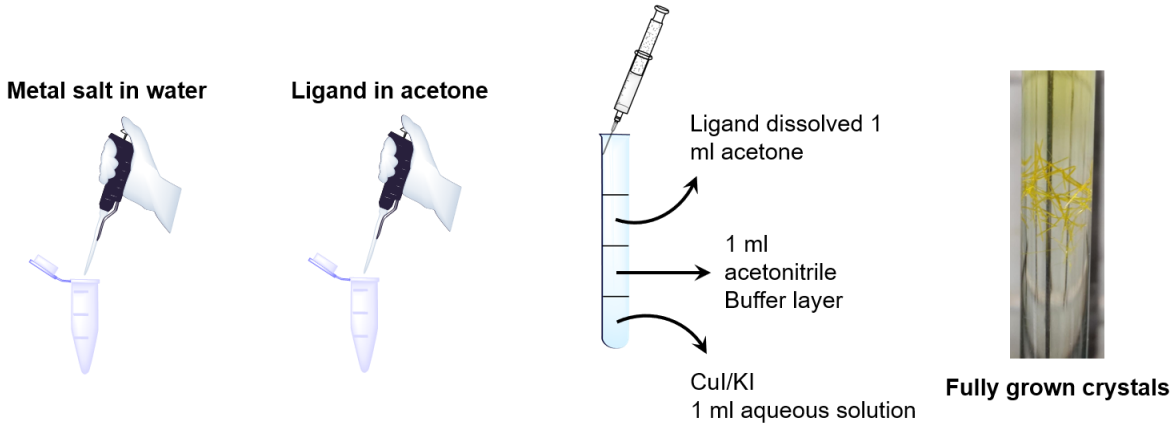

Scheme 4.2. Synthesis of P1.

4.2.5. Synthesis of polymer 2 (P2)

The single crystals were synthesized in a two-layer slow diffusion method. 95 mg of CuI (0.5 mmol) was dissolved in 1 mL saturated aqueous solution of KI. 47 mg (0.5 mmol) of 3-aminopyridine was dissolved in 1.5 mL of ethanol. The aqueous solution was placed in a glass tube with a diameter of 5 mm and became the bottom layer. The ligand solution was added very slowly along the glass wall with a syringe and it formed the upper layer. The tube was kept closed overnight yielding rhombus-shaped brown crystals in the middle layer. The product was characterized by using SCXRD and PXRD techniques.

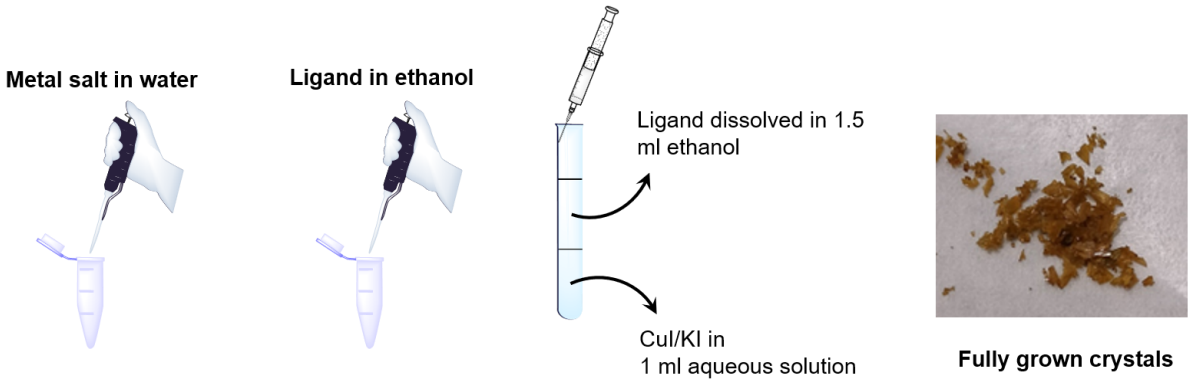

Scheme 4.3. Synthesis of P2.

4.2.6. DFT calculations

Density functional theory (DFT) calculations were performed using the Vienna Ab initio Simulation Package[52–54] (VASP), version 5.4.4. The Perdew−Burke−Ernzerhof46 (PBE) functional and projector-augmented wave[55,56] (PAW) pseudopotentials were used with a plane-wave cutoff energy of 500 eV. Structure relaxation was performed using the DFT-D3 method[57] with Becke-Johnson damping[58] for forces <0.01 eV/Å. Automatically generated Γ-centered Monkhorst-Pack (MP) grids are used for self-consistent calculations and DOS calculations. For band-structure calculations, an appropriate k-path was generated using Xcrysden[59,60]. Given the substantial underestimation of band gaps in both compounds by DFT calculations, hybrid functional[61] calculations were employed to achieve better results for P1.

For P1, Heyd-Scuseria-Ernzerhof (HSE) calculation gave a band gap of 2.27 eV. Also, density of states (DOS) calculations and charge density calculations confirmed the atomic character of both VB and CB. For P2, the unit cell contains a larger number of atoms. Hence, HSE calculations were not possible due to the high computational cost. The DFT band gap is 1.95 eV.

4.2.7. Calculation of absolute quantum yields

P1:

Φ = 27%. Absolute error = ± 0.023, relative error = $\pm\ 8.55 \times 10^{-4}$.

P2:

Φ = 31.3%. Absolute error = ± 0.027, relative error = $\pm\ 8.51 \times 10^{-4}$.

4.3. Results and Discussion.

4.3.1. Crystal structures.

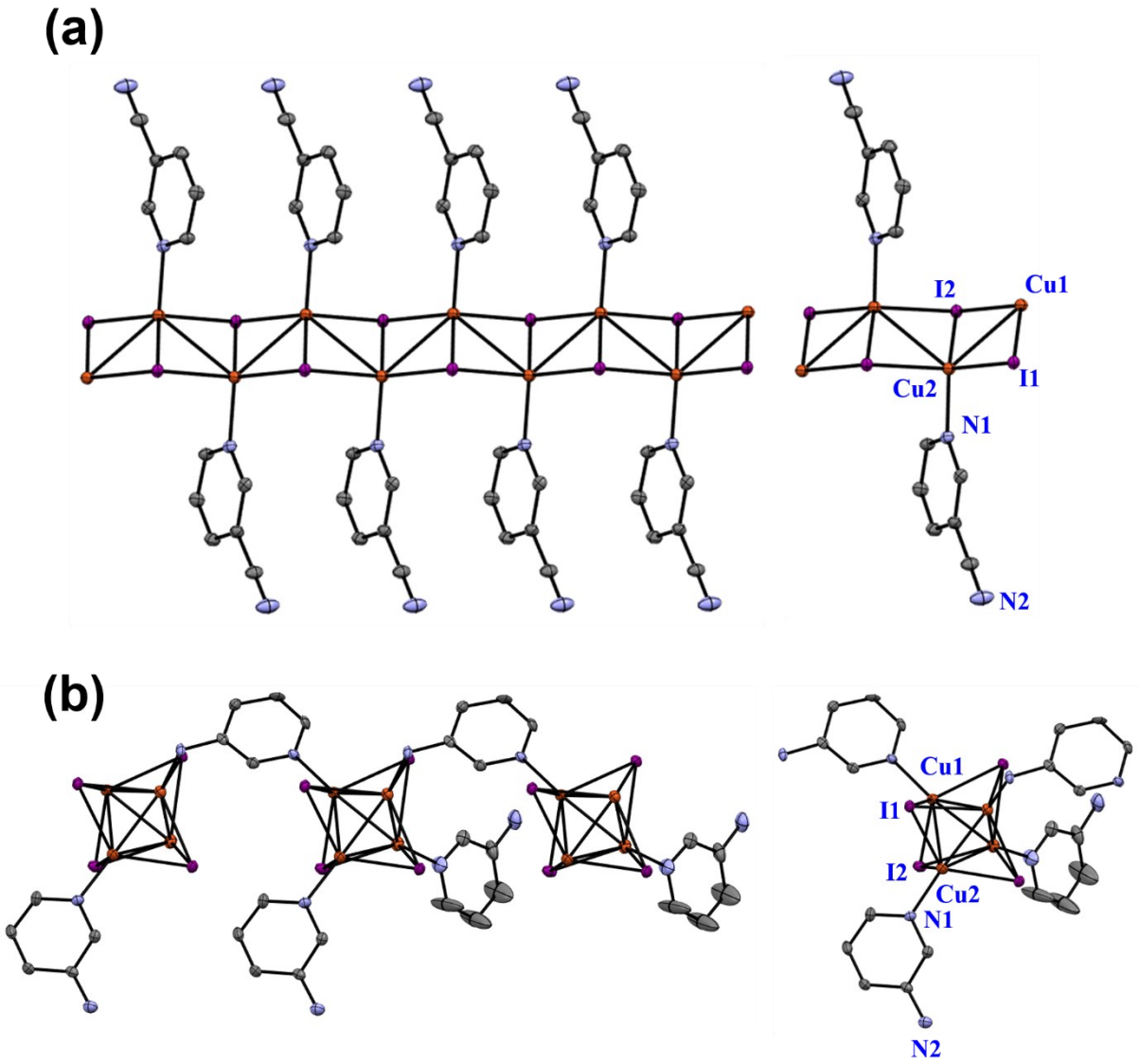

Figure 4.1. Crystal structures of (a) P1, and (b) P2.

The crystal structure of P1 was previously reported[62] and can be found under the CCDC number 1990790. Cu_2I_2 rhombic moieties are connected in a zigzag staircase fashion and form a coordination polymer (**Figure 4.1a**). The Cu centers are coordinated to 3-cyanopyridine ligands. The Cu-I, Cu-I, Cu-N, and Cu-Cu distances were found to be 2.65 Å, 2.63 Å, 2.05 Å, and 2.77 Å, respectively. The Cu-Cu distance is slightly less than the van der Waals distance (2.8 Å) of the Cu atom, indicating a moderate cuprophilic interaction. The crystal structure of P2 is shown in **Figure 4.1b**, and the Cu(I)-iodide inorganic module is entirely different compared to P1. Here, four Cu(I) and four I are corner-shared in an alternate fashion and form a distorted Cu_4I_4 cubic structure. The Cu centers are coordinated to 3-aminopyridine ligands, and the adjacent Cu_4I_4 clusters are connected by one bridging 3-aminopyridine ligand, forming a long 1D polymer of the Cu_4I_4 cluster. The formation of such cluster polymer is attributed to

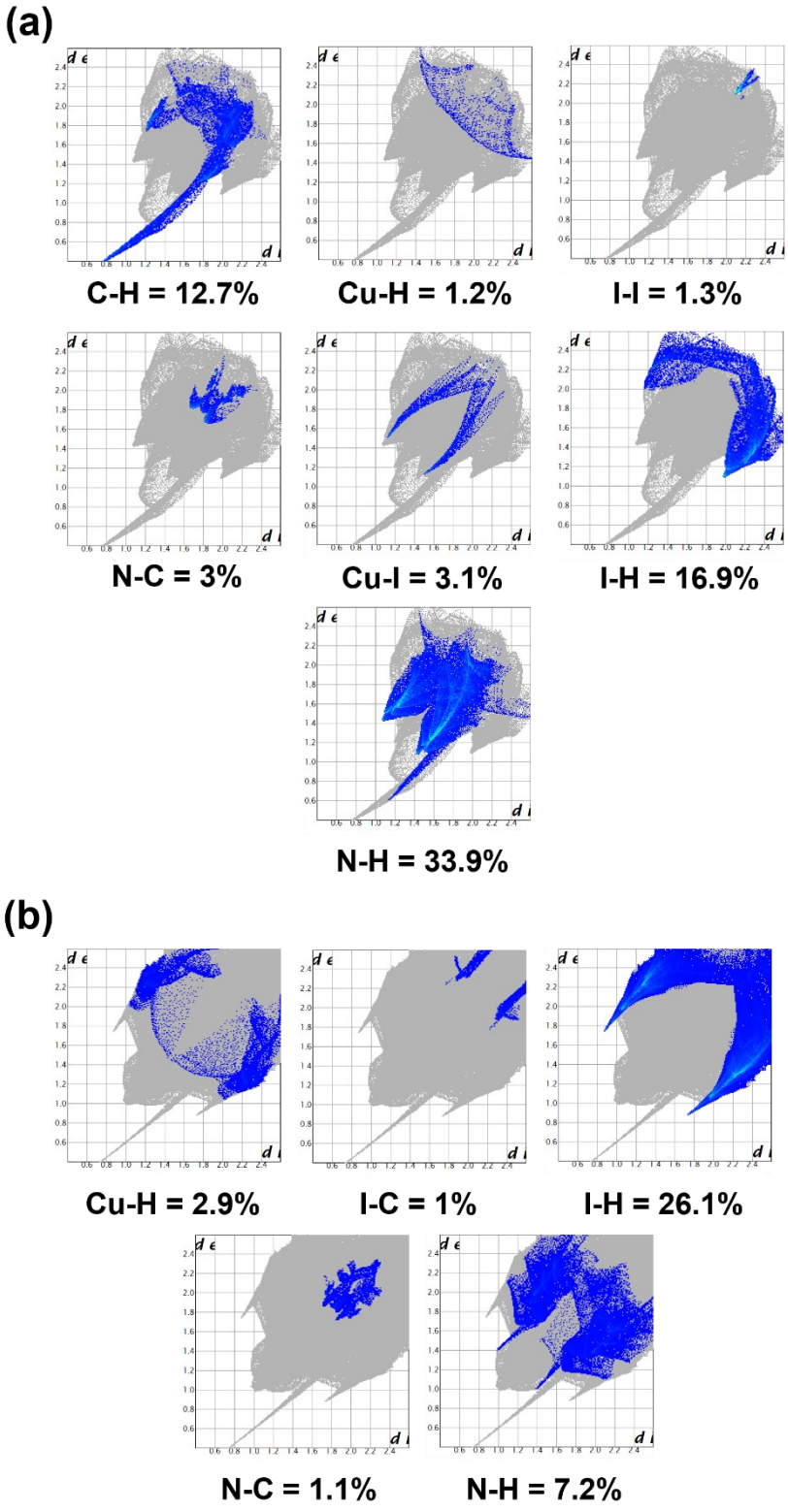

Figure 4.2. Hirshfeld surface analysis[82–84] of the complexes. Fingerprint plots revealing quantitative descriptions of several non-covalent interactions were quantified by using Crystal Explorer 3.1 software[85]. Fingerprint plots from normalized distance (d_{norm}) mapped over Hirshfeld surface to calculate the percentage of each non-covalent interaction for (a) P1, (b) P2.

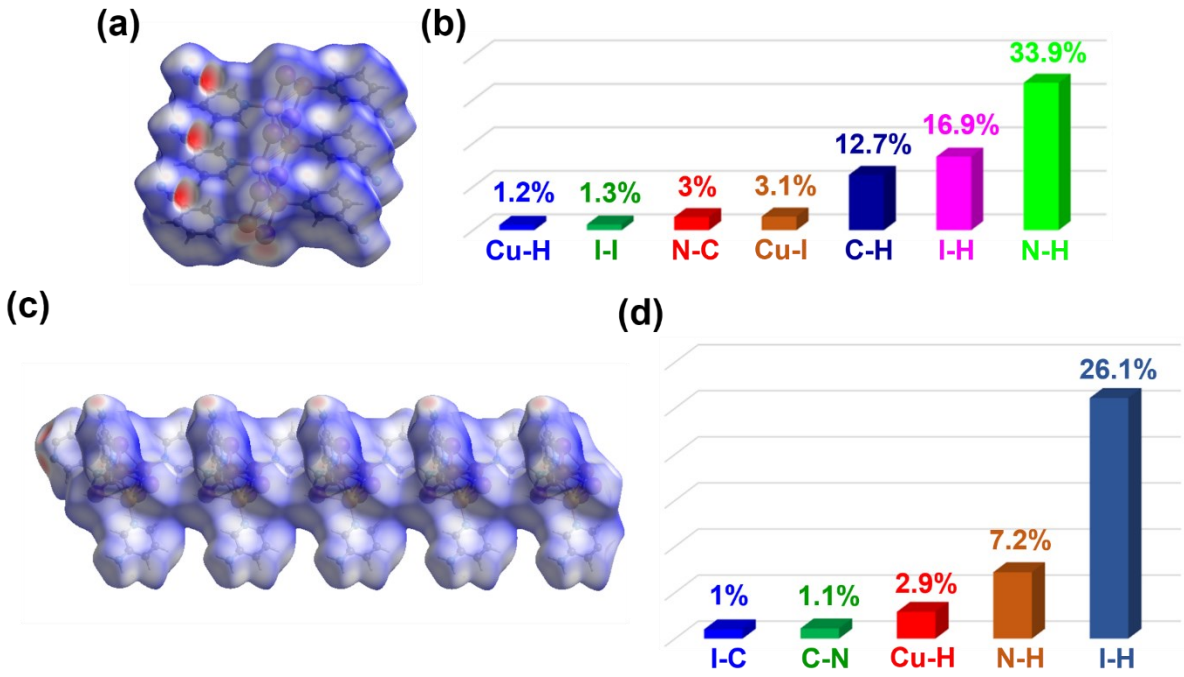

Figure 4.3. Normalized distance (d_{norm}) mapped over Hirshfeld surface for (a) complex-1 and (c) complex-2. Histogram of the percentagecontributions of different noncovalent interactions in (b) complex-1 and (d) complex-2.

the 3-aminopyridine having two donor sites: a strong pyridinic nitrogen (sp^2) donor and a relatively weaker aromatic amine nitrogen (sp^3) donor. The distinct coordination characteristic of this ligand makes it suitable for the formation of a robust, novel cluster polymer structure. Cu-N (pyridinic, nonbridging), Cu-N (pyridinic, bridging), and Cu-N (amine) distances were found to be 2.01 Å, 2.03 Å, and 2.08 Å, respectively. The intracluster Cu-I, and Cu-Cu distances are within the range of 2.6-2.7 Å, and 2.5-2.7 Å respectively. The small Cu-Cu distance within the cluster indicates a strong cuprophilic interaction.

4.3.2. Non-covalent interactions in the bulk phase.

Several non-covalent interactions with high enthalpy values can moderately influence several of the photophysical processes in the solid phase. In order to evaluate these possible influences, Hirshfeld surface analysis calculations were carried out using the crystal structures (**Figure 4.2**). The normalized distance (d_{norm}) mapped over the Hirshfeld surface for both samples is given in **Figure 4.3a** and **4.3c**. The histogram containing the percentage contributions of several interactions is shown in **Figure 4.3b** and **Figure 4.3d**. We observe that in both complexes, strong interactions such as N···H (enthalpy ~2.97 kJ/mol)[63], C···H (enthalpy ~10.3 kJ/mol)[64], and I···H (enthalpy ~16-25 kJ/mol)[65] are present in the bulk phase. However, the total percentage of these three interactions is much higher in P1 (63.5%) than in P2 (33.3%).

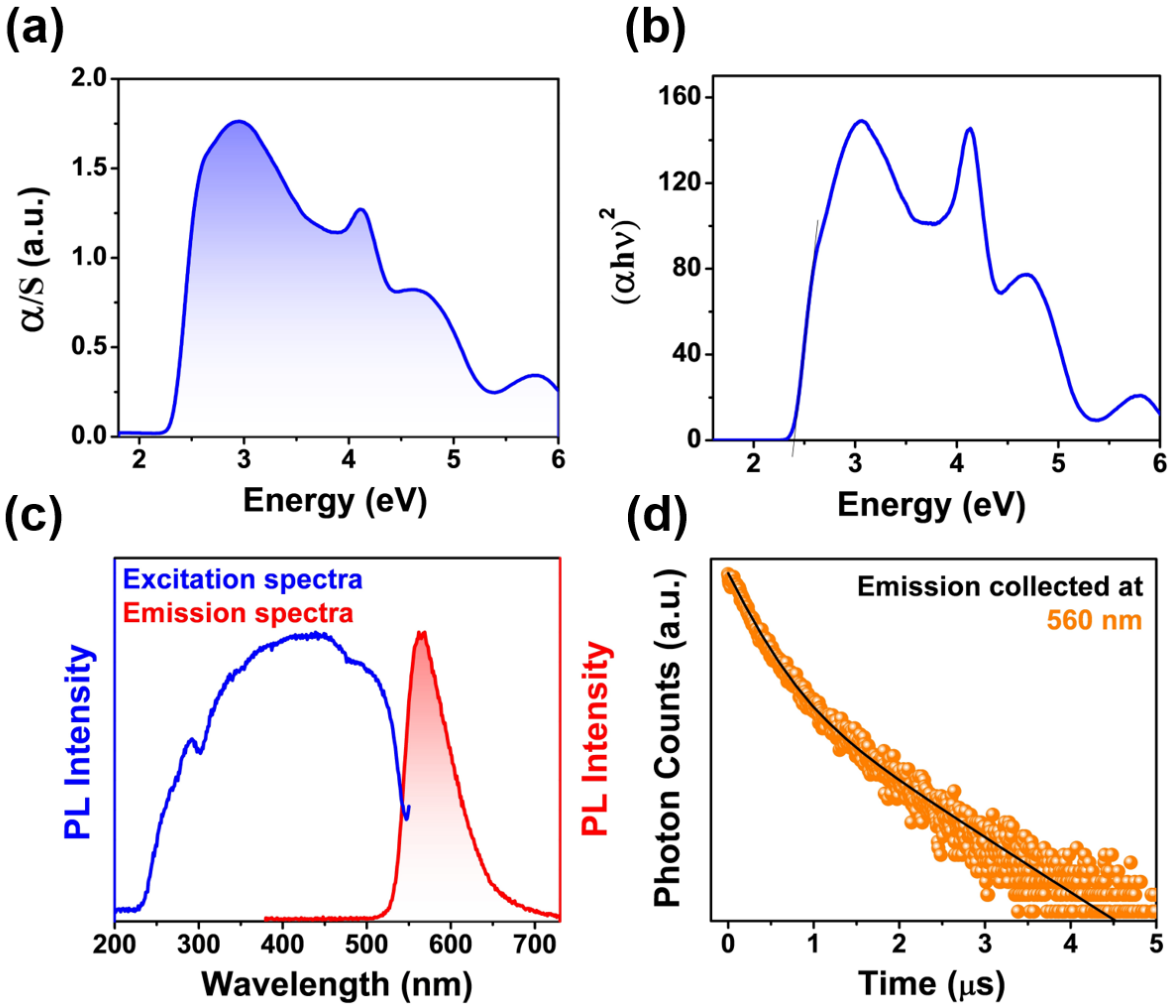

Figure 4.4. (a) Kubelka-Munk transformed absorption spectra of P1, (b) Tauc plot for P1, (c) excitation and emission spectra for P1, and (d) PL decay profile for P1.

These non-covalent interactions can effectively enhance the ISC rate associated with the singlet and triplet excited states in the bulk-phase, which is essential for efficient triplet state harvesting. In addition, strong non-covalent interactions can also dictate the direction of the polarizability tensor in the bulk condensed phase, which can have a larger impact on the non-linear optical (NLO) properties of the complexes.[66,67]

4.3.3. Photophysical properties of P1.

The absorption spectra in the solid-state shows multiple peaks corresponding to optical excitations to several conduction bands (**Figure 4.4a**). The absence of any long absorption tail in the low-energy band-edge region indicates that no defect states are present within the valance band and conduction band. The electronic band-gap value is estimated from the Tauc plot and found to be 2.40 eV (**Figure 4.4b**). DFT calculations show that the sample has a direct band-

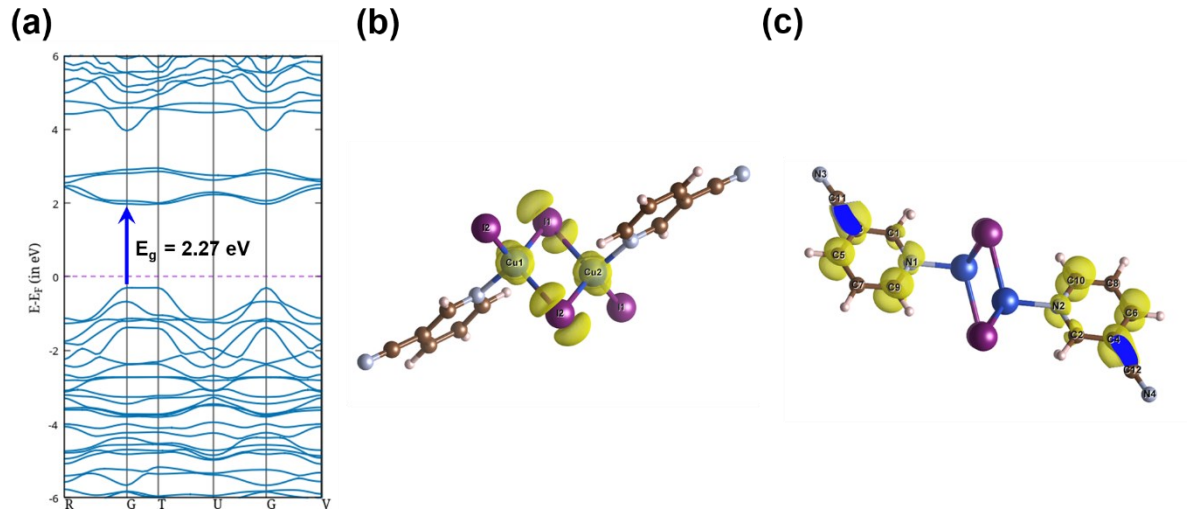

Figure 4.5. (a) HSE band structure of P1, (b) charge density plot for VBM of P1, and (c) Charge density plot for CBM of P1.

gap and the theoretically calculated band-gap was found to be 2.27 eV, which corroborates well with the experimental value (**Figure 4.5a**). The charge density calculations show that the valance band maxima (VBM) is comprised of Cu (3d) and I (5p) orbitals; on the other hand, the conduction band minima (CBM) is comprised of π*-orbitals of the ligand's aromatic ring, revealing a (metal+halide)-to-ligand charge transfer ((M+X)LCT) nature in the low-energy excited states (**Figure 4.5b, 4.5c**). The sample manifests a bright yellow color under UV light and exhibits an emission band with a peak at ~560 nm (**Figure 4.4c)**. The quantum yield was determined to be 27%. Additionally, the PL decay profile of P1 shows a biexponential decay with lifetime components of 0.29 µs and 1.04 µs, while the average lifetime was found to be 0.6 µs (**Figure 4.4d, Table A2 in Appendix)**, indicating the participation of triplet states in the emission mechanism. The high charge-transfer nature of the sample is indicated by the spatially well-separated charge densities in the valance band maxima and conduction band minima (**Figure 4.5b, 4.5c**). This particular observation prompted us to investigate the thermal equilibrium of the singlet and triplet state populations. Temperature-dependent emission studies show a sequential increment in the emission intensity with decreasing temperature which can be partially attributed to the suppression in the non-radiative decay pathways at lower temperatures (**Figure 4.6a)**. In order to measure the excitonic contribution in the emission mechanism, integrated emission intensity vs. 1/T was plotted (**Figure 4.6b, Table A3 in Appendix)** and was fitted to the following equation[39],

$$I(T) = \frac{I_0}{1 + Ae^{-\frac{E_b}{k_B T}}} \qquad \text{Eq. 4.1}$$

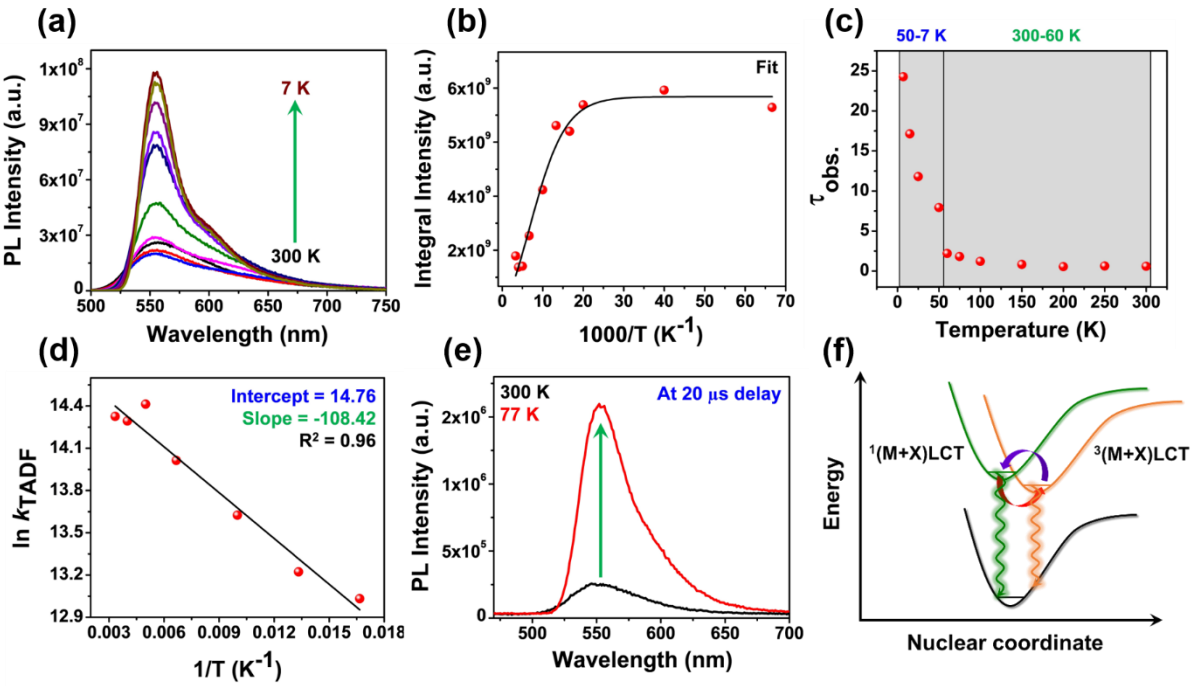

Figure 4.6. (a) Temperature-dependent emission spectra of P1, (b) integral emission intensity *vs.* 1/T plot for P1, (c) τobs. *vs.* temperature plot for P1, (d) ln(k_{TADF}) *vs.* 1/T plot for P1, (e) gated emission spectra of P1 at 300 K and 77 K, and (f) schematic representation of emission mechanism.

where I(T), I_0, E_b, and k_B represent integrated intensity at temperature T, integrated intensity at 0 K, excitonic binding energy, and Boltzmann constant, respectively. The experimental binding energy was evaluated from the fitting parameters and was found to be ~19 meV, which is much less than room-temperature thermal energy. Therefore, the possibility of radiative relaxation through exciton luminescence is ruled out, and the radiative decay of the excited state principally occurs through band-edge luminescence. Temperature-dependent lifetime studies show that the lifetime of P1 increases slowly upon reducing the temperature from 300 K to ~60 K (**Figure 4.6c, Table A4 in Appendix)**. Upon further reducing the temperature, the lifetime drastically increased up to 24.28 μs in the range of 50-7 K (**Figure 4.6c, Table A4 in Appendix)**. This sharp increase of lifetime in this range clearly indicates the activation of the low-energy triplet states with longer lifetimes in the lower temperature regime. The much shorter lifetime at room temperature suggests that excitons predominantly decay through singlet states via TADF. In the 300-60 K range, the emission is a mixture of TADF and phosphorescence. The significant increase in lifetime within the 50-7 K range indicates a substantial enhancement in the phosphorescence contribution. The absence of prompt fluorescence supports the observation that the intersystem crossing (ISC) rate is higher in these systems compared to organic molecules due to stronger spin-orbit coupling (SOC). Although the lifetime versus temperature profile in the 50-7 K range does not reach a plateau

corresponding to pure phosphorescence, it suggests that a small contribution from the TADF mechanism persists even at these lower temperatures. Due to the absence of a plateau region, the dependence of the radiative decay rate upon temperature was analyzed using the Arrhenius equation (**Figure 4.6d, Table A5 in Appendix**) and was found to be well-fitted to a two-state TADF model under a fast thermalization process.[68]

$$\ln(k_{TADF}) = \ln(A) - \frac{\Delta E_{ST}}{k_B T} \qquad \text{Eq. 4.2}$$

$$A = \frac{k_{ISC}}{3}\left(1 - \frac{k_{ISC}}{k_{S_1} + k_{ISC}}\right)$$

$$k_{S_1} = \frac{3Ak_{ISC}}{k_{ISC} - 3A} \approx 3A, \qquad \text{since } k_{ISC} \gg A$$

$k_{TADF} = \frac{1}{\tau_{TADF}} = \frac{1}{\tau_{obs.}}$, since TADF is the predominant decay pathway at the 300-60 K temperature range. k_{TADF}, τ_{TADF}, $\tau_{obs.}$, k_{S_1}, and k_{ISC} are the rate of TADF, TADF lifetime, observed lifetime, the intrinsic decay rate of singlet state, and ISC rate, respectively. ΔE_{ST} and k_{S_1} were found to be 9 meV and 7.71×10^6 s^{-1} (intrinsic lifetime of singlet ~129.7 ns) respectively. The evaluated ΔE_{ST} value is much smaller than the room-temperature thermal energy, and thus, the triplet state population can revert back to the singlet state by the RISC process (**Figure 4.6f**). The increase in the triplet population at lower temperatures can also be observed by comparing the gated emission spectra at 300 K and 77 K. At 300 K, applying a 20 µs detector delay significantly reduces the emission band intensity (**Figure 4.6e**), indicating a shorter lifetime of the emissive state, which is characteristic of predominant delayed fluorescence. However, at 77 K, the emission intensity dramatically increases with the same detector delay (**Figure 4.6e**). This significant rise in emission intensity at the low temperature indicates that the emissive state has a much longer lifetime, corresponding to phosphorescence emission.

4.3.4. Photophysical properties of P2.

The absorption spectra in the solid state shows multiple peaks corresponding to optical excitations to several conduction bands (**Figure 4.7a**). The electronic band-gap value is estimated from the Tauc plot and found to be 2.47 eV (**Figure 4.7b**). The absence of any long absorption tail in the low-energy band-edge region indicates that no defect states are present

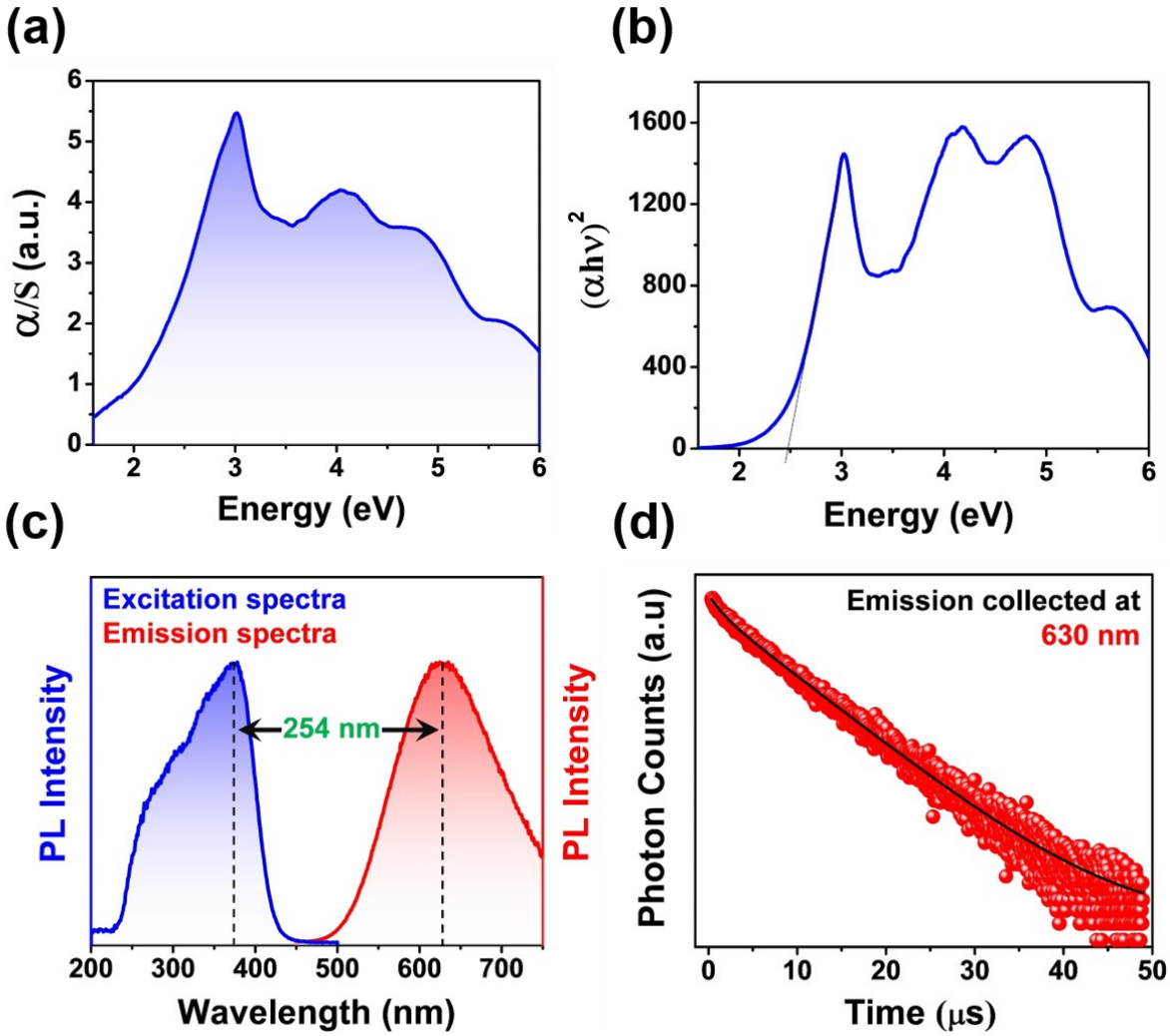

Figure 4.7. (a) Kubelka-Munk transformed absorption spectra of P2, (b) Tauc plot for P2, (c) excitation and emission spectra for P2, and (d) PL decay profile for P2.

within the valance band and conduction band. DFT calculations show that the sample has a direct band-gap, and the theoretically calculated band-gap was found to be 1.95 eV, which corroborates well with the experimental value (**Figure 4.8a**). The charge density calculations show that the valance band maxima (VBM) is comprised of Cu (3d) orbitals; on the other hand, the conduction band minima (CBM) is comprised of π*-orbitals of the ligand's aromatic ring, revealing a metal-to-ligand charge transfer (MLCT) nature in the low-energy excited states (**Figure 4.8b, 4.8c**). The sample shows a bright yellow-orange emission under UV exposure along with a quantum yield of 31.3%. The emission spectra show an exceptionally broad emission characteristic with a maximum at ~630 nm (**Figure 4.7c**). The emission band is also ~254 nm Stokes' shifted compared to its excitation spectra, which indicates a large reorganization to take place in the excited state (**Figure 4.7c**). The PL decay profile manifests a bi-exponential fit along with lifetime components of 1.4 μs and 8.43 μs (**Figure 4.7d**). At 77

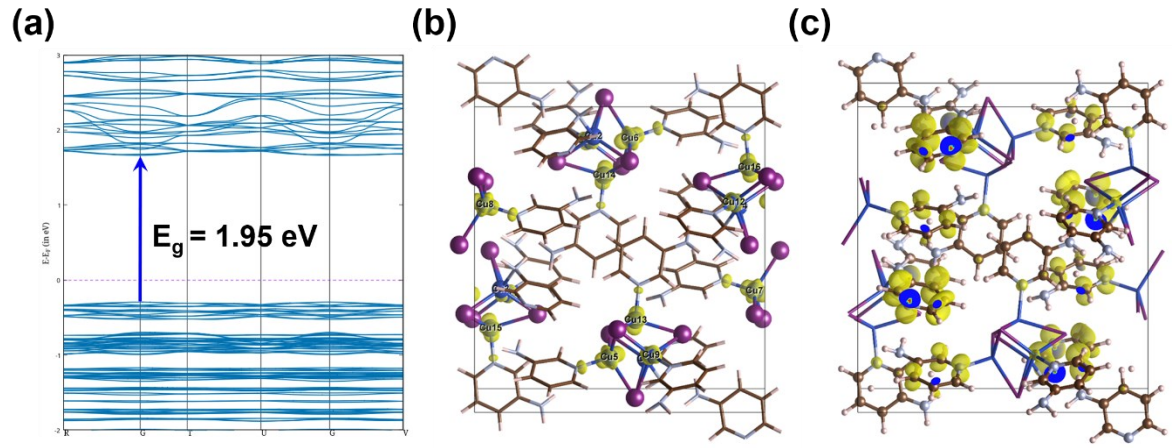

Figure 4.8. (a) GGA band structure of P2, (b) charge density plot for VBM of P2, (c) charge density plot for CBM of P2.

K, the emission spectra shows a significant decrement in the fwhm of the Stokes' shifted broad peak along with the emergence of another high-energy peak having a maximum at ~470 nm (**Figure 4.9a**). P2 has a 1D polymeric chain of Cu_4I_4 cluster; therefore, the highly Stokes' shifted broad peak is attributed to the emission from the ^{3}CC state. The high-energy peak at low temperature is thus attributed to the ^{3}(M+X)LCT emission emerging as a consequence of the thermal equilibrium between ^{3}CC and ^{3}(M+X)LCT states (**Figure 4.9b**).[12] It should be noted that fwhm of the ^{3}CC emission band, in this case, undergoes a significant decrement compared to previously reported other isolated non-polymeric Cu_4I_4 clusters (**Figure 4.9c**).[12,13,69] A ~240 meV decrement in the fwhm upon decreasing the temperature to 77 K clearly indicates that the dynamics of this particular state are strongly coupled with the phonon modes of the cluster polymer (**Figure 4.9c**). In order to investigate the role of phonon modes in the emission temperature-dependent emission studies were conducted. Upon decreasing the temperature to 180 K, fwhm of the ^{3}CC band undergoes sequential shortening along with a red-shift and enhancement in the emission intensity (**Figure 4.10a**). From 180-40 K, the emission intensity decreased with declining temperature along with the sequential shortening in the fwhm in the emission band, but the red-shift was found to be masked (**Figure 4.10a**). From 120 K-40 K, the decrement in the ^{3}CC band intensity was accompanied by a concomitant emergence of the high-energy ^{3}(M+X)LCT band (**Figure 4.10a**), which evolves as a result of the thermal equilibrium between ^{3}CC and ^{3}(M+X)LCT population. The sequential declination of the fwhm of the ^{3}CC band was observed upon the normalization of the temperature-dependent emission spectra against the ^{3}CC peak (**Figure 4.10b**). The significant decrement in the fwhm is a consequence of the lower average phonon energy at low temperatures. The

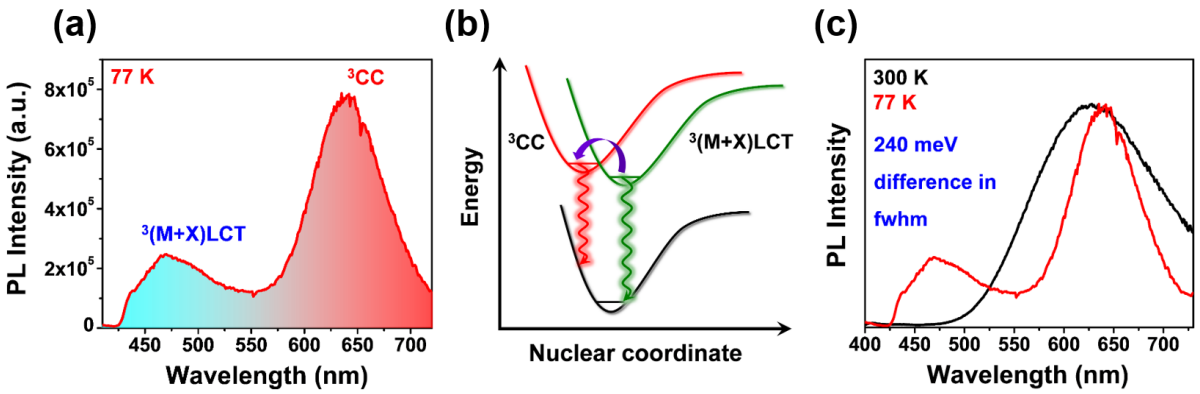

Figure 4.9. (a) Emission spectra of P2 at 77 K, (b) schematic representation of emission mechanism for P2, and (c) comparison of fwhm of 3CC emission band at 300 K and 77 K.

temperature dependence of the emission bandwidth in these frameworks is described by the following equation[70],

$$\mathrm{FWHM} = \Gamma_0 + \sigma T + \frac{\Gamma_{LO}}{e^{\frac{\hbar\omega_{LO}}{k_B T}} - 1} \qquad \text{Eq 4.3}$$

where Γ_0, σ, Γ_{LO}, and $\hbar\omega_{LO}$ represent the inhomogeneous broadening, the interaction energy between excitons and acoustic phonons, the interaction energy between excitons and longitudinal optical phonons, and the average energy of longitudinal optical phonons, respectively. For P2, the FWHM *vs.* 1/T plot was fitted with Eq 3, and Γ_0, σ, Γ_{LO}, and $\hbar\omega_{LO}$ were evaluated from the fitting parameters (**Figure 4.10c, Table A6 in Appendix**). Temperature-independent inhomogeneous broadening of the emission band is due to some fundamental properties of the crystal and is attributed to the thermal effect of the optical excitation, intrinsic defects, and so on. Γ_0 was determined to be 193 meV, which would prevail at very low temperatures ($T \rightarrow 0$) when the phonon modes are no longer effective. σ was found to be negligible with a value of 2.4×10^{-10} eVK^{-1}, which indicates almost no scattering of excitons by acoustic phonons. On the other hand, Γ_{LO} was found to have a significant value of 31.8 meV, which indicates a strong interaction between exciton and longitudinal optical phonons. Therefore, P2 has a strong exciton-LO phonon coupling, which is described by Frolich interaction and is generally applicable to polar semiconductors. Furthermore, to evaluate the corresponding Huang-Rhys factor (S), the FWHM vs. T plot was fitted to the following equation (**Figure 4.10d, Table A7 in Appendix**)[38],

$$\mathrm{FWHM} = 2.36\sqrt{S}\hbar\omega_{LO}\sqrt{\coth\left(\frac{\hbar\omega_{LO}}{2k_B T}\right)} \qquad \text{Eq 4.4}$$

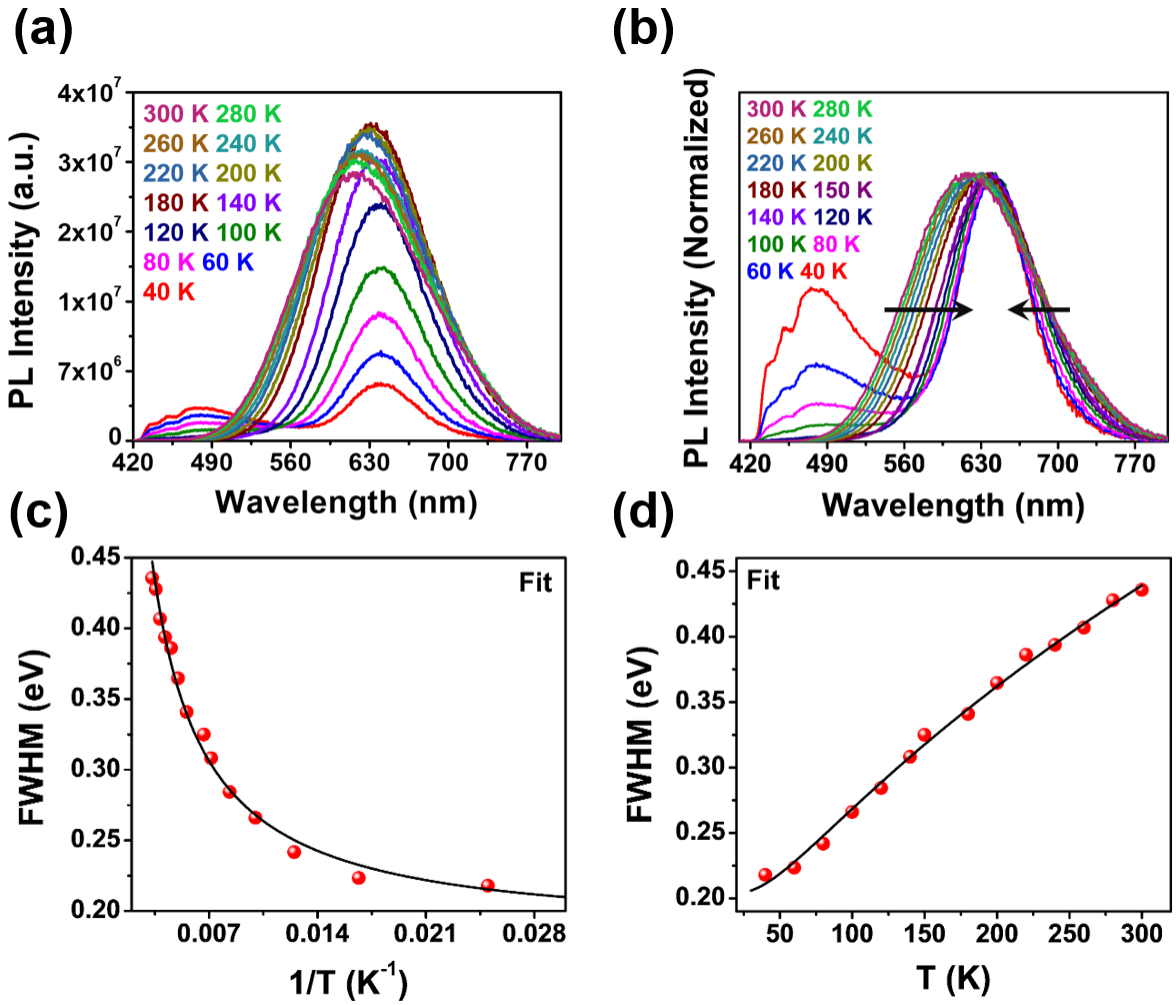

Figure 4.10. (a) Temperature-dependent emission spectra of P2 from 300 K to 40 K, (b) temperature-dependent emission spectra of P2 from 300 K to 40 K upon normalization against ^{3}CC emission peak maximum, (c) fwhm *vs.* 1/T plot for P2, and (d) fwhm *vs.* T plot for P2.

where S is the Huang-Rhys factor. From the fitting parameters, the S was evaluated to be 58.6, which is reasonably high for metal-halide semiconductors. The high value of S further confirms the presence of strong exciton-phonon coupling in P2. Consequently, the ^{3}CC emission is accompanied by an extremely significant phonon interaction and, therefore, emerges as an STE emission. $\hbar\omega_{LO}$, in this case, was found to be 11.2 meV, which is assigned to the average longitudinal optical phonon energy. For Cu_4I_4 clusters coordinated with several organic ligands, the ^{3}CC states are described as a state with high energy excitation and higher geometry distortion. However, there has seldom been a case where it has been represented and generalized as an excited state exhibiting self-trapped excitonic emission. The STE formation in P2 is also supported by the densities of the electron and hole corresponding to the electronic excitation for the ^{3}CC state. Both the electron and hole densities are localized within the Cu_4I_4

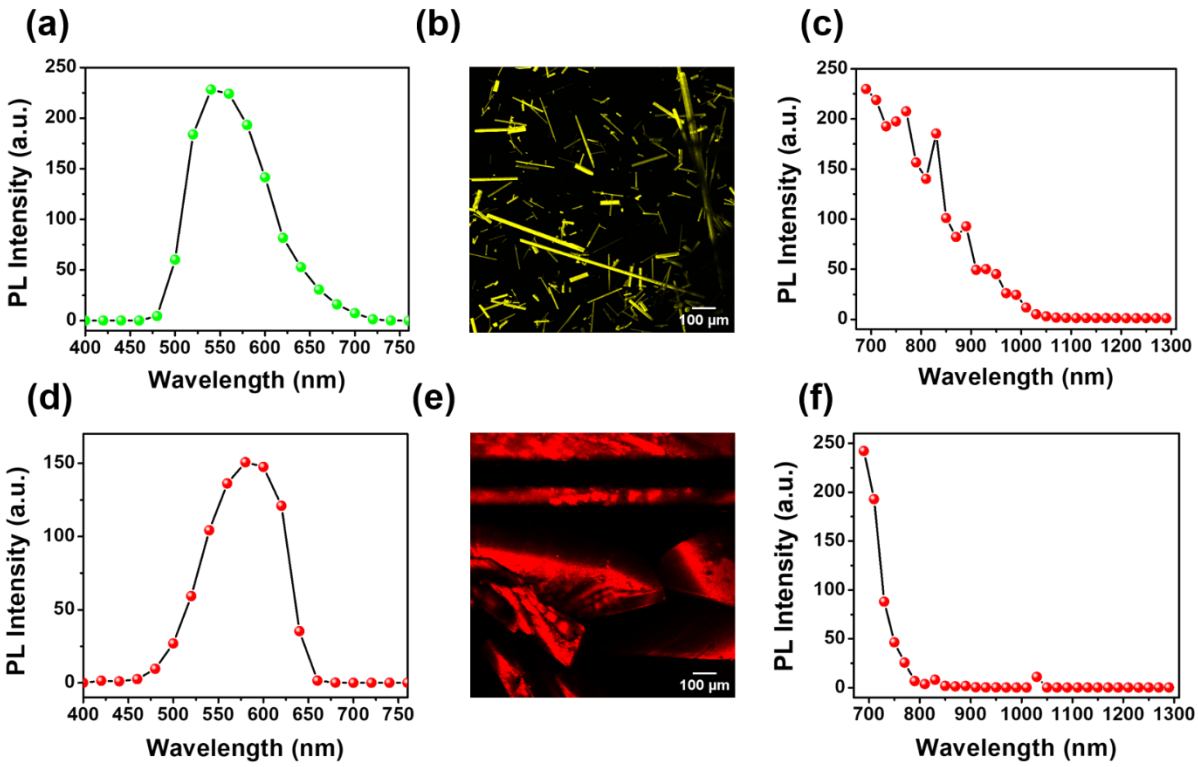

Figure 4.11. (a) Two-photon excited emission spectra, (b) microscopic image, and (c) excitation spectra for P1. (d) Two-photon excited emission spectra, (e) microscopic image, and (f) excitation spectra for P2.

cluster, which enhances the exciton-phonon coupling. The Huang-Rhys for P2 is comparable to that of the lead-halide perovskites or even higher than these systems. Lead-halide perovskites have low Huang-Rhys factor values with a broad range depending on the constituents and structures.[37] However, the Huang-Rhys factor of double perovskite structures has been found to be much higher (~40).[71]

4.3.5. Photon up-conversion properties of P1 and P2.

We have shown two-photon excited luminescence in our samples, which is a prodigious photon up-conversion process that can generate high-energy photons by utilizing much lower-energy photons (near IR or IR). Both P1 and P2 were found to exhibit excellent two-photon excited luminescence owing to their high charge-transfer nature. The PL spectra and the corresponding microscopic images of the crystals are shown in **Figures 4.11a, 4.11b, 4.11d, and 4.11e**. The excitation spectra for both samples also show their significant two-photon absorption in the near IR and IR regions (**Figure 4.11c, 4.11f**).

4.4. Conclusion.

In summary, we have applied a ligand engineering methodology to modulate the triplet harvesting mechanism of Cu(I)-iodide-based polymeric frameworks. Treatment of Cu(I)-iodide with 3-cyanopyridine results in the formation of a staircase coordination polymer of Cu(I)-iodide which shows excellent TADF properties with a ΔE_{ST} value of ~9 meV and a singlet decay rate of 7.71×10^{6} s^{-1}. On the other hand, upon replacement of the cyano group by an amino group at the same position, a structural switch of a staircase-to-cubane cluster was observed, and a cluster polymer was formed. The cluster polymer has strong exciton-phonon coupling with a high Huang-Rhys factor of 58.6 and exhibits STE emission. Both samples manifest excellent third-order nonlinearity, which is evident from their respective two-photon excited luminescence properties.

4.5. Appendices

4.5.1. Appendix 1: Characterization.

Table A1. Crystallographic data of P2

Identification code	jc5_a
CCDC	2388009
Formula weight	1043.81
Temperature/K	100(2)
Crystal system	monoclinic
Space group	P21/c
a/Å	8.7502(17)
b/Å	16.583(3)
c/Å	17.406(4)
α/°	90
β/°	98.891(6)
γ/°	90
Volume/Å^3	2495.4(9)
Z	4
ρ_{calc}g/cm^3	2.779
μ/mm^{-1}	8.326
F(000)	1911.2
Radiation	MoKα (λ = 0.71073)
2Θ range for data collection/°	4.712 to 56.93
Index ranges	-11 ≤ h ≤ 11, -22 ≤ k ≤ 22, -23 ≤ l ≤ 23
Reflections collected	41247
Independent reflections	6310 [Rint = 0.0632, Rsigma = 0.0368]
Data/restraints/parameters	6310/87/221
Goodness-of-fit on F^2	1.103
Final R indexes [I>=2σ (I)]	R1 = 0.0424, wR2 = 0.0952
Final R indexes [all data]	R1 = 0.0514, wR2 = 0.0997

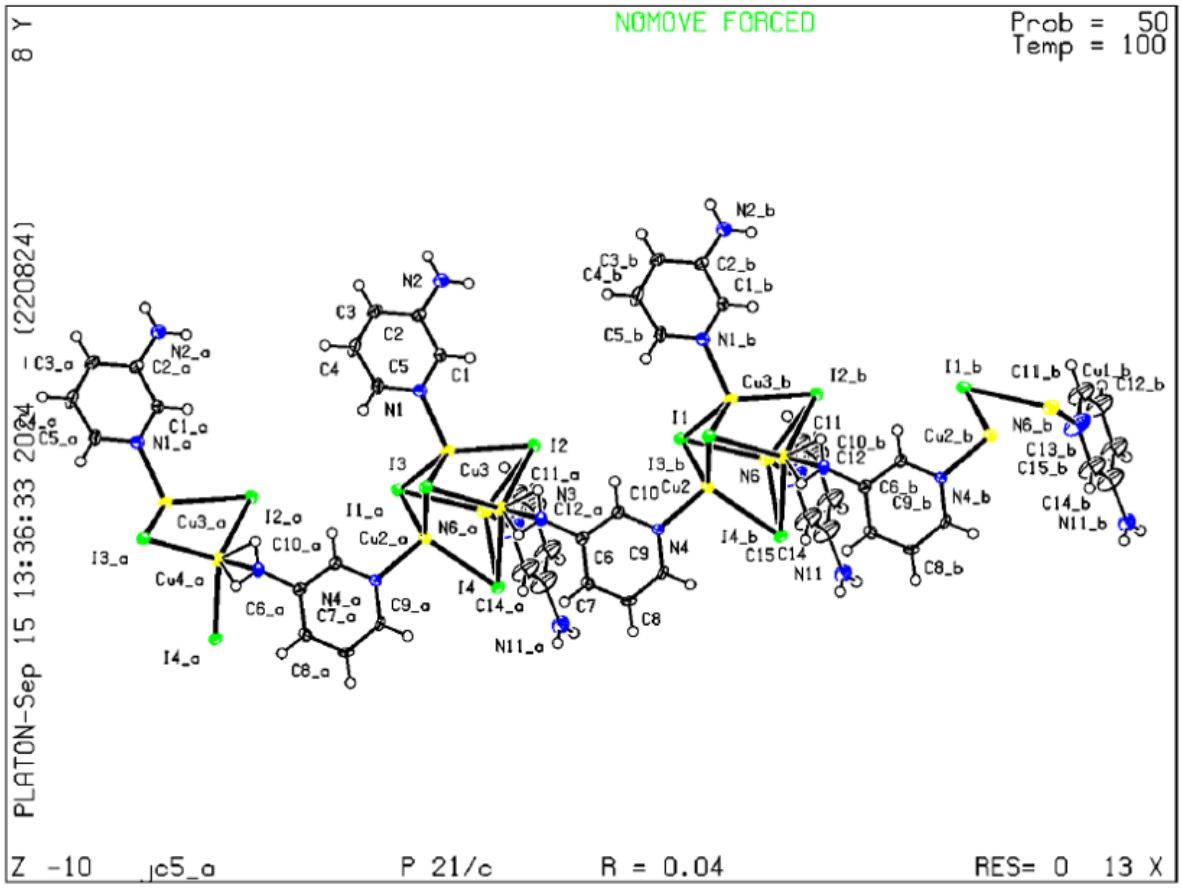

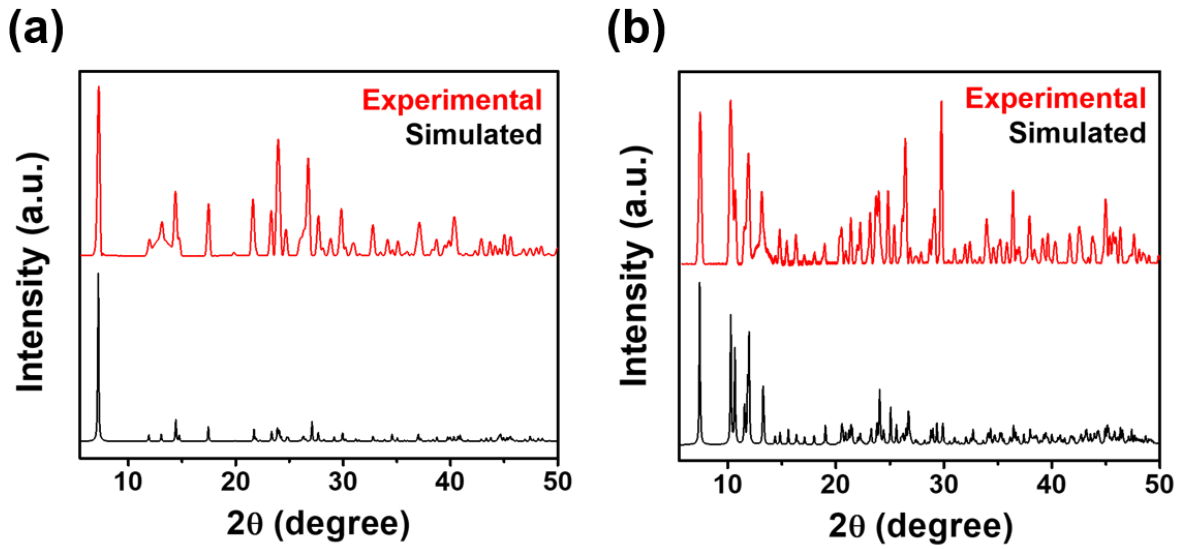

Figure A1. Powder XRD pattern of (a) P1 and (b) P2.

4.5.2. Appendix 2: Tables.

Table A2. Lifetime parameters of P1 and P2.

Sample	Emission at	α_1	τ_1 (µs)	α_2	τ_2 (µs)
P1	**560 nm**	0.87	0.29	0.18	1.04
P2	**630 nm**	0.20	1.40	0.80	8.43

Table A3. Data for I(T) vs. 1000/T plot of P1.

1000/T (K^{-1})	I(T) (a.u.)
3.33333	2.2741×10^9
4	2.02248×10^9
5	2.04714×10^9
6.66667	2.72062×10^9
10	3.74276×10^9
13.33333	5.16823×10^9
16.66667	5.03789×10^9
20	5.62607×10^9
40	5.95343×10^9
66.66667	5.56974×10^9

Table A4. Lifetime parameters of P1 from 300 K to 7 K.

Temperature (K)	α_1	τ_1 (µs)	α_2	τ_2 (µs)	$\langle\tau\rangle$ (µs)
300	0.87	0.29	0.18	1.04	0.60
250	0.80	0.25	0.26	0.94	0.62
200	0.85	0.26	0.20	0.91	0.55
150	0.74	0.35	0.27	1.21	0.82
100	0.83	0.68	0.08	2.63	1.21
75	0.76	0.97	0.21	2.86	1.81
60	0.63	1.14	0.18	3.43	2.19
50					7.93
25					11.80
15					17.14
7					24.28

Table A5. Data for ln(k_{TADF}) vs. 1/T plot of P1.

1/T (K^{-1})	ln(k_{TADF})
0.00333	14.32634
0.004	14.29355
0.005	14.41335
0.00667	14.01396
0.01	13.62489
0.01333	13.22218
0.01667	13.03161

Table A6. Data for FWHM vs. 1/T plot.

1/T (K^{-1})	FWHM (eV)
0.025	0.2179
0.01667	0.2233
0.0125	0.2417
0.01	0.266
0.00833	0.2843
0.00714	0.3081
0.00667	0.325
0.00556	0.3408
0.005	0.3646
0.00455	0.3861
0.00417	0.3937
0.00385	0.4067
0.00357	0.4277
0.00333	0.4357

Table A7. Data for FWHM vs. T plot.

T (K)	FWHM (eV)
40	0.2179
60	0.2233
80	0.2417
100	0.266
120	0.2843
140	0.3081
150	0.325
180	0.3408
200	0.3646
220	0.3861
240	0.3937
260	0.4067
280	0.4277
300	0.4357

4.5.3. Appendix 3. A Non-centrosymmetric Cu(I)-Iodide Coordination Polymer

4.5.3.1. Introduction

Crystallographic space groups containing an inversion center are called centrosymmetric space groups. However, in some cases, the difference in the crystal packing may lead to the lack of an inversion center and the crystal becomes non-centrosymmetric. Non-centrosymmetric crystal structures may arise in organic molecular crystals[72,73], metal-halides[74,75], and metal-oxide semiconductors[76,77]. The emergence of non-centrosymmetry depends upon the arrangement of the metal, halide, and oxide moieties along with the symmetry elements associated with the participating molecules and the ligands. Non-centrosymmetry in crystal structures can lead to the evolution of several intriguing properties, such as second-harmonic generation[75], piezoelectricity[72], and bulk photovoltaic effect[78], which cannot be observed in the presence of an inversion center. Previously, the phenomena have been broadly studied in halide perovskite structures[75,78–80], but other metal-halide structures have remained underexplored.

Here in, we present a non-centrosymmetric Cu(I)-iodide coordination polymer coordinated with 2-amino-3-methylpyridine having a $P2_1$ space group. The bulk crystals were synthesized

by using a two-layer slow diffusion method. The crystal structure and the non-covalent interactions in the bulk crystal have been explored.

4.5.3.2. Experimental Section

Materials and general protocol for synthesis

Copper(I) iodide powder and 2-amino-3-methylpyridine were purchased from Sigma Aldrich and used as received. Ethanol, dichloromethane, acetonitrile, toluene, and *n*-pentane were purchased from Neelchem Corporation.

Characterization techniques

Single-crystal diffraction analysis data were collected at 100K with a BRUKER KAPPA APEX II CCD Duo diffractometer (operated at 1500 W power: 50 kV, 30 mA) using graphite monochromatic Mo Kα radiation (λ = 0.71073 Å). The structures were solved by direct methods and refined by least-squares against F^2 utilizing the software package SHELXL-97.[50,51] More information on crystal structures can also be obtained from the Cambridge Crystallographic Data Centre under the CCDC deposition number. Powder XRD experiments were performed using BRUKER D8 advanced X-ray diffractometer with a Cu-K_α radiation source.

Synthesis of polymer 3 (P3)

The single crystals were synthesized in a two-layer slow diffusion method. 95 mg of CuI (0.5 mmol) was dissolved in 1 mL saturated aqueous solution of KI. 101 µL (0.5 mmol) of 2-amino-3-methylpyridine was dissolved in 1.5 mL of toluene. The aqueous solution was placed in a glass tube with a diameter of 5 mm and became the bottom layer. The ligand solution was added very slowly along the glass wall with a syringe and it formed the upper layer. The tube was kept closed overnight yielding long rectangular colorless crystals in the middle layer. The product was characterized by using SCXRD and PXRD techniques.

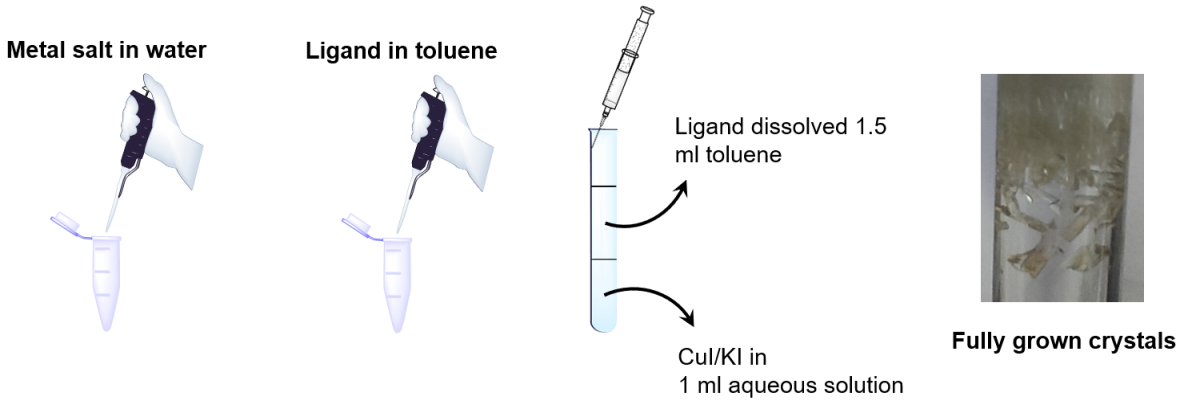

Scheme A1. Synthesis of P3.

Characterization

Table A8. Crystallographic data of P3.

Identification code	3MAPCuI
Empirical formula	$C_2H_2Cu_2I_2N_2$
Formula weight	298.59
Temperature/K	100(2)
Crystal system	monoclinic
Space group	$P2_1$
a/Å	9.344(2)
b/Å	4.2401(9)
c/Å	10.699(2)
α/°	90
β/°	109.254(5)
γ/°	90
Volume/Å^3	400.16(15)
Z	2
ρcalcg/cm^3	2.478
μ/mm^{-1}	6.509
F(000)	280.0
Crystal size/mm^3	0.31 × 0.04 × 0.02
Radiation	MoKα (λ = 0.71073)
2Θ range for data collection/°	4.032 to 56.876
Index ranges	$-12 \leq h \leq 12$, $-5 \leq k \leq 5$, $-14 \leq l \leq 14$
Reflections collected	4296
Independent reflections	2032 [Rint = 0.0473, Rsigma = 0.0508]
Data/restraints/parameters	2032/1/92
Goodness-of-fit on F^2	0.697
Final R indexes [I>=2σ (I)]	R1 = 0.0293, wR2 = 0.0842
Final R indexes [all data]	R1 = 0.0298, wR2 = 0.0852
Largest diff. peak/hole / e Å^{-3}	0.67/-1.86

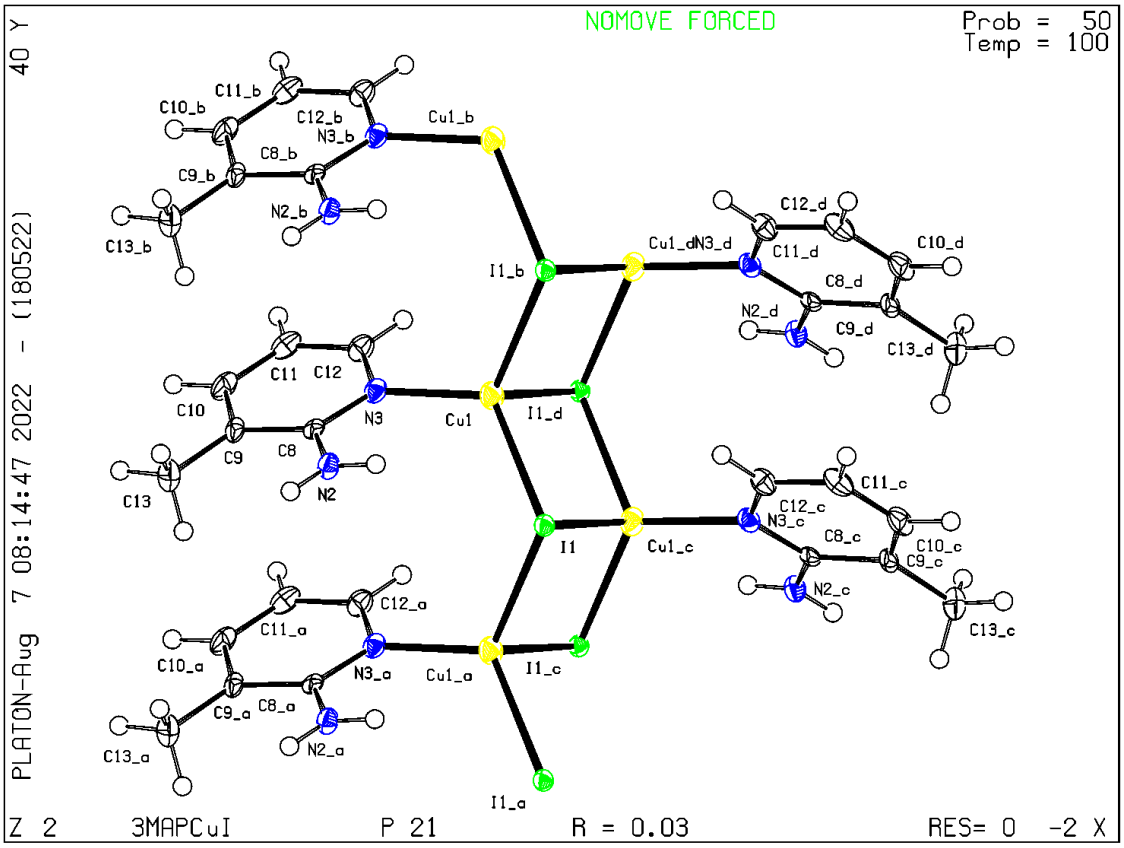

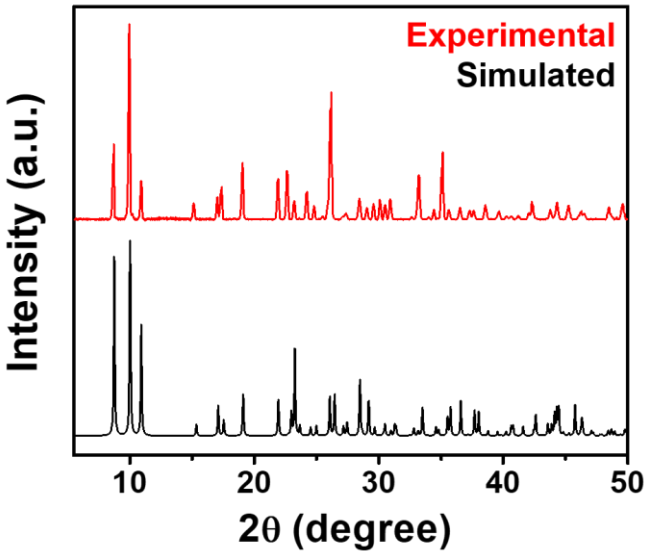

Figure A2. Powder XRD pattern of P3.

Photocurrent measurements.

The photocurrent measurements were performed using an electrochemical workstation (Metrohm) and using a method described below.[81] The crystals (5 mg) of P3 were dispersed in 500 µL ethanol, and naphthol (0.5 wt. %, 10 uL) was added to it, and the disperse was sonicated

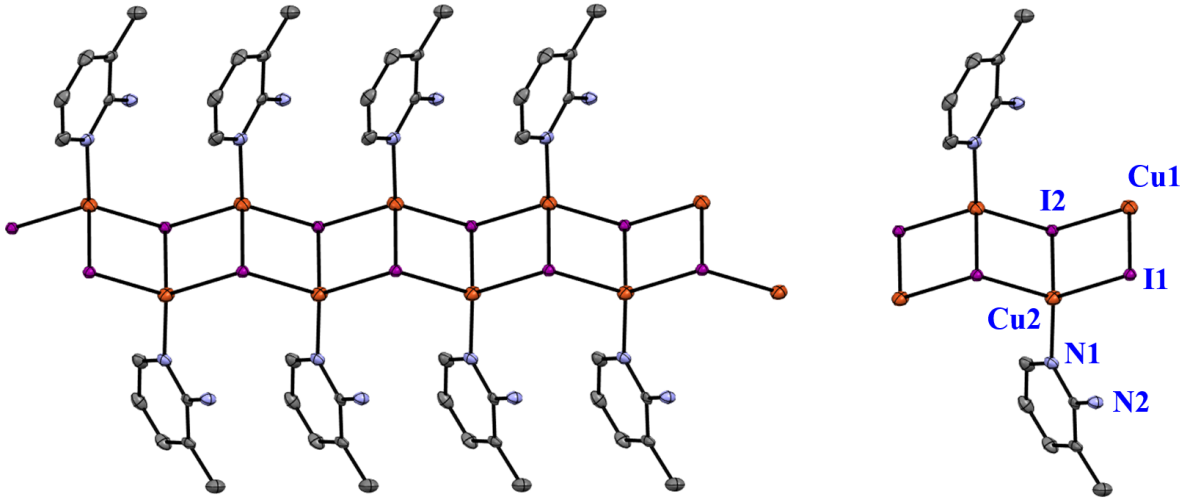

Figure A3. Crystal structure of P3.

for 30 min. Then 50 µL solution was taken from the mixture and drop-casted on a cleaned ITO glass. The coordination polymer-coated film was obtained after evaporation under vacuum for 1 h. The polymer-coated ITO glass was used as the working electrode, a Pt wire was used as the counter electrode, and an Ag/AgCl/Cl^- electrode was used as the reference electrode. A Na_2SO_4 aqueous solution (0.2 M) was used as the electrolyte medium. The measurements were done at a 0 V bias, and 390 nm LED was used as the excitation source.

4.5.3.3. Results and discussion

Crystal structure.

The crystal structure of P3 is shown in **Figure A3**. Cu_2I_2 rhombic moieties are connected in a zigzag staircase fashion and form a coordination polymer. The Cu centers are coordinated to 2-amino-3-methylpyridine ligands. The Cu-I (along the chain), Cu-I (perpendicular to the chain), Cu-N, and Cu-Cu distances were found to be 2.62 Å and 2.64 Å, 2.76 Å, 2.03 Å, and 3.33 Å, respectively. The Cu-Cu distance is much larger than the van der Waals distance (2.8 Å) of the Cu atom, indicating the complete absence of cuprophilic interaction.

Non-covalent interactions in the bulk phase.

Several non-covalent interactions with high enthalpy values can moderately influence several of the photophysical processes in the solid phase. In order to evaluate these possible influences, Hirshfeld surface analysis calculations were carried out using the crystal structures (**Figure A4**). The normalized distance (d_{norm}) mapped over the Hirshfeld surface is given in **Figure A5a**. The histogram containing the percentage contributions of several interactions is shown in

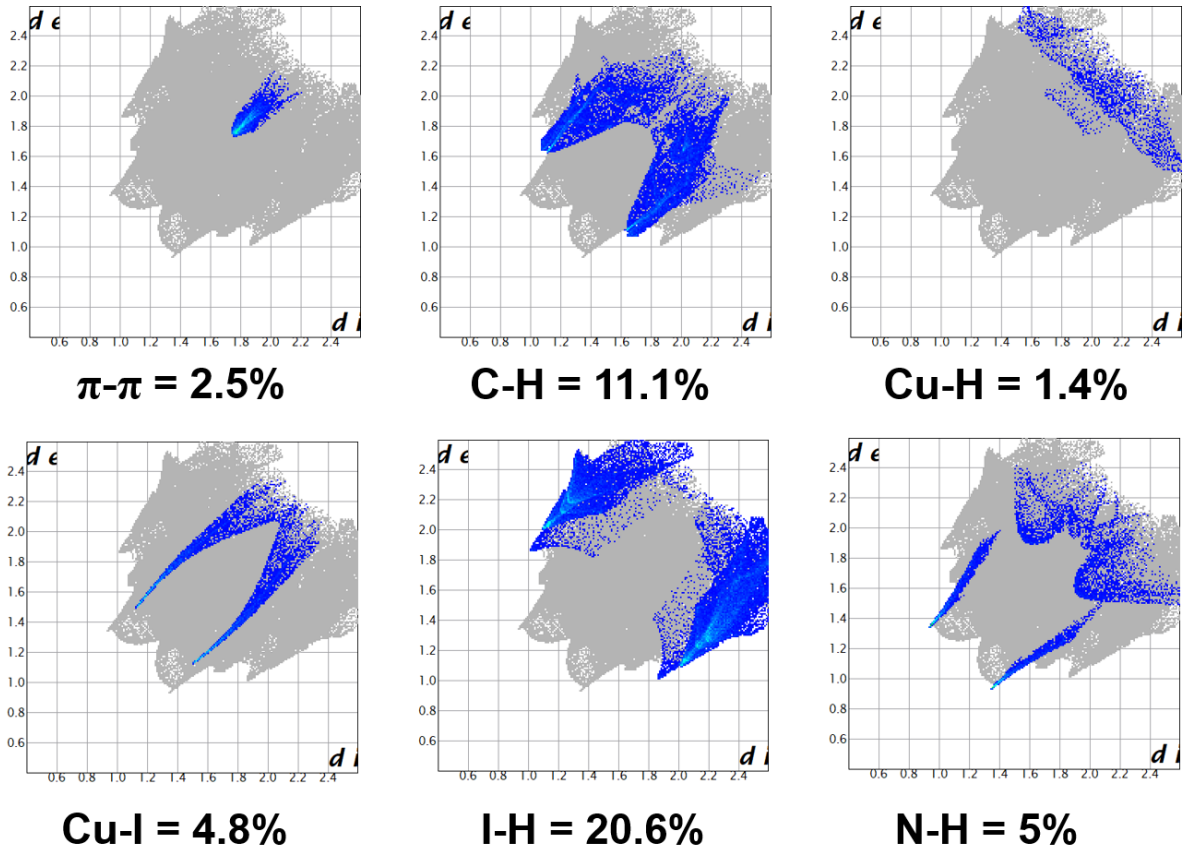

Figure A4. Hirshfeld surface analysis[82–84] of the complexes. Fingerprint plots revealing quantitative descriptions of several non-covalent interactions were quantified by using Crystal Explorer 3.1 software[85]. Fingerprint plots from normalized distance (d_{norm}) mapped over Hirshfeld surface to calculate the percentage of each non-covalent interaction for P3.

Figure A5b. We observe that in both complexes, strong interactions such as N···H (enthalpy ~2.97 kJ/mol)[63], C···H (enthalpy ~10.3 kJ/mol)[64], and I···H (enthalpy ~16-25 kJ/mol)[65] are present in the bulk phase. These non-covalent interactions can effectively enhance the ISC rate associated with the singlet and triplet excited states in the bulk-phase, which is essential for efficient triplet state harvesting. In addition, strong non-covalent interactions can also dictate the direction of the polarizability tensor in the bulk condensed phase, which can have a larger impact on the non-linear optical (NLO) properties of the complexes.[66,67]

Photocurrent activities.

Light on-off cycle of photocurrent on P3 was performed where it was observed that upon exposure of 390 nm LED light the photoinduced current of the sample reached ~1.4 μAcm^{-2} at a constant bias of 0 V (**Figure A6b**). The constant current of ~1.4 μAcm^{-2} was retained till 900 s time span. Further studies are going on to characterize the photovoltaic properties of this sample.

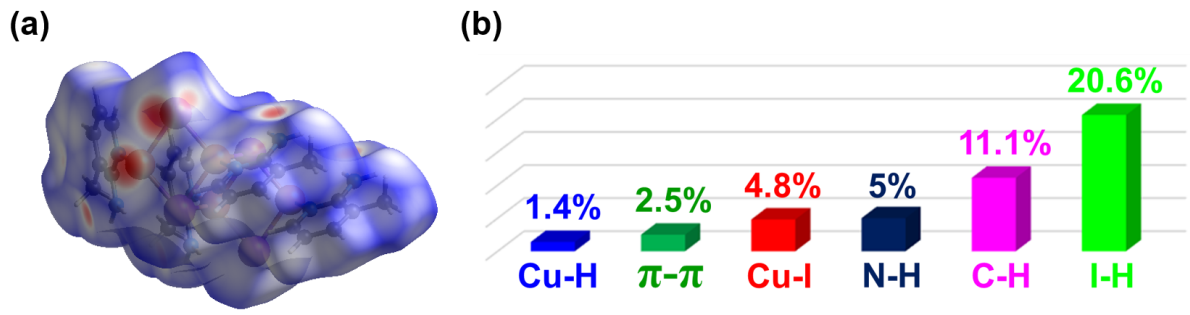

Figure A5. Normalized distance (d_{norm}) mapped over Hirshfeld surface for (a) P3. Histogram of the percentagecontributions of different noncovalent interactions in (b) P3.

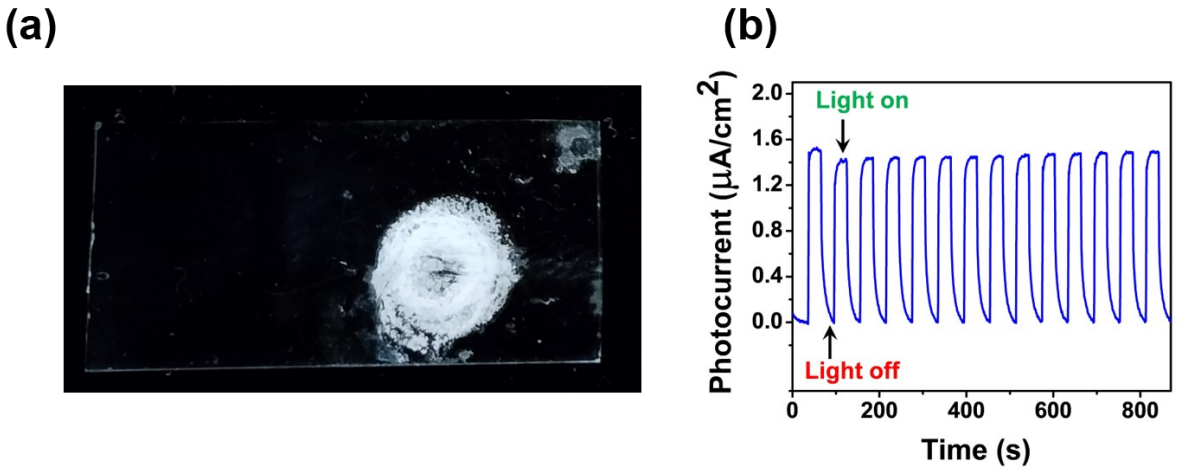

Figure A6. (a) P3-coated ITO glass, (b) Light on-off cycle of the photocurrent activities of P3.

4.5.3.4. Conclusion and future direction

A non-centrosymmetric Cu(I)-iodide coordination polymer was successfully synthesized with high purity and crystallinity. The presence of several strong non-covalent interactions within the bulk phase was identified. There is a large pool of possibilities that can explore several useful and intriguing properties such as piezoelectric effects, second-harmonic generation, and bulk photovoltaic effect in this system.

Bibliography

1 C. Chen, R.-H. Li, B.-S. Zhu, K.-H. Wang, J.-S. Yao, Y.-C. Yin, M.-M. Yao, H.-B. Yao and S.-H. Yu, *Angew. Chemie Int. Ed.*, 2018, **57**, 7106–7110.

2 M. W. Mara, K. A. Fransted and L. X. Chen, *Coord. Chem. Rev.*, 2015, **282**–**283**, 2–18.

3 N. Zhang, H. Hu, L. Qu, R. Huo, J. Zhang, C. Duan, Y. Meng, C. Han and H. Xu, *J. Am. Chem. Soc.*, 2022, **144**, 6551–6557.

4 H. Li, Y. Lv, Z. Zhou, H. Tong, W. Liu and G. Ouyang, *Angew. Chemie Int. Ed.*, 2022, **61**, e202115225.

5 P. Darnige, Y. Thimont, L. Presmanes and A. Barnabé, *J. Mater. Chem. C*, 2023, **11**, 630–644.

6 C. Wegeberg and O. S. Wenger, *JACS Au*, 2021, **1**, 1860–1876.

7 M. Klein, N. Rau, M. Wende, J. Sundermeyer, G. Cheng, C.-M. Che, A. Schinabeck and H. Yersin, *Chem. Mater.*, 2020, **32**, 10365–10382.

8 R. Hamze, J. L. Peltier, D. Sylvinson, M. Jung, J. Cardenas, R. Haiges, M. Soleilhavoup, R. Jazzar, P. I. Djurovich, G. Bertrand and M. E. Thompson, *Science (80-.).*, 2019, **363**, 601–606.

9 S. Wang, E. E. Morgan, S. Panuganti, L. Mao, P. Vishnoi, G. Wu, Q. Liu, M. G. Kanatzidis, R. D. Schaller and R. Seshadri, *Chem. Mater.*, 2022, **34**, 3206–3216.

10 J. Chatterjee, A. Chatterjee, R. Tanwar, P. Panwaria, S. Saikia, M. D. Ambhore, P. Mandal and P. Hazra, *J. Phys. Chem. Lett.*, 2024, **15**, 6069–6080.

11 J. López, J. G. Platas, U. R. Rodríguez-Mendoza, J. I. Martínez, S. Delgado, G. Lifante-Pedrola, E. Cantelar, R. Guerrero-Lemus, C. Hernández-Rodríguez and P. Amo-Ochoa, *Inorg. Chem.*, 2021, **60**, 1208–1219.

12 S. Perruchas, C. Tard, X. F. Le Goff, A. Fargues, A. Garcia, S. Kahlal, J.-Y. Saillard, T. Gacoin and J.-P. Boilot, *Inorg. Chem.*, 2011, **50**, 10682–10692.

13 B. Huitorel, H. El Moll, R. Utrera-Melero, M. Cordier, A. Fargues, A. Garcia, F. Massuyeau, C. Martineau-Corcos, F. Fayon, A. Rakhmatullin, S. Kahlal, J.-Y. Saillard, T. Gacoin and S. Perruchas, *Inorg. Chem.*, 2018, **57**, 4328–4339.

14 W. Liu, Y. Fang, G. Z. Wei, S. J. Teat, K. Xiong, Z. Hu, W. P. Lustig and J. Li, *J. Am. Chem. Soc.*, 2015, **137**, 9400–9408.

15 Z. Ma, Z. Shi, C. Qin, M. Cui, D. Yang, X. Wang, L. Wang, X. Ji, X. Chen, J. Sun, D. Wu, Y. Zhang, X. J. Li, L. Zhang and C. Shan, *ACS Nano*, 2020, **14**, 4475–4486.

16 M.-H. Du, *ACS Energy Lett.*, 2020, **5**, 464–469.

17 R. Lin, Q. Zhu, Q. Guo, Y. Zhu, W. Zheng and F. Huang, *J. Phys. Chem. C*, 2020, **124**, 20469–20476.

18 L. Lian, P. Zhang, G. Liang, S. Wang, X. Wang, Y. Wang, X. Zhang, J. Gao, D. Zhang,

L. Gao, H. Song, R. Chen, X. Lan, W. Liang, G. Niu, J. Tang and J. Zhang, *ACS Appl. Mater. Interfaces*, 2021, **13**, 22749–22756.

19 A. V Shamsieva, I. E. Kolesnikov, I. D. Strelnik, T. P. Gerasimova, A. A. Kalinichev, S. A. Katsyuba, E. I. Musina, E. Lähderanta, A. A. Karasik and O. G. Sinyashin, *J. Phys. Chem. C*, 2019, **123**, 25863–25870.

20 R. Zhang, H. Xie, F. Wang, Q. Zhao, L. Meng, Z. Tang, B. Su and H. Liu, *Laser Photon. Rev.*, 2024, **n/a**, 2400450.

21 A. Kobayashi, Y. Yoshida, M. Yoshida and M. Kato, *Chem. – A Eur. J.*, 2018, **24**, 14750–14759.

22 A. V Artem'ev, E. P. Doronina, M. I. Rakhmanova, X. Hei, D. V Stass, O. A. Tarasova, I. Y. Bagryanskaya, D. G. Samsonenko, A. S. Novikov, N. A. Nedolya and J. Li, *Dalt. Trans.*, 2023, **52**, 4017–4027.

23 Z. Liu, J. Qiu, F. Wei, J. Wang, X. Liu, M. G. Helander, S. Rodney, Z. Wang, Z. Bian, Z. Lu, M. E. Thompson and C. Huang, *Chem. Mater.*, 2014, **26**, 2368–2373.

24 M. Xie, C. Han, Q. Liang, J. Zhang, G. Xie and H. Xu, *Sci. Adv.*, 2024, **5**, eaav9857.

25 M. Wallesch, D. Volz, C. Fléchon, D. M. Zink, S. Bräse and T. Baumann, in *Proc.SPIE*, 2014, vol. 9183, p. 918309.

26 X. Li, J. Zhang, Z. Zhao, X. Yu, P. Li, Y. Yao, Z. Liu, Q. Jin, Z. Bian, Z. Lu and C. Huang, *ACS Appl. Mater. Interfaces*, 2019, **11**, 3262–3270.

27 M. Xie, C. Han, J. Zhang, G. Xie and H. Xu, *Chem. Mater.*, 2017, **29**, 6606–6610.

28 N. Zhang, Y. Li, S. Han, Y. Wei, H. Hu, R. Huo, C. Duan, J. Zhang, C. Han, G. Xie and H. Xu, *Angew. Chemie Int. Ed.*, 2023, **62**, e202305018.

29 T.-Y. Li, S.-J. Zheng, P. I. Djurovich and M. E. Thompson, *Chem. Rev.*, 2024, **124**, 4332–4392.

30 J.-J. Wang, L.-Z. Feng, G. Shi, J.-N. Yang, Y.-D. Zhang, H. Xu, K.-H. Song, T. Chen, G. Zhang, X.-S. Zheng, F. Fan, Z. Xiao and H.-B. Yao, *Nat. Photonics*, 2024, **18**, 200–206.

31 Y. Okano, H. Ohara, A. Kobayashi, M. Yoshida and M. Kato, *Inorg. Chem.*, 2016, **55**, 5227–5236.

32 A. Schinabeck, M. J. Leitl and H. Yersin, *J. Phys. Chem. Lett.*, 2018, **9**, 2848–2856.

33 S. K. Gibbons, R. P. Hughes, D. S. Glueck, A. T. Royappa, A. L. Rheingold, R. B. Arthur, A. D. Nicholas and H. H. Patterson, *Inorg. Chem.*, 2017, **56**, 12809–12820.

34 J. M. Busch, D. S. Koshelev, A. A. Vashchenko, O. Fuhr, M. Nieger, V. V Utochnikova and S. Bräse, *Inorg. Chem.*, 2021, **60**, 2315–2332.

35 A. Y. Baranov, M. I. Rakhmanova, X. Hei, D. G. Samsonenko, D. V Stass, I. Y. Bagryanskaya, M. R. Ryzhikov, V. P. Fedin, J. Li and A. V Artem'ev, *Chem. Commun.*, 2023, **59**, 2923–2926.

36 K. Xu, B.-L. Chen, F. Yang, L. Liu, X.-X. Zhong, L. Wang, X.-J. Zhu, F.-B. Li, W.-Y. Wong and H.-M. Qin, *Inorg. Chem.*, 2021, **60**, 4841–4851.

37 S. Li, J. Luo, J. Liu and J. Tang, *J. Phys. Chem. Lett.*, 2019, **10**, 1999–2007.

38 Q. Guo, X. Zhao, B. Song, J. Luo and J. Tang, *Adv. Mater.*, 2022, **34**, 2201008.

39 Q. Hu, C. Zhang, X. Wu, G. Liang, L. Wang, X. Niu, Z. Wang, W.-D. Si, Y. Han, R. Huang, J. Xiao and D. Sun, *Angew. Chemie Int. Ed.*, 2023, **62**, e202217784.

40 R. Chakraborty and A. Nag, *Phys. Chem. Chem. Phys.*, 2021, **23**, 82–93.

41 R. Scholz, A. Y. Kobitski, D. R. T. Zahn and M. Schreiber, *Phys. Rev. B*, 2005, **72**, 245208.

42 W. B. Fowler, M. J. Marrone and M. N. Kabler, *Phys. Rev. B*, 1973, **8**, 5909–5919.

43 R. T. Williams, K. S. Song, W. L. Faust and C. H. Leung, *Phys. Rev. B*, 1986, **33**, 7232–7240.

44 Y. Shi, W. Zhao, Z. Ma, G. Xiao and B. Zou, *Chem. Sci.*, 2021, **12**, 14711–14717.

45 F. Jiang, Z. Wu, M. Lu, Y. Gao, X. Li, X. Bai, Y. Ji and Y. Zhang, *Adv. Mater.*, 2023, **35**, 2211088.

46 B. Yang and K. Han, *J. Phys. Chem. Lett.*, 2021, **12**, 8256–8262.

47 J. Yu, J. Kong, W. Hao, X. Guo, H. He, W. R. Leow, Z. Liu, P. Cai, G. Qian, S. Li, X. Chen and X. Chen, *Adv. Mater.*, 2019, **31**, 1806385.

48 A. V Dev, M. G. Basavarajappa, S. S. Deshpande, P. Mukherjee, A. Ajayakumar, C. Muthu, T. Okamoto, S. Chakraborty, D. D. Sarma, V. Biju and C. Vijayakumar, *Chem. Mater.*, 2024, **36**, 5912–5921.

49 S. Chatterjee, P. Mukherjee, A. Sen and P. Sen, *J. Phys. Chem. Lett.*, 2024, **15**, 4191–4196.

50 G. M. Sheldrick, *Acta Crystallogr. Sect. A*, 2008, **64**, 112–122.

51 G. M. Sheldrick, *Acta Crystallogr. Sect. C Struct. Chem.*, 2015, **71**, 3–8.

52 G. Kresse and J. Furthmüller, *Comput. Mater. Sci.*, 1996, **6**, 15–50.

53 G. Kresse and J. Hafner, *Phys. Rev. B*, 1994, **49**, 14251–14269.

54 G. Kresse and J. Furthmüller, *Phys. Rev. B*, 1996, **54**, 11169–11186.

55 G. Kresse and D. Joubert, *Phys. Rev. B*, 1999, **59**, 1758–1775.

56 P. E. Blöchl, *Phys. Rev. B*, 1994, **50**, 17953–17979.

57 S. Grimme, J. Antony, S. Ehrlich and H. Krieg, *J. Chem. Phys.*, 2010, **132**, 154104.

58 S. Grimme, S. Ehrlich and L. Goerigk, *J. Comput. Chem.*, 2011, **32**, 1456–1465.

59 A. Kokalj, *J. Mol. Graph. Model.*, 1999, **17**, 176–179.

60 A. Kokalj, *Comput. Mater. Sci.*, 2003, **28**, 155–168.

61 J. Paier, M. Marsman, K. Hummer, G. Kresse, I. C. Gerber and J. G. Ángyán, *J. Chem. Phys.*, 2006, **124**, 154709.

62 M. D. Kessler, T. Duston, M. Parker and R. D. Pike, *Inorganica Chim. Acta*, 2020, **509**, 119706.

63 K. Wendler, J. Thar, S. Zahn and B. Kirchner, *J. Phys. Chem. A*, 2010, **114**, 9529–9536.

64 A. Chatterjee, J. Chatterjee, S. Sappati, T. Sheikh, R. M. Umesh, M. D. Ambhore, M. Lahiri and P. Hazra, *J. Phys. Chem. B*, 2021, **125**, 12832–12846.

65 D. A. Smith, L. Brammer, C. A. Hunter and R. N. Perutz, *J. Am. Chem. Soc.*, 2014, **136**, 1288–1291.

66 T. Viswanathan and N. Palanisami, *New J. Chem.*, 2021, **45**, 12509–12518.

67 C. L. Shiny, A. Rathika, J. D. D. Tarika, S. Alen and T. J. Beaula, *Polycycl. Aromat. Compd.*, 2023, **43**, 4621–4639.

68 R. Tang, S. Xu, T.-L. Lam, G. Cheng, L. Du, Q. Wan, J. Yang, F.-F. Hung, K.-H. Low, D. L. Phillips and C.-M. Che, *Angew. Chemie Int. Ed.*, 2022, **61**, e202203982.

69 Q. Benito, X. F. Le Goff, G. Nocton, A. Fargues, A. Garcia, A. Berhault, S. Kahlal, J.-Y. Saillard, C. Martineau, J. Trébosc, T. Gacoin, J.-P. Boilot and S. Perruchas, *Inorg. Chem.*, 2015, **54**, 4483–4494.

70 A. K. Viswanath, J. I. Lee, D. Kim, C. R. Lee and J. Y. Leem, *Phys. Rev. B*, 1998, **58**, 16333–16339.

71 J. Luo, X. Wang, S. Li, J. Liu, Y. Guo, G. Niu, L. Yao, Y. Fu, L. Gao, Q. Dong, C. Zhao, M. Leng, F. Ma, W. Liang, L. Wang, S. Jin, J. Han, L. Zhang, J. Etheridge, J. Wang, Y. Yan, E. H. Sargent and J. Tang, *Nature*, 2018, **563**, 541–545.

72 S. Bhunia, S. Chandel, S. K. Karan, S. Dey, A. Tiwari, S. Das, N. Kumar, R. Chowdhury, S. Mondal, I. Ghosh, A. Mondal, B. B. Khatua, N. Ghosh and C. M. Reddy, *Science*, 2021, **373**, 321–327.

73 S. Mondal, P. Tanari, S. Roy, S. Bhunia, R. Chowdhury, A. K. Pal, A. Datta, B. Pal and C. M. Reddy, *Nat. Commun.*, 2023, **14**, 6589.

74 F. Ge, B.-H. Li, P. Cheng, G. Li, Z. Ren, J. Xu and X.-H. Bu, *Angew. Chemie Int. Ed.*, 2022, **61**, e202115024.

75 R. Chakraborty, P. K. Rajput, G. M. Anilkumar, S. Maqbool, R. Das, A. Rahman, P. Mandal and A. Nag, *J. Am. Chem. Soc.*, 2023, **145**, 1378–1388.

76 D. Puggioni and J. M. Rondinelli, *Nat. Commun.*, 2014, **5**, 3432.

77 I. C. Amaechi, A. Hadj Youssef, A. Dörfler, Y. González, R. Katoch and A. Ruediger, *Angew. Chemie Int. Ed.*, 2022, **61**, e202207975.

78 P.-J. Huang, K. Taniguchi and H. Miyasaka, *J. Am. Chem. Soc.*, 2019, **141**, 14520–14523.

79 A. Phutela, S. Sheoran, D. Gill and S. Bhattacharya, *J. Mater. Chem. C*, 2024, **12**, 2165–2172.

80 W. Mihalyi-Koch, S. Guo, Z. Dai, D. Pan, D. P. Lafayette, J. M. Scheeler, K. M. Sanders, S. J. Teat, J. C. Wright, X. Lü, A. M. Rappe and S. Jin, *Chem*, , DOI:https://doi.org/10.1016/j.chempr.2024.03.012.

81 X.-Q. Liang, R. K. Gupta, Y.-W. Li, H.-Y. Ma, L.-N. Gao, C.-H. Tung and D. Sun, *Inorg. Chem.*, 2020, **59**, 2680–2688.

82 A. D. Martin, J. Britton, T. L. Easun, A. J. Blake, W. Lewis and M. Schröder, *Cryst. Growth Des.*, 2015, **15**, 1697–1706.

83 J. J. McKinnon, D. Jayatilaka and M. A. Spackman, *Chem. Commun.*, 2007, 3814–3816.

84 A. D. Martin, K. J. Hartlieb, A. N. Sobolev and C. L. Raston, *Cryst. Growth Des.*, 2010,

10, 5302–5306.

85 P. R. Spackman, M. J. Turner, J. J. McKinnon, S. K. Wolff, D. J. Grimwood, D. Jayatilaka and M. A. Spackman, *J. Appl. Crystallogr.*, 2021, **54**, 1006–1011.

Chapter 5:

Thesis Summary and Future Outlook

5.1. Thesis summary

The central motivation of this thesis is to explore the possibility of achieving broadband emission tunability along with investigating several triplet harvesting pathways and non-linear photon up-conversion properties in organic-inorganic hybrid Cu(I)-based frameworks. At first, we showcased that time-dependent broadband emission tunability can be achieved in a thiol-templated Cu nanocluster system by an *in-situ* ligand engineering process. Further, we went on to improve the emission yield of the system by effective utilization of triplet excitons in Cu(I)-iodide-based frameworks, where the extent of spin-orbit coupling is much higher. Iodide-bridged Cu_2I_2 complexes have emerged as potential resources of triplet excitons owing to the strong charge transfer emission and intrinsically high quantum yield. However, shorter Cu-Cu distance can give rise to cluster-centered emissive states in these complexes due to strong Cu···Cu bonding interactions, which can significantly quench the emission yield of the complexes. We proposed a ligand engineering approach, which could successfully eradicate the Cu···Cu bonding interactions by increasing the Cu-Cu distance and thereby activating TADF in iodide-bridged Cu_2I_2 complex. We further applied the ligand engineering approach in higher-order Cu(I)-iodide frameworks to regulate the triplet harvesting pathways and structure-property relationship. We showcased that a well-designed ligand engineering approach can lead to a structural switch in Cu(I)-iodide-based organic-inorganic polymers. This approach results in a complete paradigm shift in the triplet harvesting pathways of these polymers from charge transfer-based TADF to self-trapped excitonic emission. Moreover, we have explored the non-linear photon up-conversion properties of these frameworks, which can be utilized in generating high-energy photons. These phenomena include third-harmonic generation, two-photon excited luminescence, multi-photon luminescence, and so on, which emerge due to their high charge transfer nature, bulk-phase polarizability, and crystal packing arrangements.

5.2. Future outlook

Present findings show substantial progress in the field of Cu(I)-based emitters in terms of their emission tunability, efficiency in optoelectronics, and photosensitization yield. However, there are several accessible avenues through which further exploration and advancement can take place. New ligands with high donation strength and low-lying π*-orbitals could be designed to enhance the stability and emission efficiency of the Cu(I)-halide clusters and complexes. These ligands include several types of carbenes and their derivatives which are strong σ-donor as well as strong π-acceptor. Exploring the spin-vibronic mechanism of the ISC process of these

clusters and complexes is another branch of study that remains underexplored. Several ultrafast spectroscopic techniques, such as transient absorption and time-resolved IR, could be employed to explore these mechanisms. In the series of Cu(I)-halide emitters and newly developed carbene-Cu-amide emitters, the emergence of red and near-IR emission and the structure-property relationship is rarely documented in the literature. It could be another path of exploration in the near future. Another important and relevant application of these TADF emitters is in the field of photocatalysis, particularly to activate the bonds with high energy. These inorganic TADF emitters can also be used to fabricate efficient triplet-triplet annihilation-upconversion (TTA-UC) system, where a small ΔE_{ST} value can increase the upconverted photon energy and strong SOC can increase the yield of triplet excitons as well. As the thesis targets the emission tunability and efficient harvest of triplet excitons through TADF, the materials can be applied to numerous kinds of reduction reactions. Color-tunable copper nanoclusters can be used as photocatalysts for organic reduction reactions across the reduction potentials. The TADF-active complexes can harvest larger number of excitons compared to other fluorescent molecules, and thus these can be used to improve the yield of several organic reduction reactions.

List of Publications

Publications included in the thesis

1. Joy Chatterjee, Riteeka Tanwar, Avinash Mahapatra, Anupama S., Madan D. Ambhore, Mukul Kabir, Atikur Rahman, Pankaj Mandal, and Partha Hazra*. Second-order Non-linearity and Anomalous Photovoltaic Effect in a Non-centrosymmetric Cu(I)-iodide Coordination Polymer. *Manuscript under preparation*.
2. Joy Chatterjee, Riteeka Tanwar, Anupama S., Abhijit Chatterjee, Madan D. Ambhore, Mukul Kabir, Pankaj Mandal, and Partha Hazra*. Ligand-Mediated Structural Switch in Cu(I)-Iodide Polymer: Engineering Triplet Harvesting Pathways and Non-linear Optical Properties. *Manuscript submitted*.
3. Joy Chatterjee, Abhijit Chatterjee, Riteeka Tanwar, Prakash Panwaria, Sajid Saikia, Madan D. Ambhore, Pankaj Mandal,* and Partha Hazra*. Activation of TADF in Photon Upconverting Crystals of Dinuclear Cu(I)-Iodide Complexes by Ligand Engineering. *J. Phys. Chem. Lett.* **2024**, 15, 6069−6080.
4. Joy Chatterjee, Abhijit Chatterjee and Partha Hazra*. Intrinsic-to-Extrinsic Emission Tuning in Luminescent Cu Nanoclusters by *in-situ* Ligand Engineering. *Phys. Chem. Chem. Phys.* **2021**, 23, 25850-25865.

Publications not included in the thesis

5. Moushakhi Ghosh, Joy Chatterjee, Prakash Panwaria, Aswath Kudlu, Srinu Tothadi, and Shabana Khan*. Silylene-Copper-Amide Emitters: From Thermally Activated Delayed Fluorescence to Dual Emission. *Angew. Chem. Int. Ed.* **2024**, e202410792.
6. Abhijit Chatterjee, Joy Chatterjee, Subrahmanyam Sappati, Riteeka Tanwar, Madan D. Ambhore, Habibul Arfin, Rintu M. Umesh, Mayurika Lahiri, Pankaj Mandal, and Partha Hazra*. Engineering TADF, Mechanochromism, and Second Harmonic Up-conversion Properties in Regioisomeric Substitution Space. *Chem. Sci.* **2023**, 14, 13832-13841.
7. Joy Chatterjee, Raj Kumar Koninti, Prakash Panwaria, and Partha Hazra*. Excited State Intramolecular Double-proton Transfer Dynamics of [2,2′-bipyridyl]-3,3′-diol Inside Mesoporous Silica Nanochannels. *Chemical Physics Impact* **2023**, 7, 100285.
8. Rohit Kumar, Sanjukta Pahar, Joy Chatterjee, Soumya Ranjan Dash, Rajesh G. Gonnade, Kumar Vanka, and Sakya S. Sen*. Luminescent Magnesium Complexes with Intra- and Inter-ligand Charge Transfer. *Chem. Commun.* **2022**, 58, 11843-11846.

9. Abhijit Chatterjee, Joy Chatterjee, Subrahmanyam Sappati, Tariq Sheikh, Rintu M. Umesh, Madan D. Ambhore, Mayurika Lahiri, and Partha Hazra*. Emergence of Aggregation Induced Emission (AIE), Room-Temperature Phosphorescence (RTP), and Multistimuli Response from a Single Organic Luminogen by Directed Structural Modification. *J. Phys. Chem. B* **2021**, 125, 12832–12846.

Copyrights and permissions

American Physical Society
Reuse and Permissions License

Figure 1.2a

21-Jun-2024

This license agreement between the American Physical Society ("APS") and Joy Chatterjee ("You") consists of your license details and the terms and conditions provided by the American Physical Society and SciPris.

Licensed Content Information

License Number:	**RNP/24/JUN/080539**
License date:	21-Jun-2024
DOI:	10.1103/PhysRevLett.93.077402
Title:	Highly Fluorescent, Water-Soluble, Size-Tunable Gold Quantum Dots
Author:	Jie Zheng, Caiwei Zhang, and Robert M. Dickson
Publication:	Physical Review Letters
Publisher:	American Physical Society
Cost:	USD $ 0.00

Request Details

Does your reuse require significant modifications: No

Specify intended distribution locations:	Worldwide
Reuse Category:	Reuse in a thesis/dissertation
Requestor Type:	Student
Items for Reuse:	Figures/Tables
Number of Figure/Tables:	1
Figure/Tables Details:	FIG. 1 (color). (a) Excitation (dashed) and emission (solid) spectra of different gold nanoclusters. Emission from the longest wavelength sample was limited by the detector response. Excitation and em
Format for Reuse:	Print and Electronic
Total number of print copies:	Up to 1000

Information about New Publication:

University/Publisher:	Indian Institute of Science Education and Research Pune
Title of dissertation/thesis:	Emission tunability, triplet state harvesting, and photon up-conversion properties in selected organic-inorganic hybrid Cu(I)-based frameworks.
Author(s):	Joy Chatterjee
Expected completion date:	Sep. 2024

License Requestor Information

Name:	Joy Chatterjee
Affiliation:	Individual
Email Id:	chatterjee.joy@students.iiserpune.ac.in
Country:	India

American Physical Society
Reuse and Permissions License

TERMS AND CONDITIONS

The American Physical Society (APS) is pleased to grant the Requestor of this license a non-exclusive, non-transferable permission, limited to Print and Electronic format, provided all criteria outlined below are followed.

1. You must also obtain permission from at least one of the lead authors for each separate work, if you haven't done so already. The author's name and affiliation can be found on the first page of the published Article.

2. For electronic format permissions, Requestor agrees to provide a hyperlink from the reprinted APS material using the source material's DOI on the web page where the work appears. The hyperlink should use the standard DOI resolution URL, http://dx.doi.org/{DOI}. The hyperlink may be embedded in the copyright credit line.

3. For print format permissions, Requestor agrees to print the required copyright credit line on the first page where the material appears: "Reprinted (abstract/excerpt/figure) with permission from [(FULL REFERENCE CITATION) as follows: Author's Names, APS Journal Title, Volume Number, Page Number and Year of Publication.] Copyright (YEAR) by the American Physical Society."

4. Permission granted in this license is for a one-time use and does not include permission for any future editions, updates, databases, formats or other matters. Permission must be sought for any additional use.

5. Use of the material does not and must not imply any endorsement by APS.

6. APS does not imply, purport or intend to grant permission to reuse materials to which it does not hold copyright. It is the requestor's sole responsibility to ensure the licensed material is original to APS and does not contain the copyright of another entity, and that the copyright notice of the figure, photograph, cover or table does not indicate it was reprinted by APS with permission from another source.

7. The permission granted herein is personal to the Requestor for the use specified and is not transferable or assignable without express written permission of APS. This license may not be amended except in writing by APS.

8. You may not alter, edit or modify the material in any manner.

9. You may translate the materials only when translation rights have been granted.

10. APS is not responsible for any errors or omissions due to translation.

11. You may not use the material for promotional, sales, advertising or marketing purposes.

12. The foregoing license shall not take effect unless and until APS or its agent, Aptara, receives payment in full in accordance with Aptara Billing and Payment Terms and Conditions, which are incorporated herein by reference.

13. Should the terms of this license be violated at any time, APS or Aptara may revoke the license with no refund to you and seek relief to the fullest extent of the laws of the USA. Official written notice will be made using the contact information provided with the permission request. Failure to receive such notice will not nullify revocation of the permission.

14. APS reserves all rights not specifically granted herein.

15. This document, including the Aptara Billing and Payment Terms and Conditions, shall be the entire agreement between the parties relating to the subject matter hereof.

Marketplace

Figure 1.2b

Order Date	22-Jun-2024	**Type of Use**	Republish in a thesis/dissertation
Order License ID	1497043-1		
ISSN	1545-1593	**Publisher**	ANNUAL REVIEWS
		Portion	Image/photo/illustration

LICENSED CONTENT

Publication Title	Annual review of physical chemistry	**Publication Type**	e-Journal
Article Title	Highly fluorescent noble-metal quantum dots.	**Start Page**	409
		End Page	431
Date	01/01/1950	**Issue**	1
Language	English	**Volume**	58
Country	United States of America	**URL**	http://arjournals.annualreviews.org/loi/physchem
Rightsholder	Annual Reviews, Inc.		

REQUEST DETAILS

Portion Type	Image/photo/illustration	**Distribution**	Worldwide
Number of Images / Photos / Illustrations	1	**Translation**	Original language of publication
Format (select all that apply)	Print, Electronic	**Copies for the Disabled?**	No
		Minor Editing Privileges?	No
Who Will Republish the Content?	Academic institution	**Incidental Promotional Use?**	No
Duration of Use	Life of current and all future editions	**Currency**	USD
Lifetime Unit Quantity	Up to 499		
Rights Requested	Main product		

NEW WORK DETAILS

Title	Emission tunability, triplet state harvesting, and photon up-conversion properties in selected organic-inorganic hybrid Cu(I)-based frameworks.	**Institution Name**	Indian Institute of Science Education and Research Pune
		Expected Presentation Date	2024-09-01
Instructor Name	Joy Chatterjee		

ADDITIONAL DETAILS

Order Reference Number	N/A	**The Requesting Person / Organization to Appear on the License**	Joy Chatterjee

REQUESTED CONTENT DETAILS

Title, Description or Numeric Reference of the Portion(s)	Figure 5	**Title of the Article / Chapter the Portion Is From**	Highly fluorescent noble-metal quantum dots.
Editor of Portion(s)	Zheng, Jie; Nicovich, Philip R.; Dickson, Robert M.	**Author of Portion(s)**	Zheng, Jie; Nicovich, Philip R.; Dickson, Robert M.
Volume / Edition	58	**Issue, if Republishing an Article From a Serial**	1
Page or Page Range of Portion	409-431	**Publication Date of Portion**	2007-05-05

Marketplace Permissions General Terms and Conditions

The following terms and conditions ("General Terms"), together with any applicable Publisher Terms and Conditions, govern User's use of Works pursuant to the Licenses granted by Copyright Clearance Center, Inc. ("CCC") on behalf of the applicable Rightsholders of such Works through CCC's applicable Marketplace transactional licensing services (each, a "Service").

1) **Definitions.** For purposes of these General Terms, the following definitions apply:

"License" is the licensed use the User obtains via the Marketplace platform in a particular licensing transaction, as set forth in the Order Confirmation.

"Order Confirmation" is the confirmation CCC provides to the User at the conclusion of each Marketplace transaction. "Order Confirmation Terms" are additional terms set forth on specific Order Confirmations not set forth in the General Terms that can include terms applicable to a particular CCC transactional licensing service and/or any Rightsholder-specific terms.

"Rightsholder(s)" are the holders of copyright rights in the Works for which a User obtains licenses via the Marketplace platform, which are displayed on specific Order Confirmations.

"Terms" means the terms and conditions set forth in these General Terms and any additional Order Confirmation Terms collectively.

"User" or "you" is the person or entity making the use granted under the relevant License. Where the person accepting the Terms on behalf of a User is a freelancer or other third party who the User authorized to accept the General Terms on the User's behalf, such person shall be deemed jointly a User for purposes of such Terms.

"Work(s)" are the copyright protected works described in relevant Order Confirmations.

2) **Description of Service.** CCC's Marketplace enables Users to obtain Licenses to use one or more Works in accordance with all relevant Terms. CCC grants Licenses as an agent on behalf of the copyright rightsholder identified in the relevant Order Confirmation.

3) **Applicability of Terms.** The Terms govern User's use of Works in connection with the relevant License. In the event of any conflict between General Terms and Order Confirmation Terms, the latter shall govern. User acknowledges that Rightsholders have complete discretion whether to grant any permission, and whether to place any limitations on any grant, and that CCC has no right to supersede or to modify any such discretionary act by a Rightsholder.

4) **Representations; Acceptance.** By using the Service, User represents and warrants that User has been duly authorized by the User to accept, and hereby does accept, all Terms.

5) **Scope of License; Limitations and Obligations.** All Works and all rights therein, including copyright rights, remain the sole and exclusive property of the Rightsholder. The License provides only those rights expressly set forth in the terms and conveys no other rights in any Works

6) **General Payment Terms.** User may pay at time of checkout by credit card or choose to be invoiced. If the User chooses to be invoiced, the User shall: (i) remit payments in the manner identified on specific invoices, (ii) unless otherwise specifically stated in an Order Confirmation or separate written agreement, Users shall remit payments upon receipt of the relevant invoice from CCC, either by delivery or notification of availability of the invoice via the Marketplace platform, and (iii) if the User does not pay the invoice within 30 days of receipt, the User may incur a service charge of 1.5% per month or the maximum rate allowed by applicable law, whichever is less. While User may exercise the rights in the License immediately upon receiving the Order Confirmation, the License is automatically revoked and is null and void, as if it had never been issued, if CCC does not receive complete payment on a timely basis.

7) **General Limits on Use.** Unless otherwise provided in the Order Confirmation, any grant of rights to User (i) involves only the rights set forth in the Terms and does not include subsequent or additional uses, (ii) is non-exclusive and non-transferable, and (iii) is subject to any and all limitations and restrictions (such as, but not limited to, limitations on duration of use or circulation) included in the Terms. Upon completion of the licensed use as set forth in the Order Confirmation, User shall either secure a new permission for further use of the Work(s) or immediately cease any new use of the Work(s) and shall render inaccessible (such as by deleting or by removing or severing links or other locators) any further copies of the Work. User may only make alterations to the Work if and as expressly set forth in the Order Confirmation. No Work may be used in any way that is unlawful, including without limitation if such use would violate applicable sanctions laws or regulations, would be defamatory, violate the rights of third parties (including such third parties' rights of copyright, privacy, publicity, or other tangible or intangible property), or is otherwise illegal, sexually explicit, or obscene. In addition, User may not conjoin a Work with any other material that may result in damage to the reputation of the Rightsholder. Any unlawful use will render any licenses hereunder null and void. User agrees to inform CCC if it becomes aware of any infringement of any rights in a Work and to cooperate with any reasonable request of CCC or the Rightsholder in connection therewith.

8) **Third Party Materials.** In the event that the material for which a License is sought includes third party materials (such as photographs, illustrations, graphs, inserts and similar materials) that are identified in such material as having been used by permission (or a similar indicator), User is responsible for identifying, and seeking separate licenses (under this Service, if available, or otherwise) for any of such third party materials; without a separate license, User may not use such third party materials via the License.

9) **Copyright Notice.** Use of proper copyright notice for a Work is required as a condition of any License granted under the Service. Unless otherwise provided in the Order Confirmation, a proper copyright notice will read substantially as follows: "Used with permission of [Rightsholder's name], from [Work's title, author, volume, edition number and year of copyright]; permission conveyed through Copyright Clearance Center, Inc." Such notice must be provided in a reasonably legible font size and must be placed either on a cover page or in another location that any person, upon gaining access to the material which is the subject of a permission, shall see, or in the case of republication Licenses, immediately adjacent to the Work as used (for example, as part of a by-line or footnote) or in the place where substantially all other credits or notices for the new work containing the republished Work are located. Failure to include the required notice results in loss to the Rightsholder and CCC, and the User shall be liable to pay liquidated damages for each such failure equal to twice the use fee specified in the Order Confirmation, in addition to the use fee itself and any other fees and charges specified.

10) **Indemnity.** User hereby indemnifies and agrees to defend the Rightsholder and CCC, and their respective employees and directors, against all claims, liability, damages, costs, and expenses, including legal fees and expenses, arising out of any use of a Work beyond the scope of the rights granted herein and in the Order Confirmation, or any use of a Work which has been altered in any unauthorized way by User, including claims of defamation or infringement of rights of copyright, publicity, privacy, or other tangible or intangible property.

11) **Limitation of Liability.** UNDER NO CIRCUMSTANCES WILL CCC OR THE RIGHTSHOLDER BE LIABLE FOR ANY DIRECT, INDIRECT, CONSEQUENTIAL, OR INCIDENTAL DAMAGES (INCLUDING WITHOUT LIMITATION DAMAGES FOR LOSS OF BUSINESS PROFITS OR INFORMATION, OR FOR BUSINESS INTERRUPTION) ARISING OUT OF THE USE OR INABILITY TO USE A WORK, EVEN IF ONE OR BOTH OF THEM HAS BEEN ADVISED OF THE POSSIBILITY OF SUCH DAMAGES. In any event, the total liability of the Rightsholder and CCC (including their respective employees and directors) shall not exceed the total amount actually paid by User for the relevant License. User assumes full liability for the actions and omissions of its principals, employees, agents, affiliates, successors, and assigns.

12) **Limited Warranties.** THE WORK(S) AND RIGHT(S) ARE PROVIDED "AS IS." CCC HAS THE RIGHT TO GRANT TO USER THE RIGHTS GRANTED IN THE ORDER CONFIRMATION DOCUMENT. CCC AND THE RIGHTSHOLDER DISCLAIM ALL OTHER WARRANTIES RELATING TO THE WORK(S) AND RIGHT(S), EITHER EXPRESS OR IMPLIED, INCLUDING WITHOUT LIMITATION IMPLIED WARRANTIES OF MERCHANTABILITY OR FITNESS FOR A PARTICULAR PURPOSE. ADDITIONAL RIGHTS MAY BE REQUIRED TO USE ILLUSTRATIONS, GRAPHS, PHOTOGRAPHS, ABSTRACTS, INSERTS, OR OTHER PORTIONS OF THE WORK (AS OPPOSED TO THE ENTIRE WORK) IN A MANNER CONTEMPLATED BY USER; USER UNDERSTANDS AND AGREES THAT NEITHER CCC NOR THE RIGHTSHOLDER MAY HAVE SUCH ADDITIONAL RIGHTS TO GRANT.

13) **Effect of Breach.** Any failure by User to pay any amount when due, or any use by User of a Work beyond the scope of the License set forth in the Order Confirmation and/or the Terms, shall be a material breach of such License. Any breach not cured within 10 days of written notice thereof shall result in immediate termination of such License without further notice. Any unauthorized (but licensable) use of a Work that is terminated immediately upon notice thereof may be liquidated by payment of the Rightsholder's ordinary license price therefor; any unauthorized (and unlicensable) use that is not terminated immediately for any reason (including, for example, because materials containing the Work cannot reasonably be recalled) will be subject to all remedies available at law or in equity, but in no event to a payment of less than three times the Rightsholder's ordinary license price for the most closely analogous licensable use plus Rightsholder's and/or CCC's costs and expenses incurred in collecting such payment.

14) **Additional Terms for Specific Products and Services.** If a User is making one of the uses described in this Section 14, the additional terms and conditions apply:

a) ***Print Uses of Academic Course Content and Materials (photocopies for academic coursepacks or classroom handouts).*** For photocopies for academic coursepacks or classroom handouts the following additional terms apply:

i) The copies and anthologies created under this License may be made and assembled by faculty members individually or at their request by on-campus bookstores or copy centers, or by off-campus copy shops and other similar entities.

ii) No License granted shall in any way: (i) include any right by User to create a substantively non-identical copy of the Work or to edit or in any other way modify the Work (except by means of deleting material immediately preceding or following the entire portion of the Work copied) (ii) permit "publishing ventures" where any particular anthology would be systematically marketed at multiple institutions.

iii) Subject to any Publisher Terms (and notwithstanding any apparent contradiction in the Order Confirmation arising from data provided by User), any use authorized under the academic pay-per-use service is limited as follows:

A) any License granted shall apply to only one class (bearing a unique identifier as assigned by the institution, and thereby including all sections or other subparts of the class) at one institution;

B) use is limited to not more than 25% of the text of a book or of the items in a published collection of essays, poems or articles;

C) use is limited to no more than the greater of (a) 25% of the text of an issue of a journal or other periodical or (b) two articles from such an issue;

D) no User may sell or distribute any particular anthology, whether photocopied or electronic, at more than one institution of learning;

E) in the case of a photocopy permission, no materials may be entered into electronic memory by User except in order to produce an identical copy of a Work before or during the academic term (or analogous period) as to which any particular permission is granted. In the event that User shall choose to retain materials that are the subject of a photocopy permission in electronic memory for purposes of producing identical copies more than one day after such retention (but still within the scope of any permission granted), User must notify CCC of such fact in the applicable permission request and such retention shall constitute one copy actually sold for purposes of calculating permission fees due; and

F) any permission granted shall expire at the end of the class. No permission granted shall in any way include any right by User to create a substantively non-identical copy of the Work or to edit or in any other way modify the Work (except by means of deleting material immediately preceding or following the entire portion of the Work copied).

iv) Books and Records; Right to Audit. As to each permission granted under the academic pay-per-use Service, User shall maintain for at least four full calendar years books and records sufficient for CCC to determine the numbers of copies made by User under such permission. CCC and any representatives it may designate shall have the right to audit such books and records at any time during User's ordinary business hours, upon two days' prior notice. If any such audit shall determine that User shall have underpaid for, or underreported, any photocopies sold or by three percent (3%) or more, then User shall bear all the costs of any such audit; otherwise, CCC shall bear the costs of any such audit. Any amount determined by such audit to have been underpaid by User shall immediately be paid to CCC by User, together with interest thereon at the rate of 10% per annum from the date such amount was originally due. The provisions of this paragraph shall survive the termination of this License for any reason.

b) ***Digital Pay-Per-Uses of Academic Course Content and Materials (e-coursepacks, electronic reserves, learning management systems, academic institution intranets).*** For uses in e-coursepacks, posts in electronic reserves, posts in learning management systems, or posts on academic institution intranets, the following additional terms apply:

i) The pay-per-uses subject to this Section 14(b) include:

A) **Posting e-reserves, course management systems, e-coursepacks for text-based content,** which grants authorizations to import requested material in electronic format, and allows electronic access to this material to members of a designated college or university class, under the direction of an instructor designated by the college or university, accessible only under appropriate electronic controls (e.g., password);

B) **Posting e-reserves, course management systems, e-coursepacks for material consisting of photographs or other still images not embedded in text,** which grants not only the authorizations

described in Section 14(b)(i)(A) above, but also the following authorization: to include the requested material in course materials for use consistent with Section 14(b)(i)(A) above, including any necessary resizing, reformatting or modification of the resolution of such requested material (provided that such modification does not alter the underlying editorial content or meaning of the requested material, and provided that the resulting modified content is used solely within the scope of, and in a manner consistent with, the particular authorization described in the Order Confirmation and the Terms), but not including any other form of manipulation, alteration or editing of the requested material;

C) **Posting e-reserves, course management systems, e-coursepacks or other academic distribution for audiovisual content,** which grants not only the authorizations described in Section 14(b)(i)(A) above, but also the following authorizations: (i) to include the requested material in course materials for use consistent with Section 14(b)(i)(A) above; (ii) to display and perform the requested material to such members of such class in the physical classroom or remotely by means of streaming media or other video formats; and (iii) to "clip" or reformat the requested material for purposes of time or content management or ease of delivery, provided that such "clipping" or reformatting does not alter the underlying editorial content or meaning of the requested material and that the resulting material is used solely within the scope of, and in a manner consistent with, the particular authorization described in the Order Confirmation and the Terms. Unless expressly set forth in the relevant Order Conformation, the License does not authorize any other form of manipulation, alteration or editing of the requested material.

ii) Unless expressly set forth in the relevant Order Confirmation, no License granted shall in any way: (i) include any right by User to create a substantively non-identical copy of the Work or to edit or in any other way modify the Work (except by means of deleting material immediately preceding or following the entire portion of the Work copied or, in the case of Works subject to Sections 14(b)(1)(B) or (C) above, as described in such Sections) (ii) permit "publishing ventures" where any particular course materials would be systematically marketed at multiple institutions.

iii) Subject to any further limitations determined in the Rightsholder Terms (and notwithstanding any apparent contradiction in the Order Confirmation arising from data provided by User), any use authorized under the electronic course content pay-per-use service is limited as follows:

A) any License granted shall apply to only one class (bearing a unique identifier as assigned by the institution, and thereby including all sections or other subparts of the class) at one institution;

B) use is limited to not more than 25% of the text of a book or of the items in a published collection of essays, poems or articles;

C) use is limited to not more than the greater of (a) 25% of the text of an issue of a journal or other periodical or (b) two articles from such an issue;

D) no User may sell or distribute any particular materials, whether photocopied or electronic, at more than one institution of learning;

E) electronic access to material which is the subject of an electronic-use permission must be limited by means of electronic password, student identification or other control permitting access solely to students and instructors in the class;

F) User must ensure (through use of an electronic cover page or other appropriate means) that any person, upon gaining electronic access to the material, which is the subject of a permission, shall see:

- a proper copyright notice, identifying the Rightsholder in whose name CCC has granted permission,
- a statement to the effect that such copy was made pursuant to permission,
- a statement identifying the class to which the material applies and notifying the reader that the material has been made available electronically solely for use in the class, and
- a statement to the effect that the material may not be further distributed to any person outside the class, whether by copying or by transmission and whether electronically or in paper form, and User must also ensure that such cover page or other means will print out in the event that the person accessing the material chooses to print out the material or any part thereof.

G) any permission granted shall expire at the end of the class and, absent some other form of authorization, User is thereupon required to delete the applicable material from any electronic storage or to block electronic access to the applicable material.

iv) Uses of separate portions of a Work, even if they are to be included in the same course material or the same university or college class, require separate permissions under the electronic course content pay-per-use Service. Unless otherwise provided in the Order Confirmation, any grant of rights to User is limited to use completed no later than the end of the academic term (or analogous period) as to which any particular permission is granted.

v) Books and Records; Right to Audit. As to each permission granted under the electronic course content Service, User shall maintain for at least four full calendar years books and records sufficient for CCC to determine the numbers of copies made by User under such permission. CCC and any representatives it may designate shall have the right to audit such books and records at any time during User's ordinary business hours, upon two days' prior notice. If any such audit shall determine that User shall have underpaid for, or underreported, any electronic copies used by three percent (3%) or more, then User shall bear all the costs of any such audit; otherwise, CCC shall bear the costs of any such audit. Any amount determined by such audit to have been underpaid by User shall immediately be paid to CCC by User, together with interest thereon at the rate of 10% per annum from the date such amount was originally due. The provisions of this paragraph shall survive the termination of this license for any reason.

c) ***Pay-Per-Use Permissions for Certain Reproductions (Academic photocopies for library reserves and interlibrary loan reporting) (Non-academic internal/external business uses and commercial document delivery).*** The License expressly excludes the uses listed in Section (c)(i)-(v) below (which must be subject to separate license from the applicable Rightsholder) for: academic photocopies for library reserves and interlibrary loan reporting; and non-academic internal/external business uses and commercial document delivery.

i) electronic storage of any reproduction (whether in plain-text, PDF, or any other format) other than on a transitory basis;

ii) the input of Works or reproductions thereof into any computerized database;

iii) reproduction of an entire Work (cover-to-cover copying) except where the Work is a single article;

iv) reproduction for resale to anyone other than a specific customer of User;

v) republication in any different form. Please obtain authorizations for these uses through other CCC services or directly from the rightsholder.

Any license granted is further limited as set forth in any restrictions included in the Order Confirmation and/or in these Terms.

d) ***Electronic Reproductions in Online Environments (Non-Academic-email, intranet, internet and extranet).*** For "electronic reproductions", which generally includes e-mail use (including instant messaging or other electronic transmission to a defined group of recipients) or posting on an intranet, extranet or Intranet site (including any display or performance incidental thereto), the following additional terms apply:

i) Unless otherwise set forth in the Order Confirmation, the License is limited to use completed within 30 days for any use on the Internet, 60 days for any use on an intranet or extranet and one year for any other use, all as measured from the "republication date" as identified in the Order Confirmation, if any, and otherwise from the date of the Order Confirmation.

ii) User may not make or permit any alterations to the Work, unless expressly set forth in the Order Confirmation (after request by User and approval by Rightsholder); provided, however, that a Work consisting of photographs or other still images not embedded in text may, if necessary, be resized, reformatted or have its resolution modified without additional express permission, and a Work consisting of audiovisual content may, if necessary, be "clipped" or reformatted for purposes of time or content management or ease of delivery (provided that any such resizing, reformatting, resolution modification or "clipping" does not alter the underlying editorial content or meaning of the Work used, and that the resulting material is used solely within the scope of, and in a manner consistent with, the particular License described in the Order Confirmation and the Terms.

15) **Miscellaneous.**

a) User acknowledges that CCC may, from time to time, make changes or additions to the Service or to the Terms, and that Rightsholder may make changes or additions to the Rightsholder Terms. Such updated Terms will replace the prior terms and conditions in the order workflow and shall be effective as to any subsequent Licenses but shall not apply to Licenses already granted and paid for under a prior set of terms.

b) Use of User-related information collected through the Service is governed by CCC's privacy policy, available online at www.copyright.com/about/privacy-policy/.

c) The License is personal to User. Therefore, User may not assign or transfer to any other person (whether a natural person or an organization of any kind) the License or any rights granted thereunder; provided, however, that, where

applicable, User may assign such License in its entirety on written notice to CCC in the event of a transfer of all or substantially all of User's rights in any new material which includes the Work(s) licensed under this Service.

d) No amendment or waiver of any Terms is binding unless set forth in writing and signed by the appropriate parties, including, where applicable, the Rightsholder. The Rightsholder and CCC hereby object to any terms contained in any writing prepared by or on behalf of the User or its principals, employees, agents or affiliates and purporting to govern or otherwise relate to the License described in the Order Confirmation, which terms are in any way inconsistent with any Terms set forth in the Order Confirmation, and/or in CCC's standard operating procedures, whether such writing is prepared prior to, simultaneously with or subsequent to the Order Confirmation, and whether such writing appears on a copy of the Order Confirmation or in a separate instrument.

e) The License described in the Order Confirmation shall be governed by and construed under the law of the State of New York, USA, without regard to the principles thereof of conflicts of law. Any case, controversy, suit, action, or proceeding arising out of, in connection with, or related to such License shall be brought, at CCC's sole discretion, in any federal or state court located in the County of New York, State of New York, USA, or in any federal or state court whose geographical jurisdiction covers the location of the Rightsholder set forth in the Order Confirmation. The parties expressly submit to the personal jurisdiction and venue of each such federal or state court.

Last updated October 2022

IISER PUNE

Figure 1.3

Chatterjee Joy <chatterjee.joy@students.iiserpune.ac.in>

Request for copyright license to reuse figure of a paper in my thesis/dissertation

1 message

ACS Publications <acs@service-now.com> Mon, Jun 24, 2024 at 4:10 PM
Reply-To: support@services.acs.org
To: chatterjee.joy@students.iiserpune.ac.in

Dear Dr. Chatterjee Joy,

Thank you for contacting ACS Publications Support.

Your permission requested is granted as long as your thesis won't be sold, and there is no fee for this reuse. In your planned reuse, you must cite the ACS article as the source, add this direct link https://pubs.acs.org/doi/10.1021/acs.chemrev.7b00776.

I hope that you find this useful! If you require any further assistance, please feel free to contact us.

Best regards,
Dimitrije Bozovic
ACS Publications Support
Customer Services & Information
Website: https://acs.service-now.com/acs
Email: support@services.acs.org
Phone: 800-227-9919 | 202-872-(HELP) 4357

Case Info:

Case Number : CSCSI0218326

Created On: 06-24-2024 06:13:37 AM EDT

Short Description: Request for copyright license to reuse figure of a paper in my thesis/dissertation

Description: Dear ACS copyright office,
I would like to reuse a
figure from a *Chemical Reviews* paper for my PhD thesis/dissertation. The
details of the paper are as follows,
*Paper: * *Chem. Rev.**2018*, 118, 10, 4981–5079. (DOI:
10.1021/acs.chemrev.7b00776).
Figure no. 1.

Please provide the copyright at your earliest convenience.

Sincerely Yours,

জয় চ্যাটার্জি
Joy Chatterjee
Senior Research Fellow
IISER Pune
Reg. No. 20162016
LinkedIn <http://www.linkedin.com/in/joy-chatterjee-787923235>
Google Scholar
<https://scholar.google.com/citations?user=XDncyucAAAAJ&hl=en>
Twitter <https://twitter.com/CJoy_sapiens>

Ref:MSG1722130_TJm8V5cXewQTVcv7CPQW

Figure 1.4b

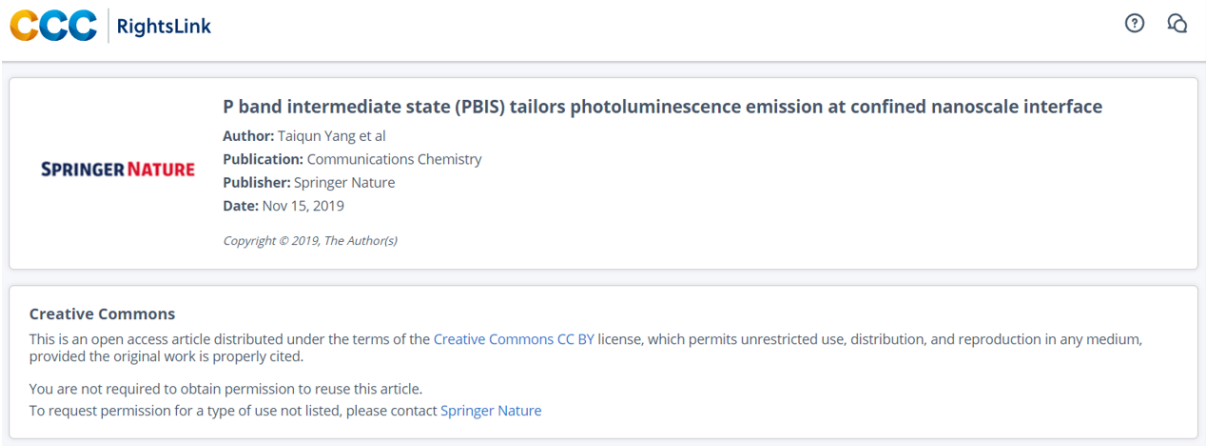
RightsLink
SPRINGER NATURE
P band intermediate state (PBIS) tailors photoluminescence emission at confined nanoscale interface
Author: Taiqun Yang et al
Publication: Communications Chemistry
Publisher: Springer Nature
Date: Nov 15, 2019
Copyright © 2019, The Author(s)
Creative Commons
This is an open access article distributed under the terms of the Creative Commons CC BY license, which permits unrestricted use, distribution, and reproduction in any medium, provided the original work is properly cited.
You are not required to obtain permission to reuse this article.
To request permission for a type of use not listed, please contact Springer Nature

SPRINGER NATURE LICENSE
TERMS AND CONDITIONS

Figure 1.5

Jun 21, 2024

This Agreement between Joy Chatterjee ("You") and Springer Nature ("Springer Nature") consists of your license details and the terms and conditions provided by Springer Nature and Copyright Clearance Center.

License Number	5813840116000
License date	Jun 21, 2024
Licensed Content Publisher	Springer Nature
Licensed Content Publication	Nature
Licensed Content Title	Highly efficient organic light-emitting diodes from delayed fluorescence
Licensed Content Author	Hiroki Uoyama et al
Licensed Content Date	Dec 12, 2012
Type of Use	Thesis/Dissertation
Requestor type	academic/university or research institute
Format	print and electronic
Portion	figures/tables/illustrations
Number of figures/tables/illustrations	1
Would you like a high resolution image with your order?	no

Will you be translating?	no
Circulation/distribution	1 - 29
Author of this Springer Nature content	no
Title of new work	Emission tunability, triplet state harvesting, and photon up-conversion properties in selected organic-inorganic hybrid Cu(I)-based frameworks.
Institution name	Indian Institute of Science Education and Research Pune
Expected presentation date	Sep 2024
Portions	Figure 1
The Requesting Person / Organization to Appear on the License	Joy Chatterjee
Requestor Location	Mr. Joy Chatterjee IISER Hostel 2, Dr. Homi Bhabha Road Pashan Pune-411008 Pune, Maharashtra 411008 India Attn: Mr. Joy Chatterjee
Billing Type	Invoice
Billing Address	Mr. Joy Chatterjee IISER Hostel 2, Dr. Homi Bhabha Road Pashan Pune-411008 Pune, India 411008 Attn: Mr. Joy Chatterjee
Total	0.00 USD
Terms and Conditions	

Springer Nature Customer Service Centre GmbH Terms and Conditions

The following terms and conditions ("Terms and Conditions") together with the terms specified in your [RightsLink] constitute the License ("License") between you as Licensee and Springer Nature Customer Service Centre GmbH as Licensor. By clicking 'accept' and completing the transaction for your use of the material ("Licensed Material"), you confirm your acceptance of and obligation to be bound by these Terms and Conditions.

1. Grant and Scope of License

1. 1. The Licensor grants you a personal, non-exclusive, non-transferable, non-sublicensable, revocable, world-wide License to reproduce, distribute, communicate to the public, make available, broadcast, electronically transmit or create derivative works using the Licensed Material for the purpose(s) specified in your RightsLink Licence Details only. Licenses are granted for the specific use requested in the order and for no other use, subject to these Terms and Conditions. You acknowledge and agree that the rights granted to you under this License do not include the right to modify, edit, translate, include in collective works, or create derivative works of the Licensed Material in whole or in part unless expressly stated in your RightsLink Licence Details. You may use the Licensed Material only as permitted under this Agreement and will not reproduce, distribute, display, perform, or otherwise use or exploit any Licensed Material in any way, in whole or in part, except as expressly permitted by this License.

1. 2. You may only use the Licensed Content in the manner and to the extent permitted by these Terms and Conditions, by your RightsLink Licence Details and by any applicable laws.

1. 3. A separate license may be required for any additional use of the Licensed Material, e.g. where a license has been purchased for print use only, separate permission must be obtained for electronic re-use. Similarly, a License is only valid in the language selected and does not apply for editions in other languages unless additional translation rights have been granted separately in the License.

1. 4. Any content within the Licensed Material that is owned by third parties is expressly excluded from the License.

1. 5. Rights for additional reuses such as custom editions, computer/mobile applications, film or TV reuses and/or any other derivative rights requests require additional permission and may be subject to an additional fee. Please apply to journalpermissions@springernature.com or bookpermissions@springernature.com for these rights.

2. Reservation of Rights

Licensor reserves all rights not expressly granted to you under this License. You acknowledge and agree that nothing in this License limits or restricts Licensor's rights in or use of the Licensed Material in any way. Neither this License, nor any act, omission, or statement by Licensor or you, conveys any ownership right to you in any Licensed Material, or to any element or portion thereof. As between Licensor and you, Licensor owns and retains all right, title, and interest in and to the Licensed Material subject to the license granted in Section 1.1. Your permission to use the Licensed Material is expressly conditioned on you not impairing Licensor's or the applicable copyright owner's rights in the Licensed Material in any way.

3. Restrictions on use

3. 1. Minor editing privileges are allowed for adaptations for stylistic purposes or formatting purposes provided such alterations do not alter the original meaning or

intention of the Licensed Material and the new figure(s) are still accurate and representative of the Licensed Material. Any other changes including but not limited to, cropping, adapting, and/or omitting material that affect the meaning, intention or moral rights of the author(s) are strictly prohibited.

3. 2. You must not use any Licensed Material as part of any design or trademark.

3. 3. Licensed Material may be used in Open Access Publications (OAP), but any such reuse must include a clear acknowledgment of this permission visible at the same time as the figures/tables/illustration or abstract and which must indicate that the Licensed Material is not part of the governing OA license but has been reproduced with permission. This may be indicated according to any standard referencing system but must include at a minimum 'Book/Journal title, Author, Journal Name (if applicable), Volume (if applicable), Publisher, Year, reproduced with permission from SNCSC'.

4. STM Permission Guidelines

4. 1. An alternative scope of license may apply to signatories of the STM Permissions Guidelines ("STM PG") as amended from time to time and made available at https://www.stm-assoc.org/intellectual-property/permissions/permissions-guidelines/.

4. 2. For content reuse requests that qualify for permission under the STM PG, and which may be updated from time to time, the STM PG supersede the terms and conditions contained in this License.

4. 3. If a License has been granted under the STM PG, but the STM PG no longer apply at the time of publication, further permission must be sought from the Rightsholder. Contact journalpermissions@springernature.com or bookpermissions@springernature.com for these rights.

5. Duration of License

5. 1. Unless otherwise indicated on your License, a License is valid from the date of purchase ("License Date") until the end of the relevant period in the below table:

Reuse in a medical communications project	Reuse up to distribution or time period indicated in License
Reuse in a dissertation/thesis	Lifetime of thesis
Reuse in a journal/magazine	Lifetime of journal/magazine
Reuse in a book/textbook	Lifetime of edition
Reuse on a website	1 year unless otherwise specified in the License
Reuse in a presentation/slide kit/poster	Lifetime of presentation/slide kit/poster. Note: publication whether electronic or in print of presentation/slide kit/poster may require further permission.
Reuse in conference proceedings	Lifetime of conference proceedings
Reuse in an annual report	Lifetime of annual report
Reuse in training/CME materials	Reuse up to distribution or time period indicated in License
Reuse in newsmedia	Lifetime of newsmedia

Reuse in coursepack/classroom materials	Reuse up to distribution and/or time period indicated in license

6. Acknowledgement

6. 1. The Licensor's permission must be acknowledged next to the Licensed Material in print. In electronic form, this acknowledgement must be visible at the same time as the figures/tables/illustrations or abstract and must be hyperlinked to the journal/book's homepage.

6. 2. Acknowledgement may be provided according to any standard referencing system and at a minimum should include "Author, Article/Book Title, Journal name/Book imprint, volume, page number, year, Springer Nature".

7. Reuse in a dissertation or thesis

7. 1. Where 'reuse in a dissertation/thesis' has been selected, the following terms apply: Print rights of the Version of Record are provided for; electronic rights for use only on institutional repository as defined by the Sherpa guideline (www.sherpa.ac.uk/romeo/) and only up to what is required by the awarding institution.

7. 2. For theses published under an ISBN or ISSN, separate permission is required. Please contact journalpermissions@springernature.com or bookpermissions@springernature.com for these rights.

7. 3. Authors must properly cite the published manuscript in their thesis according to current citation standards and include the following acknowledgement: '*Reproduced with permission from Springer Nature*'.

8. License Fee

You must pay the fee set forth in the License Agreement (the "License Fees"). All amounts payable by you under this License are exclusive of any sales, use, withholding, value added or similar taxes, government fees or levies or other assessments. Collection and/or remittance of such taxes to the relevant tax authority shall be the responsibility of the party who has the legal obligation to do so.

9. Warranty

9. 1. The Licensor warrants that it has, to the best of its knowledge, the rights to license reuse of the Licensed Material. **You are solely responsible for ensuring that the material you wish to license is original to the Licensor and does not carry the copyright of another entity or third party (as credited in the published version).** If the credit line on any part of the Licensed Material indicates that it was reprinted or adapted with permission from another source, then you should seek additional permission from that source to reuse the material.

9. 2. EXCEPT FOR THE EXPRESS WARRANTY STATED HEREIN AND TO THE EXTENT PERMITTED BY APPLICABLE LAW, LICENSOR PROVIDES THE LICENSED MATERIAL "AS IS" AND MAKES NO OTHER REPRESENTATION OR WARRANTY. LICENSOR EXPRESSLY DISCLAIMS ANY LIABILITY FOR ANY CLAIM ARISING FROM OR OUT OF THE CONTENT, INCLUDING BUT NOT LIMITED TO ANY ERRORS, INACCURACIES, OMISSIONS, OR DEFECTS CONTAINED THEREIN, AND ANY IMPLIED OR EXPRESS WARRANTY AS TO MERCHANTABILITY OR FITNESS FOR A PARTICULAR PURPOSE. IN NO EVENT SHALL LICENSOR

BE LIABLE TO YOU OR ANY OTHER PARTY OR ANY OTHER PERSON OR FOR ANY SPECIAL, CONSEQUENTIAL, INCIDENTAL, INDIRECT, PUNITIVE, OR EXEMPLARY DAMAGES, HOWEVER CAUSED, ARISING OUT OF OR IN CONNECTION WITH THE DOWNLOADING, VIEWING OR USE OF THE LICENSED MATERIAL REGARDLESS OF THE FORM OF ACTION, WHETHER FOR BREACH OF CONTRACT, BREACH OF WARRANTY, TORT, NEGLIGENCE, INFRINGEMENT OR OTHERWISE (INCLUDING, WITHOUT LIMITATION, DAMAGES BASED ON LOSS OF PROFITS, DATA, FILES, USE, BUSINESS OPPORTUNITY OR CLAIMS OF THIRD PARTIES), AND WHETHER OR NOT THE PARTY HAS BEEN ADVISED OF THE POSSIBILITY OF SUCH DAMAGES. THIS LIMITATION APPLIES NOTWITHSTANDING ANY FAILURE OF ESSENTIAL PURPOSE OF ANY LIMITED REMEDY PROVIDED HEREIN.

10. Termination and Cancellation

10. 1. The License and all rights granted hereunder will continue until the end of the applicable period shown in Clause 5.1 above. Thereafter, this license will be terminated and all rights granted hereunder will cease.

10. 2. Licensor reserves the right to terminate the License in the event that payment is not received in full or if you breach the terms of this License.

11. General

11. 1. The License and the rights and obligations of the parties hereto shall be construed, interpreted and determined in accordance with the laws of the Federal Republic of Germany without reference to the stipulations of the CISG (United Nations Convention on Contracts for the International Sale of Goods) or to Germany´s choice-of-law principle.

11. 2. The parties acknowledge and agree that any controversies and disputes arising out of this License shall be decided exclusively by the courts of or having jurisdiction for Heidelberg, Germany, as far as legally permissible.

11. 3. This License is solely for Licensor's and Licensee's benefit. It is not for the benefit of any other person or entity.

Questions? For questions on Copyright Clearance Center accounts or website issues please contact springernaturesupport@copyright.com or +1-855-239-3415 (toll free in the US) or +1-978-646-2777. For questions on Springer Nature licensing please visit https://www.springernature.com/gp/partners/rights-permissions-third-party-distribution

Other Conditions:

Version 1.4 - Dec 2022

Questions? customercare@copyright.com.

Figure 1.6a

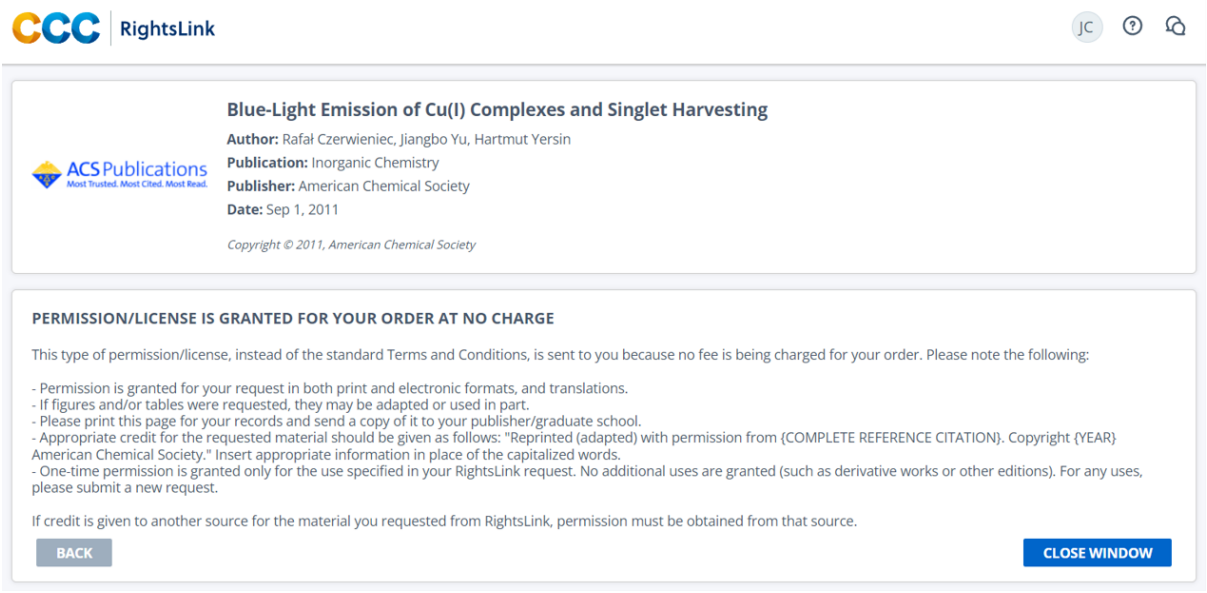
RightsLink
JC
Blue-Light Emission of Cu(I) Complexes and Singlet Harvesting
Author: Rafał Czerwieniec, Jiangbo Yu, Hartmut Yersin
Publication: Inorganic Chemistry
Publisher: American Chemical Society
Date: Sep 1, 2011
Copyright © 2011, American Chemical Society
PERMISSION/LICENSE IS GRANTED FOR YOUR ORDER AT NO CHARGE
This type of permission/license, instead of the standard Terms and Conditions, is sent to you because no fee is being charged for your order. Please note the following:
- Permission is granted for your request in both print and electronic formats, and translations.
- If figures and/or tables were requested, they may be adapted or used in part.
- Please print this page for your records and send a copy of it to your publisher/graduate school.
- Appropriate credit for the requested material should be given as follows: "Reprinted (adapted) with permission from {COMPLETE REFERENCE CITATION}. Copyright {YEAR} American Chemical Society." Insert appropriate information in place of the capitalized words.
- One-time permission is granted only for the use specified in your RightsLink request. No additional uses are granted (such as derivative works or other editions). For any uses, please submit a new request.
If credit is given to another source for the material you requested from RightsLink, permission must be obtained from that source.
BACK
CLOSE WINDOW

IISER PUNE

Figure 1.6b

Chatterjee Joy <chatterjee.joy@students.iiserpune.ac.in>

Automatic reply: Request for copyright license to reuse figure of a paper in my thesis/dissertation

1 message

permissions <permissions@aaas.org> Mon, Jun 24, 2024 at 4:04 PM
To: Chatterjee Joy <chatterjee.joy@students.iiserpune.ac.in>

****This is an automated response****

You have reached the AAAS Rights & Permissions office, thank you very much for your interest in our material.

We are pleased to announce our partnership with Copyright Clearance Center's Rightslink & Republication services. With these services it is faster and easier than ever before to obtain permission to use and republish material from *Science* and its sister journals. If CCC supports the material and the reuse, you may obtain a license instantaneously. Please note that there are fees associated with most reuse of our content – the system will provide you a 'quick price' quote before you purchase.

Use one of these CCC services for an immediate response in most cases:

CCC's RightsLink Service:

When seeking reuse in a journal article, website, scientific society meetings, film & TV and others. Rightslink is accessed by clicking on the "Request Permissions" link on the right side of our online journal articles.

CCC's Republication Services:

When seeking reuse for academic books, textbooks with ancillary and derivative products and others accessed here: http://www.copyright.com

Science Advances:

CCC does not support the processing of requests for *Science Advances* content. Please submit your permission requests directly to permissions@aaas.org

Dissertation/Thesis:

You need not obtain a license. To include figures from the journals in your Dissertation/Thesis, please see our TERMS & CONDITIONS here: https://www.science.org/content/page/reprints-and-permissions. Scroll down to *Can I use AAAS material in a thesis or dissertation?*

If your reuse is not supported by either of the above CCC services please submit a request directly to permissions@aaas.org. Requests are responded to in the order received and can take up to 5-6 weeks. Per our submission guidelines, http://www.sciencemag.org/help/reprints-and-permissions Please include:

AAAS MATERIAL REQUESTED

AAAS Journal name

Article citation

Portion (eg: specific figure/photo, full article, text excerpt etc.)

DETAILS OF YOUR REUSE:

Publication Type (eg: book, journal, website, educational e-learning platform etc.)

Publication title

Article/chapter title

Author/s

Publisher

Expected publication date

Print run, eBook circulation, estimated # of views

Formats needed

Your full postal mailing address

Thank you,

***Science*/AAAS Rights & Permissions**

Figure 1.7

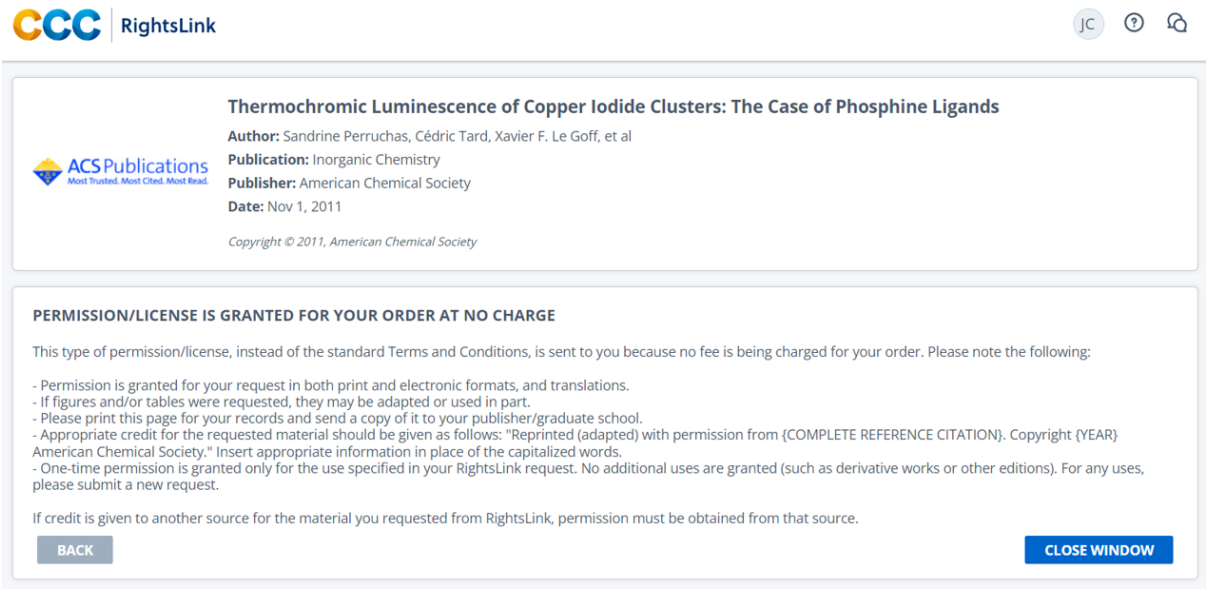
RightsLink
JC
Thermochromic Luminescence of Copper Iodide Clusters: The Case of Phosphine Ligands
Author: Sandrine Perruchas, Cédric Tard, Xavier F. Le Goff, et al
Publication: Inorganic Chemistry
Publisher: American Chemical Society
Date: Nov 1, 2011
Copyright © 2011, American Chemical Society
ACS Publications
Most Trusted. Most Cited. Most Read.
PERMISSION/LICENSE IS GRANTED FOR YOUR ORDER AT NO CHARGE
This type of permission/license, instead of the standard Terms and Conditions, is sent to you because no fee is being charged for your order. Please note the following:
- Permission is granted for your request in both print and electronic formats, and translations.
- If figures and/or tables were requested, they may be adapted or used in part.
- Please print this page for your records and send a copy of it to your publisher/graduate school.
- Appropriate credit for the requested material should be given as follows: "Reprinted (adapted) with permission from {COMPLETE REFERENCE CITATION}. Copyright {YEAR} American Chemical Society." Insert appropriate information in place of the capitalized words.
- One-time permission is granted only for the use specified in your RightsLink request. No additional uses are granted (such as derivative works or other editions). For any uses, please submit a new request.
If credit is given to another source for the material you requested from RightsLink, permission must be obtained from that source.
BACK
CLOSE WINDOW

Figure 1.8a

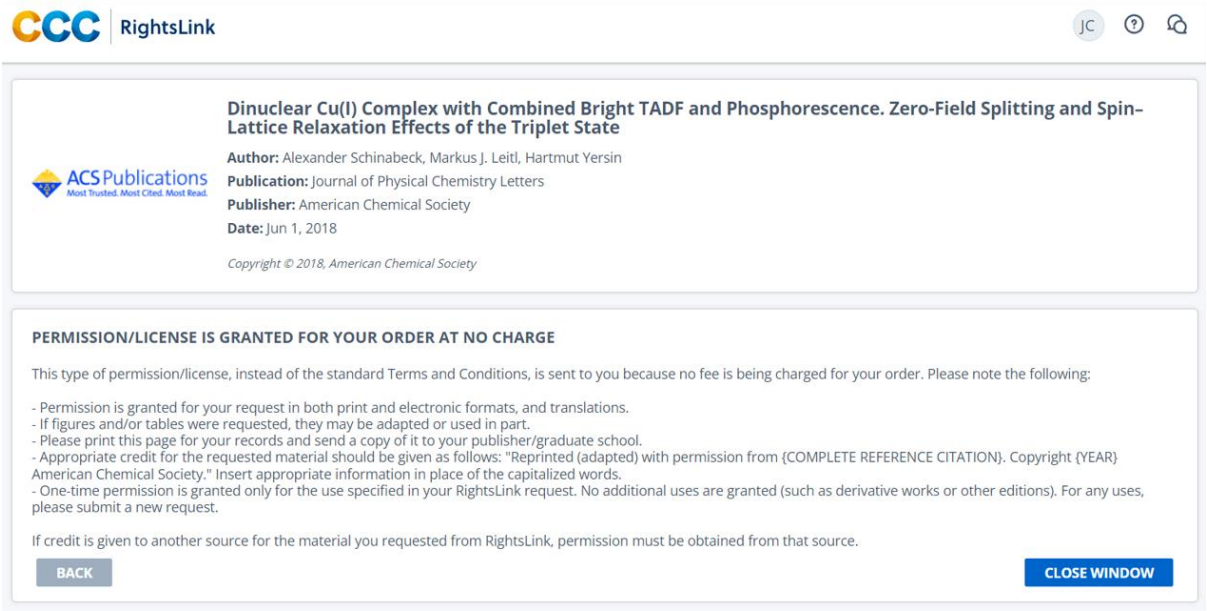
RightsLink
JC
Dinuclear Cu(I) Complex with Combined Bright TADF and Phosphorescence. Zero-Field Splitting and Spin–Lattice Relaxation Effects of the Triplet State
Author: Alexander Schinabeck, Markus J. Leitl, Hartmut Yersin
Publication: Journal of Physical Chemistry Letters
Publisher: American Chemical Society
Date: Jun 1, 2018
Copyright © 2018, American Chemical Society
ACS Publications
Most Trusted. Most Cited. Most Read.
PERMISSION/LICENSE IS GRANTED FOR YOUR ORDER AT NO CHARGE
This type of permission/license, instead of the standard Terms and Conditions, is sent to you because no fee is being charged for your order. Please note the following:
- Permission is granted for your request in both print and electronic formats, and translations.
- If figures and/or tables were requested, they may be adapted or used in part.
- Please print this page for your records and send a copy of it to your publisher/graduate school.
- Appropriate credit for the requested material should be given as follows: "Reprinted (adapted) with permission from {COMPLETE REFERENCE CITATION}. Copyright {YEAR} American Chemical Society." Insert appropriate information in place of the capitalized words.
- One-time permission is granted only for the use specified in your RightsLink request. No additional uses are granted (such as derivative works or other editions). For any uses, please submit a new request.
If credit is given to another source for the material you requested from RightsLink, permission must be obtained from that source.
BACK
CLOSE WINDOW

Figure 1.8b

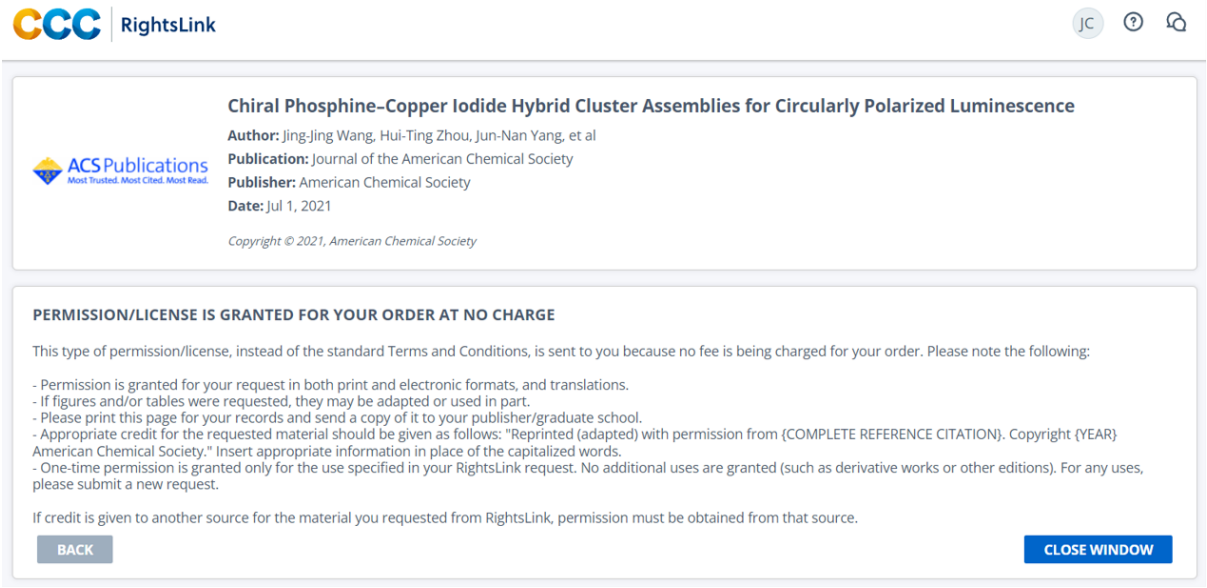
RightsLink
JC
Chiral Phosphine–Copper Iodide Hybrid Cluster Assemblies for Circularly Polarized Luminescence
Author: Jing-Jing Wang, Hui-Ting Zhou, Jun-Nan Yang, et al
Publication: Journal of the American Chemical Society
Publisher: American Chemical Society
Date: Jul 1, 2021
Copyright © 2021, American Chemical Society
ACS Publications
Most Trusted. Most Cited. Most Read.
PERMISSION/LICENSE IS GRANTED FOR YOUR ORDER AT NO CHARGE
This type of permission/license, instead of the standard Terms and Conditions, is sent to you because no fee is being charged for your order. Please note the following:
- Permission is granted for your request in both print and electronic formats, and translations.
- If figures and/or tables were requested, they may be adapted or used in part.
- Please print this page for your records and send a copy of it to your publisher/graduate school.
- Appropriate credit for the requested material should be given as follows: "Reprinted (adapted) with permission from {COMPLETE REFERENCE CITATION}. Copyright {YEAR} American Chemical Society." Insert appropriate information in place of the capitalized words.
- One-time permission is granted only for the use specified in your RightsLink request. No additional uses are granted (such as derivative works or other editions). For any uses, please submit a new request.
If credit is given to another source for the material you requested from RightsLink, permission must be obtained from that source.
BACK
CLOSE WINDOW

Figure 1.9a

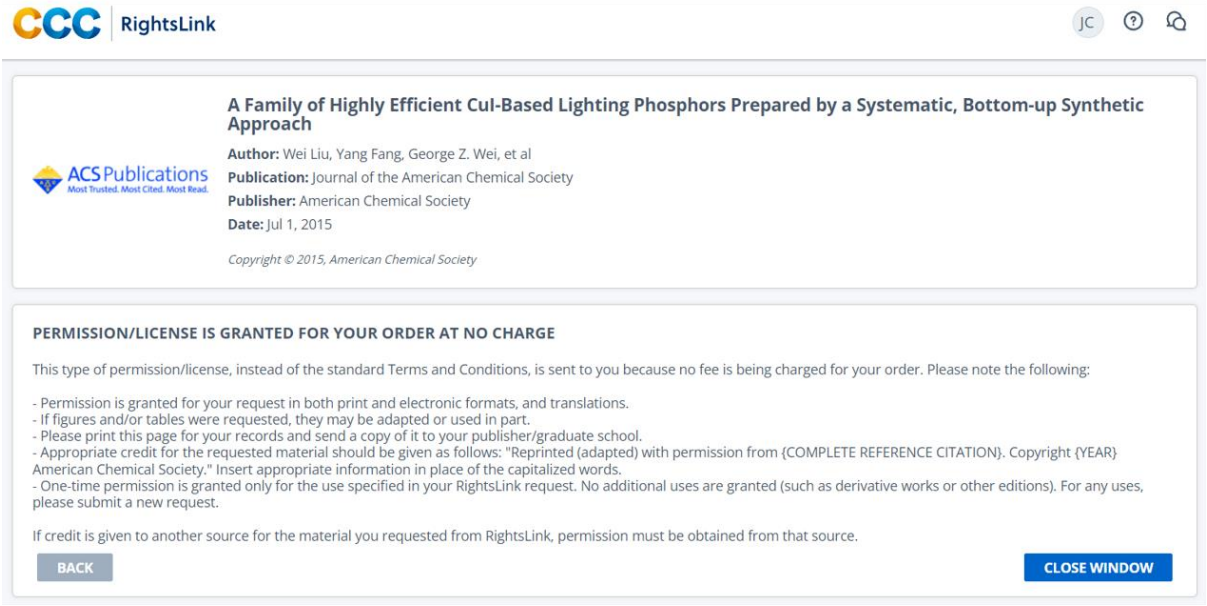
CCC RightsLink
JC
A Family of Highly Efficient CuI-Based Lighting Phosphors Prepared by a Systematic, Bottom-up Synthetic Approach
Author: Wei Liu, Yang Fang, George Z. Wei, et al
Publication: Journal of the American Chemical Society
Publisher: American Chemical Society
Date: Jul 1, 2015
Copyright © 2015, American Chemical Society
ACS Publications
Most Trusted. Most Cited. Most Read.
PERMISSION/LICENSE IS GRANTED FOR YOUR ORDER AT NO CHARGE
This type of permission/license, instead of the standard Terms and Conditions, is sent to you because no fee is being charged for your order. Please note the following:
- Permission is granted for your request in both print and electronic formats, and translations.
- If figures and/or tables were requested, they may be adapted or used in part.
- Please print this page for your records and send a copy of it to your publisher/graduate school.
- Appropriate credit for the requested material should be given as follows: "Reprinted (adapted) with permission from {COMPLETE REFERENCE CITATION}. Copyright {YEAR} American Chemical Society." Insert appropriate information in place of the capitalized words.
- One-time permission is granted only for the use specified in your RightsLink request. No additional uses are granted (such as derivative works or other editions). For any uses, please submit a new request.
If credit is given to another source for the material you requested from RightsLink, permission must be obtained from that source.
BACK
CLOSE WINDOW

Figure 1.9b

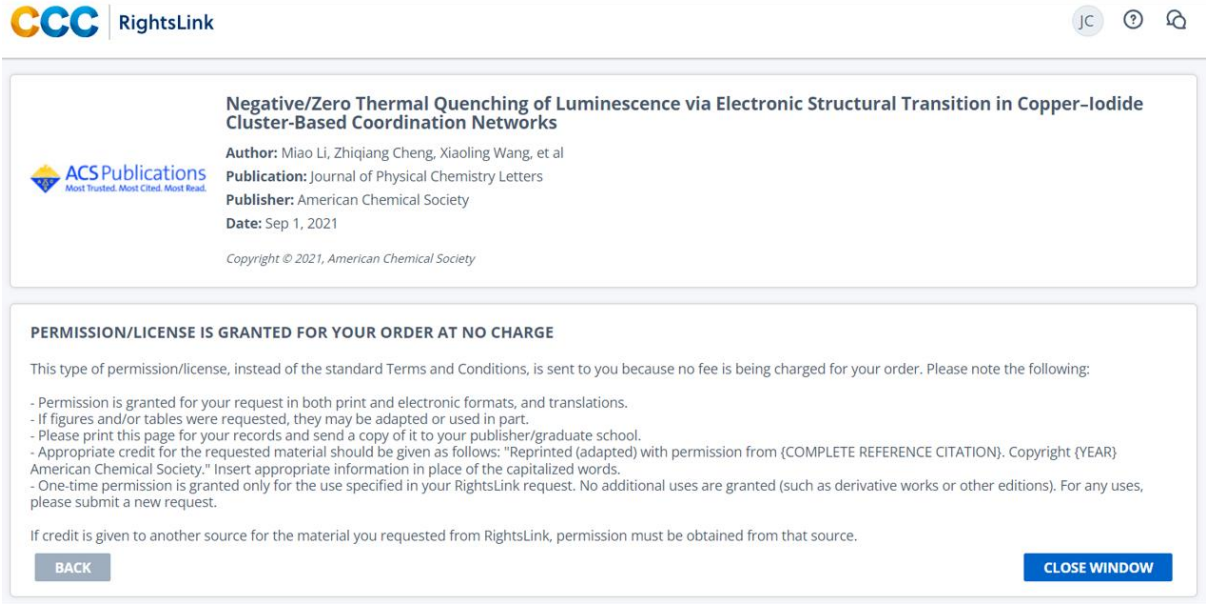
RightsLink
JC
Negative/Zero Thermal Quenching of Luminescence via Electronic Structural Transition in Copper–Iodide Cluster-Based Coordination Networks
Author: Miao Li, Zhiqiang Cheng, Xiaoling Wang, et al
Publication: Journal of Physical Chemistry Letters
Publisher: American Chemical Society
Date: Sep 1, 2021
Copyright © 2021, American Chemical Society
PERMISSION/LICENSE IS GRANTED FOR YOUR ORDER AT NO CHARGE
This type of permission/license, instead of the standard Terms and Conditions, is sent to you because no fee is being charged for your order. Please note the following:
- Permission is granted for your request in both print and electronic formats, and translations.
- If figures and/or tables were requested, they may be adapted or used in part.
- Please print this page for your records and send a copy of it to your publisher/graduate school.
- Appropriate credit for the requested material should be given as follows: "Reprinted (adapted) with permission from {COMPLETE REFERENCE CITATION}. Copyright {YEAR} American Chemical Society." Insert appropriate information in place of the capitalized words.
- One-time permission is granted only for the use specified in your RightsLink request. No additional uses are granted (such as derivative works or other editions). For any uses, please submit a new request.
If credit is given to another source for the material you requested from RightsLink, permission must be obtained from that source.
BACK
CLOSE WINDOW

Chapter 2

Intrinsic-to-extrinsic emission tuning in luminescent Cu nanoclusters by *in situ* ligand engineering

J. Chatterjee, A. Chatterjee and P. Hazra, *Phys. Chem. Chem. Phys.*, 2021, **23**, 25850 **DOI:** 10.1039/D1CP03596G

Chapter 3

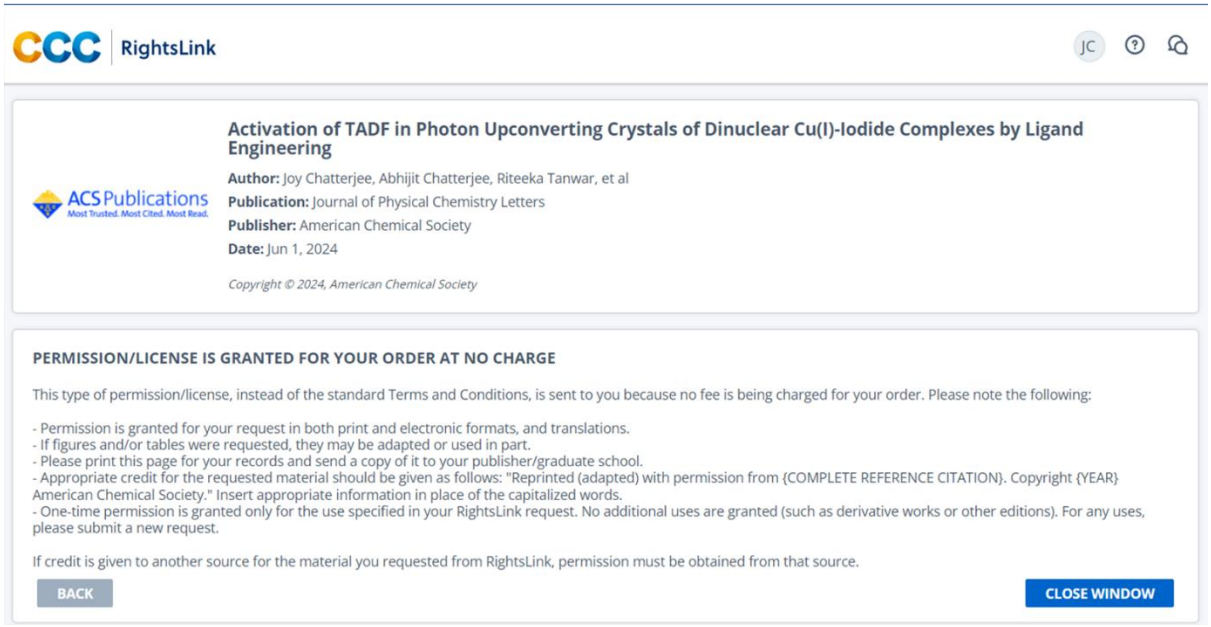
RightsLink
JC
Activation of TADF in Photon Upconverting Crystals of Dinuclear Cu(I)-Iodide Complexes by Ligand Engineering
Author: Joy Chatterjee, Abhijit Chatterjee, Riteeka Tanwar, et al
Publication: Journal of Physical Chemistry Letters
Publisher: American Chemical Society
Date: Jun 1, 2024
Copyright © 2024, American Chemical Society
ACS Publications
Most Trusted. Most Cited. Most Read.
PERMISSION/LICENSE IS GRANTED FOR YOUR ORDER AT NO CHARGE
This type of permission/license, instead of the standard Terms and Conditions, is sent to you because no fee is being charged for your order. Please note the following:
- Permission is granted for your request in both print and electronic formats, and translations.
- If figures and/or tables were requested, they may be adapted or used in part.
- Please print this page for your records and send a copy of it to your publisher/graduate school.
- Appropriate credit for the requested material should be given as follows: "Reprinted (adapted) with permission from {COMPLETE REFERENCE CITATION}. Copyright {YEAR} American Chemical Society." Insert appropriate information in place of the capitalized words.
- One-time permission is granted only for the use specified in your RightsLink request. No additional uses are granted (such as derivative works or other editions). For any uses, please submit a new request.
If credit is given to another source for the material you requested from RightsLink, permission must be obtained from that source.
BACK
CLOSE WINDOW